Light Regime Modelling in Structurally Complex Forests

Dissertation
zur
Erlangung der naturwissenschaftlichen Doktorwürde
(Dr. sc. nat.)
vorgelegt der
Mathematisch-naturwissenschaftlichen Fakultät
der
Universität Zürich

von
Daniel Kükenbrink
von
Winterthur ZH

Promotionskommission
Prof. Dr. Michael E. Schaepman
(Vorsitz der Dissertation)
Dr. Felix Morsdorf (Leitung der Dissertation)
Dr. Andreas Hueni
Prof. Dr. Romain Teyssier

Zürich, 2019

Summary

Forests are amongst the most biologically diverse terrestrial ecosystems on Earth and play a key role in the global biogeochemical and biophysical cycles. Solar radiation is the driving force in forest ecosystem functioning and productivity. The distribution of solar radiation within forest canopies further influences the abundance and diversity of species and therefore also species competition and coexistence. However, the interaction of light with canopy material and its distribution within forest canopies is still widely unknown. The structural complexity of forest canopies further complicates three-dimensional (3D), continuous measurements of the distribution of light. 3D radiative transfer models are a viable alternative to cumbersome, and often inaccurate measurements of the distribution of light within the canopy. For the parameterization of such a 3D radiative transfer model, accurate reconstruction of the forest canopy is essential. Remote sensing, and laser scanning technologies in particular, allow for high resolution assessments of the canopy structure. However, a quantitative assessment of the quality of such laser scanning acquisitions, and therefore also an assessment of the retrieved canopy structure parameters, is still a challenge.

This thesis introduces a consistent approach to quantify and assess the quality and coverage of laser scanning acquisitions of forest canopies from different platforms (airborne (ALS), terrestrial (TLS), and from unmanned aerial vehicle (UAV)). Occlusion in laser scanning acquisitions is a well known issue, causing biases in retrieved biophysical and structural parameters. With the proposed approach, we were able to quantify occluded canopy volume and to assess the influence of important acquisition parameters (e.g. pulse density, number of observation angles etc.) on the amount of occlusion. Based on the acquired laser scanning acquisition we established a 3D forest structure reconstruction approach at unprecedented levels of detail.

The high resolution canopy reconstruction builds the baseline for modelling the radiative transfer within the two studied, contrasting forest ecosystems of the temperate mixed forest on the Laegern mountain, Switzerland, and the tropical rain forest in the Lambir Hills National Park, Borneo, Malaysia. We parameterized the 3D radiative transfer model DART using the structural information retrieved from TLS and UAVLS acquisitions and leaf optical properties derived from field spectroradiometer measurements. We then simulated the 3D distribution of light within the two forest canopies at very high spatial and temporal resolution. The resulting 3D light extinction map confirmed the canopy structure as the main driver of the distribution of solar radiation within the canopy. Leaf optical properties, as measured in this thesis, were found to have only a minor influence on the overall distribution of light within the canopy. Quantified large differences to layered big-leaf models, often employed in Earth system models due to their simplicity, highlight the necessity of such highly detailed canopy reconstructions and radiative transfer models for the analysis of light related mechanisms in forest ecosystems. The introduced

approach could therefore be used to improve or benchmark the radiative transfer modules in Earth system models in order to reduce known biases caused by inaccurate modelling of the light regime within the forest canopy.

This thesis further shows and discusses the influence of vegetation on its surrounding irradiance field, based on radiative transfer modelling and *in-situ* measurements. Our results show a large impact of the irradiance field due to the presence of vegetation, both in *in-situ* measurements as well as in simulated irradiance values. We highlight the need for accurate irradiance estimates for reliable retrievals of surface reflectance and geophysical information from imaging spectroscopy data. Comparisons between measured and modelled irradiance values further validated the use of the DART radiative transfer model in conjunction with the parameterization approach introduced in this thesis.

This thesis discusses in-depth the importance of 3D canopy structure assessment and light-matter interaction modelling for the analysis of forest ecosystem functioning and productivity. Potential future research directions include upscaling of the introduced plot-level 3D light distribution modelling approach to regional- or even global-scale. With two new space-borne LiDAR instruments currently in orbit (Global Ecosystem Dynamics Investigation (GEDI) and Ice, Cloud, and land Elevation Satellite 2 (ICESat-2)) large scale information on 3D forest canopy structure will be increasingly available, albeit at a lower level of detail compared to the instruments assessed in this thesis. Radiative transfer model based sensor fusion and machine learning based emulation of radiative transfer models show further large potential in firstly decreasing computational demands of these physically complex models and secondly, in increasing the scale for analysing the radiative transfer through forest canopies. Future work on the integration of remotely sensed canopy structure and modelling of complex 3D light-matter interactions within Earth system models will further improve our understanding of forest ecosystem functioning and development.

Zusammenfassung

Wälder gehören zu den biologisch vielfältigsten terrestrischen Ökosystemen der Erde und spielen eine Schlüsselrolle in den globalen biogeochemischen und biophysikalischen Kreisläufen. Die Sonneneinstrahlung ist die treibende Kraft für die Funktionsfähigkeit und Produktivität des Waldökosystems. Die Verteilung der Sonneneinstrahlung innerhalb des Waldes beeinflusst weiterhin den Artenreichtum und die Artenvielfalt und damit auch die Konkurenz und das Zusammenleben zwischen den Arten. Wie das Licht jedoch mit der Vegetation interagiert und wie es sich innerhalb des Waldes verteilt, ist noch weitgehend unbekannt. Die strukturelle Komplexität der Wälder erschwert die dreidimensionale (3D), kontinuierliche Messungen der Lichtverteilung. 3D-Strahlungstransfermodelle sind eine nützliche Alternative zu komplizierten und oft ungenauen Messungen der Lichtverteilung im Wald. Für die Parametrisierung eines solchen 3D-Strahlungstransfermodells ist eine genaue Rekonstruktion der Waldstruktur unerlässlich. Die Fernerkundung, insbesondere die Laserscanning-Technologie, ermöglichen hochauflösende Abschätzungen der Waldstruktur. Eine quantitative Beurteilung der Qualität solcher Laserscans und damit auch eine Validierung der abgeleiteten Waldstrukturparameter ist jedoch nach wie vor eine Herausforderung.

Diese Dissertation stellt einen konsistenten Ansatz zur Quantifizierung und Bewertung der Qualität und Abdeckung von Laserscans über Wälder vor, basierend auf Messungen von verschiedenen Plattformen (luftgestützt (ALS), terrestrisch (TLS), und von unbemannten Luftfahrzeugen (UAV)). Abschattungen in Laserscans sind ein bekanntes Problem, welches zu Fehlern in Abschätzungen von biophysikalischen Parameter führt. Mit dem vorgeschlagenen Ansatz konnten wir das abgeschattete Volumen quantifizieren und den Einfluss wichtiger Laseraufnahmeparameter (z.B. Pulsdichte, Anzahl der Beobachtungswinkel etc.) auf den Grad der Abschattung beurteilen. Basierend auf multiple Laserscans haben wir einen 3D-Ansatz zur Rekonstruktion von Waldstrukturen mit beispiellosem Detaillierungsgrad entwickelt.

Die hochauflösende Waldstrukturrekonstruktion bildet die Grundlage für die Modellierung des Strahlungstransfers innerhalb der beiden untersuchten, kontrastierenden Waldkosysteme des gemigten Mischwaldes auf der Lägern in der Schweiz und des tropischen Regenwaldes im Lambir Hills Nationalpark, Borneo, Malaysia. Wir parametrierten das 3D-Strahlungstransfermodell DART unter Verwendung der Strukturinformationen aus TLS- und UAVLS-Aufnahmen und der optischen Blatteigenschaften aus Feldspektroradiometermessungen. Anschliessend simulierten wir die 3D-Lichtverteilung innerhalb der beiden Wälder mit sehr hoher räumlicher und zeitlicher Auflösung. Die daraus resultierende 3D-Lichtlverteilungskarte bestätigte die Waldstruktur als Haupttreiber für die Verteilung der Sonneneinstrahlung innerhalb des Waldes. Die optischen Eigenschaften der Blätter, wie sie in dieser Arbeit gemessen wurden, haben nur einen geringen Einfluss auf die Gesamtverteilung des

Lichts innerhalb der Waldes. Quantifizierte grosse Unterschiede zu mehrschichtigen Big-Leaf Modellen, die aufgrund ihrer Einfachheit oft in Erdsystemmodellen verwendet werden, unterstreichen die Notwendigkeit solcher hochdetaillierter Waldstrukturrekonstruktionen und Strahlungstransfermodelle für die Analyse lichtbedingter Mechanismen in Waldökosystemen. Der vorgestellte Ansatz könnte daher genutzt werden, um die Strahlungstransfermodule in Erdsystemmodellen zu verbessern oder zu benchmarken, um bekannte Fehlerquellen zu reduzieren, die durch ungenaue Modellierung des Lichtregimes innerhalb des Waldes verursacht werden.

Diese Dissertation zeigt und diskutiert zusätzlich den Einfluss der Vegetation auf das umgebende Einstrahlungsfeld, basierend auf Strahlungstransfersmodellierung und *in-situ* Messungen. Unsere Ergebnisse zeigen einen grossen Einfluss der Vegetation auf das Einstrahlungsfeld, sowohl bei *in-situ* Messungen als auch bei simulierten Einstrahlungswerten. Wir betonen die Notwendigkeit genauer Einstrahlungsstärke-Schätzungen für zuverlässige Abschätzungen von Oberflächenreflexion und geophysikalischen Informationen aus bildgebenden Spektroskopiedaten. Vergleiche zwischen gemessenen und modellierten Einstrahlungswerten validieren weiter die Verwendung des DART Strahlungstransfermodells in Verbindung mit dem in dieser Dissertation vorgestellten Parametrisierungsansatz.

Diese Dissertation beschäftigt sich eingehend mit der Bedeutung der 3D Beschreibung der Waldstruktur sowie der Modellierung der Wechselwirkung zwischen Licht und Materie für die Analyse der Funktionsweise und Produktivität von Waldökosystemen. Zu den möglichen zukünftigen Forschungsrichtungen gehört die Hochskalierung des eingeführten Modellierungsansatzes der 3D-Lichtverteilung von der Plot-Ebene auf regionaler oder sogar globaler Ebene. Mit zwei neuen weltraumgestützten LiDAR-Instrumenten (Global Ecosystem Dynamics Investigation (GEDI) und Ice, Cloud, and Land Elevation Satellite 2 (ICESat-2)), werden grossflächige Informationen über die Struktur des Waldes zunehmend verfügbar sein, wenn auch auf einem niedrigeren Detaillierungsgrad. Die Strahlungstransfermodell basierte Sensorfusion sowie die Machine Learning basierte Emulation von Strahlungstransfermodellen zeigen grosses Potenzial bei der Verringerung der rechnerischen Anforderungen dieser physikalisch komplexen Modelle und bei der Vergrösserung der Skala für die Analyse des Strahlungstransfers durch Wald Ökosysteme. Zukünftige Arbeiten zur Integration komplexer Waldstrukturinformationen und höchst detaillierte Strahlungstransfermodelle in Erdsystemmodellen werden unser Verständnis der Funktionsweise und Entwicklung des Waldökosystems weiter verbessern.

Table of Contents

List of Abbreviations

1D	One-Dimensional
3D	Three-Dimensional
a.s.l.	Above Sea Level
ALS	Airborne Laser Scanning
AMAP	botAny and Modelling of Plant Architecture and vegetation
AOD	Aerosol Optical Depth
APAR	Absorbed Photosynthetically Active Radiation
APEX	Airborne Prism EXperiment
ASD	Analytical Spectral Devices
BoA	Bottom of Atmosphere
BoC	Bottom of Canopy
BRDF	Bidirectional Reflectance Distribution Function
CAR	Carotenoids
CHL	Chlorophyll
DART	Discrete Anisotropic Radiative Transfer
DBH	Diameter at Breast Hight
DEM	Digital Elevation Model
DGVM	Dynamic Global Vegetation Model
DHP	Digital Hemispherical Photography
DSM	Digital Surface Model
DTM	Digital Terrain Model
DVM	Dynamic Vegetation Model
ED	Ecosystem Demography
ESS	Evolutionary Stable State
EUFAR	European Facility for Airborne Research
FAO	Food Agriculture Organization
FLUXNET	Flux Network
FOEN	Federal Office for the Environment
FW	Full-Waveform
FWHM	Full Width at Half Maximum
GEDI	Global Ecosystem Dynamics Investigation
GPP	Gorss Primary Productivity
GPS	Global Positioning System
ICESat-2	Ice Cloud and Elevation Satellite 2
IMU	Inertial Measurement Unit
ISS	International Space Station
LAD	Leaf Angle Distribution
LAI	Leaf Area Index
LiDAR	Light Detection And Ranging
LOP	Leaf Optical Properties
LOPEX	Leaf Optical Properties Experiment
LPJ	Lund Potsdamm Jena
LSM	Land Surface Model

LUE ..... Light Use Efficiency
LUT ..... Look Up Table
LVIS ..... Land, Vegetation, and Ice Sensor
MLS ..... Mobile Laser Scanning
MODTRAN .... MODerate resolution atmospheric TRANsmission
MOSES ..... Met Office Surface Exchange Scheme
NASA ..... National Aeronautics and Space Administration
NFI ..... National Forest Inventory
NIR ..... Near Infrared
NIST ..... National Institute of Standards and Technology
PAD ..... Plant Area Density
PAI ..... Plant Area Index
PAR ..... Photosynthetically Active Radiation
PPFD ..... Photosynthetic Photon Flux Density
PRI ..... Photochemical Reflectance Index
PRR ..... Pulse Repetition Rate
QSM ..... Quantitative Structure Model
RAMI ..... Radiation Transfer Model Intercomparison
RASTA ..... Spectral Radiance Transfer Standard
REFETREE .... REFErence Tree
RGB ..... Red Green Blue
RMSE ..... Root Mean Square Error
RT ..... Radiative Transfer
SiB3 ..... Simple Biosphere Model 3
SNR ..... Signal to Noise Ratio
STD ..... Standard Deviation
SWIR ..... Short Wave Infrared
TLS ..... Terrestrial Laser Scanning
ToA ..... Top of Atmosphere
ToC ..... Top of Canopy
UAV ..... Unmanned Aerial Vehicle
UAVLS ..... Unmanned Aerial Vehicle Laser Scanning
URPP GCB ..... University Research Priority Program on Global Change and Biodiversity
UV ..... Ultra Violet
VIS ..... Visible

Chapter

1

Introduction

The three-dimensional distribution of canopy material and their variation in morphological and physiological traits within the canopy are important parameters to analyse and assess forest ecosystem functioning, diversity and productivity. Especially the radiative transfer through forest ecosystems is of special interest to broaden our understanding on forest ecosystem functioning, productivity, species competition and coexistence as well as the microclimate within the forests. Recent advances in laser scanning technologies deliver the tools to acquire and analyse the three dimensional structure of forest ecosystems in unprecedented levels of detail, allowing us to reconstruct and model complex forest ecosystems and their functioning. Section 1.1 provides an overview on a multitude of applications, possibilities and challenges of close-range laser scanning for three-dimensional reconstruction of forest canopies, but without going into detail on the radiative transfer through forest ecosystems and its ecological relevance. Therefore more details on challenges, opportunities and the ecological relevance on three-dimensional forest reconstruction and the radiative transfer within the canopy are discussed in Section 1.2. Finally, the thesis aims with the research questions and hypotheses as well as the structure of the thesis are introduced in Section 1.3.

1.1 Close-range laser scanning in forests: towards physically based semantics across scales

Morsdorf, F., **Kükenbrink, D.**, Schneider, F. D., Abegg, M., Schaepman, M.E.

This section is based on the peer-reviewed article:
Close-range laser scanning in forests: towards physically based semantics across scales
Interface Focus, 2018 (8), 1-10
DOI:10.1098/rsfs.2017.0046
and is reprinted as the final submitted manuscript.
It has been modified to fit into the layout of this thesis.

All authors designed research and wrote the paper, with main contributions of F.M.
D.K. contributed results concerning occlusion mapping from different platforms and tree structure modelling using QSM.

Abstract

Laser scanning with its unique measurement concept holds the potential to revolutionize the way we assess and quantify 3d vegetation structure. Modern laser systems used at close-range, be it on terrestrial, mobile or unmanned aerial platforms, provide dense and accurate 3D data whose information *just* waits to be harvested. However, the transformation of such data to information is not as straightforward as for airborne and space-borne approaches, where typically empirical models are built using ground-truth of target variables. Simpler variables, such as diameter at breast height, can be readily derived and validated. More complex variables, e.g. leaf area index (LAI), need a thorough understanding and consideration of the physical particularities of the measurement process and semantic labeling of the point cloud. Quantified structural models provide a framework for such labelling by deriving stem and branch architecture, a basis for many of the more complex structural variables. The physical information of the laser scanning process is still under-used and we show how it could play a vital role in conjunction with 3D radiative transfer models to shape the information retrieval methods of the future. Using such a combined forward and physically-based approach will make methods robust and transferable. In addition, it avoids replacing observer bias from field inventories with instrument bias from different laser instruments. Still, an intensive dialogue with the users of the derived information is mandatory to potentially re-design structural concepts and variables so that they profit most of the rich data that close-range laser scanning provides.

1.1.1 Introduction

Within forests, the horizontal and vertical arrangement of plants has a large impact on ecological processes, such as competition, carbon balance and nutrient and water cycling. This large role of forest structure for ecosystem functioning establishes a link between structure and diversity (MacArthur & Horn, 1969; McElhinny *et al.*, 2005), making forests of special relevance for biodiversity (Barlow *et al.*, 2007). For instance, light scattering within the forest is strongly influenced by vegetation structure and can itself feedback to structure, as light availability is an important aspect of plant establishment and survival. Thus, forest ecologists have long sought to describe the structure of forests, e.g. by measuring foliage profiles (MacArthur & Horn, 1969) or by establishing semantics and topology of tree architecture, such as Hallé (1986). Looking back, the used tools may appear to be simple, MacArthur & Horn (1969) used adapted photographic cameras to estimate height and abundance of leaves in the canopy, while Hallé (1986) used observations and drawings to derive modular structural concepts of tropical trees.

However, the variables of interest are still very relevant today. MacArthur & Horn (1969) provided a method to derive a biophysical parameter (the foliage profile) devoid of architectural semantics or topology. Hallé (1986)'s aim was to represent the complex tree architecture in forms of smaller, repeating patterns, effectively capturing the tree structure *and* semantically labeling the constituent objects (e.g. shoots, leaves and branches).

Nowadays, laser scanning is a unique and established technology, offering a convenient way to assess 3d vegetation structure. Laser scanning can be applied on different scales, from airborne systems to very high resolution ground based sensors. Such systems provide extremely dense and illustrative data sets, named "point-clouds". Opposed to traditional airborne laser scanners, close-range laser systems provide point clouds where stem, branches and even single leaves are resolved and easily identified by the human observer (see Figure 1.1). The point-cloud itself is, however, devoid of any semantic information or topology. As the datasets are typically very large and unorganized, the meaningful derivation of information is a major challenge and remains an obstacle in the way of widespread application of this technology in ecology.

Traditionally (i.e. for airborne laser scanning, ALS), many forest variables were derived in an empirical fashion by correlating field inventoried parameters (biomass, stem volume, basal area) with a set of ALS derived predictor variables (Næsset, 1997, 2002). Such approaches are infeasible with close-range laser scanning, as it is very time consuming and in most cases impossible to provide ground truth at the relevant scales (branches, leaves). Hence, for close-range laser scanning, a different, forward approach is needed to convert data to information, without the need for

prior information. This manifests the particular relevance of semantic labeling and physically-based approaches for close-range laser scanning.

In this paper, we will highlight the physical basics of laser scanning, provide some relevant technical information on current implementations in instruments (Section 1.1.2) and introduce a selection of methods that convert data to information (Section 1.1.3), devided into physical approaches and semantic labeling. In addition, we will discuss and illustrate the problematic validation of close-range laserscanning derived variables and a possible solution by radiative transfer modeling of the measurement process (Section 1.1.4). Furthermore, we will show that different types of instruments provide valuable information across scales (Section 1.1.5). Concluding, we discuss what will be needed to make the most of this recent technology for forest structure assessments.

1.1.2 Laser scanning - principles and implementations

Although the terms LiDAR and laser scanning are often used synonymously, strictly speaking, a LiDAR (Light Detection and Ranging) is only one part of an laser scanning system. With LiDARs, a laser pulse is used to measure distances between the instrument and reflecting objects (e.g. leaves, branches or stems). The distance can either be computed using the time-of-flight of a laser pulse or the phase difference of an amplitude-modulated signal. Using the instrument's location and orientation, this distance measurement can then be converted to a 3d coordinate. In terrestrial laser scanning systems, high precision measurements of the instruments rotational angles (azimuth and elevation) provide data in a local, polar coordinate system, i.e. the scanning is performed by rotating the instrument in two dimensions, while the instrument itself is stationary.

On the other hand, differential GPS and inertial navigation systems are used along side a physical scanning mechanism to transform a LiDAR into a laser scanner in airborne systems. In these systems, only one dimension is covered by the scanner, generally with a narrow field of view, while the second dimension to get 2d coverage is covered by the platform movement itself. These distinct scanning approaches lead to large within point-cloud differences in point spacing, footprint size and occlusion, which need to be considered when deriving physically-based information such as plant area index (PAI).

Since the scanning frequencies of modern systems have moved beyond the mega-Hertz mark (i.e. more than 100.000 distance measurements per second), very dense point clouds of the 3d coordinate triplets can be obtained. Most modern laser scanning systems are inherently full-waveform (FW), recording the backscattered energy over time (and range) and using processing such a Gaussian decomposition to detect the range distances of reflecting objects. FW systems provide as well the backscattered energy (opposed to just amplitude) (Wagner, 2010) and allow for the derivation of higher order moments potentially useful for discrimination of

Fig. 1.1: Laser scanning point cloud as obtained by multi-view terrestrial laser scanning in a mature temperate beech forest in leaf-off conditions. Each dot has an exact 3d coordinate and the brightness of the points is depicting the strength of the backscattered signal.

vegetation traits (Bruggisser *et al.*, 2017). Using the intensity as an additional source of information, detailed and to the human eye informative visualizations of the point clouds can be made. These have ever since led to high expectations as to what information could be derived from such datasets (Figure 1.1).

Opposed to passive optical imaging, laser intensity is not ridden by the problem of shadows, since the mono-static LiDAR setup always measures in the ”hot-spot”, i.e. the angle of maximum reflectance (Maignan *et al.*, 2004). Thus, LiDAR intensity should be very well suited to capture the reflectance of objects at the particular laser wavelength and with a properly chosen wavelength, e.g. 1064 nm, it should be possible to differ between ”green” and ”brown” biomass. However, one problem of laser intensity in forests (which is valid for all scales, from space-borne to ground-based) are effects of partially hit leaves leading to mixed pixels. As the laser footprint, i.e. the area that is illuminated by the laser, has a certain extent, some laser shots may only partially hit leaves or branches. Consequently, the measured intensity is not only a function of leaf reflectance at the laser wavelength (and leaf inclination angle in case of non-Lambertian behaving leaves), but as well of the illuminated area, which can be more or less randomly distributed. For time-of-flight systems, only the intensity is affected by this, but for phase measurements even the range measurement is impaired, leading to ghost points in-between two partially illuminated reflecting objects, often termed mixed-pixels in literature. If it was not for this setback, phase-based terrestrial laser scanners (TLS) were actually better suited for forest applications, since they are scanning much faster than time-of-flight system and are often implemented as panorama scanners, being able to cover the whole hemisphere with one scan.

Time-of-flight systems are often camera or hybrid scanners, where a second scan using a tilt mount is needed to capture the canopy directly above the scanner. Typical examples for hybrid, time-of-flight scanners is the Riegl VZ-XXXX range, while FARO

and Zoller and Fröhlich a mostly using the phase measurement concept and a full-hemispherical design. A blend of airborne laser scanning and TLS are mobile laser scanning (MLS) systems and laser scanners mounted on ultra-light aerial vehicles (UAVs or drones). MLS systems are typically using cars as the measurement platform, which limits the application in forests somewhat. These systems generally have as well a close-range to the objects of interest, so that branches and potentially leaves can be resolved, but use the advantage of the moving platform to cover more area. Depending on the choice of platform, the distribution of echoes and the perspective of the point cloud can be very different, making cross-comparisons between MLS, TLS and UAVLS difficult (Section 1.1.5b). For a technical reference, please see Vosselman & Maas (2010) and for an overview of forest applications see Maltamo *et al.* (2014). The latter provides as well very relevant theoretical considerations for LiDAR systems in forested environments (Chapters 2 and 3).

1.1.3 The point cloud - from data to information

As discussed above, modern laser scanning systems can produce a wealth of data, quickly reaching several gigabytes of points per plot unit or even within a single scan. In contrast to image data, where pixels in a grid establish spatial reference and neighborhoods and enable efficient compression, this data is unorganized and much more difficult to store, access and process. Thankfully, with the advance of the LAS format[1] and the open-source compressor LASZip[2], the former two are less of problem nowadays; the times where point-clouds would mostly come in the flavor of ill-suited ASCII files are thankfully over. However, information derivation from the point-cloud is still a challenge and we will provide some more details on typical variables and approaches, split into two parts along the lines of the works of MacArthur & Horn (1969) (physical parameters, Section 1.1.3a) and Hallé (1986) (semantic labeling, Section 1.1.3b).

1.1.3a Physical parameters and approaches

Ever since the ground-breaking work of MacArthur & Horn (1969), ecologists have used sunlight and its interception to derive quantitative biophysical parameters such as LAI or canopy cover.

The current state of the art in that respect is digital hemispherical photography (DHP), where below canopy photographs are brightness thresholded and the number of vegetation and sky pixel are computed for a range of azimuth and elevation angles. (Jonckheere *et al.*, 2004; Weiss *et al.*, 2004). When the ground-based laser systems became available, first studies showed that the gap fraction information derived by TLS and DHP are very comparable (Danson *et al.*, 2007). However, only with TLS it is possible to measure gap sizes, as in DHPs large distant gaps and close small gaps

[1] www.lasformat.org
[2] www.laszip.org

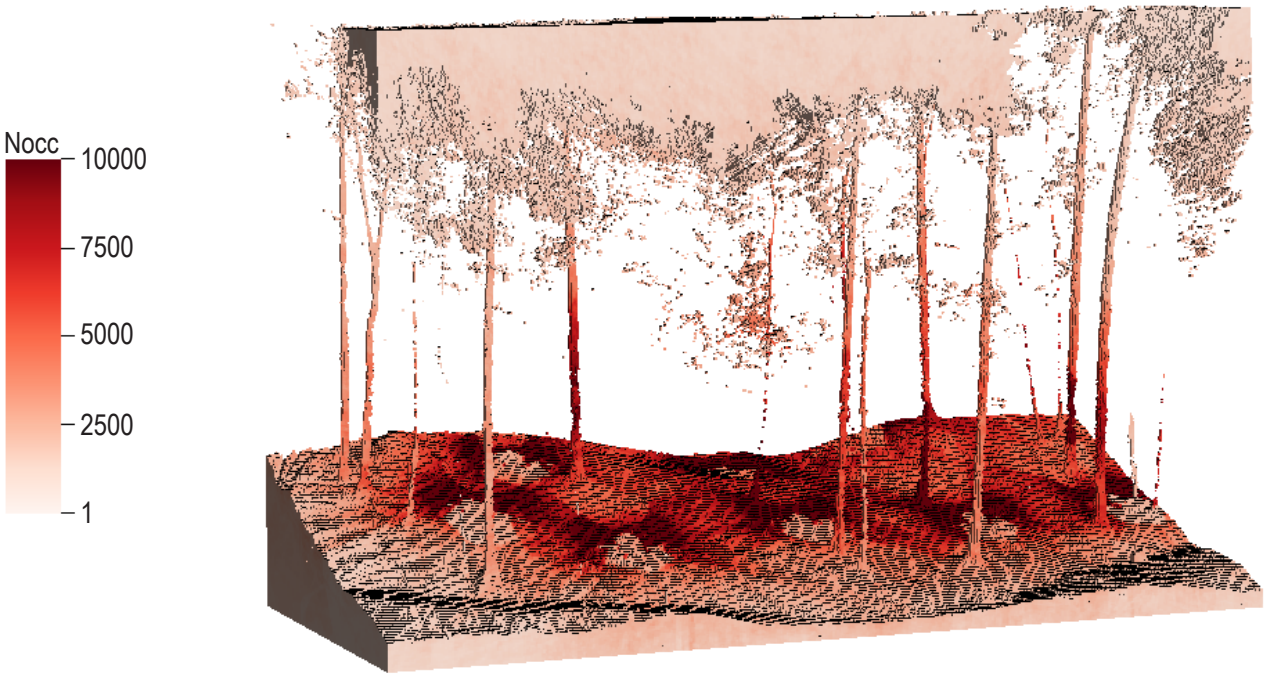

Fig. 1.2: Number of occluded laser shots per voxel as derived by ray-tracing each laser shot. Voxel size is 10 cm. Tree trunks occlude a high number (all) of the incoming shots. This physically derived information could be used to aid semantic labeling of the point cloud. For details of the methodology, see Kükenbrink *et al.* (2017).

may have the same gap fraction value. TLS produced hemispherical images add a range distance to each pixel, which helps to discern gaps of different sizes at different distances from the instrument. It has been shown that this additional information is very helpful for LAI computation (Woodgate *et al.*, 2015) and snow interception modeling (Moeser *et al.*, 2014, 2015).

One problem with estimating gap-fraction or LAI from laser scanning systems is that many approaches are very sensitive to changes in sensor and survey configuration. For instance, the echo ratios used a predictor variable can depend on laser wavelength and echo detection method implemented in a particular system. Although developed for ALS, approaches such as the one of Armston *et al.* (2013) could as well contribute to making close-range laser scanning based biophysical parameters transferable across sites and sensors. Armston *et al.* (2013) basically established a vicarious (i.e. in-situ) calibration of their laser-based gap fraction estimate under the assumption of a constant reflectance ratio between canopy and ground. This worked well in the Savannah-type ecosystem used in their study, but its performance in more complex forests and with the different constraints of close-range laser scanning still needs to be tested.

TLS focused studies have exploited laser intensity as well, for instance to derive leaf chlorophyll content (Eitel *et al.*, 2010) or wheat nitrogen content (Eitel *et al.*, 2011). However, as laser intensity can suffer from edge effects making the retrieval of leaf reflectance ill-posed (Section 1.1.2), such approaches are better suited in canopies with large leaves (such as in Eitel *et al.* (2010)) or extensive filtering of the

point cloud is needed to retain only returns from extended targets, where the laser footprint is fully contained within the reflecting object (Eitel *et al.*, 2011).

While the information content of the point-cloud depicted in Figure 1.1 may already seem overwhelming, the measurement process of laser scanning actually provides much more data. For instance, for each laser shot, we know the origin and the pointing direction, together with detected returns along the one-dimensional range spanned by the LiDAR distance measurement. Thus, we can setup a voxel grid, and trace each shot and populate the voxel with information on how many shots went through, were intersected (i.e. produced returns) or were occluded from a particular voxel. The power of this approach has been introduced to TLS by Bienert *et al.* (2010) and applied and extended to ALS by Kükenbrink *et al.* (2017) and a similar approach is used in Grau *et al.* (2017). These approaches provide additional information useful for a better derivation of PAI and help to reduce the data to facilitate segmentation of single trees (Bienert *et al.*, 2010).

Using the approach from Kükenbrink *et al.* (2017), Figure 1.2 shows the occluded voxel in multi-station TLS dataset from a winterly (leaf-off) beech forest (Lägeren, Switzerland). Interestingly, besides below ground and upper canopy (or above the canopy) showing up as occluded, the inside of the stems are occluded as well. Thus, the quite simple physics of wood (i.e. that it is not transparent) in conjunction with a ray-tracing approach help us to bring some semantics into the data, in the form of stem candidate voxel.

An additional feature, that can be derived from full-waveform laser scanning, is the skewness of the echo. It was shown that multiple scattering could lead to asymmetrical return waveforms for large footprint airborne laser scanners (Hancock *et al.*, 2011, 2012) and such effects might be visible in smaller footprint laser scanning data as well. For instance, Bruggisser *et al.* (2017) were able to show that the skewness of the echo had some explanatory power in discriminating tree species.

Most laser scanning based derivations of leaf area index have effectively computed plant area index, since it was not possible to differentiate echoes from leafy and woody canopy components. Hence, the problem of computing true LAI based on laser scanning returns is one of semantic labeling of the point cloud into leaf and wood returns. Here several approaches seem feasible, e.g. by using a genuine multi-spectral LiDAR (Woodhouse *et al.*, 2011) or by applying approaches such as the one presented in Section 1.1.3b to label stems and branches and then remove those points from the subsequent LAI computation.

1.1.3b Geometric reconstruction and semantic labeling

For trees growing in forests, extensive biomass reference data including allometries is already available (Chave *et al.*, 2014). For urban trees however, such reference data is currently mostly unavailable and this research gap recently received some attention (McPherson *et al.*, 2016). The Swiss research project REFETREE appointed by the

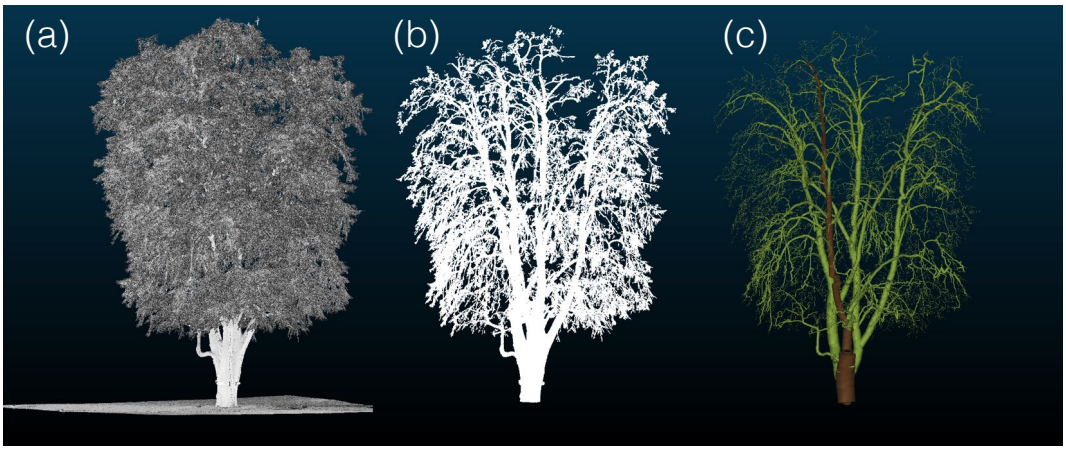

Fig. 1.3: QSM processing of an urban tree in the context of deriving better biomass allometries for carbon accounting. The original point cloud [a], the segmented and filtered point cloud [b] and the resulting cylindrical model [c] are shown.

Swiss Federal Office for the Environment (FOEN) seeks to build a reference database of 52 trees distributed over five major cities and 29 species naturally found in the Swiss mid-lands. The trees were measured with conventional field measurement protocols according to the national forest inventory (NFI) and the following variables were derived: tree height, diameter at breast height (DBH), crown diameter and crown base height. Later, the trees were cut down and weighted using a lorry scale. Additionally, multi-station TLS acquisitions of the trees were performed using a Riegl VZ-1000 at a resolution of 0.02°. For each tree, 3-4 scan locations have been used, each resulting in a point cloud of up to 45 million points. From the co-registered point cloud a 3D cylindrical representation of the tree was extracted by using a quantitative structural model (QSM) (Raumonen *et al.*, 2013) implemented in the SimpleTree plug-in for the CompuTree toolbox (Hackenberg *et al.*, 2015).

The QSM fits cylindrical elements into the point cloud from which essential tree parameters such as the wood volume can be extracted. However, for the QSM to work properly, heavy filtering of the original point cloud is required to exclude noise from foliar material, moving branches due to wind or scanning artifacts (Figure 1.3). With the extensive reference values acquired, these tree parameters extracted from TLS measurements can now be validated and biomass allometries can be established for urban trees. One of the aims of the project was to derive coarse wood volume, i.e. the volume of all stem and branch parts being larger than 7 cm in diameter. Given the urban multi-station scan setting, occlusion was minimized and it was possible to estimate coarse wood volume. From the reconstructed cylinders and their topology (connections), further information can be derived, for instance branching structures and angles and the tapering of branch diameter and branch lengths. Such variables form a valuable set of morphological traits, which can be used in species classification (Åkerblom *et al.*, 2017).

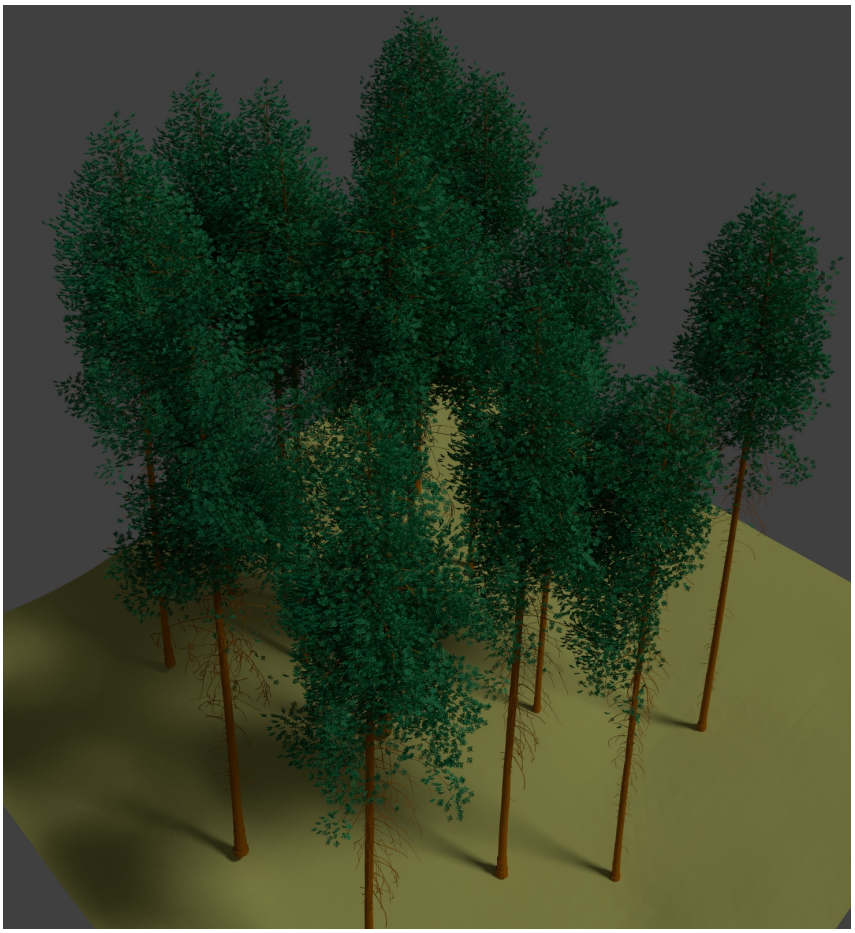

Fig. 1.4: Virtual pine tree stand as established in the European Space Agency "3D Vegetation Laboratory" project. Stems and branches were geometrically reconstructed using the approach of Eysn *et al.* (2013) and a lab-derived shoot model was cloned into the tree models to match the distribution of canopy material derived by TLS and ALS point clouds. The ALS point clouds were needed to mitigate the occlusion-caused lack of TLS points towards the crown tops.

1.1.4 Abstracting reality - sensors in the virtual domain

Ever since the early days, forestry applications of TLS faced a validation problem. DBH is quickly validated in the field using a tape measure, but it is a less sophisticated variable in respect to the general ability of TLS and the associated surveying and processing costs. When it comes to more complex variables, such as canopy cover and LAI for instance, validation is either very complex, costly, time consuming or all of those. For LAI, the most accurate approach would be destructive sampling and leaf counting and sizing, but this is impractical for larger areas or impossible for natural conservation sites. Consequently, indirect methods (Weiss *et al.*, 2004) are most often used for validation, but such attempts are merely a cross-validation. In Danson *et al.* (2007), the TLS obtained angular gap fraction was compared to DHP based estimates, and while showing high correlation, the experimental design was not suited to prove the hypothesis of a better performance of the TLS, especially so considering effects such as sun flare and bright spots negatively affecting DHPs.

Hence, taking the TLS and the forest stand into the virtual domain using radiative transfer models and a detailed 3d representation of the vegetation canopy (e.g. as in Widlowski *et al.* (2015) or Schneider *et al.* (2014)) is a possible solution. Almost everything (e.g. LAI, biomass, wood volume) can be measured for 3d models of trees and their assemblages into virtual forest stands as in Figure 1.4. The modeling of TLS systems and their use in different stands and survey configurations enables the testing of various environmental constraints on the measurement and to test the accuracy of different retrieval methods for a set of target variables (e.g. coarse wood volume).

The Swiss NFI is currently considering to use TLS to provide additional information for their several thousand sampling plots all over Switzerland. To apply TLS at such a large scale, the cost-benefit ratio of the technology needs to be positively evaluated. Using a too high scan resolution or inappropriate scanner locations can result in tremendous costs. Consequently, Abegg *et al.* (2017) used a virtual modeling setup within the *Blender* software to test different scanner location patterns and scanning resolution settings in more than 2000 simulated stands. They were able to show that the scanner locations in a multi-scan design need to be evenly distributed within a plot, and not placed at the plot edges. Such simulations complement real-world experiments like the one from Wilkes *et al.* (2017).

On the other hand, TLS derived information like tree models (Eysn *et al.*, 2013) and PAI can be used to parameterize 3d radiative transfer models to facilitate simulation of other earth observation data. Schneider *et al.* (2014) used ALS and TLS derived voxel grids of PAI to simulate spectra of the airborne imaging spectrometer APEX (Schaepman *et al.*, 2015) and were able to show good agreement between real-world measured spectra and simulated ones. Such approaches can be further extended to provide detailed simulations of the light regime within a canopy, which is highly relevant for a number of ecological processes and will increase our understanding of such.

1.1.5 Scales and perspectives

1.1.5a A change of perspective - TLS from a crane

When measuring a forest plot with TLS, the quality and completeness of the data is mainly determined by the applied measurement scheme. The main goal is to reduce occlusion and reach a complete coverage among all vertical layers of the canopy. Occlusion has been identified as a major source of uncertainty in forest reconstruction (Béland *et al.*, 2014), but very few studies have specifically investigated occlusion in TLS data, likely since occlusion is hard to map in real-world data.

In this experiment, we applied a ray tracing based algorithm developed by Kükenbrink *et al.* (2017) to map occlusion in a 1 ha forest plot. We scanned 1 ha of tropical rain-forest in the Lambir Hills National Park (Sarawak, Malaysia) from

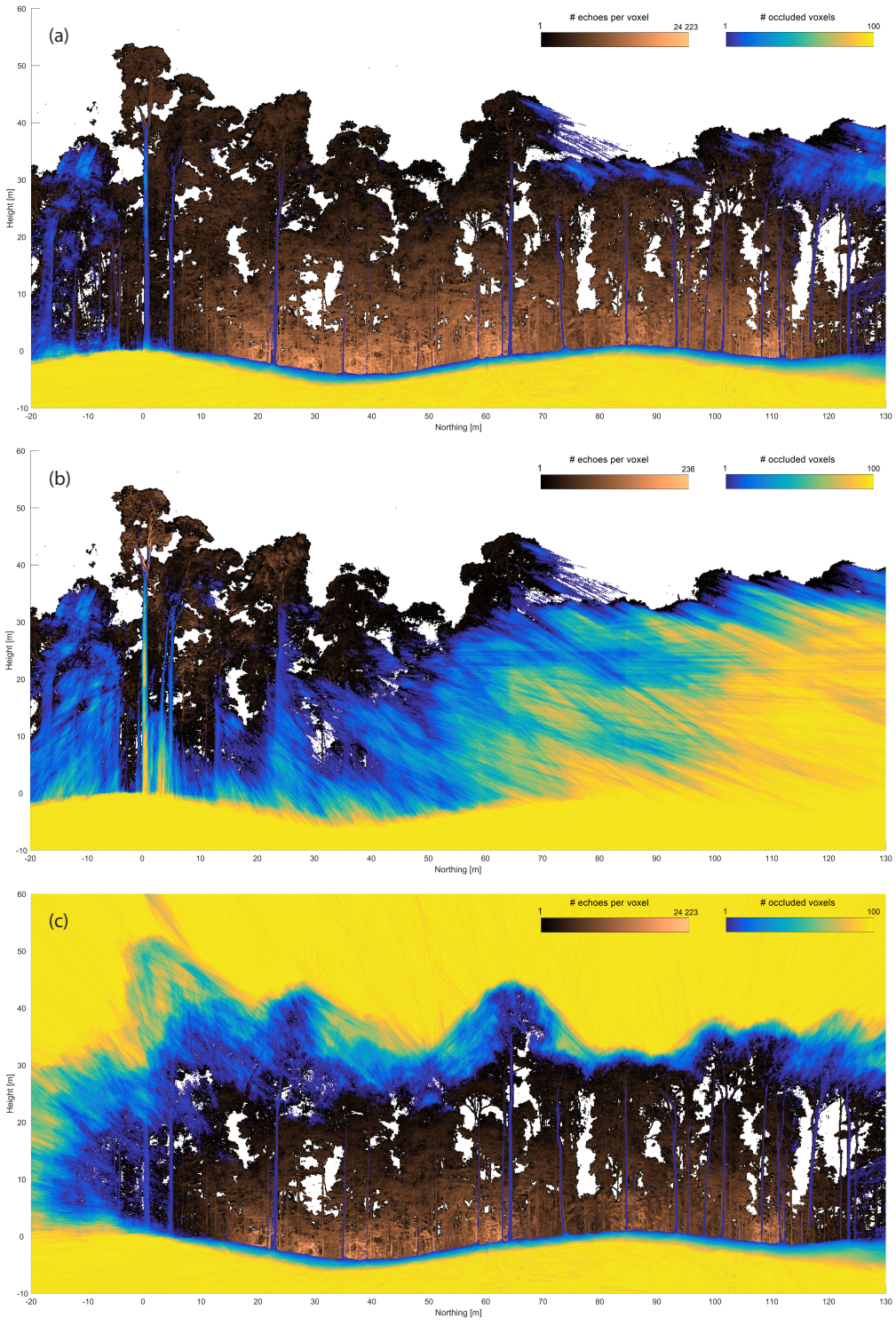

Fig. 1.5: Occlusion mapping in a 10 x 150 m transect of tropical rain-forest based on (a) TLS scans from the canopy crane and the ground, (b) scans from the crane only, and (c) scans from the ground only. Black to orange colors indicate the number of echoes per voxel with a side length of 10 cm. Blue to yellow colors show the number of occluded voxel across the 10 m depth of the transect, whereas 100% occlusion corresponds to 100 occluded voxel.

93 positions on the ground. Additionally, we performed 32 TLS scans from four platforms of a canopy crane at 24, 39, 59 and 76 m above ground. The profile in

Figure 1.5 shows parts of the canopy close to the crane (crane is at 0 m in distance, but outside image plane) with a 10 m deep transect through the surrounding trees.

Our results show that it is crucial to have many different scan positions to maximize tree coverage in a tropical forest. Furthermore, Figure 1.5 (c) shows that parts of the upper canopy are occluded when scanning from the ground only. This suggests that the scans from the canopy crane mainly contribute to the coverage and quality of the data in the uppermost canopy layers. The occlusion in the top-most layers may not be too large of a problem for biomass estimation, as stems generally taper off towards the top.

However, if the data is planned to be used to derive general 3d structure information, e.g. to be used in radiative-transfer modeling approaches Schneider *et al.* (2014); Widlowski *et al.* (2015), missing top-of-canopy information will severely impact the comparability with other remote sensing data acquired from above the canopy. Missing out on the top-of-canopy information in ground-based laser scanning is not only a function of occlusion by canopy material within the canopy, but as well a function of distance from the scanner.

As Abegg *et al.* (2017) showed in their simulation study, the point density above TLS scanners is the lowest when compared with all considered elevation angles and decreases with distance from the scanner. Thus, this under-sampling of the upper canopy is partly system imminent and can only be mitigated by very dense placement of scanner locations, i.e. as if the TLS was used as a vertical profiler.

1.1.5b UAVs to bridge the scale gap between ground-based and airborne laser scanning

A recent development in laser scanning is the deployment of lightweight laser scanners such as the Riegl VUX-1 on unmanned aerial vehicles (UAV) platforms (Lin *et al.*, 2011; Wallace *et al.*, 2012; Mandlburger *et al.*, 2015). These systems fall in-between TLS and ALS, being close to TLS in terms of resolution (i.e. point density), but closer to ALS in terms of perspective (top-down) and sampling distribution. Using Aeroscout's gas powered helicopter as UAV platform, 12 ha of the Laegeren forest research site were surveyed on a wind-still day in March 2017, with the trees still in leaf-off condition. During the same day of the UAV laser acquisition, a ground-based TLS survey was carried out, using a Riegl VZ1000 instrument. A total of 40 scans on 20 scan locations in a area of roughly 60 m by 60 m in size were taken. About 50 reflective targets were placed within the scene, to be later used for co-registration of the scans. The single-scans were co-registered using RiScan Pro and the UAV data was subsequently globally adjusted to the unified TLS point cloud. The absolute lack of wind on that day greatly facilitated matching of finer features, such as small branches.

Table 1.1 presents the most relevant survey settings; for more details on the UAV acquisition and processing see Morsdorf *et al.* (2017). Figure 1.6 illustrates the

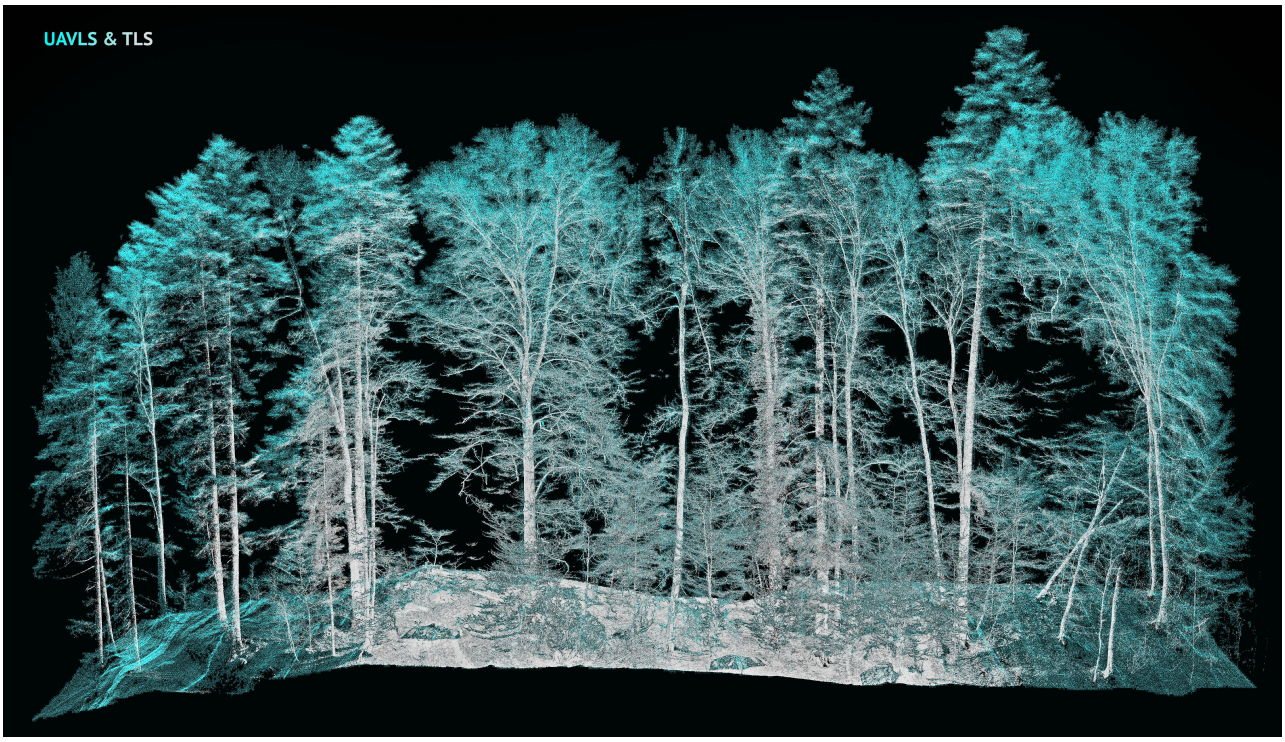

Fig. 1.6: Combination of TLS (grey-scale) and UAVLS (cyan) point-clouds acquired on the same day at Laegeren Forest, Switzerland. Foliage condition was leaf-off.

complementarity of TLS and UAV laser scanning, with UAV not providing as many stem returns, and TLS providing less information on the upper parts of the canopy.

Flying an UAV with a large field of view low above the canopy should yield minimal occlusion, as many different viewing angles into the canopy are sampled. As Figure 1.7 shows, this is the case. Compared to TLS, which suffers again from some occlusion towards the top of the canopy, UAV laser scanning is able to penetrate the canopy in leaf-off conditions fully, with only very little occlusion. The leaf-on data shows some more occlusion of lower canopy layers (Figure 1.7c), but the flying altitude was higher and the flight line spacing was lower for the summer UAV data. The findings of this experiment in a temperate mixed forest agree very well with

Tab. 1.1: Settings of UAV laser scanning acquisition. Please note that nominal values are per flight strip and actual point density is computed using all returns, including strip overlap and multiple returns.

Nominal flying height above ground	80 m
Nominal flying height above tree canopy	50 m
Spacing between flight lines	20 m
Scanned area	12 ha
Scanning rate	550 kHz
Field of view	240 deg
Nominal shot density	230 points/m^2
Nominal shot spacing	0.06 m
Actual point density returns	3200 points/m^2

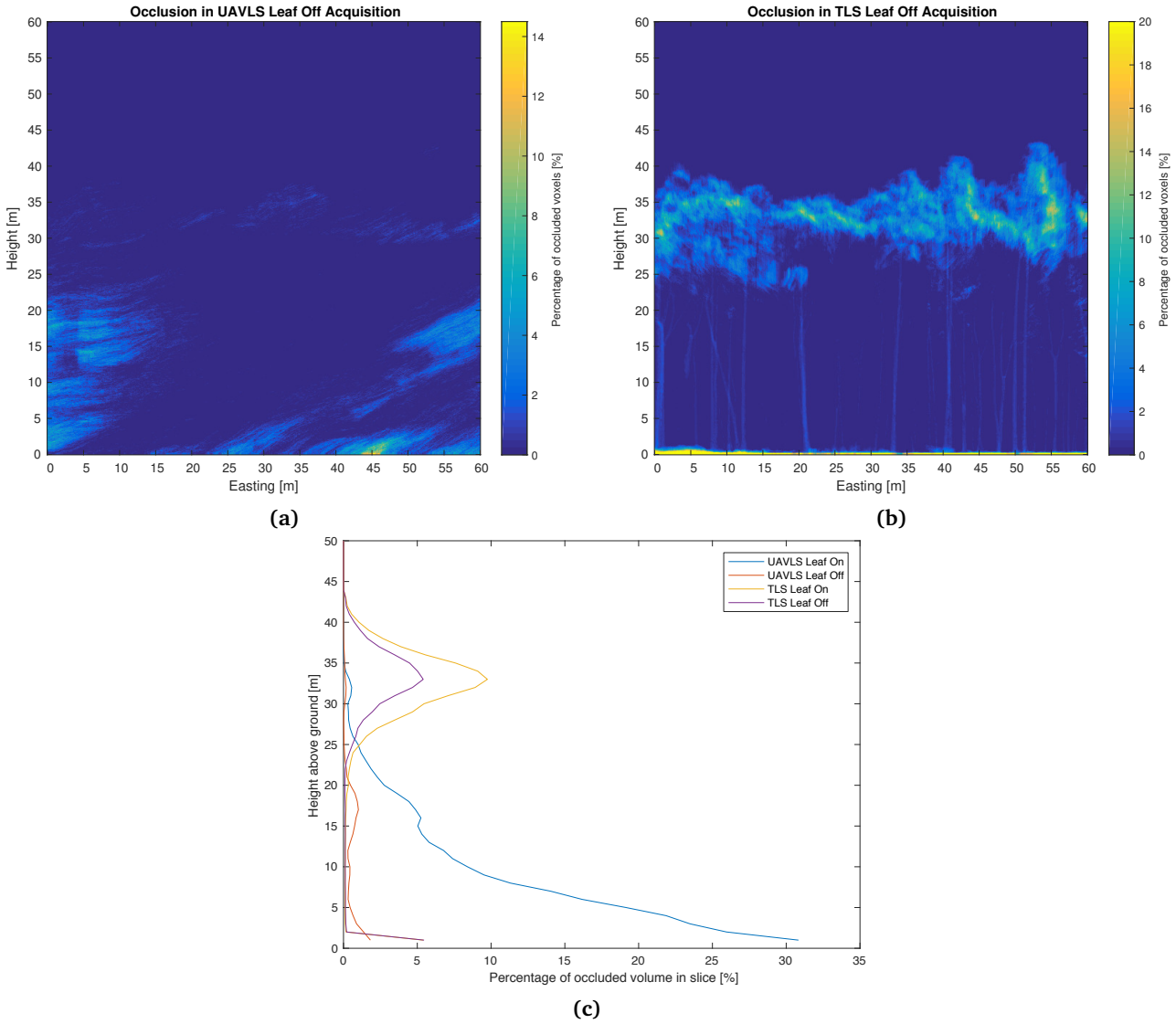

Fig. 1.7: Occlusion mapping using the approach of Kükenbrink *et al.* (2017) for the UAV data (a) and the TLS data (b) acquired over the same area and the same day in leaf-off conditions. Aggregated profiles for occlusion over transect shown in (a) and (b) are shown in (c), both for leaf-on and -off cases. Voxel size was 0.1 m and the percentage denotes the amount of voxel occluded related to all voxel in the 60 m deep transect. The profiles in (c) are based on the full 60 m by 60 m dataset.

both the simulation experiment from Abegg *et al.* (2017), who was able to show that TLS suffers from lower sampling density towards the top-of-canopy, which only can be mitigated by a large increase of the number of scans, which might come at prohibitively high costs.

On the other hand, having more points does not always mean getting more information. Comparing plot-level canopy profiles of the UAV and traditional airborne laser scanning data, very high correlations were observed, despite the large difference in point density of about $15/m^2$ for ALS and $3200/m^2$ for UAV laser scanning (Morsdorf *et al.*, 2017). This corresponds well to the ALS based findings of Leiterer *et al.* (2015), who observed a saturation of information towards higher point densities

and underlines the issue of dedicated experiments to test cost-benefit relationship before large-scale application of TLS technology, as e.g. in NFIs.

1.1.6 Summary and Conclusion

TLS and the upcoming UAV-based laser scanners provide data which has the potential to revolutionize the way the assess and quantify 3D vegetation structure. However, the transformation of data to information is not always straightforward and empirical approaches known from ALS will not work as well in close-range laserscanning.

Consequently, better use of the extensive physical information provided by the instruments is key to advance information retrieval, e.g. the voxel-based occlusion mapping can be used to aid the filtering and semantic labeling of the point clouds. However, the particular implementations in instruments need to be considered as well, otherwise we might just replace the well-known observer bias of traditional field inventories with an instrument bias.

QSMs are a promising way of abstracting the point cloud and are able to derive topological information, but the pre-processing (e.g. filtering) needed still hinders a wide-spread operational application of this method. But the semantic labeling done in QSMs is mandatory to derive variables such as stem and branch volume.

The validation problem for variables which are too cumbersome or costly to measure in the field (almost all except for DBH) can be overcome by 3d modeling of virtual forest stands. This will help us to learn about instrument biases and to test and implement the methods needed to make this technology a valuable asset in the toolboxes of foresters and ecologists alike.

Technology is evolving quickly and the costs, both in terms of labor and hardware, of laser scanner use in forests is decreasing. There are certain limitations regarding further miniaturization of UAV laser scanners in their current form, i.e. the dependence on highly accurate inertial navigation systems. However, new technologies such as focal plane arrays, driven by the demand for self-driving cars, will become mass market products and will fuse the power of range imaging with computer vision and photogrammetric approaches, ultimately making small, self-navigating laser drones possible. Once these devices will become available, the methods need to be ready to automatically convert the huge data-streams into meaningful information, otherwise such drones will remain not much more than toys.

While the data collected by TLS and UAV laser scanning is impressive, it can only be complementary to a full NFI approach, as many relevant variables, e.g. the management history of a site or the occurrence of pests can only be determined through manual interpretation on the respective sites.

But when applied properly, laser scanning can provide objective and accurate structural measurements of semantic objects constituting the forest canopies across scales (i.e. trees, stems, branches, leaves). This will leave more time for the humans

in the plot to assess the biotic variables of the forest ecosystem invisible to the laser. Hence, we see close-range laser scanning as valuable complement to NFI approaches, but not as a replacement.

Acknowledgments

The contributions of Felix Morsdorf, Fabian D. Schneider, and Michael E. Schaepman are supported by the University of Zurich Research Priority Program on *Global Change and Biodiversity* and the contribution of Daniel Kükenbrink was with support from the European Union's 7th Framework Programme (FP7/2014-2018) under EUFAR2 contract no. 312609.

1.2 Ecological relevance

Section 1.1 discussed the importance of canopy structure for forest ecosystem assessment and how it can be measured using laser-scanning technology. With the three-dimensional information we are now able to quantify and reconstruct forest canopy structure at a level of detail never seen before. In this section we are discussing the importance of 3D forest reconstruction for modelling the complex interaction of light with the canopy in order to study forest ecosystem functioning.

The radiative transfer of solar light within the forest canopy is a driving variable for a multitude of biological, ecological, physiological, and hydrological processes (Leuchner *et al.*, 2012; Martens *et al.*, 2000; Van der Zande *et al.*, 2011). Solar radiation is responsible for photosynthesis and transpiration within the forest canopy and therefore affects vegetation patterns (Leuchner *et al.*, 2012; Peng *et al.*, 2014), stand development (Oliver & Larson, 1996), forest and biomass growth (Leuchner *et al.*, 2012; Grant, 1997; Stark *et al.*, 2012), and productivity (Stark *et al.*, 2012). The influence of solar radiation can be observed throughout the whole canopy down to the forest floor, where it is highly responsible for germination and understorey growth (Beaudet *et al.*, 2004; Grant, 1997), regeneration and succession (Van der Zande *et al.*, 2010; Sakai & Akiyama, 2005), soil conditions (Musselman *et al.*, 2013; Von Arx *et al.*, 2012), as well as biodiversity (Battisti *et al.*, 2013; Théry, 2010). It is reported (e.g. Niinemets, 2007, 2012) that light availability typically varies up to 50-fold within the canopies of closed vegetation stands, and even within the crown of an isolated plant, significant variation in light occurs (Baldocchi *et al.*, 2002; Valladares, 2003). The variability in light availability within the canopy induces extensive modifications in foliage structure and physiology such that it is hardly possible to find two leaves with the exact same combination of leaf-trait values (Niinemets, 2007). Seasonal and diurnal changes in light availability within the canopy promote leaf plasticity allowing for leaves to adapt to the changing light conditions within the canopy (e.g. Keenan & Niinemets, 2017; Niinemets *et al.*, 2003; Valladares *et al.*, 2016). For a better understanding of ecosystem functioning and productivity of forest ecosystems, advanced knowledge of the distribution as well as the utilization of light in the canopy is vital. (Jennings *et al.*, 1999).

The distribution of light within the canopy is mainly driven by canopy structure, site characteristics, atmospheric conditions and solar elevation (Jennings *et al.*, 1999; Alexander *et al.*, 2013; Bode *et al.*, 2014; Jones *et al.*, 2003). These factors produce complex light patterns within the canopy over time, both in the horizontal as well as vertical domain (Peng *et al.*, 2014). The distribution of available light within the canopy as the energy source for vegetation functioning and productivity is therefore also a major driver in species competition, coexistence and canopy complementarity. It is argued that a more heterogeneous canopy structure often also holds higher species richness and biodiversity (McElhinny *et al.*, 2005). The more heterogeneous

light distribution within the canopy allows for more niches of additional species with varying resource-use strategies (e.g. shade tolerant vs. shade intolerant species) to find their matching biotope space to thrive. However, the question to which degree a heterogeneous canopy structure is a consequence or cause (via feedback effects) of diversity is largely unexplored (see e.g. Sapijanskas *et al.*, 2014). The vegetation structure not only drives the interception of solar radiation, but also affects microclimatic conditions within the canopy on temporal and spatial scales (Zellweger *et al.*, 2019) as well as gradients in surface temperature of different canopy parts (e.g. wood vs. leaves) (Pau *et al.*, 2018).

Due to the importance of solar radiation for forest ecosystem functioning, productivity and development, it is also an important variable in dynamic vegetation models (DVM), where the development of vegetation canopies over time is modeled. However, the radiative transfer through the canopy is still regarded as one of the biggest sources of uncertainty within such models (Fisher *et al.*, 2017). The problem often lies in the complexity needed by which the canopy structure and the radiative transfer through the canopy is parameterized within these models. However, quantifying the actual three-dimensional distribution of solar radiation within the canopy is a non-trivial task. Three-dimensional light distribution measurements are mere impossible due to the complexity of the forest structure as well as due to fast changing irradiance conditions (e.g. moving clouds, change in solar angle). Therefore, modelling of the radiative transfer through the forest canopy shows more potential in order to quantify the trhee-dimensional distribution of light within the canopy and give important insights into light related functions of the forest ecosystem.

There are multiple radiative transfer approaches available for modeling the transfer of light through forest canopies at varying levels of complexity. So-called Big-Leaf models are often used in large scale regional to global vegetation and land surface models, where the whole canopy is assumed to be a single layer with an exponential decrease in incoming light within this canopy layer based on Beer-Lambert's law of light extinction (e.g. in MOSES (Cox *et al.*, 1999), LPJ (Sitch *et al.*, 2003), and SiB3 (Denning *et al.*, 2003)). This assumption, however, completely neglects the presence of diffuse irradiance, as well as horizontal and vertical heterogeneity in canopy structure. So-called two-stream models resolve upward and downward radiation streams as well as diffuse and direct radiation (Jogireddy *et al.*, 2006). Alton *et al.* (2007) further improved the above mentioned two-stream model by treating the canopy as multiple discrete vertical layers and explicitly modelling leaf orientation rather than averaging irradiance into a mean light profile. More complex approaches are describing the canopy structure on a cohort or even individual level, also accounting to some extent for horizontal and vertical variations in canopy densities (Longo *et al.*, 2019) (e.g. the Ecosystem Demography model ED (Moorcroft *et al.*, 2001) or ED2 (Medvigy *et al.*, 2009)). However, also by using cohort or even individual based representations of the forest canopy, these models sometimes fail to represent the actual structural complexity found in forest ecosystems, especially those of high species richness where

species with fundamentally different architecture and leaf traits may coexist on small areas. Coupled 3D canopy-atmosphere models, incorporating radiative transfer through the atmosphere and interactions with the 3D vegetated Earth surface, such as the Discrete Anisotropic Radiative Transfer model DART (Gastellu-Etchegorry *et al.*, 2015) can give most valuable insights into small scale variabilities of the light environment within the canopy. These complex 3D radiative transfer models can be parameterized using 3D structural information acquired by laser-scanning data (see Section 1.1) and measurements of optical characteristics of vegetation material, allowing us to analyse the impact of the 3D canopy structure as well as the optical properties on the distribution of solar radiation within the canopy. This allows us to study the 3D light distribution within the canopy on a level of detail never seen before, giving us important insights into light related mechanisms of forest ecosystem functioning.

1.3 Thesis aims and structure

The aim of this thesis is to develop a method to assess and reconstruct complex three-dimensional forest structure using laser scanning technology for the parameterization of a radiative transfer model in order to analyse and quantify the three-dimensional irradiance field within the forest canopy. The challenges related to this overarching research goal lead to four main research questions.

1.3.1 Research questions

In this thesis, we address the following four research questions:

> *1) How can we quantify the actual observed canopy volume by laser scanning instruments and how much is the occluded volume affected by laser acquisition parameters or vegetation phenology*

This question is essential for understanding the coverage of laser scanning acquisitions and to assess the suitability of the data for three-dimensional forest canopy reconstruction. We used a voxel traversal algorithm to trace the path of every laser pulse through the forest canopy in order to detect observed, unobserved, and occluded (the laser pulse would have reached the volume in question, however, it was blocked by canopy material) space. This study was performed using an airborne laser scanning acquisition of the Laegern mountain. We assess how laser acquisition parameters, voxel size, and seasonal differences in the forest canopy influence the occluded forest volume and quantify the amount of hidden vegetation elements inside occluded forest volume by cross-comparing with voxelized TLS measurements. Even though developed for ALS acquisitions, this approach can be transferred to any kind of laser scanning acquisitions in order to quantify occluded canopy volume

and therefore acquire a criterion for assessing the quality of the coverage of the acquisition. The approach was therefore also the foundation for addressing our second research question, where we analyse the occluded volume in TLS and UAVLS acquisitions in two contrasting forests.

> *2) How well can we represent the three-dimensional canopy structure with close-range laser scanning instruments (TLS and UAVLS) for the parameterization of a radiative transfer model and is there a bias introduced by occluded canopy volume when quantifying vegetation densities?*

The main goal is to assess the completeness of close-range laser scanning acquisitions from TLS and UAVLS instruments to represent the canopy structure and is therefore an immediate follow-up on the first research question. We analysed the vertical distribution of occlusion among canopy layers in (a) measurements from the ground, (b) measurements from above the canopy and (c) combined above and below canopy measurements. Furthermore the difference in occlusion patterns between a temperate and a tropical forest were analysed. Finally we addressed the bias in vegetation density estimation caused by occlusion within the canopy if we only acquired measurements from the ground or above the canopy. This information is vital for assessing the accuracy of estimated 3D vegetation density distribution. It is further important for the parameterization of the radiative transfer modelling in forest canopies. This will be addressed in the third research question.

> *3) How are contrasting canopy structures and optical characteristics as found in a temperate and a tropical forest affecting the distribution of solar light within the canopy?*

This research question builds on the findings from research questions one, two and four and implements an approach to simulate the three-dimensional distribution of incoming solar radiation within the canopy using a radiative transfer model. Two forest sites, one temperate forest patch at the Laegern mountain, Switzerland, and one tropical forest patch in the Lambir Hills National park, Borneo, Malaysia, were compared. We analysed the influence of the contrasting canopy structure, as well as leaf optical properties on the distribution of light within the canopy. We hypothesise that the three-dimensional distribution of canopy material is the major driver for the distribution of solar radiation within the canopy. The knowledge gained by answering this research question can help understand, how light is distributed throughout the canopy, giving valuable insights into forest ecosystem functioning, productivity as well as coexistence and competition between and within species.

4) How does vegetation influence the irradiance field around it? What are the consequences of vegetation induced adjacency effects for processing and analysis of imaging spectroscopy data?

In this research question we are looking at vegetation induced adjacency effects by simulating the full radiative transfer around a single, isolated tree and quantify the irradiance variability caused by the 3-D object at different wavelengths. The modeled irradiance values were validated with *in-situ* measured irradiance values. Finally, we evaluated the impact of erroneous irradiance estimates on the retrieval of reflectance and vegetation information, such as chlorphyll content or photochemical reflectance index (PRI). We hypothesise, that the introduced radiative transfer modeling approach is capable of simulating the actual irradiance field around vegetation and that substantial bias in imaging spectroscopy derived vegetation parameters can be expected if such adjacency effects are not accounted for.

1.3.2 Structure of the thesis

The four research questions resulted in four main chapters of this thesis, namely Chapter 2, 3, 4 and 5. Additionally, we provide an introduction and synthesis in Chapter 1 and 6.

Chapter 1 provides the general context of the thesis based on a peer-reviewed article in Interface Focus (Morsdorf *et al.*, 2018) and a discussion on the challenges, opportunities and the ecological relevance of three-dimensional forest reconstruction and radiative transfer modeling. Furthermore, the thesis aim and related research questions are stated in this chapter.

Chapter 2 addresses the first research question with a peer-reviewed article published in Remote Sensing of Environment (Kükenbrink *et al.*, 2017). This article introduces an approach to quantify canopy volume that is occluded or hidden from laser scanning instruments, not allowing for canopy structure assessments and reconstruction in the identified areas. Based on this published work, multiple conference contributions as well as peer-reviewed articles were published (Abegg *et al.*, 2017; Morsdorf *et al.*, 2018; Schneider *et al.*, 2019), including the two articles portrayed in Section 1.1 and Chapter 3.

Chapter 3 addresses the second research question with a peer-reviewed article published in Agricultural and Forest Meteorology (Schneider *et al.*, 2019). This publication adapted the approach introduced in Chapter 2 to TLS and UAVLS data to quantify occlusion and the possible bias in estimated vegetation densities caused by occlusion effects in a temperate and tropical forest patch. This study further introduced the study sites of and built the foundation for the study introduced in Chapter 4.

Chapter 4 addresses the third research question with an article currently under review in Remote Sensing of Environment. It extends Chapter 2, 3, as well as the approach described in Chapter 5 to finally link the complex three-dimensional forest structure to the light distribution within the canopy, which gives us valuable insights into forest ecosystem functioning, productivity as well as species competition and coexistence.

Chapter 5 addresses the fourth research question with a peer-reviewed article published in IEEE Transaction on Geoscience and Remote Sensing (Kükenbrink *et al.*, 2019). It addresses the impact of vegetation on the irradiance field around it and builds up the methodological framework needed for answering the research questions addressed in Chapter 4. It further analyses the impact of major input parameters to the radiative transfer modeling scheme on modeled irradaiance necessary for understanding the portrayed results in Chapter 4.

Chapter 6 discusses the main findings of the thesis and general contributions to the research field, and presents an outlook to possible future research.

1.4 References

Abegg M, Kükenbrink D, Zell J, Schaepman ME, Morsdorf F (2017) Terrestrial laser scanning for forest inventories-tree diameter distribution and scanner location impact on occlusion. *Forests*, **8**, 1–29.

Åkerblom M, Raumonen P, Mäkipää R, Kaasalainen M (2017) Automatic tree species recognition with quantitative structure models. *Remote Sensing of Environment*, **191**, 1–12.

Alexander C, Moeslund JE, Bøcher PK, Arge L, Svenning JC (2013) Airborne laser scanner (LiDAR) proxies for understory light conditions. *Remote Sensing of Environment*, **134**, 152–161.

Alton PB, North PR, Los SO (2007) The impact of diffuse sunlight on canopy light-use efficiency, gross photosynthetic product and net ecosystem exchange in three forest biomes. *Global Change Biology*, **13**, 776–787.

Armston J, Disney M, Lewis P, *et al.* (2013) Direct retrieval of canopy gap probability using airborne waveform lidar. *Remote Sensing of Environment*, **134**, 24–38.

Baldocchi DD, Wilson KB, Gu L (2002) How the environment, canopy structure and canopy physiological functioning influence carbon, water and energy fluxes of a temperate broad-leaved deciduous forest - An assessment with the biophysical model CANOAK. *Tree Physiology*, **22**, 1065–1077.

Barlow J, Gardner TA, Araujo IS, *et al.* (2007) Quantifying the biodiversity value of tropical primary, secondary, and plantation forests. *Proceedings of the National Academy of Sciences*, **104**, 18555–18560.

Battisti A, Marini L, Pitacco A, Larsson S (2013) Solar radiation directly affects larval performance of a forest insect. *Ecological Entomology*, **38**, 553–559.

Beaudet M, Messier C, Leduc A (2004) Understorey light profiles in temperate deciduous forests: Recovery process following selection cutting. *Journal of Ecology*, **92**, 328–338.

Béland M, Baldocchi DD, Widlowski JL, Fournier RA, Verstraete MM (2014) On seeing the wood from the leaves and the role of voxel size in determining leaf area distribution of forests with terrestrial LiDAR. *Agricultural and Forest Meteorology*, **184**, 82–97.

Bienert A, Queck R, Schmidt A (2010) Voxel Space Analysis of Terrestrial Laser Scans in Forests for Wind Field Modeling. *International Archives of the Photogrammetry, Remote Sensing and Spatial Information Sciences - ISPRS Archives*, **38**, 92–97.

Bode CA, Limm MP, Power ME, Finlay JC (2014) Subcanopy Solar Radiation model: Predicting solar radiation across a heavily vegetated landscape using LiDAR and GIS solar radiation models. *Remote Sensing of Environment*, **154**, 387–397.

Bruggisser M, Roncat A, Schaepman ME, Morsdorf F (2017) Retrieval of higher order statistical moments from full-waveform LiDAR data for tree species classification. *Remote Sensing of Environment*, **196**, 28–41.

Chave J, Réjou-Méchain M, Búrquez A, *et al.* (2014) Improved allometric models to estimate the aboveground biomass of tropical trees. *Global Change Biology*, **20**, 3177–3190.

Cox PM, Betts RA, Bunton CB, Essery RLH, Rowntree PR, Smith J (1999) The impact of new land surface physics on the GCM simulation of climate and climate sensitivity. *Climate Dynamics*, **15**, 183–203.

Danson FM, Hetherington D, Morsdorf F, Koetz B, Allgower B (2007) Forest Canopy Gap Fraction From Terrestrial Laser Scanning. *IEEE Geoscience and Remote Sensing Letters*, **4**, 157–160.

Denning SA, Nicholls M, Prihodko L, Baker I, Vidale PL, Davis K, Bakwin P (2003) Simulated variations in atmospheric CO2 over a Wisconsin forest using a coupled ecosystem-atmosphere model. *Global Change Biology*, **9**, 1241–1250.

Eitel JU, Vierling LA, Long DS, Hunt ER (2011) Early season remote sensing of wheat nitrogen status using a green scanning laser. *Agricultural and Forest Meteorology*, **151**, 1338–1345.

Eitel JUH, Vierling LA, Long DS (2010) Simultaneous measurements of plant structure and chlorophyll content in broadleaf saplings with a terrestrial laser scanner. *Remote Sensing of Environment*, **114**, 2229–2237.

Eysn L, Pfeifer N, Ressl C, Hollaus M, Grafl A, Morsdorf F (2013) A practical approach for extracting tree models in forest environments based on equirectangular projections of terrestrial laser scans. *Remote Sensing*, **5**, 5424–5448.

Fisher RA, Koven CD, Anderegg WRL, *et al.* (2017) Vegetation Demographics in Earth System Models: a review of progress and priorities. *Global Change Biology*, pp. 1–20.

Gastellu-Etchegorry JP, Yin T, Lauret N, *et al.* (2015) Discrete Anisotropic Radiative Transfer (DART 5) for Modeling Airborne and Satellite Spectroradiometer and LIDAR Acquisitions of Natural and Urban Landscapes. *Remote Sensing*, **7**, 1667–1701.

Grant RH (1997) Partitioning of biologically active radiation in plant canopies. *International Journal of Biometeorology*, **40**, 26–40.

Grau E, Durrieu S, Fournier R, Gastellu-etchegorry Jp, Yin T (2017) Estimation of 3D vegetation density with Terrestrial Laser Scanning data using voxels . A sensitivity analysis of influencing parameters . *Remote Sensing of Environment*, **191**, 373–388.

Hackenberg J, Spiecker H, Calders K, Disney M, Raumonen P (2015) SimpleTree - An efficient open source tool to build tree models from TLS clouds. *Forests*, **6**, 4245–4294.

Hallé F (1986) Modular growth in seed plants. *Philosophical Transactions of the Royal Society of London. B, Biological Sciences*, **313**, 77–87.

Hancock S, Disney M, Muller JP, Lewis P, Foster M (2011) A threshold insensitive method for locating the forest canopy top with waveform lidar. *Remote Sensing of Environment*, **115**, 3286–3297.

Hancock S, Lewis P, Foster M, Disney M, Muller JP (2012) Measuring forests with dual wavelength lidar: A simulation study over topography. *Agricultural and Forest Meteorology*, **161**, 123–133.

Jennings SB, Brown ND, Sheil D (1999) Jennings etal 1999 Assessing forest canopies and understorey illumination: Canopy closure, canopy cover and other measures. *Forestry: An International Journal of Forest Research*, **72**, 59–74.

Jogireddy V, Cox PM, Huntingford C, Harding RJ, Mercado LM (2006) An improved description of canopy light interception for use in a GCM land-surface scheme: calibration and testing against carbon fluxes at a coniferous forest. *Hadley Centre technical note*, **63**, 1–13.

Jonckheere I, Fleck S, Nackaerts K, Muys B, Coppin P, Weiss M, Baret F (2004) Review of methods for in situ leaf area index determination Part I. Theories, sensors and hemispherical photography. *Agricultural and Forest Meteorology*, **121**, 19–35.

Jones HG, Archer N, Rotenberg E, Casa R (2003) Radiation measurement for plant ecophysiology. *Journal of Experimental Botany*, **54**, 879–889.

Keenan TF, Niinemets Ü (2017) Global leaf trait estimates biased due to plasticity in the shade. *Nature Plants*, **3**, 16201.

Kükenbrink D, Hueni A, Schneider FD, Damm A, Gastellu-Etchegorry JP, Schaepman ME, Morsdorf F (2019) Mapping the Irradiance Field of a Single Tree: Quantifying Vegetation-Induced Adjacency Effects. *IEEE Transactions on Geoscience and Remote Sensing*, pp. 1–18.

Kükenbrink D, Schneider FD, Leiterer R, Schaepman ME, Morsdorf F (2017) Quantification of hidden canopy volume of airborne laser scanning data using a voxel traversal algorithm. *Remote Sensing of Environment*, **194**, 424–436.

Leiterer R, Furrer R, Schaepman ME, Morsdorf F (2015) Forest canopy-structure characterization: A data-driven approach. *Forest Ecology and Management*, **358**, 48–61.

Leuchner M, Hertel C, Rötzer T, Seifert T, Weigt R, Werner H, Menzel A (2012) *Solar Radiation as a Driver for Growth and Competition in Forest Stands*, pp. 175–191. Springer Berlin Heidelberg, Berlin, Heidelberg.

Lin Y, Hyyppä J, Jaakkola A (2011) Mini-UAV-borne LIDAR for fine-scale mapping. *IEEE Geoscience and Remote Sensing Letters*, **8**, 426–430.

Longo M, Knox RG, Medvigy DM, *et al.* (2019) The biophysics, ecology, and biogeochemistry of functionally diverse, vertically- and horizontally-heterogeneous ecosystems: the Ecosystem Demography Model, version 2.2 Part 1: Model description. *Geoscientific Model Development Discussions*, pp. 1–53.

MacArthur RH, Horn HS (1969) Foliage profile by vertical measurements. *Ecology*, **50**, 802–804.

Maignan F, Bréon FM, Lacaze R (2004) Bidirectional reflectance of Earth targets: Evaluation of analytical models using a large set of spaceborne measurements with emphasis on the Hot Spot. *Remote Sensing of Environment*, **90**, 210–220.

Maltamo M, Næsset E, Vauhkonen J (2014) *Forestry applications of airborne laser scanning*, vol. 27. Springer, 460 pp.

Mandlburger G, Pfennigbauer M, Riegl U, Haring A, Wieser M, Glira P, Winiwarter L (2015) Complementing airborne laser bathymetry with UAV-based lidar for capturing alluvial landscapes. In: *Proc. SPIE*, vol. 9637 (eds. Neale CMU, Maltese A), p. 96370A.

Martens SN, Breshears DD, Meyer CW (2000) Spatial distributions of understory light along the grassland/forest continuum: Effects of cover, height, and spatial pattern of tree canopies. *Ecological Modelling*, **126**, 79–93.

McElhinny C, Gibbons P, Brack C, Bauhus J (2005) Forest and woodland stand structural complexity: Its definition and measurement. *Forest Ecology and Management*, **218**, 1–24.

McPherson EG, Van Doorn NS, Peper PJ (2016) Urban Tree Database and Allometric Equations. Tech. Rep. October, US Department of Agriculture, Forest Service, Pacific Southwest Research Station, Albany, CA.

Medvigy D, Wofsy SC, Munger JW, Hollinger DY, Moorcroft PR (2009) Mechanistic scaling of ecosystem function and dynamics in space and time: Ecosystem Demography model version 2. *Journal of Geophysical Research: Biogeosciences*, **114**, 1–21.

Moeser D, Morsdorf F, Jonas T (2015) Novel forest structure metrics from airborne LiDAR data for improved snow interception estimation. *Agricultural and Forest Meteorology*, **208**, 40–49.

Moeser D, Roubinek J, Schleppi P, Morsdorf F, Jonas T (2014) Canopy closure, LAI and radiation transfer from airborne LiDAR synthetic images. *Agricultural and Forest Meteorology*, **197**, 158–168.

Moorcroft APR, Hurtt GC, Pacala SW (2001) A Method for Scaling Vegetation Dynamics : The Ecosystem Demography Model (ED). *Ecological Monographs*, **71**, 557–585.

Morsdorf F, Eck C, Zgraggen C, Imbach B, Schneider FD, Kükenbrink D (2017) UAV-based LiDAR acquisition for the derivation of high-resolution forest and ground information. *The Leading Edge*, **36**, 566–570.

Morsdorf F, Kükenbrink D, Schneider FD, Abegg M, Schaepman ME (2018) Close-range laser scanning in forests: towards physically based semantics across scales. *Interface Focus*, **8**, 20170046.

Musselman KN, Margulis SA, Molotch NP (2013) Estimation of solar direct beam transmittance of conifer canopies from airborne LiDAR. *Remote Sensing of Environment*, **136**, 402–415.

Næsset E (1997) Estimating timber volume of forest stands using airborne laser scanner data. *Remote Sensing of Environment*, **61**, 246–253.

Næsset E (2002) Predicting forest stand characteristics with airborne scanning laser using a practical two-stage procedure and field data. *Remote Sensing of Environment*, **80**, 88–99.

Niinemets Ü (2007) Photosynthesis and resource distribution through plant canopies. *Plant, Cell & Environment*, **30**, 1052–1071.

Niinemets U (2012) Optimization of foliage photosynthetic capacity in tree canopies: towards identifying missing constraints. *Tree Physiology*, **32**, 505–509.

Niinemets Ü, Valladares F, Ceulemans R (2003) Leaf-level phenotypic variability and plasticity of invasive Rhododendron pontificum and non- . . . . *Plant Cell Environ*, pp. 941–956.

Oliver CD, Larson BC (1996) *Forest stand dynamics: updated edition.* Wiley New York, 520 pp.

Pau S, Detto M, Kim Y, Still CJ (2018) Tropical forest temperature thresholds for gross primary productivity. *Ecosphere*, **9**, 1–12.

Peng S, Zhao C, Xu Z (2014) Modeling spatiotemporal patterns of understory light intensity using airborne laser scanner (LiDAR). *ISPRS Journal of Photogrammetry and Remote Sensing*, **97**, 195–203.

Raumonen P, Kaasalainen M, Åkerblom M, *et al.* (2013) Fast Automatic Precision Tree Models from Terrestrial Laser Scanner Data. *Remote Sensing*, **5**, 491–520.

Sakai T, Akiyama T (2005) Quantifying the spatio-temporal variability of net primary production of the understory species, Sasa senanensis, using multipoint measuring techniques. *Agricultural and Forest Meteorology*, **134**, 60–69.

Sapijanskas J, Paquette A, Potvin C, Kunert N, Loreau M (2014) Tropical tree diversity enhances light capture through crown plasticity and spatial and temporal niche differences. *Ecology*, **95**, 2479–2492.

Schaepman ME, Jehle M, Hueni A, *et al.* (2015) Advanced radiometry measurements and Earth science applications with the Airborne Prism Experiment (APEX). *Remote Sensing of Environment*, **158**, 207–219.

Schneider FD, Kükenbrink D, Schaepman ME, Schimel DS, Morsdorf F (2019) Quantifying 3D structure and occlusion in dense tropical and temperate forests using close-range LiDAR. *Agricultural and Forest Meteorology*, **268**, 249–257.

Schneider FD, Leiterer R, Morsdorf F, Gastellu-Etchegorry JP, Lauret N, Pfeifer N, Schaepman ME (2014) Simulating imaging spectrometer data: 3D forest modeling based on LiDAR and in situ data. *Remote Sensing of Environment*, **152**, 235–250.

Sitch S, Smith B, Prentice IC, *et al.* (2003) Evaluation of ecosystem dynamics, plant geography and terrestrial carbon cycling in the LPJ dynamic global vegetation model. *Global Change Biology*, **9**, 161–185.

Stark SC, Leitold V, Wu JL, *et al.* (2012) Amazon forest carbon dynamics predicted by profiles of canopy leaf area and light environment. *Ecology Letters*, **15**, 1406–1414.

Théry M (2010) Forest light and its influence on habitat selection. *Plant Ecology*, **153**, 251–261.

Valladares F (2003) Light Heterogeneity and Plants: from Ecophysiology to Species Coexistence and Biodiversity. In: *Progress in botany* (ed. K Esser, U Lüttge WB&FH), pp. 439–471. Springer Berlin Heidelberg.

Valladares F, Laanisto L, Niinemets Ü, Zavala MA (2016) Shedding light on shade: ecological perspectives of understorey plant life. *Plant Ecology & Diversity*, **9**, 1–15.

Van der Zande D, Stuckens J, Verstraeten WW, Mereu S, Muys B, Coppin P (2011) 3D modeling of light interception in heterogeneous forest canopies using ground-based LiDAR data. *International Journal of Applied Earth Observation and Geoinformation*, **13**, 792–800.

Van der Zande D, Stuckens J, Verstraeten WW, Muys B, Coppin P (2010) Assessment of light environment variability in broadleaved forest canopies using terrestrial laser scanning. *Remote Sensing*, **2**, 1564–1574.

Von Arx G, Dobbertin M, Rebetez M (2012) Spatio-temporal effects of forest canopy on understory microclimate in a long-term experiment in Switzerland. *Agricultural and Forest Meteorology*, **166-167**, 144–155.

Vosselman G, Maas HG (2010) *Airborne and terrestrial laser scanning*. CRC.

Wagner W (2010) Radiometric calibration of small-footprint full-waveform airborne laser scanner measurements: Basic physical concepts. *ISPRS Journal of Photogrammetry and Remote Sensing*, **65**, 505–513.

Wallace L, Lucieer A, Watson C, Turner D (2012) Development of a UAV-LiDAR system with application to forest inventory. *Remote Sensing*, **4**, 1519–1543.

Weiss M, Baret F, Smith GJ, Jonckheere I, Coppin P (2004) Review of methods for in situ leaf area index (LAI) determination Part II. Estimation of LAI, errors and sampling. *Agricultural and Forest Meteorology*, **121**, 37–53.

Widlowski JL, Mio C, Disney M, *et al.* (2015) The fourth phase of the radiative transfer model intercomparison (RAMI) exercise: Actual canopy scenarios and conformity testing. *Remote Sensing of Environment*, **169**, 418–437.

Wilkes P, Lau A, Disney M, *et al.* (2017) Data acquisition considerations for Terrestrial Laser Scanning of forest plots. *Remote Sensing of Environment*, **196**, 140–153.

Woodgate W, Jones SD, Suarez L, *et al.* (2015) Understanding the variability in ground-based methods for retrieving canopy openness, gap fraction, and leaf area index in diverse forest systems. *Agricultural and Forest Meteorology*, **205**, 83–95.

Woodhouse IH, Nichol C, Sinclair P, Jack J, Morsdorf F, Malthus TJ, Patenaude G (2011) A multispectral canopy LiDAR demonstrator project. *IEEE Geoscience and Remote Sensing Letters*, **8**, 839–843.

Zellweger F, De Frenne P, Lenoir J, Rocchini D, Coomes D (2019) Advances in Microclimate Ecology Arising from Remote Sensing. *Trends in Ecology & Evolution*, **xx**, 1–15.

Chapter

2

Quantification of hidden canopy volume of airborne laser scanning data using a voxel traversal algorithm

Kükenbrink, D., Schneider, F.D., Leiterer, R., Schaepman, M.E., Morsdorf, F.

This chapter is based on the peer-reviewed article:
Quantification of hidden canopy volume of airborne laser scanning data using a voxel traversal algorithm.
Remote Sensing of Environment, 2017 (194), 424-436
DOI:10.1016/j.rse.2016.10.023
and is reprinted as the final submitted manuscript.
It has been modified to fit into the layout of this thesis.

D.K., F.D.S., R.L., F.M., and M.E.S. designed research;
all authors performed research and wrote the paper,
with main contributions of D.K.

Abstract

Accurate three-dimensional information on canopy structure contributes to better understanding of radiation fluxes within the canopy and the physiological processes associated with them. Small-footprint airborne laser scanning (ALS) data proved valuable for characterising the three-dimensional structure of forest canopies and the retrieval of biophysical parameters such as plant and leaf area index (PAI and LAI), fractional cover or canopy layering. Nevertheless, few studies analysed combined occluded and observed canopy elements in dense vegetation as a result of airborne laser scanning geometries. The occluded space contains a substantial amount of vegetation elements (i.e. leaf, needle and wood material), which are missing in the analysis of the three-dimensional canopy structure. Consequently, this will lead to erroneous retrieval of biophysical parameters. In this study, we introduce a voxel traversal algorithm to characterise ALS observation patterns inside a voxel grid. We analyse the dependence of occluded and unobserved canopy volume on pulse density, flight strip overlap and season of overflight in a temperate mixed forest. ALS measurements under leaf-on and leaf-off conditions were used. For cross-comparison purposes, terrestrial laser scanning (TLS) measurements on a 50x50 m^2 subplot under leaf-on conditions were used. TLS acquisitions were able to depict the three-dimensional structure of the forest plot in high detail, ranging up to the top-most canopy layer.

Our results at 1 m voxel size show that even with the highest average pulse density of 11 pulses/m^2, at least 25% of the forest canopy volume remains occluded in the ALS acquisition under leaf-on conditions. Comparison with TLS acquisitions further showed that roughly 28% of the vegetation elements detected by the TLS acquisitions were not detected by the ALS system due to occlusion effects. By combining leaf-on and leaf-off acquisitions, we were able to recover roughly 7% of the occluded vegetation elements from the leaf-on acquisition. We find that larger flight strip overlap can significantly increase the amount of observed canopy volume due to the added observation angles and increased pulse density.

2.1 Introduction

Forests cover approximately one third of the Earth's total land area (FAO, 2010), accounting for 75% of terrestrial gross primary production (Beer *et al.*, 2010), 80% of plant biomass (Kindermann *et al.*, 2008), and the majority of species on Earth (Pan *et al.*, 2013). Therefore, forests play a crucial role in the global biogeochemical and biophysical cycles (Betts *et al.*, 2001; Bonan, 2008; Ross, 2012). The importance of understanding and monitoring these complex ecosystems in the face of a changing climate is therefore ever increasing. In order to understand and manage forests, we need to describe and categorise their complex and dynamic structural and spatial components (Robertson, 1987; Groffman & Tiedje, 1989; Martens *et al.*, 1991), as well as their biochemical properties (Asner, 1998). Monitoring and assessing canopy structure is of special interest as it highly influences the energy fluxes between the atmosphere and forests (Yang & Friedl, 2003; Shugart *et al.*, 2010; Xue *et al.*, 2011) and therefore has important implications for forest growth, productivity and biodiversity(e.g. Givnish, 1988; Ishii *et al.*, 2004; Zellweger *et al.*, 2014, 2015).

Canopy structure is often defined as the three-dimensional distribution of structural elements such as leaves, branches, and tree trunks (Pan *et al.*, 2013; Nadkarni *et al.*, 2008; Disney *et al.*, 2006). It is often assessed by measuring tree height, tree diameter distribution, foliage and wood density, or stand volume (McElhinny *et al.*, 2005). Traditionally, canopy structure is assessed by time-consuming and occasionally subjective fieldwork on relatively small sampling areas (McElhinny *et al.*, 2005; Haara & Leskinen, 2009; Foody, 2010). Recent advances in the field of remote sensing have greatly improved medium to large scale assessment of canopy-structure variables, not only in the horizontal, but also in the vertical dimension (Roberts *et al.*, 2007; Asner *et al.*, 2012; Jones *et al.*, 2012). Light detection and ranging (LiDAR), with airborne laser scanning (ALS) systems in particular, have shown promising results in retrieval of canopy structure variables such as canopy height, fractional cover, and leaf area index (LAI) (e.g Morsdorf *et al.*, 2006; Coops *et al.*, 2007; Solberg *et al.*, 2009), as well as in mapping tree positions and species (e.g. Morsdorf *et al.*, 2004; Lee & Lucas, 2007; Suratno *et al.*, 2009). Moreover, LiDAR data is increasingly used for parameterising ecological or radiative transfer models due to its ability to depict the horizontal and vertical distribution of vegetation elements (i.e. leaf, needle, and wood material) (Antonarakis *et al.*, 2014; Schneider *et al.*, 2014).

Very few studies have actually analysed occlusion from ALS due to dense vegetation or scanning patterns (Korpela *et al.*, 2012). Nevertheless, several studies have identified occlusion to be a major source of uncertainty for retrieval of canopy structure variables both from ALS (e.g. Morsdorf *et al.*, 2009; Musselman *et al.*, 2013) as well as terrestrial laser scanner (TLS) measurements (e.g Béland *et al.*, 2011; Côté *et al.*, 2011; Béland *et al.*, 2014a). An approach to map and quantify occluded volume inside forest canopy is therefore of particular interest for canopy structure variable retrieval.

Occlusion in ALS measurements is often caused by very dense vegetation in the top-most canopy layers, obstructing the laser pulses from reaching lower canopy layers. Additionally, inappropriate scanning configurations, such as too low pulse density, partly caused by a lack of flight strip overlap, can be a cause for occlusion. Whereas occlusion in ALS measurements mostly occurs in the lower canopy layers (Korpela *et al.*, 2012), TLS measurements show an increase in occlusion towards the top of the canopy as well as in the middle of tree crowns (Béland *et al.*, 2011,

2014a). With an adequate scan pattern and well defined scan positions, the amount of occlusion in TLS measurements can be minimised (Hilker *et al.*, 2010).

In TLS studies, several approaches have been introduced to quantify and map occluded areas inside forest canopies (e.g. Béland *et al.*, 2011, 2014a; Bienert *et al.*, 2010). Also attempts to compensate occluded volume have been made by using light transmission models (Béland *et al.*, 2011) or by statistical methods (e.g. Lovell *et al.*, 2011; Strahler *et al.*, 2008). However, for ALS measurements, such an occlusion mapping and quantification approach is still missing.

One way to map and quantify occlusion in ALS acquisitions is the reconstruction of the path of each laser pulse via ray tracing. Ray tracing is a commonly used tool to simulate and analyse data acquisition of different sensors (e.g. Disney *et al.*, 2006, 2010; Hovi & Korpela, 2014). A simple and computationally inexpensive way to trace laser pulses is a voxel traversal algorithm as introduced by Amanatides & Woo (1987). The algorithm divides the three-dimensional space into small rectangular cubes, also known as voxels and traces each pulse through the voxel grid. By knowing the exact location of each laser return as well as the origin of the pulse, one is able to analyse the laser acquisition pattern inside the forest canopy for a given voxel size, allowing to quantify occluded and observed volumes. Béland *et al.* (2014b) introduced a parametric model using computational geometry instead of a complex ray tracing algorithm in order to estimate leaf area density at the voxel scale and showed in Béland *et al.* (2014a) that this model can also be used to map occluded areas.

In this study, we introduce an approach to map and quantify occluded forest canopy volume by tracing ALS laser pulses through a pre-defined voxel grid using a voxel traversal algorithm (Amanatides & Woo, 1987). The occlusion map has been analysed regarding (i) the influence of laser acquisition parameters such as pulse density or flight strip overlap on the amount of occlusion, (ii) seasonal influence (leaf-on vs. leaf-off) on the occluded canopy volume, and (iii) the quantification of hidden vegetation elements inside occluded forest volume by cross-comparing with voxelized TLS measurements.

2.2 Study site and materials

2.2.1 Study site

The Laegern site (47° 28'N, 8° 21'E) is a semi-natural mixed deciduous forest north-west of Zurich, Switzerland. It is an old-growth forest with a complex, multilayered canopy structure. The predominant tree species are the common beech (*Fagus sylvatica*), European ash (*Fraxinus excelsior*), and sycamore maple (*Acer pseudoplatanus*), with scattered silver fir (*Abies alba*) and Norway spruce (*Picea abies*) trees (Leiterer *et al.*, 2015a). The canopy is well structured with distinct background, understory, and overstory layering. Trees are up to 165 years old, with a diameter at breast height (DBH) distribution of up to 150 cm (Eugster *et al.*, 2007). The study site shows significant variation in canopy structure, including areas undergoing different forest management practices (ranging from semi-natural forests to highly intensive regimes with silvicultural interventions) (Leiterer *et al.*, 2015a).

The site is approximately 400 ha in size and the elevation ranges from 515 to 860 m above sea level, with primarily north- and south-facing slopes with inclinations

between 10° to 65°. A 300x300 m^2 core study site located on the south-facing slope of the Laegern mountain and centered around the FLUXNET site ('Laegeren', site CH-Lae) was chosen for in-depth analysis (i.e. voxel size influence and beam width influence on occlusion). The core study site is representative for the whole 400 ha large study site showing a diverse mixture of deciduous and coniferous forest stands (Leiterer *et al.*, 2015a).

2.2.2 ALS Data

The full-waveform ALS data acquired over the Laegern site was part of a larger ALS flight campaign in 2014 covering an area of 180,000 ha. The area was flown both under foliated (leaf-on) and defoliated (leaf-off) conditions. The sensor specifications are summarised in Table 2.1. The ALS acquisitions were acquired and processed by Milan Geoservice GmbH (Kamenz, Germany). The processing steps involved the extraction of laser returns from the full waveform data, transformation of the point cloud into the Swiss CH-1903 (LV03) Cartesian coordinate system, flight strip adjustment, filtering and classification of the point cloud into ground and vegetation points and generation of a digital terrain model (DTM) using TerraScan software (TerraScan v014, TerraSolid, Helsinki, Finland) as well as quality checks for positional and height accuracy. The processed ALS point cloud was provided to us in the LAS 1.2 format. The positional accuracy of the processed ALS data was below 0.15 m in horizontal and 0.07 m in vertical direction (Milan Geoservice GmbH, 2014).

Tab. 2.1: Specifications for the ALS data acquisition.

ALS Parameter	Leaf-off	Leaf-on
Acquisition date	March/April 2014	June/July 2014
ALS Sensor	LMS-Q680i	
Operating platform	airplane	
Mean operating altitude above ground [m]	600	700
Scanning method	rotating multi-facet mirror	
Pulse detection method	full-waveform processing	
Pulse length [ns]	<4	
Sampling interval [ns]	1	
Scan angle [deg]	$\pm$ 22	
Mean point density [pts/m^2]	15	30
Mean pulse density [pls/m^2]	$\approx$ 11	$\approx$ 11
Pulse footprint [cm]	30	35
Laser wavelength [nm]	1550	
Scan rate [Hz]	120	
Pulse Repetition Frequency [kHz]	300	
Beam divergence [mrad]	0.5	
Angular step width [deg]	0.0176	

2.2.3 TLS Data

A TLS measurement campaign was performed on the 4th and 7th of August 2015 under foliated (leaf-on) conditions to survey a 50x50 m^2 plot located inside the 300x300 m^2 core study site. The selected plot is located in a protected nature reserve and therefore no significant changes between the acquisition of the ALS and TLS data were observed. The plot was covered with a total of 36 TLS scans arranged on a rectangular grid with 10 m spacing. To improve the co-registration of scans, reflective cylindrical targets were placed in the forest resulting in at least four common targets between two consecutive scans. The TLS instrument was operated at a wavelength of

1550 nm and a pulse repetition frequency of 150 kHz, resulting in a maximum range of 950 m (Riegl VZ-1000, Riegl, Austria). A scan pattern of 0.04° spacing between pulses and a field of view of 100° by 360° in vertical and horizontal directions was used for each scan. In addition to cover the whole sphere, a horizontal and 90° tilted scan were performed at each scan position. The dense sampling design in combination with high-resolution scans minimised occlusion and enabled a detailed representation of the 50x50 m^2 plot that can be used as a reference dataset to cross-compare ALS measurements. The scan configurations used are summarised in Table 2.2.

Tab. 2.2: TLS data acquisition specifications for the 50x50 m^2 validation plot.

TLS Parameter	TLS specifications
Acquisition dates	4th and 7th of August 2015
TLS Sensor	Riegl VZ-1000
Laser wavelength [nm]	1550
Beam divergence [mrad]	0.3
Beam width when leaving instrument [mm]	7
Laser pulse repetition rate PRR [kHz]	150
Max. measurement range [m]	950
Angular resolution [deg]	0.04
Accuracy [mm]	8
Precision [mm]	5

2.3 Methods

2.3.1 Voxel traversal algorithm

The voxel traversal algorithm is based on an approach introduced by Amanatides & Woo (1987). The voxel grid is defined by the extent of the analysed laser data and the user defined voxel dimension. In this study, a voxel size of 1x1x1 m^3 was used for all voxel traversal runs with the ALS data. The resolution of ALS systems is generally a function of pulse density, footprint size and single-shot geolocation accuracy. Balancing these with a minimum number of pulses required per voxel to map occlusion, we chose 1 m voxel size as the best suited resolution for our study. Additionally, the impact of voxel size on occlusion was analysed in a separate sensitivity study outlined in Section 2.3.3b. In order to trace each ALS pulse through the voxel grid, the pulse origin and its direction need to be defined. The direction of each pulse is derived by vector subtraction of the positions of the last laser return and the origin:

$$\vec{d} = \vec{p_l} - \vec{p_o} \tag{2.1}$$

where $\vec{d}$ is the pulse direction, $\vec{p_l}$ is the position vector of the last laser return of the pulse and $\vec{p_o}$ is the position vector of the origin of the pulse. If exact sensor positions are known, this information can be used as the pulse origin. However, for the used ALS data, no sensor positions were available. In that case the first laser return is used as an initial estimate of the pulse origin. The pulse origin was then moved along the negative direction vector up to a height of approximately 500 m above ground to approximate the actual sensor position. For pulses with only one return, the direction vector of the closest non-single return pulse (according to GPS time) is

used. This approach is not feasible for large flat areas without any vegetation, as the closest multiple return pulse would be too far away, leading to an inaccurate pulse direction approximation. Yet, as we are solely analysing the occlusion effects in hilly and densely forested areas, this issue can be neglected. The pulse direction vector was estimated for all pulses before any pulse decimation (see Section 2.3.3c) was performed.

In order to traverse the pulse through the pre-defined voxel grid, the pulse needs to be represented as a vector $\vec{x}$ as described in Equation 2.2:

$$\vec{x} = \vec{p_o} + t\vec{d} \tag{2.2}$$

where t defines the distance along the directional vector $\vec{d}$ to get to point $\vec{x}$. If $t = 1$, $\vec{x}$ points to the location of the last laser return. The voxel traversal splits the ray into intervals of t, each spanning one voxel. The algorithm consists of an initialisation and incremental traversal stage. The initialisation phase starts by identifying the voxel where the laser pulse first intersects the voxel grid and stores the X-, Y-, and Z-indices of the voxel inside the voxel grid. If the pulse origin lies inside the voxel grid, it will extract the voxel where the origin is located. Additionally, the stepping in x-, y-, and z-direction is initialised to either 1 or -1 ($stepX$, $stepY$, $stepZ$), indicating whether X, Y, and Z are incremented or decremented as the ray crosses voxel boundaries, given by the sign of the x, y, and z components of $\vec{d}$. Next, we determine for each direction the value of t at which the ray crosses the voxel boundary ($tMaxX$, $tMaxY$, $tMaxZ$). The minimum of these three values will indicate how far along the ray we can travel and still remain in the same voxel. For the final step of the initialisation phase, we determine for each of the three dimensions how far along the ray we must move (in units of t) for the x-, y-, and z-component of the movement to equal the side length of the voxel ($tDeltaX$, $tDeltaY$, $tDeltaZ$). The basic incremental phase of the algorithm is outlined below:

```
if (tMaxX < tMaxY)
        if (tMaxX < tMaxZ)
                X = X + stepX;
                tMaxX = tMaxX + tDeltaX;
        else
                Z = Z + stepZ;
                tMaxZ = tMaxZ + tDeltaZ;
        end
else
        if (tMaxY < tMaxZ)
                Y = Y + stepY;
                tMaxY = tMaxY + tDeltaY;
        else
                Z = Z + stepZ;
                tMaxZ = tMaxZ + tDeltaZ;
        end
end
```

A more detailed description of the voxel traversal algorithm can be found in Amanatides & Woo (1987). For simplification and computational reasons, the pulse diameter was assumed to be infinitesimally small for the analyses done in this study. However, the implications of this assumption are discussed in the dedicated Section 2.3.3a.

For each traversed voxel, it was checked whether a laser return is located inside the voxel. If this was the case, the number of hits (N_{hit}) for this voxel was increased by 1. Otherwise the number of misses (N_{miss}) was increased. For voxels traversed after the last registered return of the pulse, the number of occluded rays (N_{occ}) was increased. The voxel traversal was stopped when the pulse reached the border of the voxel grid or the underlying terrain as defined by the DTM.

2.3.2 Occlusion mapping

Once all pulses intersecting the voxel grid were traversed, a classification grid was established. The voxel classification discriminates between voxels observed with (filled) and without (empty) a laser return inside the voxel, voxels which were completely hidden from the laser instrument (occluded), and voxels which were completely unobserved by the instrument (i.e. voxels which were never traversed by the voxel traversal algorithm (c.f Section 2.3.1)). Occluded voxels are voxels, which are theoretically traversed by the pulses, meaning the pulses would have reached the voxel, but all energy was already intercepted due to earlier interactions of the laser pulses with canopy material. Unobserved voxels on the other hand, are voxels which were never traversed by the algorithm. This occurs for example at very low pulse densities or at the border of the flight swath. This classification scheme is based on the approach proposed by Bienert *et al.* (2010) and is further outlined in Table 2.3.

Tab. 2.3: Voxel classification matrix after Bienert *et al.* (2010).

	Number of		
	hits (N_{hit})	misses (N_{miss})	occlusions (N_{occ})
filled	>0	≥ 0	≥ 0
empty	$=0$	>0	≥ 0
occluded	$=0$	$=0$	>0
unobserved	$=0$	$=0$	$=0$

For further analysis, only voxels lying between the DTM and the top of canopy (upper most observed voxel with $N_{hit} \geq 1$) were considered.

2.3.3 Occlusion sensitivity analysis

2.3.3a Implications of the infinitesimally small laser pulse width assumption

The occlusion estimation underlies the assumption that the diameter of the pulses were infinitesimally small. However, the laser pulse diameter can have implications on gap fraction and therefore also on occlusion as reported by Danson *et al.* (2007) and Béland *et al.* (2011, 2014a). In order to assess the effect of the infinitesimally small laser pulse width assumption on the amount of occlusion, a small experiment on the 300x300 m^2 core study site for the leaf-on ALS acquisition was performed. For each laser pulse an additional 100 pulses were traced, evenly distributed in four concentric circles around the pulse centre (25 pulses per circle). This distribution allowed to mimic the energy distribution of the laser pulse with the energy maximum around the middle of the pulse. Due to the small laser beam divergence of 0.5 mrad, the change of beam width was not considered in this analysis and all additional pulses were modelled parallel to the center pulse. As the laser return information is always referenced to the middle of the pulse, neither the exact location of the laser

return inside the footprint is known nor which part of the laser pulse was intercepted. Occluded voxels caused by the partially occluded part of the pulses (i.e. the section of the pulse between first and last return) could therefore not be analysed. However, we know that a laser pulse is fully occluded as soon as it reached its last return. Therefore, we discarded all first and intermediary returns of each pulse, after we have calculated the pulse origin of each pulse as shown in Section 2.3.1. The last return of the center pulse was projected orthogonally to the laser pulse direction to each additionally traced pulse and all parallel pulses were traced through the voxel grid. In that way, all voxels traversed before the last laser return are classified as observed for this pulse, while all voxels traversed after the last return are classified as fully occluded for the respective pulse. Non-occluded pulses are considered to be intercepted at the ground level. After all laser pulses were traced, the amount of occluded voxels caused by the fully occluded part of the pulses was extracted. The total occluded volume derived from this approach was then compared to the occluded volume derived with the assumption of an infinitesimally small laser footprint.

2.3.3b Voxel size influence on occlusion

The chosen voxel size has a large impact on the amount of occlusion found in ALS acquisitions. We assessed the impact of voxel size on the detected amount of occlusion for the 300x300 m^2 core study site by tracing the unfiltered ALS pulse dataset through a voxel grid at 5, 4, 3, 2, 1, 0.5, and 0.25 m voxel side lengths. For each voxel size, the observed, occluded, and unobserved volume in relation to the total canopy volume was extracted and analysed.

2.3.3c Pulse density influence on occlusion

The influence of pulse density on occlusion was tested with a systematic regular thinning approach. The majority of techniques that simulate a reduction in pulse density are based on a random selection of pulses inside a superimposed regular grid with specified resolution (e.g. Jakubowski *et al.*, 2013; Korhonen *et al.*, 2011; Næsset, 2009). However, this approach may not replicate the scan pattern of an ALS system (Wilkes *et al.*, 2015). In this study we reduced the pulse density by systematically discarding pulses based on the GPS time of the pulse (e.g. Khosravipour *et al.*, 2014). All pulses of one flight strip have to be sorted according to their GPS time tag. The pulse dataset was then thinned by subsequently only selecting every 2nd, 3rd, 4th, 5th or 10th pulse of the dataset. This allows us to reduce the pulse density, while keeping the inherent inhomogeneity of the ALS acquisition due to changes in pitch, yaw, and roll of the aircraft as well as changes in the topography. As the first filtering step (i.e. only take every 2nd pulse) already reduces the pulse density by 50%, we further applied two additional filtering steps where every 3rd or every 4th pulse was discarded. However, the results of these two filtering steps may be taken with care, as we introduce some additional irregularities by discarding every 3rd or 4th pulse while keeping the pulses between them.

In order to reduce effects of multiple observation geometries, only a single flight strip covering mainly forested areas was analysed. The reduced as well as the original pulse dataset of this single flight strip were traversed through the specified voxel grid and a voxel classification was performed as outlined in Sections 2.3.1 and 2.3.2. The number of occluded, observed and unobserved voxels were then analysed in relation to the total amount of voxels within the forest canopy.

2.3.3d Flight strip overlap influence on occlusion

Even though flight strip overlap of 50% was planned, the number of flight strips covering the same area varied between one and three due to a constant flight altitude and topographic changes. In order to assess the influence of flight strip overlap on occlusion, we first identified areas covered by three flight strips (approximately 18.4 ha) and then subsequently traced each area with either one, two or three of the overlapping flight strips. Pulse densities were additionally thinned by only taking every 2nd, 4th, and 6th pulse of each flight strip as described in Section 2.3.3c. The influence of the different flight strip coverage was then analysed by comparing the amount of occluded and observed (filled and empty) voxels in relation to the total number of voxels covered by three flight strips.

2.3.3e Seasonal influences on occlusion

We analyse the difference in the amount of occlusion between laser acquisitions at different seasonal stages (leaf-on vs. leaf-off) by performing the voxel traversal for both leaf-on and leaf-off datasets for the whole 400 ha large study site. The different voxel classification grids were compared by analysing how the voxels were classified under leaf-off condition, in the case of voxels being classified as occluded, observed, or unobserved under leaf-on condition.

2.3.4 ALS-TLS cross-comparison

2.3.4a Processing of TLS Data

The in-situ TLS dataset was used to quantify the vegetated volume not detected by the ALS system. The registration of the TLS point clouds of the 36 scan positions was performed in two steps using the RiscanPro software (RiscanPro v2.0.2 r7440, Riegl, Austria). First a coarse registration of the point clouds using the reflective cylindrical targets distributed on the plot was performed. Afterwards a fine registration was done using the Multi Station Adjustment tool of RiscanPro. For the absolute geo-referencing of the TLS point cloud to the Swiss CH-1903 (LV03) Cartesian coordinate system, the co-registered point cloud was registered to a previously geo-referenced point cloud of a measurement campaign from 2010 (see Schneider *et al.* (2014) for details on the 2010 TLS dataset). The co-registration of the 2015 scans with the 2010 measurements was first performed by manually identifying tie points with a subsequent Multi Station Adjustment. The fine registration using RiscanPro's Multi Station Adjustment tool improved the co-registration error (standard deviation) for all scans from 3.9 cm to 1.4 cm.

Laser returns with very low reflectance ($<$ -25 dB) were discarded in order to remove noise, occurring at the edges of leaves or trunks as well as atmospheric particle scattering.

The TLS laser pulses were traced through a voxel grid covering the 50x50 m^2 plot with a voxel size of 10 cm. The origin of each pulse was given by the scanner location as measured by the Riegl VZ-100 instrument. Occluded voxels were then extracted with the same classification scheme as described in Section 2.3.2 and Table 2.3.

2.3.4b Quantification of undetected vegetation elements

For the quantification of undetected vegetation elements, only occluded and unobserved voxels in the ALS voxel classification grid were selected. Of this selection, only voxels were analysed which are at least 1 m above ground and that were fully observed by the TLS measurements (i.e. all 1000 TLS voxels inside one ALS voxel were observed by at least one scan position). For the selected ALS voxels, the amount of filled (i.e. number of TLS laser returns > 0) TLS voxels was extracted, giving us an estimate of the volume potentially filled with vegetation, which was not detected by the ALS acquisition. Due to different observation geometries of the ALS and TLS systems, they encounter occlusion effects at different areas. Yet, these differences in canopy representation can be an advantage for quantifying hidden vegetation elements in ALS acquisitions as the TLS acquisitions are able to represent the lower canopy parts, where ALS acquisitions are often occluded.

The approach was performed for unfiltered and filtered ALS pulse densities as described in Section 2.3.3c in order to further quantify the effects of pulse densities on the amount of occluded vegetation elements inside the ALS dataset.

Additionally, it was tested how much of the undetected vegetation elements in the leaf-on dataset could be recovered by filling occluded voxels in the ALS leaf-on dataset with information from the ALS leaf-off dataset. Such a filling of occluded voxels was only performed, if the leaf-off acquisition registered a laser return inside these voxels.

2.4 Results

2.4.1 Occlusion mapping

In Figure 2.1, the fractions of occluded volume to the total canopy volume per vertical profile is shown for both, leaf-on (Figure 2.1a) and leaf-off (Figure 2.1b) conditions. In the leaf-on case, some regular occurring patches with increased occlusion are visible. These are mostly caused by reduced flight strip overlap due to changes in topography in combination with a decreased pulse density. In the leaf-off case, the amount of occlusion is reduced due to the missing foliar material. Only a few larger patches with higher occlusion fractions occur, which are mostly caused by lower flight strip overlap, in combination with a decreased pulse density, or by coniferous trees.

In Figure 2.2 the distribution of occluded fractions to the total canopy volume per vertical column is shown for both leaf-on and leaf-off conditions. Over all voxel columns with occlusion fractions larger than 0, the average occlusion fraction lies at 0.35 and 0.26 under leaf-on and leaf-off conditions respectively.

2.4.2 Occlusion sensitivity analysis

2.4.2a Implications of the infinitesimally small laser pulse width assumption

The comparison between the occluded volume extracted with and without pulse width simulation showed that the infinitesimally small laser pulse width assumption will overestimate occluded volume by 7% (percentage of occluded volume with infinitesimally small laser pulse width assumption in relation to the total canopy

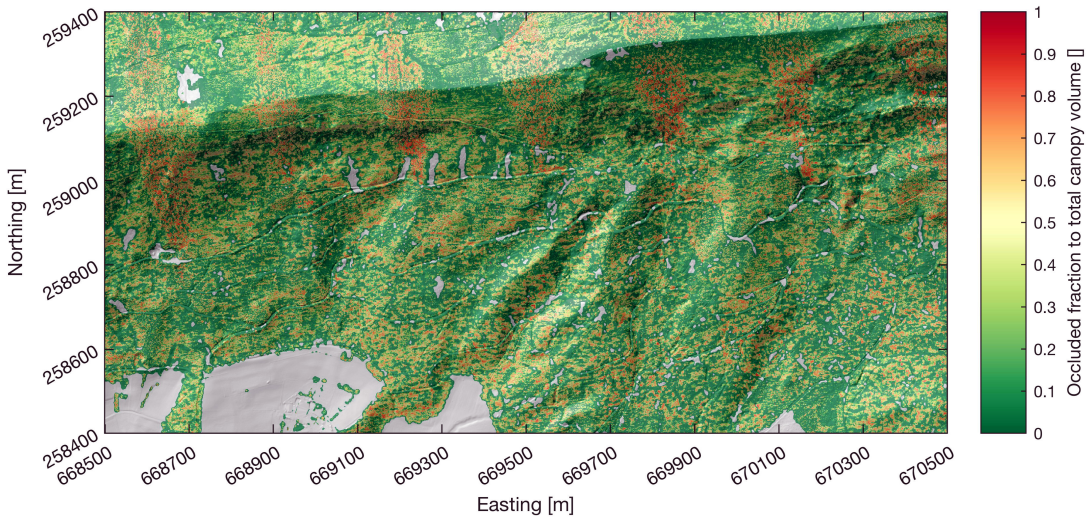

(a)

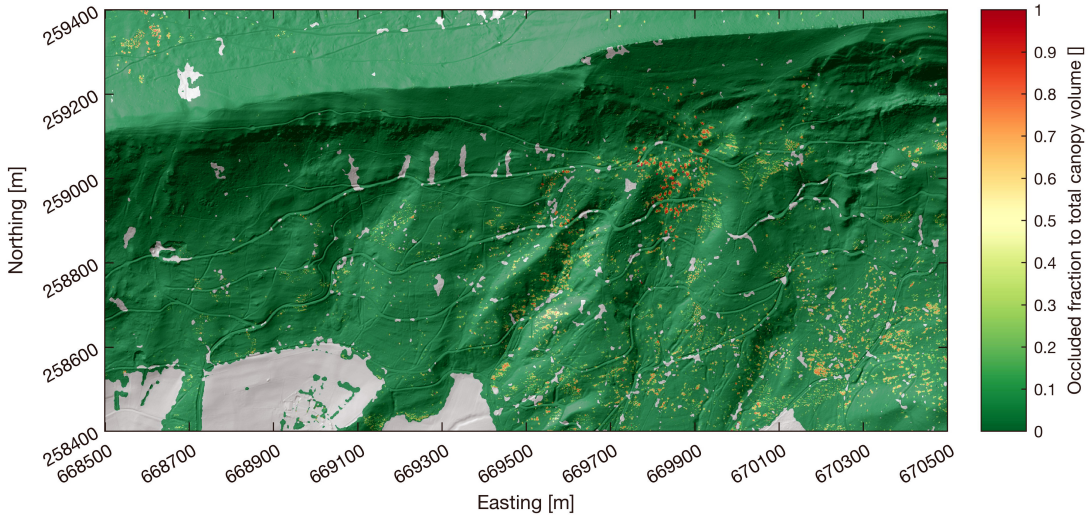

(b)

Fig. 2.1: Fractions of occluded voxels per vertical profile for leaf-on (2.1a) and leaf-off (2.1b) conditions on hill-shaded terrain. Occlusion fractions were derived at a voxel side length of 1 m.

volume: 27%, with beam width simulation: 20%). However, we assume that the overestimation due to the infinitesimally small laser pulse width assumption would be smaller, as we could not account for occluded voxels caused by the section of pulses that were partially occluded (i.e. section of the pulse between first and last laser return of the pulse).

2.4.2b Voxel size influence on occlusion

In Figure 2.3 the influence of voxel size on the amount of occluded, observed, and unobserved voxels in relation to the total canopy volume is shown. At 5 m voxel side length, 100% of the canopy voxels was observed. This percentage decreases with decreasing voxel size, while the amount of detected occluded voxels increases. At 1 m voxel side length, around 73% of all the voxels inside the forest canopy were observed, whereas 27% were classified as occluded. When we decrease the voxel side length to and below the laser footprint size (35 cm), the amount of unobserved

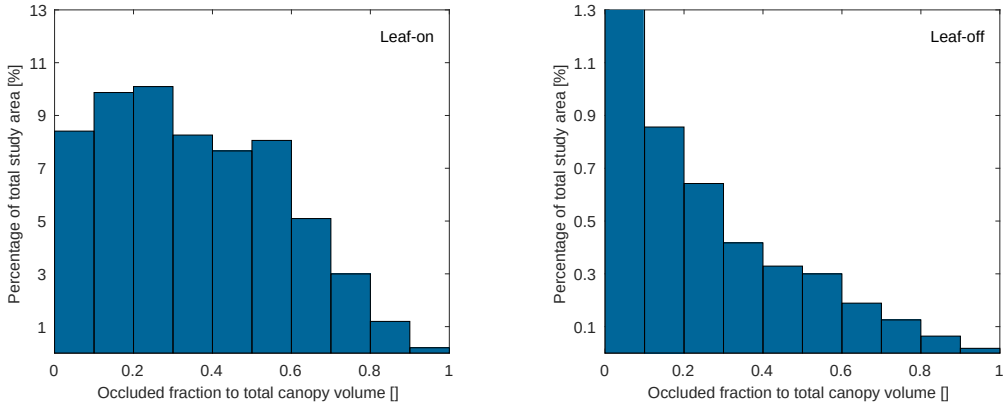

(a) **(b)**

Fig. 2.2: Histogram of occluded fraction per vertical voxel column relative to total study area for leaf-on and leaf-off conditions. Only occlusion fractions > 0 are included in the histogram. Occlusion fractions were derived at a voxel side length of 1 m.

voxels increases from 0 up to 37% of the total amount of canopy voxels. A voxel side length of 1 m represents a compromise allowing to minimize the amount of occlusions while retaining a high spatial resolution as supported by the ALS system. Consequently, this approach represents a site-optimized solution, depending on stand density and ALS instrument parameter settings, and must be adjusted for differing site conditions. The following results were all obtained with this voxel side length.

2.4.2c Pulse density influence on occlusion

The influence of pulse density on the amount of occluded, observed, and unobserved voxels in relation to the total number of voxels inside the forest canopy is plotted in Figure 2.4. Only data of a single flight strip covering mainly forested area was analysed for an area of approximately 68.5 ha. The graph shows the average fraction of occluded, observed and unobserved voxels per hectare as well as the standard deviation. The pulse density was thinned to approximately 10, 20, 25, 33, 50, 67, and 75% (i.e. only taking every 10th, 5th, 4th, 3rd, 2nd and discarding every 3rd and 4th pulse respectively) of the original unthinned average pulse density of 5.18 pulses/m^2 (std: 1.4 pulses/m^2, min: 1 pulse/m^2, max: 23 pulses/m^2, 95% of all pulse densities are between 3 and 8 pulses/m^2; statistics retrieved over the whole analysed area covered by the flight strip) with the approach described in Section 2.3.3c. With only 0.5 pulses/m^2, roughly 16% of the total canopy volume is observable by the ALS system, while 57% are unobserved and 27% are occluded. With increasing pulse density the amount of observed voxel increases, whereas the rate in increase decreases gradually after reaching a pulse density of approximately 2 pulses/m^2. At the original pulse density of 5.18 pulses/m^2, the ALS system was able to observe 58$\pm$6.5% of the total canopy volume covered by the single flight strip. The maximum in occlusion is reached at 1.7 pulses/m^2 with 54$\pm$5.2% of the total canopy volume occluded. At pulse densities below 2.5 pulses/m^2 the amount of voxels that were never traversed by any pulses increases from 0% to up to 57$\pm$4.5% at a pulse density of 0.5 pulses/m^2.

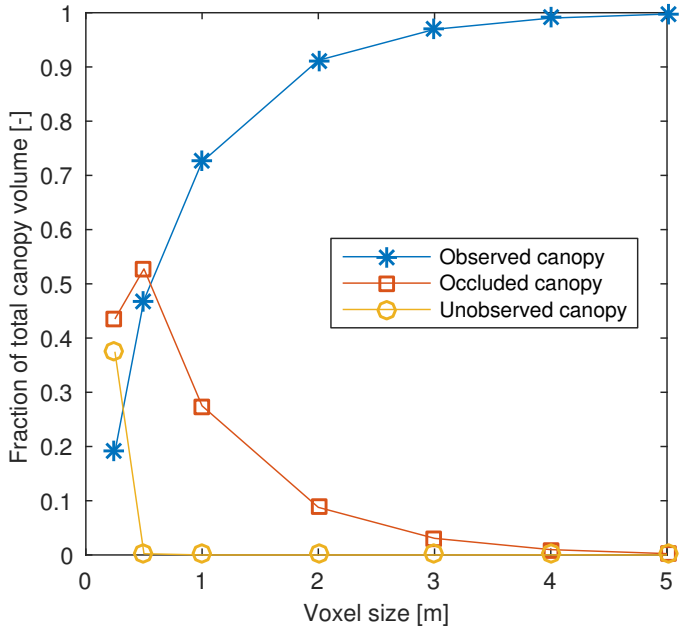

Fig. 2.3: Influence of voxel size on occluded, observed, and unobserved voxels in relation to the total canopy volume. Results are shown for leaf-on conditions.

2.4.2d Flight strip overlap influence on occlusion

The fraction of observed as well as undetected (i.e. unobserved plus occluded voxels) voxels to the total number of voxels covered by three flight strips is shown in Figure 2.5 in relation to the number of overlapping flight strips as well as pulse density. The different lines denote the amount of flight strips observing the area. The pulse density was additionally reduced to half, 1/4, and 1/6 of the original pulse density (4.6 pulses/m^2 at single coverage, 9.7 pulses/m^2 at double coverage, and 15 pulses/m^2 for triple coverage). Figure 2.5 shows, that additional observation angles from further flight strips increase the amount of observed canopy volume from 57% to 81% of the total canopy volume covered by three flight strips when analysing the original pulse density. With strongly decreased pulse densities of just 1/6 of the original pulse density (i.e. 0.76 pulses/m^2 at single coverage, 1.6 pulses/m^2 at double coverage, and 2.5 pulses/m^2 at triple coverage) the observed volume is decreased to 25%, 39%, and 50% of the total canopy volume covered by three flight strips for single, double, and triple flight strip coverage respectively.

2.4.2e Seasonal influence on occlusion

Figure 2.6 shows the voxel classification for a 300 m x 1 m transect under leaf-on and leaf-off conditions. Only voxels observed with a laser return (N_{hit}) and occluded voxels (N_{occ}) are shown. Occluded voxels are shown ranging from yellow to red. Observed voxels with a registered laser return are shown ranging from green to blue. The redder the occluded voxels are, the more pulses would have theoretically traversed the voxels, if they were not obstructed by the canopy. The bluer the voxels are, the more laser returns were registered by the ALS system inside the corresponding voxel.

In Figure 2.7, the differences between voxel classifications at 1 m voxel size for the unfiltered leaf-on and leaf-off datasets for the entire study area are shown. In general, we see that the occluded volume under leaf-off conditions is reduced with only

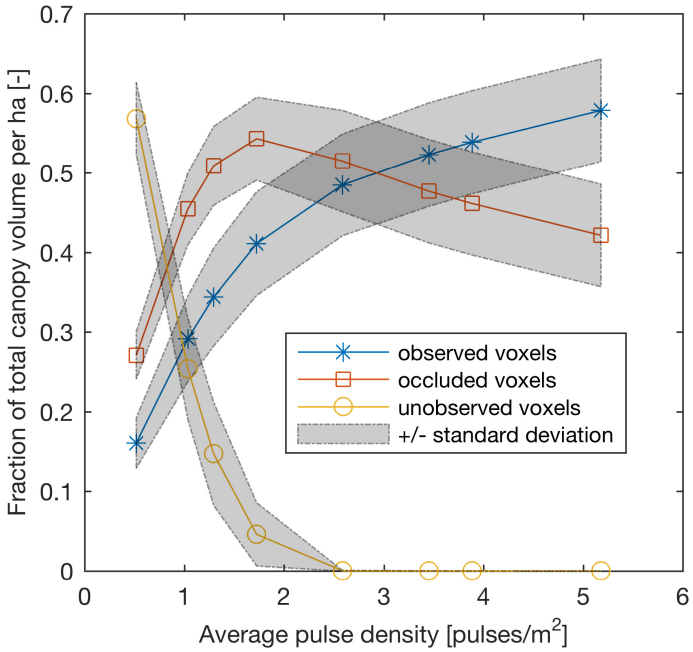

Fig. 2.4: Pulse density dependence on fractions of occluded, observed and unobserved forest canopy volume per hectare for a single flight strip under leaf-on conditions. Occlusion fractions were derived at a voxel side length of 1 m.

$1.1 * 10^6$ m^3 (1.5% of total canopy volume) as compared to leaf-on conditions with $19.4 * 10^6$ m^3 (25% of total canopy volume). Table 2.4 shows the overall distribution of the voxel classification for the leaf-on and leaf-off case respectively. Also the amount of leaf-off occluded voxels inside leaf-on occluded voxels is small with only $0.8 * 10^6$ m^3 (3.9% of total leaf-on occluded volume). The majority of leaf-on occluded voxels are actually classified as empty in the leaf-off voxel classification with a volume of $14.9 * 10^6$ m^3 (76.9% of total leaf-on occluded volume). In the case of leaf-on filled voxels, the majority of the volume (62.8% of leaf-on filled volume) is also filled under leaf-off condition, followed by empty voxels (36.9%) and a small amount of occluded voxels. For leaf-on empty voxels the majority (81.8% of total leaf-on empty volume) is also classified as empty in the leaf-off case, whereas filled and occluded voxels only cover a small amount of total leaf-on empty volume with 17.5% and 0.7% respectively.

Additionally, Table 2.4 shows the percentage of occluded volume in relation to the total volume found in coniferous or deciduous forest types respectively. The forest type map was retrieved from the ALS data on a 5 m pixel scale following the approach described in Leiterer *et al.* (2015b). Leiterer *et al.* (2015b) achieved an overall accuracy of 90.7% in their approach to discriminate forest types from the same ALS dataset as employed in this study. Table 2.4 shows that deciduous forests

Tab. 2.4: Voxel classification for leaf-on vs. leaf-off acquisitions and amount of occlusion present in coniferous vs. deciduous forests. Voxel classification was derived at a voxel side length of 1m.

	Classification [% of total canopy volume]			Occlusion in forest type [% of total canopy volume in forest type]	
	Occluded	Filled	Empty	Coniferous	Deciduous
Leaf-on	25.0	31.9	43.1	17.7	25.3
Leaf-off	1.5	34.9	63.6	9.3	1.1

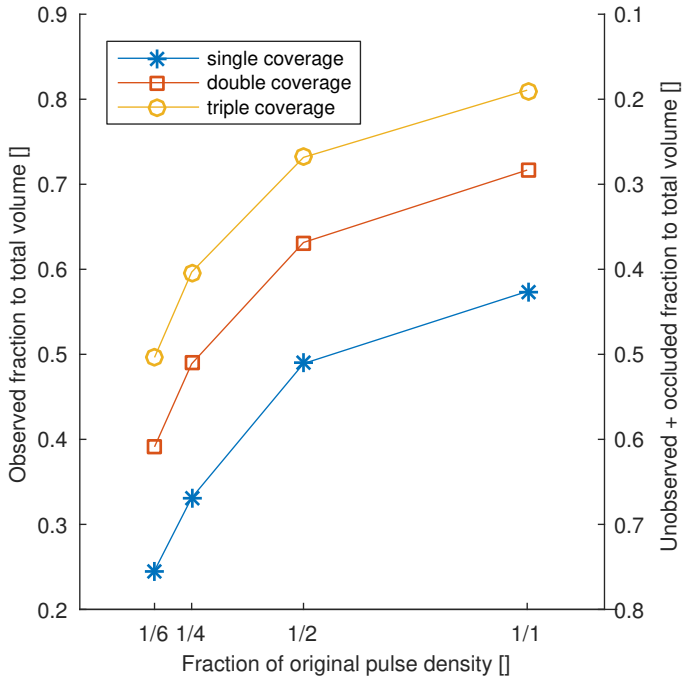

Fig. 2.5: Influence of varying observation geometries on observed and undetected (occluded + unobserved) voxels at 1 m side length in relation to the total number of voxels covered by three flight strips. The original pulse density was at 4.6, 9.7, and 15 for single, double, and triple coverage respectively.

encounter a bigger change in the amount of occlusion between leaf-on and leaf-off acquisitions as compared to coniferous forests.

2.4.3 ALS-TLS cross-comparison

2.4.3a Processing of TLS Data

In Figure 2.8 the point clouds and point distribution of ALS (leaf-on and leaf-off) as well as TLS acquisitions on a 50 m x 10 m transect is shown. Due to the tight TLS measuring scheme utilised, we were able to capture the forest canopy up to the top most layer with low occlusion. Even-though the point density of the TLS acquisition is slightly decreased towards the top of canopy, it can be used to quantify scattering material inside ALS occluded voxels, as ALS occlusion often occurs towards the bottom of canopy, where the TLS acquisitions were able to depict the canopy structure with low occlusion. The voxel traversal of the TLS acquisitions showed that only 6% of the total canopy volume was occluded. This includes the occluded volume found inside tree trunks. Particularly of interest are the differences between ALS leaf-on and leaf-off acquisitions. Due to the missing foliar material under leaf-off conditions, the laser pulses were able to penetrate much deeper into the canopy, covering also a substantial part of the underlying terrain.

2.4.3b Quantification of undetected vegetation elements

The fraction of filled TLS voxels (TLS voxels containing at least one TLS return) undetected by ALS in relation to all filled TLS voxels is shown in Figure 2.9 for varying pulse densities. The 50x50 m^2 large test site measured with the TLS instrument was consistently covered by two ALS flight strips. The blue line denotes the amount of

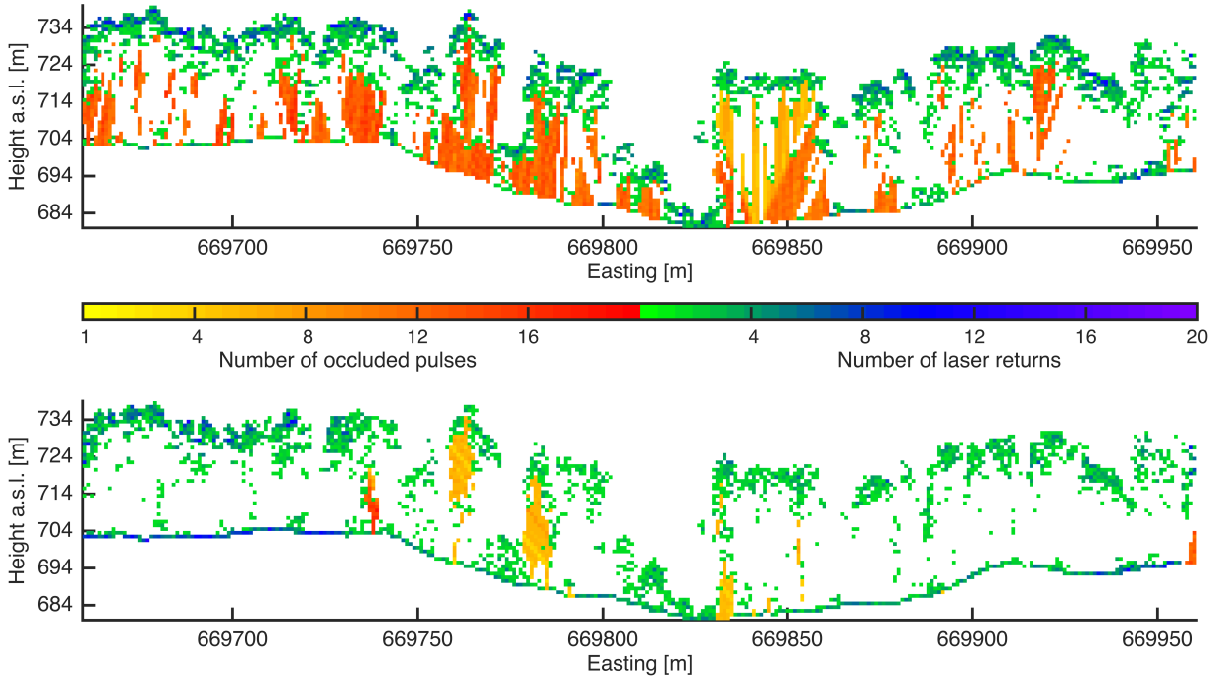

Fig. 2.6: Leaf-on (upper panel) and leaf-off (lower panel) voxel classification for a 300x1 m transect at 259074 m Northing (Swiss CH-1903 (LV03) Cartesian coordinate system) traversed with the unfiltered pulse dataset at a voxel side length of 1 m. Occluded voxels are shown ranging from yellow to red following the number of pulses theoretically reaching a voxel, if not occluded. Observed filled voxels are shown ranging from green to blue corresponding to the number of laser returns contained in the voxel.

filled TLS voxels (at 10 cm voxel side length) inside occluded and unobserved voxels of the ALS leaf-on dataset (at 1 m voxel side length) in relation to the total amount of filled TLS voxels. Only occluded and unobserved ALS voxels were taken which were fully observed by the TLS scans. Figure 2.9 shows the decrease in undetected volume with increasing pulse density from 64% at 1.3 pulses/m^2 to 28% at 12.7 pulse/m^2 of the total amount of filled TLS voxels. The rate in decrease of undetected filled TLS voxels is getting smaller with increasing pulse density indicating again a saturation level for the amount of observable forest volume from the ALS point of view. However, full saturation is not reached with the original pulse density (12.7 pulses/m^2) of the ALS data used in this study. The red line in Figure 2.9 denotes the amount of undetected filled TLS voxels inside occluded and unobserved voxels of the ALS leaf-on dataset in relation to the total amount of filled TLS voxels, when we fill the ALS leaf-on occluded and unobserved voxels with the information retrieved from the ALS leaf-off dataset. Such a filling of occluded and unobserved voxels was only performed when the leaf-off voxel was classified as observed with a laser return inside the voxel. Empty voxels in the leaf-off condition were not considered here. At the highest pulse density, such a filling of occluded and unobserved voxels decreased the undetected potentially filled volume from 28% to 21% of the total volume containing TLS laser returns.

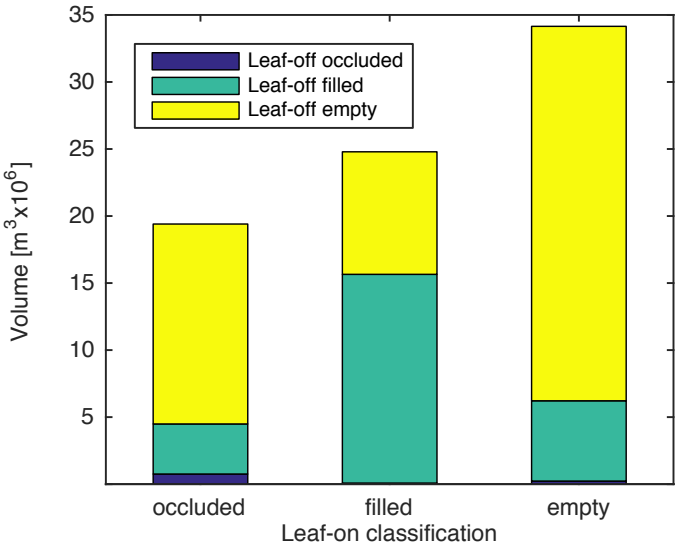

Fig. 2.7: Voxel classification of leaf-off acquisition inside leaf-on occluded, filled and empty classified voxels. Voxel classification was derived at a voxel side length of 1 m. The three bars denote the volume that was classified as occluded, filled, or empty under leaf-on conditions. The coloured bars denote the volume inside the leaf-on occluded, filled and empty voxels that were classified as occluded (blue), filled (green), or empty (yellow) under leaf-off conditions.

2.5 Discussion

2.5.1 Occlusion mapping

Several factors may affect the amount of occlusion such as the canopy height and cover as well as the slope of the terrain. As the flight lines were oriented nearly perpendicular to the orientation of the mountain ridge, the influence of the slope is assumed relatively small. Further sources of uncertainties can be found in the processing of the raw ALS data. The raw ALS data was projected into the Swiss CH-1903 Cartesian coordinate system, which could lead to non rectilinear pulse paths when reconstructing the pulse from the three-dimensional laser return positions. However, as first return locations were used instead of system positions as the pulse origin to assess the pulse directions, the modelled path length of the pulse is relatively short, minimising such an effect. In fact, only a very small positional deviation of intermediary returns from the laser pulse path described by the locations of the first and last laser return was found (0.7 mm in average, 0.37 mm standard deviation, distances calculated orthogonally to the laser pulse direction). Considering the accuracy of the ALS system itself as well as the used voxel size of 1 m, this source of uncertainty is negligible. To be sure that no laser return was missed during the voxel traversal due to small deviations from the modelled laser pulse path, all returns were projected orthogonally to the pulse direction onto the modelled laser path.

A bigger source of uncertainty can be found in the approximation of the laser pulse direction for single return pulses. The further away the closest multiple return pulse is, the less accurate the pulse direction approximation will be. This is specifically a problem for flat, unvegetated areas where a large scan angle range without registering any multiple return pulses might occur. However, as we focused our analyses on forested terrain, such large plain surfaces are masked out, minimising this problem. Nevertheless, 25% of all laser pulses are single return pulses even in

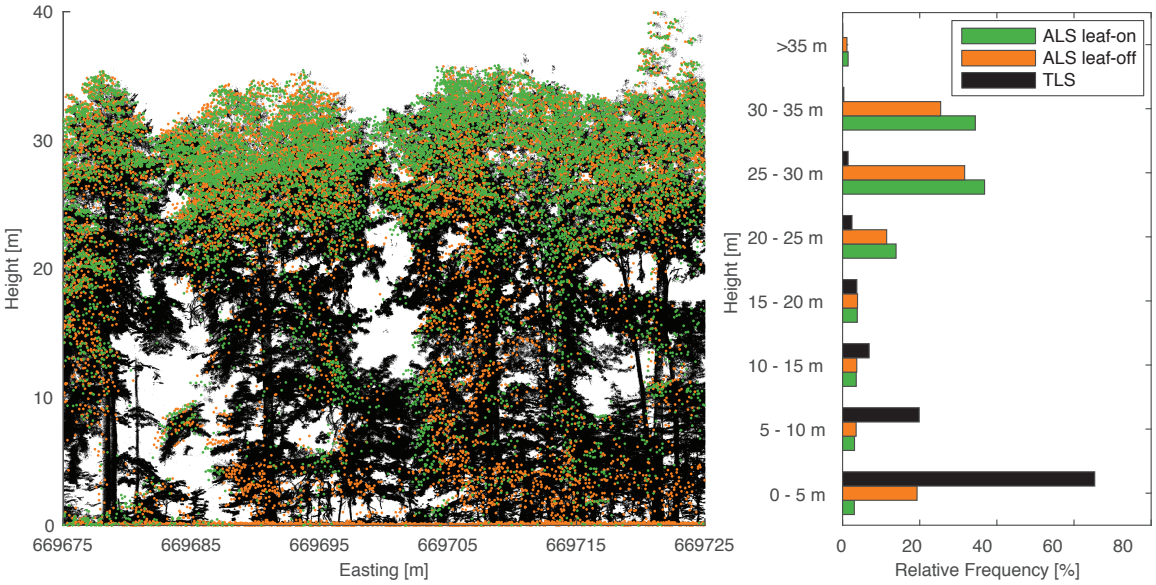

Fig. 2.8: Comparison of ALS and TLS point-clouds for a 10 m x 50 m transect. Right panel shows the relative frequency of the three point-clouds as a function of height.

forested areas, indicating that the effects of inaccurate pulse direction estimation should be accounted for. Yet, the average scan angle step from a single return pulse to the nearest multiple return pulse (according to GPS time) was calculated to 1.42 with a standard deviation of 1.25. Considering the angular step width of 0.0176°, the error introduced by taking the pulse direction of the closest multiple return pulse is assumed to be minimal in average, especially compared to the voxel size of 1 m.

The influences of voxel size, pulse density, flight strip overlap, season of overflight as well as the implications of the infinitesimally small laser pulse width assumption are discussed in more details in the following sections.

2.5.2 Occlusion sensitivity analysis

2.5.2a Implications of the infinitesimally small laser pulse width assumption

The analysis on the implications of the infinitesimally small laser pulse width assumption showed that by neglecting the pulse width during the voxel traversal, the amount of occlusion detected in the forest canopy is overestimated by 7% compared to a voxel traversal where the pulse width is considered for. However, as we do not know, which part of the laser pulse was intercepted for each laser return, it is not possible to quantify the occluded volume caused by the partial occluded sections of the pulses. In order to fully assess this assumption, a virtual simulation of ALS acquisitions would be needed (e.g. Morsdorf *et al.*, 2009; Disney *et al.*, 2010) and should be subject to future studies. Nevertheless, we assume that the overestimation of the occluded volume due to the infinitesimally small laser pulse width assumption might be even smaller if we account for partially occluded pulses. We argue that the results based on an infinitesimally small laser pulse footprint show the general trend and will not differ significantly when beam width is accounted for in the voxel traversal algorithm.

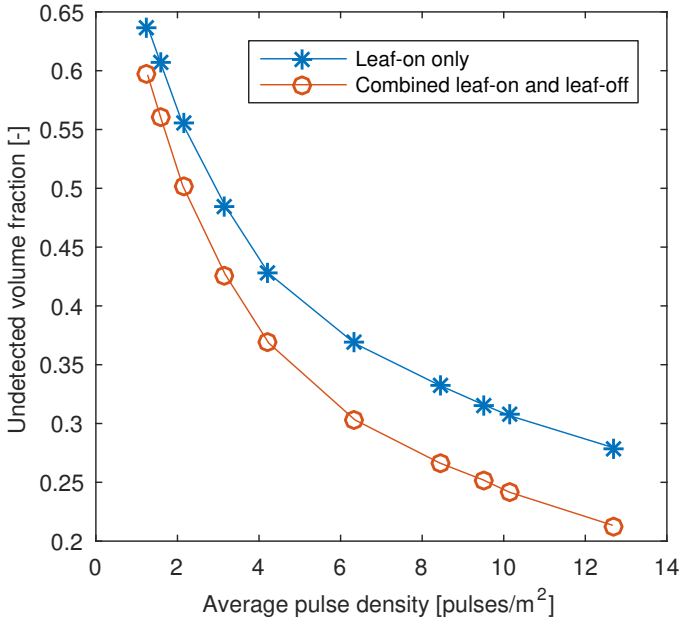

Fig. 2.9: Fraction of filled TLS voxels (at voxel side length of 10 cm) undetected by ALS in relation to all filled TLS voxels. The blue line denotes the undetected volume fraction from leaf-on data only. The red line denotes the undetected volume fraction when the leaf-on occluded voxels were filled using observed voxels from the leaf-off dataset. For the voxel traversal of the ALS data, a voxel side length of 1 m was chosen.

2.5.2b Voxel size influence on occlusion

As was shown in Figure 2.3, the voxel size plays an important role in the amount of detected occluded voxels. However, the decreased amount of occlusion at larger voxel sizes does not mean that we encounter less occlusion, but rather that we are unable to detect the actual occluded volumes. The optimum voxel size therefore needs to be small enough to detect occlusion, but large enough that each voxel is traversed by at least one or preferably several pulses to increase robustness of the occlusion detection. For the remaining analyses on occlusion dependences we chose a voxel size of 1x1x1 m^3. The quantified amount of occlusion is therefore specific for this chosen voxel size. Leiterer *et al.* (2015b) recommend in their study about characterising canopy layering to use the smallest possible grid-cell size supported by the ALS data source (i.e. 1m in their case). Otherwise, a loss of spatial information regarding vertical canopy structure would occur (Leiterer *et al.*, 2015b). However, as Leiterer *et al.* (2015b) did not use a voxel traversal approach, their results might not fully apply to our study. Voxel sizes below 1 m side length may be critical due to positional inaccuracies of up to $\pm$ 0.5m mostly caused by the ALS system itself (Glennie, 2007; Joerg *et al.*, 2012). Potential tree movements due to wind between laser acquisitions is also considered a source of uncertainty, as laser returns from the same target can be located in different voxels for different laser acquisitions. By using a voxel size larger than the pulse diameter (approx. 3 times larger for 1 m voxel size), this issue can be slightly reduced.

The choice in voxel size plays also an important role in determining occluded voxels in TLS measurements. For the cross-comparison between ALS and TLS we chose a voxel side length of 10 cm for the voxel traversal of the TLS scans. This lies in the range of optimal voxel sizes between 5 and 20 cm for the detection of occlusion as suggested by Béland *et al.* (2014a) who employed a TLS instrument with similar scan configurations. Béland *et al.* (2014a) state that the optimal voxel size for

locating occlusion is largely related to the distance between consecutive laser pulses and the predominance of occlusion effects in the study site. In this study, the TLS measurements were made with an angle between consecutive laser pulses of 0.04° (0.015° to 0.016° in Béland *et al.* (2014a)) which resulted in a distance between pulses of about 14 mm at a distance of 20 m from the instrument. Therefore, about 51 pulses will traverse each voxel at a distance of 20 m from the instrument.

2.5.2c Pulse density influence on occlusion

The analysis of pulse density influence on occlusion (see Sections 2.4.2c and 2.4.3b) showed that the amount of observed voxels saturates with increasing pulse density. However, a certain pulse density is needed in order to represent the canopy structure with minimal occlusion. This saturation effect with increasing pulse density is in agreement with previous studies (e.g. Lim *et al.*, 2008; Ko *et al.*, 2012; Treitz *et al.*, 2012; Leiterer *et al.*, 2015a,b). For our study site with only one single flight strip, a pulse density of at least 3 pulses/m^2 is needed in order to observe more than 50% of the total forest canopy volume. Additional observation angles from overlapping flight strips further decrease the occluded volume to an extent that up to 80% of the total canopy volume could be observed with three overlapping flight strips at an average pulse density of 15 pulses/m^2. Yet, these suggestions are only applicable for the rather small scale applied in this study. For example, Wilkes *et al.* (2015) and Treitz *et al.* (2012) pointed out that lower pulse densities (0.5-4 pulses/m^2) are sufficient for canopy-structure analysis at plot level. However, their results are based on relatively large plots of 400 to 2000 m^2 in size. Hayashi *et al.* (2014), in contrast, concluded that in complex forests, low-density ALS data was ineffective in depicting canopy structure descriptors at stand level (i.e. maximum tree height, stem density, basal area, and stem volume) with sufficient accuracy. This is in accordance with the results of this study.

With the systematic pulse density reduction approach based on the GPS time tag of each pulse, the inhomogeneities in pulse density due to changes in pitch, yaw and roll of the aircraft remain. This enabled an analysis of pulse density influence on occlusion as if we were measuring at lower pulse repetition frequencies. However, higher pulse densities than the analysed unthinned pulse density (5 pulses/m^2) would be needed for each flight strip to thoroughly analyse the pulse density dependence on occlusion. Of special interest is the saturation point at which a further pulse density increase would not result in more canopy volume being observed.

2.5.2d Flight strip overlap influence on occlusion

The flight strip overlap analysis showed a clear trend towards an improved observation capability with larger overlaps. However, the influence of flight strip overlap and pulse density on the amount of observed voxels can never be fully decoupled in real world applications of ALS data. In order to fully quantify and assess the effects of multiple observation geometries, decoupled from pulse density, an experimental ALS campaign or a virtual simulation of ALS acquisitions (e.g. Morsdorf *et al.*, 2009; Disney *et al.*, 2010) is needed where a relatively homogenous forest area is observed at multiple observation angles and varying pulse densities. Nevertheless, we argue that a large flight strip overlap can be favourable for forest canopy assessment, as occluded canopy volume from one flight strip can be observable from another perspective. Figure 2.5 showed that an increase in flight strip overlap has a larger effect on the observable volume than a mere increase in pulse density. When adding a second

flight strip at half the original pulse density (2.3 pulses/m^2 for single coverage and 4.8 pulses/m^2 for double coverage) the observable volume increases by 14% while a doubling in pulse density (from 2.3 pulses/m^2 to 4.6 pulses/m^2) with constant single flight strip overlap only increases the observable volume by 8%. For larger pulse densities, this suggests that the additional observation angle has a larger effect on the observable volume than the mere increase in pulse density. This observation is less pronounced for lower pulse densities, as an increase in pulse density has a larger effect on the observable volume than at higher pulse densities (see Figure 2.4).

As the amount of occlusion is highly reduced under leaf-off conditions and the causes for occlusion can be mostly attributed to the type of forest analysed, no flight strip overlap analysis for the leaf-off data was performed.

2.5.2e Seasonal influence on occlusion

Figure 2.7 showed that most of the leaf-off voxels inside the leaf-on occluded voxels were actually classified as empty, and have therefore not enough vegetation elements to trigger a laser return. Yet, due to the missing foliar material under leaf-off condition, we cannot conclude that most of the occluded leaf-on voxels would actually be empty without any occlusion effects. The occlusion compensation capability by using leaf-off data is therefore limited due to the different distribution of foliar material between the two seasons. Yet, as was shown in Figure 2.9, for higher pulse densities (average pulse density $>$ 4 pulses/m^2), the use of additional leaf-off data would improve the detection of vegetation elements more than any increase in pulse density. However, the additionally detected vegetation elements will likely be woody material in deciduous and mixed forests, and therefore not improve biophysical parameter estimation based on leaf area. Several studies reported an added value of leaf-off acquisitions over leaf-on acquisitions for area-based canopy structure estimates (e.g. Næsset, 2005; Ørka *et al.*, 2010). On the other hand, Leiterer *et al.* (2015a) argues that the added value of leaf-off data is relatively low when characterising canopy structure if leaf-on data is available.

The differences in voxel classification between leaf-on and leaf-off acquisitions as shown in Figure 2.7 can mostly be explained by the missing foliar material under leaf-off. But also other temporal effects, such as different weather conditions (e.g. wind), changes in forest structure due to intensive forest management, or representation errors (Schneider *et al.*, 2015) can be a cause for the temporal differences in voxel classification.

2.5.3 ALS-TLS cross-comparison

Figure 2.9 showed that a substantial amount of filled TLS voxels were not detected due to occlusion in the ALS acquisition. Yet, these results have to be taken with care. Due to the different viewing and acquisition geometry, the two systems observe the forest in an entirely different way (Hilker *et al.*, 2010, 2012). The TLS measurements were acquired using large scan overlaps, resulting in many more observation angles compared to the ALS acquisitions. Also, the larger scan angle range found in TLS acquisitions in combination with the sensor locations close to the ground enabled the system to register the vertical features such as tree trunks and smaller branches in high detail. ALS systems, on the other hand, have difficulties to detect such vertical features in similar detail due to its top-down viewing geometry, lower pulse densities, and fewer observation angles as well as smaller scan angle ranges. This has important implications for the cross-comparison of ALS and TLS acquisitions. Many filled TLS

voxels originate from tree trunks and would therefore be difficult to detect by the ALS system, even without any apparent occlusion effects present. Therefore, some of the undetected volume found in the ALS occluded voxels would not have been detected, even if the laser pulses were not obstructed by earlier dense vegetation. Nevertheless, as we can increase the detected volume by up to 7% by combining leaf-on and leaf-off data at the highest pulse densities, we can still conclude that there is a substantial number of vegetation elements that could be observed by the ALS system, if no occlusion was present.

Also co-registration errors between ALS and TLS acquisitions have to be considered for this cross-comparison approach. Due to aggregation of the laser returns into voxels of 10 cm and 1 m side length in the TLS and ALS case respectively, such co-registration errors can be reduced.

2.6 Conclusion and Outlook

In this study, we presented an approach to map and quantify occluded volume inside a mixed temperate forest canopy using multi-temporal airborne laser scanner (ALS) measurements. The proposed approach is based on a voxel traversal algorithm tracing each laser pulse through a pre-defined voxel grid. We analysed the influence of pulse density, flight strip overlap and season of overflight on the amount of occlusion. Additionally, we quantified the potentially hidden vegetation elements due to ALS occlusion by cross-comparing the ALS voxel classification grid with voxelized terrestrial laser scanner (TLS) measurements on a 50x50 m^2 plot inside the study area.

The results of this study showed that even with high pulse densities (average pulse density of > 10 pulses/m^2), a significant amount of canopy volume remained occluded especially under leaf-on conditions (up to 25% of total canopy volume). Due to missing foliar material under leaf-off conditions, laser penetration into the canopy is improved and the amount of occlusion is hence reduced (only 1.4% of total canopy volume). Also the saturation of observed canopy volume with increasing pulse density was observed, as already discussed in previous studies (e.g Lim *et al.*, 2008; Ko *et al.*, 2012; Treitz *et al.*, 2012; Leiterer *et al.*, 2015a,b).

The increase in flight strip overlap showed an improvement in the amount of observed canopy volume. However, flight strip overlap and pulse density is never fully decoupled and is therefore difficult to assess and quantify separately. We therefore suggest further investigation of the effects of multiple observation geometries on the amount of occlusion with specifically designed experiments.

We conclude that the proposed voxel traversal approach can be an important tool for canopy structure retrieval or model parameterisation as it finally allows to quantify occluded volume in ALS acquisitions and therefore adds an enhanced view on the ALS acquisitions beyond the traditionally analysed point-cloud data. Furthermore, the algorithm has additional possible applications such as plant area index (PAI) retrieval on a voxel scale similar to approaches already introduced for TLS acquisitions (e.g. Béland *et al.*, 2011). As the algorithm extracts for each voxel the number of pulses having a laser return inside the voxel and the number of pulses going through the voxel without any interactions, we are able to extract a kind of penetration rate per voxel, which can be related to PAI (Chen *et al.*, 1997; Solberg, 2010). Based on the findings of this study, we suggest large flight strip overlaps of

at least 50% with a combined pulse density of $>$10 pulses/m^2 in order to minimise occlusion.

Acknowledgements

The research leading to these results has received funding from the European Union's 7th Framework Programme (FP7/2014 - 2018) under EUFAR2 contract n° 312609. The contributions of Felix Morsdorf, Fabian D. Schneider, and Michael E. Schaepman are supported by the University of Zurich Research Priority Program on 'Global Change and Biodiversity'. We thank the anonymous reviewers for their valuable comments.

2.7 References

Amanatides J, Woo A (1987) A fast voxel traversal algorithm for ray tracing. *Proceedings of EUROGRAPHICS*, **87**, 3–10.

Antonarakis AS, Munger JW, Moorcroft PR (2014) Imaging spectroscopy- and lidar-derived estimates of canopy composition and structure to improve predictions of forest carbon fluxes and ecosystem dynamics. *Geophysical Research Letters*, **41**, 2535–2542.

Asner GP (1998) Biophysical and Biochemical Sources of Variability in Canopy Reflectance. *Remote Sensing of Environment*, **64**, 234–253.

Asner GP, Mascaro J, Muller-Landau HC, *et al.* (2012) A universal airborne LiDAR approach for tropical forest carbon mapping. *Oecologia*, **168**, 1147–1160.

Beer C, Reichstein M, Tomelleri E, *et al.* (2010) Terrestrial gross carbon dioxide uptake: global distribution and covariation with climate. *Science (New York, N.Y.)*, **329**, 834–838.

Béland M, Baldocchi DD, Widlowski JL, Fournier RA, Verstraete MM (2014a) On seeing the wood from the leaves and the role of voxel size in determining leaf area distribution of forests with terrestrial LiDAR. *Agricultural and Forest Meteorology*, **184**, 82–97.

Béland M, Widlowski JL, Fournier RA (2014b) A model for deriving voxel-level tree leaf area density estimates from ground-based LiDAR. *Environmental Modelling & Software*, **51**, 184–189.

Béland M, Widlowski JL, Fournier RA, Côté JF, Verstraete MM (2011) Estimating leaf area distribution in savanna trees from terrestrial LiDAR measurements. *Agricultural and Forest Meteorology*, **151**, 1252–1266.

Betts AK, Ball JH, Mccaughey JH (2001) Near-surface climate in the boreal forest. *Journal of Geophysical Research*, **106**, 33529–33541.

Bienert A, Queck R, Schmidt A (2010) Voxel Space Analysis of Terrestrial Laser Scans in Forests for Wind Field Modeling. *International Archives of the Photogrammetry, Remote Sensing and Spatial Information Sciences - ISPRS Archives*, **38**, 92–97.

Bonan GB (2008) Forests and climate change: forcings, feedbacks, and the climate benefits of forests. *Science (New York, N.Y.)*, **320**, 1444–1449.

Chen JM, Rich PM, Gower ST, Norman JM, Plummer S (1997) Leaf area index of boreal forests: Theory, techniques, and measurements. *Journal of Geophysical Research*, **102**, 29429–29443.

Coops NC, Hilker T, Wulder MA, St-Onge B, Newnham G, Siggins A, Trofymow JAT (2007) Estimating canopy structure of Douglas-fir forest stands from discrete-return LiDAR. *Trees*, **21**, 295–310.

Côté JF, Fournier RA, Egli R (2011) An architectural model of trees to estimate forest structural attributes using terrestrial LiDAR. *Environmental Modelling & Software*, **26**, 761–777.

Danson FM, Hetherington D, Morsdorf F, Koetz B, Allgower B (2007) Forest Canopy Gap Fraction From Terrestrial Laser Scanning. *IEEE Geoscience and Remote Sensing Letters*, **4**, 157–160.

Disney M, Kalogirou V, Lewis P, Prieto-Blanco A, Hancock S, Pfeifer M (2010) Simulating the impact of discrete-return lidar system and survey characteristics over young conifer and broadleaf forests. *Remote Sensing of Environment*, **114**, 1546–1560.

Disney M, Lewis P, Saich P (2006) 3D modelling of forest canopy structure for remote sensing simulations in the optical and microwave domains. *Remote Sensing of Environment*, **100**, 114–132.

Eugster W, Zeyer K, Zeeman M, Michna P, Zingg a, Buchmann N, Emmenegger L (2007) Methodical study of nitrous oxide eddy covariance measurements using quantum cascade laser spectrometery over a Swiss forest. *Biogeosciences*, **4**, 927–939.

FAO (2010) Global Forest Resources Assessment 2010 Main Report. *FAO Forestry Paper*, **163**, 1–378.

Foody GM (2010) Assessing the accuracy of land cover change with imperfect ground reference data. *Remote Sensing of Environment*, **114**, 2271–2285.

Givnish TJ (1988) Adaptation to Sun and Shade : A whole-plant Perspective. *Australian Journal of Plant Physiology*, **15**, 63–92.

Glennie C (2007) Rigorous 3D error analysis of kinematic scanning LIDAR systems. *Journal of Applied Geodesy*, **1**, 147–157.

Groffman PM, Tiedje JM (1989) Denitrification in north temperate forest soils: Spatial and temporal patterns at the landscape and seasonal scales. *Soil Biology and Biochemistry*, **21**, 613–620.

Haara A, Leskinen P (2009) The assessment of the uncertainty of updated stand-level inventory data. *Silva Fennica*, **43**, 87–112.

Hayashi R, Weiskittel A, Sader S (2014) Assessing the Feasibility of Low-Density LiDAR for Stand Inventory Attribute Predictions in Complex and Managed Forests of Northern Maine, USA. *Forests*, **5**, 363–383.

Hilker T, Coops NC, Newnham GJ, van Leeuwen M, Wulder MA, Stewart J, Culvenor DS (2012) Comparison of Terrestrial and Airborne LiDAR in Describing Stand Structure of a Thinned Lodgepole Pine Forest. *Journal of Forestry*, **110**, 97–104.

Hilker T, van Leeuwen M, Coops NC, Wulder Ma, Newnham GJ, Jupp DLB, Culvenor DS (2010) Comparing canopy metrics derived from terrestrial and airborne laser scanning in a Douglas-fir dominated forest stand. *Trees*, **24**, 819–832.

Hovi A, Korpela I (2014) Real and simulated waveform-recording LiDAR data in juvenile boreal forest vegetation. *Remote Sensing of Environment*, **140**, 665–678.

Ishii HT, Tanabe S, Hiura T (2004) Exploring the relationships among canopy structure, stand productivity, and biodiversity of temperature forest ecosystems. *Forest Science*, **50**, 342–355.

Jakubowski MK, Guo Q, Kelly M (2013) Tradeoffs between lidar pulse density and forest measurement accuracy. *Remote Sensing of Environment*, **130**, 245–253.

Joerg PC, Morsdorf F, Zemp M (2012) Uncertainty assessment of multi-temporal airborne laser scanning data: A case study on an Alpine glacier. *Remote Sensing of Environment*, **127**, 118–129.

Jones TG, Coops NC, Sharma T (2012) Assessing the utility of LiDAR to differentiate among vegetation structural classes. *Remote Sensing Letters*, **3**, 231–238.

Khosravipour A, Skidmore AK, Isenburg M, Wang T, Hussin YA (2014) Generating Pit-free Canopy Height Models from Airborne Lidar. *Photogrammetric Engineering & Remote Sensing*, **80**, 863–872.

Kindermann GE, McCallum I, Fritz S, Obersteiner M (2008) A global forest growing stock, biomass and carbon map based on FAO statistics. *Silva Fennica*, **42**, 387–396.

Ko C, Sohn G, Remmel TK (2012) The impact of LiDAR point density on classifying tree genus: using geometric features and vertical profile features. In: *SilviLaser 2012*, pp. 67–74. Vancouver, Canada (September 16-19).

Korhonen L, Korpela I, Heiskanen J, Maltamo M (2011) Airborne discrete-return LIDAR data in the estimation of vertical canopy cover, angular canopy closure and leaf area index. *Remote Sensing of Environment*, **115**, 1065–1080.

Korpela I, Hovi A, Morsdorf F (2012) Understory trees in airborne LiDAR data - Selective mapping due to transmission losses and echo-triggering mechanisms. *Remote Sensing of Environment*, **119**, 92–104.

Lee AC, Lucas RM (2007) A LiDAR-derived canopy density model for tree stem and crown mapping in Australian forests. *Remote Sensing of Environment*, **111**, 493–518.

Leiterer R, Furrer R, Schaepman ME, Morsdorf F (2015a) Forest canopy-structure characterization: A data-driven approach. *Forest Ecology and Management*, **358**, 48–61.

Leiterer R, Torabzadeh H, Furrer R, Schaepman M, Morsdorf F (2015b) Towards Automated Characterization of Canopy Layering in Mixed Temperate Forests Using Airborne Laser Scanning. *Forests*, **6**, 4146–4167.

Lim K, Hopkinson C, Treitz P (2008) Examining the effects of sampling point densities on laser canopy height and density metrics. *The Forestry Chronicle*, **84**, 876–885.

Lovell JL, Jupp DLB, Newnham GJ, Culvenor DS (2011) Measuring tree stem diameters using intensity profiles from ground-based scanning lidar from a fixed viewpoint. *ISPRS Journal of Photogrammetry and Remote Sensing*, **66**, 46–55.

Martens SN, Ustin SL, Norman JM (1991) Measurement of tree canopy architecture. *International Journal of Remote Sensing*, **12**, 1525–1545.

McElhinny C, Gibbons P, Brack C, Bauhus J (2005) Forest and woodland stand structural complexity: Its definition and measurement. *Forest Ecology and Management*, **218**, 1–24.

Milan Geoservice GmbH (2014) Project Documentation - ALS flight campaign Canton of Aargau 2014.

Morsdorf F, Kötz B, Meier E, Itten K, Allgöwer B (2006) Estimation of LAI and fractional cover from small footprint airborne laser scanning data based on gap fraction. *Remote Sensing of Environment*, **104**, 50–61.

Morsdorf F, Meier E, Kötz B, Itten KI, Dobbertin M, Allgöwer B (2004) LIDAR-based geometric reconstruction of boreal type forest stands at single tree level for forest and wildland fire management. *Remote Sensing of Environment*, **92**, 353–362.

Morsdorf F, Nichol C, Malthus T, Woodhouse IH (2009) Assessing forest structural and physiological information content of multi-spectral LiDAR waveforms by radiative transfer modelling. *Remote Sensing of Environment*, **113**, 2152–2163.

Musselman KN, Margulis SA, Molotch NP (2013) Estimation of solar direct beam transmittance of conifer canopies from airborne LiDAR. *Remote Sensing of Environment*, **136**, 402–415.

Nadkarni NM, McIntosh AC, Cushing JB (2008) A framework to categorize forest structure concepts. *Forest Ecology and Management*, **256**, 872–882.

Næsset E (2005) Assessing sensor effects and effects of leaf-off and leaf-on canopy conditions on biophysical stand properties derived from small-footprint airborne laser data. *Remote Sensing of Environment*, **98**, 356–370.

Næsset E (2009) Effects of different sensors, flying altitudes, and pulse repetition frequencies on forest canopy metrics and biophysical stand properties derived from small-footprint airborne laser data. *Remote Sensing of Environment*, **113**, 148–159.

Ørka HO, Næsset E, Bollandsås OM (2010) Effects of different sensors and leaf-on and leaf-off canopy conditions on echo distributions and individual tree properties derived from airborne laser scanning. *Remote Sensing of Environment*, **114**, 1445–1461.

Pan Y, Birdsey Ra, Phillips OL, Jackson RB (2013) The Structure, Distribution, and Biomass of the World's Forests. *Annual Review of Ecology, Evolution, and Systematics*, **44**, 593–622.

Roberts J, Tesfamichael S, Gebreslasie M, van Aardt J, Ahmed F (2007) Forest structural assessment using remote sensing technologies: an overview of the current state of the art. *Southern Hemisphere Forestry Journal*, **69**, 183–203.

Robertson GP (1987) Geostatistics in ecology: interpolating with known variance. *Ecology*, **68**, 744–748.

Ross AN (2012) Boundary-layer flow within and above a forest canopy of variable density. *Quarterly Journal of the Royal Meteorological Society*, **138**, 1259–1272.

Schneider FD, Leiterer R, Morsdorf F, Gastellu-Etchegorry JP, Lauret N, Pfeifer N, Schaepman ME (2014) Simulating imaging spectrometer data: 3D forest modeling based on LiDAR and in situ data. *Remote Sensing of Environment*, **152**, 235–250.

Schneider FD, Leiterer R, Schaepman ME, Morsdorf F (2015) Canopy height and plant area index changes in a temperate forest between 2010 - 2014 using airborne laser scanning. In: *Proceedings of SilviLaser 2015 - September 28-30*, pp. 156–158. La Grande Motte, France.

Shugart HH, Saatchi S, Hall FG (2010) Importance of structure and its measurement in quantifying function of forest ecosystems. *Journal of Geophysical Research: Biogeosciences*, **115**, 1–16.

Solberg S (2010) Mapping gap fraction, LAI and defoliation using various ALS penetration variables. *International Journal of Remote Sensing*, **31**, 1227–1244.

Solberg S, Brunner A, Hanssen KH, Lange H, Næsset E, Rautiainen M, Stenberg P (2009) Mapping LAI in a Norway spruce forest using airborne laser scanning. *Remote Sensing of Environment*, **113**, 2317–2327.

Strahler AH, Jupp DLB, Woodcock CE, *et al.* (2008) Retrieval of forest structural parameters using a ground-based lidar instrument (Echidna). *Canadian Journal of Remote Sensing*, **34**.

Suratno A, Seielstad C, Queen L (2009) Tree species identification in mixed coniferous forest using airborne laser scanning. *ISPRS Journal of Photogrammetry and Remote Sensing*, **64**, 683–693.

Treitz P, Lim K, Woods M, Pitt D, Nesbitt D, Etheridge D (2012) LiDAR Sampling Density for Forest Resource Inventories in Ontario, Canada. *Remote Sensing*, **4**, 830–848.

Wilkes P, Jones SD, Suarez L, *et al.* (2015) Understanding the Effects of ALS Pulse Density for Metric Retrieval across Diverse Forest Types. *Photogrammetric Engineering and Remote Sensing*, **81**, 33–43.

Xue BL, Kumagai T, Iida S, *et al.* (2011) Influences of canopy structure and physiological traits on flux partitioning between understory and overstory in an eastern Siberian boreal larch forest. *Ecological Modelling*, **222**, 1479–1490.

Yang R, Friedl MA (2003) Modeling the effects of three-dimensional vegetation structure on surface radiation and energy balance in boreal forests. *Journal of Geophysical Research*, **108**, 8615.

Zellweger F, Braunisch V, Morsdorf F, *et al.* (2015) Disentangling the effects of climate, topography, soil and vegetation on stand-scale species richness in temperate forests. *Forest Ecology and Management*, **349**, 36–44.

Zellweger F, Morsdorf F, Purves RS, Braunisch V, Bollmann K (2014) Improved methods for measuring forest landscape structure: LiDAR complements field-based habitat assessment. *Biodiversity and Conservation*, **23**, 289–307.

Chapter

3

Quantifying 3D structure and occlusion in dense tropical and temperate forests using close-range LiDAR

Schneider, F.D., **Kükenbrink, D.**, Schaepman, M.E., Schimel, D.S., Morsdorf, F.

This section is based on the peer-reviewed article:
Quantifying 3D structure and occlusion in dense tropical and temperate forests using close-range LiDAR.
Agricultural and Forest Meteorology, 2019 (268), 249-257
DOI:10.1016/j.agrformet.2019.01.033
and is reprinted as the final submitted manuscript.
It has been modified to fit into the layout of this thesis.

F.D.S., D.K., M.E.S., D.S.S., and F.M. designed the study.
D.K. implemented and performed occlusion mapping,
F.D.S. and D.K. analysed the data and performed research.
All authors wrote the paper, with main contributions by F.D.S.

Abstract

Terrestrial laser scanning (TLS) has emerged as a reference for three-dimensional measurements of forest structure as well as forest reconstruction and modeling. Ground-based measurements can be complemented by new light-weight sensors on unmanned aerial vehicles (UAVs) or laser scans from canopy cranes or towers. However, it is still largely unknown how much of the forest canopy volume can be sampled and how occlusion is spatially distributed. We present an approach for highly detailed 3D structure measurements based on TLS on the ground and above canopy measurements from a canopy crane or UAV platform, and assess their spatial sampling in terms of occlusion. Comparing the application in a dense tropical and temperate forest, we demonstrate the ability to sample the complete canopy volume with $<$2% occlusion at very high spatial resolution when combining ground and above canopy measurements. This is necessary for a full canopy reconstruction. Ground-based TLS can provide sufficient coverage when no sampling of leaves and branches at top of canopy is required, whereas UAV or tower-based measurements show considerable occlusion in the mid- and understory. We therefore recommend to perform above canopy measurements under leaf off conditions, in sparse forests, or as an addition to ground measurements if a full representation of the whole canopy is required at very high spatial resolution. The latter can pave the way for studies on light availability, micrometeorology, sensor simulations and algorithm testing and development.

3.1 Introduction

Terrestrial laser scanning (TLS) has emerged as the reference for high-resolution 3D measurements of tree and forest structure, providing a very high level of detail and geometric accuracy. It can thus serve as a basis for models to develop and test new algorithms, measurement and sensor techniques, for validating airborne and spaceborne products, as well as for answering physical and ecological questions, as presented in a special issue by Danson *et al.* (2018). A range of applications have shown the potential of TLS for forest reconstruction, forest monitoring, and modeling of radiative transfer and biomass. Calders *et al.* (2015) have, for example, demonstrated that TLS based measures of tree height can be more accurate than traditional field-based measurements and that the diameter at breast height and biomass can be directly derived from TLS data with high accuracy (see also: Disney *et al.*, 2018; Momo Takoudjou *et al.*, 2018; Stovall *et al.*, 2017). Quantitative structure models (QSMs) have evolved as a fast and accurate method to extract the tree trunk including the branching structure from TLS point clouds, thus allowing to build detailed 3D models and deriving biomass or tree architectural traits (Raumonen *et al.*, 2013; Hackenberg *et al.*, 2015; Åkerblom *et al.*, 2017). Besides studies focusing on the woody parts of the tree, there are efforts towards a more complete reconstruction of trees and forest canopies in 3D including the density and distribution of leaves (Åkerblom *et al.*, 2018; Calders *et al.*, 2018). 3D tree or forest models derived from TLS measurements can be used in 3D radiative transfer models to simulate the interactions of radiation with the canopy (Schneider *et al.*, 2014; Gastellu-Etchegorry *et al.*, 2016; Yin *et al.*, 2016).

Widlowski *et al.* (2014) and Béland *et al.* (2014b) have shown results for a full reconstruction of single trees from TLS scans. Based on this, there are now tools and methods for a voxel-based 3D reconstruction of trees and canopies from TLS data (Grau *et al.*, 2017; Vincent *et al.*, 2017), but applications within dense forests have not been tested yet. Highly detailed measurements of the complete 3D canopy structure in dense forests that could serve as a reference for testing, validating and simulating are still sparse but emerging from new measurement strategies (Morsdorf *et al.*, 2018). One major source of uncertainty and difficulty of laser scanning and forest reconstruction in dense forests comes from occlusion, leading to unobserved volumes due to elements obstructing the measurement. When measuring a forest plot with TLS, the quality and completeness of the data is mainly determined by the applied measurement setup. The goal of reducing occlusion and reaching a complete coverage among all vertical layers of the canopy has to be traded against number of scan locations and hence costly operation time (Wilkes *et al.*, 2017).

Depending on the application, a different level of detail and coverage is needed. However, very little is known about how occlusion is occurring in dense forests and in what way it might influence forest reconstruction when working with close-range

laser scanning systems. For studying the interactions of radiation with the canopy it is important to have a complete sampling of the canopy volume especially in the uppermost parts, but that is where we expect most of the occlusion occurring when measuring with TLS from the ground. Although occlusion has been identified as a major source of uncertainty in forest reconstruction (Béland *et al.*, 2014a; Wilkes *et al.*, 2017), it has not been quantified or spatially mapped for TLS applications in dense forests. Kükenbrink *et al.* (2017) have shown the effects of occlusion for airborne laser scanning (ALS) measurements during leaf-on and leaf-off conditions, being considerable in the mid- and understory. Therefore, if a complete coverage over all vertical layers of the canopy is needed, ground-based TLS measurements might need to be complemented with above canopy measurements.

Measuring from a canopy crane or tower can be one way of acquiring high-resolution TLS data from within or above the canopy. Another way is to use miniaturized sensors on unmanned areal vehicles (UAV). UAV laser scanning (UAVLS) offers a new way to provide high-resolution data from above the canopy and might help to bridge the gap between ALS and TLS systems (Morsdorf *et al.*, 2018). However, how this improves occlusion and complements measurements from the ground is not known yet, but important to integrate the systems and assess their advantages and disadvantages. Both temperate as well as tropical forests can offer challenging conditions to get a complete measurement of forest structure and density. Temperate forests can build a very dense homogeneous canopy layer, providing limited penetration and overlap of measurements from above and below the canopy. In tropical forests, major challenges exist due to the height of emerging trees, large-leaved and dense understory as well as the complexity and density of the canopy.

In this study, we used a ray tracing approach to study the effects of occlusion on the detectability of plant elements in 3D space from above and below canopy close-range laser scanning measurements (UAVLS and TLS). The method implemented by Kükenbrink *et al.* (2017) uses a voxel-traversal algorithm and traces each laser pulse to determine sampled and occluded, empty or filled voxels. This allows to gain new insights on the influence of the measurement setup, including the advantage of new UAVLS systems, on the resulting spatial coverage and occlusion patterns in 3D space. This is crucial for deriving 3D information and modeling of dense forest canopies, as they can be found in temperate and tropical forest ecosystems. Therefore, our main research questions are: (1) How is occlusion distributed vertically among canopy layers in (a) measurements from the ground, (b) measurements from above the canopy and (c) combined above and below canopy measurements? (2) How do occlusion patterns differ between temperate and tropical forests? and (3) What is the resulting bias in the estimation of plant area density profiles when measuring from the ground or above the canopy only?

3.2 Materials and Methods

3.2.1 Study sites

We compare results from a temperate and tropical forest site with dense and tall canopies of around 30 to 50 m height. The temperate site is a mixed forest on the Laegern mountain in Switzerland (47°28'42.1" N, 8°21'51.7" E, 688 m above sea level). The site is located in a mixed beech forest with a total of 13 tree species, with about 70% deciduous broadleaf trees and about 30% evergreen coniferous trees (Schneider *et al.*, 2017). The dominant deciduous species is common beech (*Fagus sylvatica*). The 60 x 60 m measurement plot is located on the southern slope of the mountain range, west of the Laegern flux tower (CH-LAE) within a non-managed 5.5 ha research plot (see Guillén Escribà *et al.* (in review) for a detailed description of the plot). Canopy height on the beech-dominated plot ranges from 30 to 40 m in a single-layer canopy.

The tropical site is located in the Lambir Hills National Park on the island of Borneo, Malaysia. The rainforest at Lambir Hills, with perhaps 2500 species in total, is the world's most diverse forest yet studied in terms of tree species richness (Ashton, 2005). A plot of just 0.52 km^2 supports more tree species (1178 species) than the entirety of the temperate forests of the Northern Hemisphere (1166 species) (Harrison, 2011). The vegetation is classified as lowland mixed dipterocarp forest and as moist lowland tropical forest in the Holdridge system (Asner *et al.*, 2012). The most abundant species are belonging to the Euphorbiaceae and Dipterocarpaceae families. The 60 x 60 m measurement plot is located northwest of a canopy crane centered on a 4 ha research plot (see Manfroi *et al.* (2006) for a detailed description of the plot). The canopy crane is 80 m tall with a 75 m long rotating jib, providing access to all layers of the canopy from ground to above canopy level (Kenzo *et al.*, 2006). Canopy height ranges from 30 to 50 m with some emergent trees reaching up to 70 m (Hiromi *et al.*, 2012).

3.2.2 Measurement set up for ground measurements

Terrestrial laser scanning was performed on the ground using the Riegl VZ-1000 scanner operated at a pulse repetition frequency of 150 kHz with a maximum range of 950 m, and a pulse sampling interval of 0.04 degrees. The scanner has a beam divergence of 0.3 mrad, resulting in an increase of 30 mm of beam diameter per 100 m distance. Scans were conducted with active short range detection, which means that the minimum measurement distance is around 1.5 m. Since the scanner has a field of view of 360 x 100 degrees in horizontal and vertical direction, we performed a horizontal and a 90 degrees tilted scan at each scan location to cover the full sphere. At both sites, we chose a dense scan pattern on the ground with an

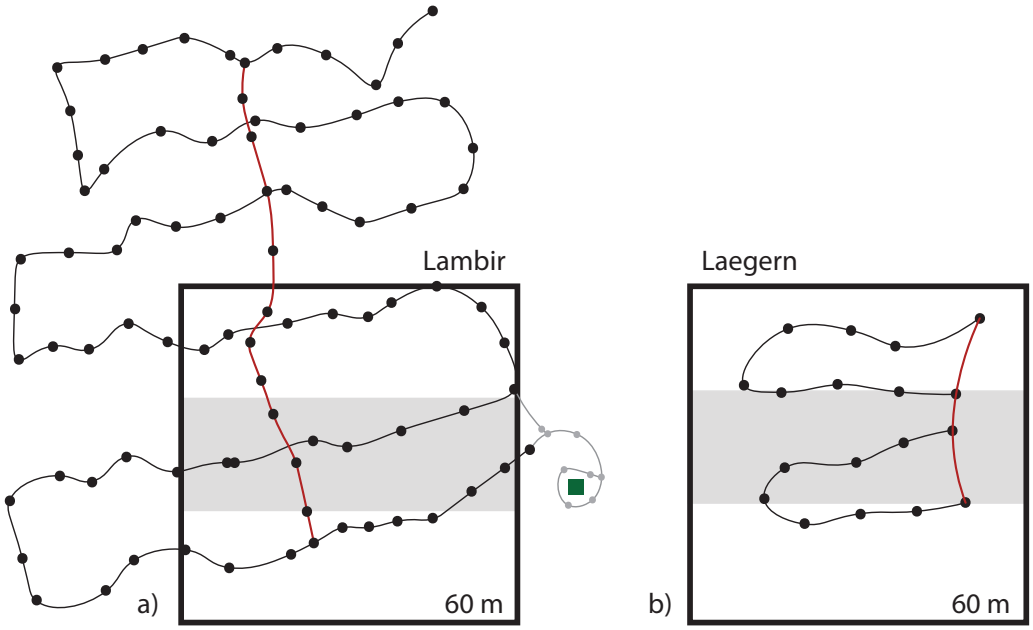

Fig. 3.1: The measurement set up for the TLS ground measurements at a) the tropical forest in Lambir Hills National Park and b) the temperate forest at Laegern. Black dots represent the scan locations, the red line represents the fixed scan line, and the gray line and dots represent the connection to the canopy crane (green square). The black rectangles show the extent of the 60 x 60 m plots, with shaded areas indicating the transects displayed in Fig. 3.3.

approximate distance between consecutive scan locations of 10-15 m. We placed reflective, cylindrical reference targets in the forest and ensured that at least five common targets were measured from two consecutive scan locations for geometric co-registration. This also led to slightly irregular scan patterns, since we had to place scans closer together in areas with very dense understory and thus low visibility. At both sites, we defined one fixed scan line spanning across the forest plot where we installed reference targets not being moved during the whole measurement campaign. We then scanned the forest in loops with starting and end points at the fixed scan line to improve geometric optimization of scan locations when co-registering all scans. We set out over 50 reference targets for each loop, so that most scans contained more than 10 reflective targets. The measurement setup at the tropical and the temperate site is shown in Fig. 3.1. At the tropical site, we covered 1 ha with 178 scans at 89 scan locations on the ground. We then selected a 60 x 60 m plot characterized by tall emergent trees being representative of the whole forest with a potentially good coverage by the ground and above canopy scans. We included the scans from outside the 60 x 60 m plot, since scans from farther away can contribute to the sampling in the upper canopy, especially in tall canopies. At the temperate site, we covered a 60 x 60 m plot representative of the dense beech forest with 80 scans at 40 scan locations on the ground. Scan and plot locations were optimized based on topography. Valleys, crests or very steep slopes did not allow to add additional scans in certain areas outside of the plots. We optimized the number of scan locations against time and

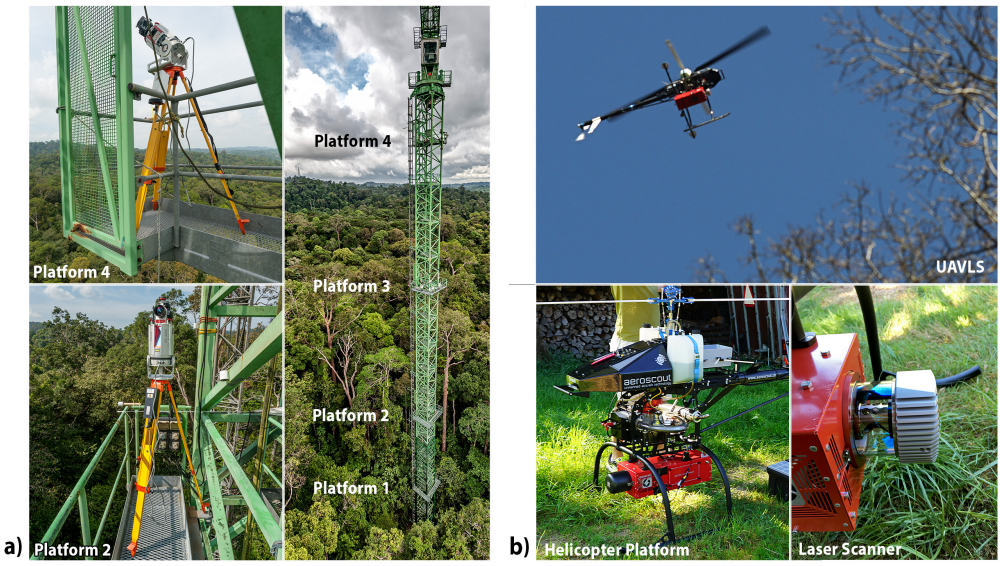

Fig. 3.2: The measurement set up for the TLS and UAVLS above canopy measurements at a) the tropical forest in Lambir Hills National Park and b) the temperate forest at Laegern. TLS measurements were taken on the canopy crane at platforms 1-4 at 24, 40, 60 and 75 m above ground. UAVLS measurements were taken using a helicopter-based platform and a laser scanner with a rotating mirror, set to an opening angle of 240°.

associated costs to measure the plots. However, some additional scans outside of the Laegern plot could have potentially helped to reduce occlusion on top of canopy.

3.2.3 Measurement set up for above canopy measurements

In the tropical forest, we made use of an 85 m tall canopy crane to scan the forest from within and above the canopy. The crane has four fixed platforms at about 24, 40, 60 and 75 m above ground that were used to scan the forest. Terrestrial laser scanning was performed at four scan locations on each platform using the Riegl VZ-1000 scanner operated at a pulse repetition frequency of 100 kHz with a maximum range of 1200 m, and a pulse sampling interval of 0.04 degrees. For geometric co-registration of the scans, we placed reflective, cylindrical reference targets on the platforms that were visible from both the scan locations on the platforms and on the ground. To connect the scan locations on the tower to the ones on the ground, it was necessary to perform high accuracy scans of the crane covering all platforms and reference targets with a pulse sampling interval of 0.02 degrees. We performed eight such scans at four locations around the canopy crane and an additional eight scans to connect the crane measurements to the main 1 ha plot (Fig. 3.1).

In the temperate forest, there was no comparable infrastructure to perform TLS measurements from a canopy crane or tower. Therefore, we used UAV based laser scanning for above canopy measurements. The LiDAR UAV set up combined the OxTS xNAV550 IMU/GPS dual-GPS-antenna navigation solution and the RIEGL VUX-1UAV

laser scanner mounted on the industrial Scout B1-100 UAV helicopter produced by Aeroscout GmbH, Switzerland. The flights were performed at an altitude of 40-50 m above the canopy top with a line spacing of 30 m. The UAV scanner has a beam divergence of 0.5 mrad, resulting in an increase of 50 mm of beam diameter per 100 m distance. The scan pattern and cruising speed of 6 m s^{-1} resulted in a point cloud with 817 pts m^{-2} on average. For a detailed description of the UAVLS measurements, processing and data quality we refer to Morsdorf *et al.* (2017). Figure 3.2 illustrates both laser scanning set ups used in the tropical and temperate forest for above canopy measurements.

3.2.4 Geometric co-registration of point clouds

The individual TLS and UAVLS point clouds were geometrically co-registered in Riscan Pro (Riegl, v2.0.2). For each TLS point cloud, the reference targets were mapped based on their high reflectivity of laser returns, and their location was manually set in 3D space to avoid erroneous attribution to noisy points or other highly reflective elements in the scans. The TLS scans were then co-registered in Riscan Pro based on common reference targets among scans in 3D space, and optimized to reduce the deviation among all targets. Plane patch filtering was applied to extract points belonging to flat surfaces. Finally, multi-station adjustment was performed in Riscan Pro using all reference targets and filtered patches to minimize the the geometric error among scans. This resulted in a geometric standard error of 1.5 cm as calculated based on 184193 filtered patches (including scans from the canopy crane).

The UAVLS point cloud was processed in RiPROCESS (Riegl) for flight strip adjustment of individual scan lines, as split up by linear scan trajectories along the terrain. The scan trajectories were optimized to minimize deviations of points between the scan lines due to possible misalignments of the laser scanner in relation to the IMU/GPS unit and varying GPS conditions during the flight (Morsdorf *et al.*, 2017). To be able to geometrically link the UAVLS and TLS acquisitions, we needed to geo-reference the TLS point cloud to the Swiss national reference system (CH1903+ LV95) according to the UAVLS point geometry. We accomplished that by a manual co-registration of the point cloud to a previously surveyed point cloud at the site as described in Schneider *et al.* (2014) and referenced following the procedure of Eysn *et al.* (2013). This allowed to match the TLS and UAVLS point cloud in the same reference system. Finally, we applied plane patch filtering to both point clouds and ran the multi-station adjustment to minimize remaining geometric deviations between filtered patches and tie points (reference targets). This resulted in a geometric standard error of 1.05 cm as calculated based on 20476 filtered patches and 3899 tie point connections.

3.2.5 Occlusion mapping and plant area density estimation

To be able to quantify the occurrence of occlusion in 3D space and investigate the spatial coverage of ground and above canopy measurements, a ray tracing algorithm was applied to track each individual laser pulse through a 3D voxel grid. We defined the voxel grid at 10 cm spatial resolution, being the highest resolution feasible under the assumption that a single laser scan samples all voxels of the 60 x 60 m plot within its field of view. This is in accordance with the recommendations by Béland *et al.* (2014a) and helps to achieve the best possible estimate of occluded volume, independent of the optimal voxel size for the retrieval of plant area index or density. A smaller voxel size would lie below the sampling density of the measurement (due to 7 cm pulse spacing at 100 m distance), and lead to an increasing number of unobserved voxels with increasing distance from the scanner. On the other hand, a larger voxel size would lead to a less accurate estimate of occluded volume simply due to the lower spatial resolution, and potentially an underestimation of occluded volume (depending on the definition of occlusion). The voxel traversal algorithm implemented by Kükenbrink *et al.* (2017) was optimized to reduce computation time with an implementation in C++ and adapted to TLS and UAVLS acquisition geometries. Therefore, it was possible to run the voxel traversal for each individual TLS scan of up to 94 Mio points and the UAVLS acquisition with 81 Mio points through the 600^3 voxel grid in less than 3 days (regular workstation, for all scans at both sites).

For occlusion mapping, the individual point clouds were first filtered to only keep single and last returns for ray tracing of pulses passing the voxel without interaction (miss), and pulses obstructed before passing the voxel (occlusion), see Kükenbrink *et al.* (2017) for more details. Here, we define occlusion of a single scan in a voxel grid as the voxels being traversed beyond the last registered return along the laser pulse trajectory. This means that possibly remaining energy leaving the forest without further interaction after the last return was treated as occluded. When combining several scans, we define occlusion as the voxels being occluded by all laser pulses possibly traversing the voxel. If a single laser pulse records information (miss, hit), a voxel is not considered occluded. For the retrieval of voxel-based information about the number of laser returns (hit), the point clouds were filtered based on a -20 db reflectance threshold to get rid of laser returns from atmospheric particles (mostly water vapor due to high humidity in the tropics) as well as noise from partial returns around the edges of objects (e.g. around the edges of leaves). Voxels, which were not traversed by any pulse, were marked as unobserved.

Pulses without returns were not considered for ray tracing, since pulses leaving the scene without interaction and pulses not measured by the instrument due to obstruction close to the instrument (below the minimum measurement distance of 1.5 m) could not be separated. Therefore, on average $<$0.5% and $<$4.3% of all pulses at the temperate and tropical site in the zenith scan angle range of -30 to 90 degrees

were omitted, see Suppl. Fig. S1 for exact percentages per zenith angle. Modeling these pulses as misses would lead to a larger bias than omitting them. Supplementary Figures S2 and S3 illustrate the percentage of occluded voxels ever unobserved in any scan due to pulse omission. At the temperate site, there is a maximum of about 4% of voxels affected that could potentially be gaps instead of occluded volume. At the tropical site, however, up to about 95% of occluded voxels would be affected in lower height levels when simulating obstructed pulses as pulses without interaction (misses). Based on this and a visual assessment of all terrestrial laser scans showing that most of the pulses without returns were occluded by elements closer than the minimum measurement distance (see Suppl. Fig. S4 for an example), we decided to exclude those pulses from ray tracing and occlusion mapping.

Merging the voxel grids at the two sites finally allowed to retrieve the total number occlusion, hits and misses for all scans on the ground, the above canopy measurements, and the combination of both. The latter should ideally lead to minimal occlusion and a complete spatial coverage of the canopy, from top of canopy down to the understory. To assess this quantitatively, we normalized the voxel grid by terrain height and calculated the percentage of occluded voxels. We excluded all voxels above the canopy by taking into account the digital surface model retrieved based on all points.

To further investigate how the measurement set up and associated occlusion is influencing the retrieval of canopy profiles or generally the modeling of forest canopies in 3D, we calculated plant area densities (PAD, m^2 m^{-3}) using the AMAPVox tool (v1.0.1, Vincent *et al.*, 2017). The software developed and validated by Vincent *et al.* (2017) runs on individual laser scans and allows to merge the resulting voxel grids to retrieve total plant area density in 3D. Since the retrieval algorithm is based on the assumption of randomly distributed scatterers within the voxels (turbid medium assumption), we had to choose a larger voxel size of 25 cm to ensure that multiple leaves and twigs would occupy a voxel in dense tropical and temperate forests. This is in accordance with the voxel size used by Grau *et al.* (2017) for high-resolution vegetation density estimation. We then derived the bias of vertical plant area density profiles from ground based and above canopy measurements compared to the profiles derived from all scans. In all cases, occluded voxels have zero plant area density. AMAPVox offers an option 'correct NaNs' (to fill occluded or unobserved voxels) for airborne laser scanning data, but it is not (yet) implemented for TLS. Depending on the application and the amount of occlusion, voxels could be filled in different ways. We implemented two simple solutions to show the impact on average PAD profiles, where occluded voxels were filled with either the mean non-occluded PAD per vegetation height layer or the total mean non-occluded PAD of the whole plot.

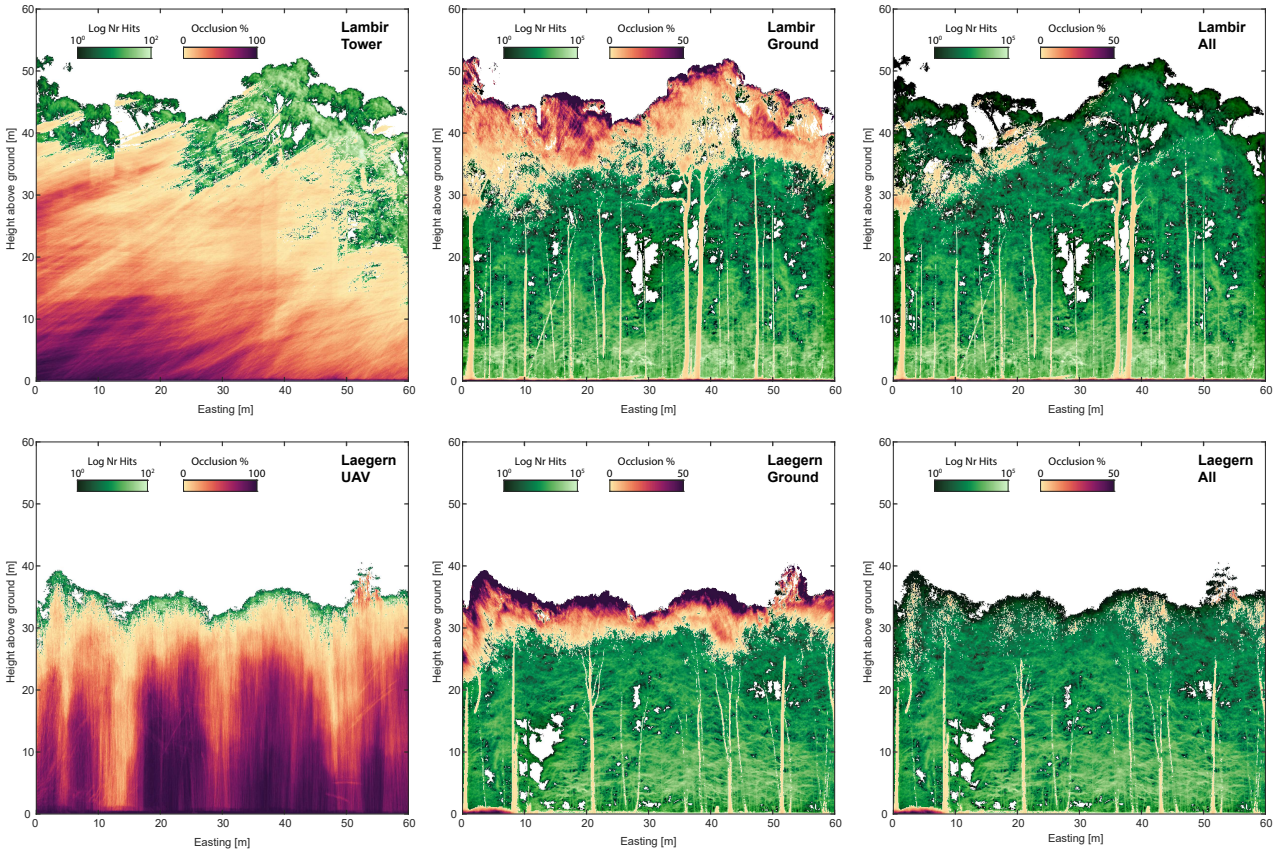

Fig. 3.3: Percentage occlusion of a 20 m deep transect through dense tropical (upper panels, Lambir Hills) and temperate (lower panels, Laegern) forest, see Fig. 3.1 for the location of the transect. Number of hits (laser returns) are shown where there is no occlusion (0%). The results from left to right show differences between above canopy (tower TLS in tropical and UAVLS in temperate forest), ground (TLS) and combined measurements.

To visualize voxels potentially belonging to tree stems in Figs. 3.5 and 3.6, we applied a simple approach for stem extraction using morphological filtering following Heinzel & Huber (2016).

3.3 Results

We quantified the occluded volume in three-dimensional space at a very high resolution of 10 cm for close-range above canopy measurements, such as laser scanning from a canopy crane and an unmanned-aerial vehicle, ground measurements using terrestrial laser scanning, and the combination of both measurement techniques. The spatial distribution of occlusion is shown in Fig. 3.3 and Supplementary Fig. S6. Above canopy measurements only show a good coverage within the first couple of meters of the canopy top, with occlusion reaching 100% close to the ground. The average occlusion up to 25 m above ground is 43% in the tropics and 71% in the temperate forest, as measured from a canopy crane and UAV respectively. Above 25 m, average occlusion drops to 5% and 9% respectively.

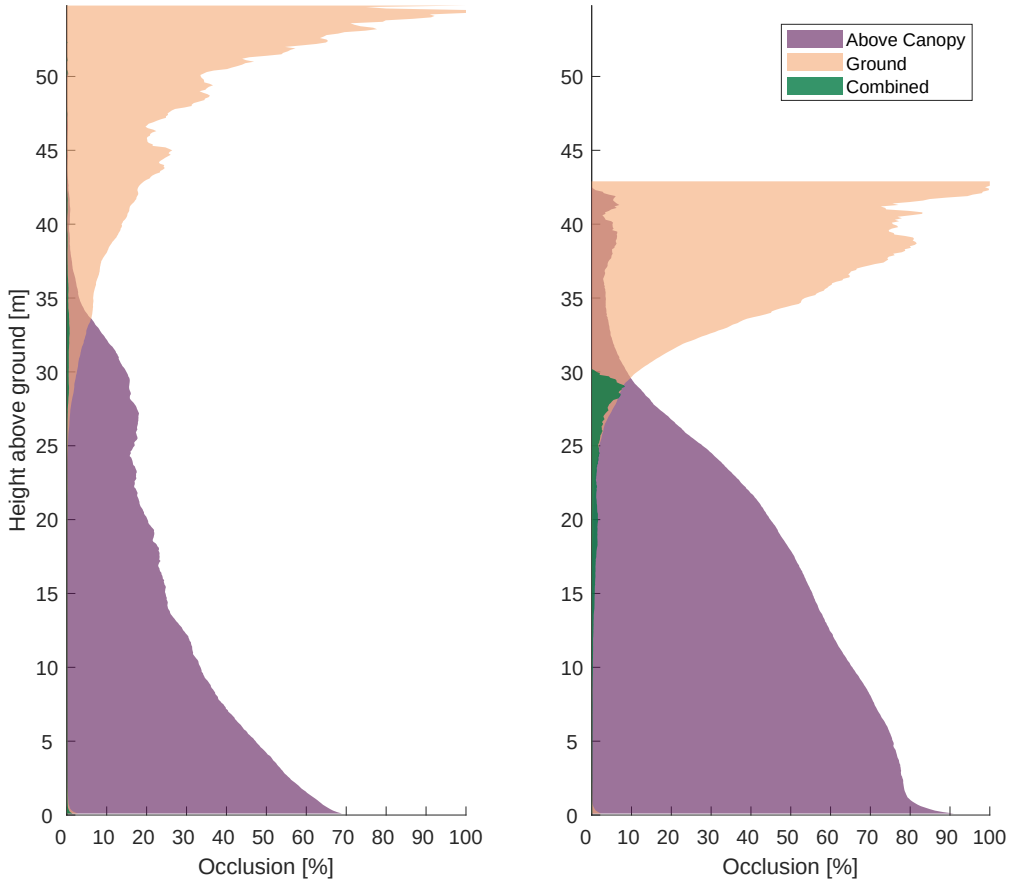

Fig. 3.4: Vertical distribution of occlusion in a tropical (left, Lambir Hills) and temperate (right, Laegern) forest based on above canopy, ground and combined measurements using UAVLS, TLS on a canopy crane and on the ground. The values are calculated as average percentage of occlusion on the whole 60 x 60 m plot.

In contrast, combined ground measurements show basically no occlusion at plot-level within the first 25 m above ground. This is astonishing considering the density of the mid- and understory in these forests. Occlusion only remains within tree stems, showing that the high-resolution occlusion mapping correctly captures the fact that the inside of a tree cannot be observed with light. Besides, occlusion occurs within the top-most parts of the crown, with an average of 21% and 43% above 25 m above ground respectively. Above canopy and ground-based measurements complement each other well, as can be seen in Fig. 3.3 and 3.4 showing the overall vertical distribution of occlusion. The intersection of occlusion profiles occurs at 34 and 30 m above ground with little overlap. In total, only 0.4% and 1.2% occlusion remain in the tropical and temperate forest when combining ground-based terrestrial laser scanning with above canopy close-range measurements. Actual occlusion in the canopy would be even smaller, since a part of it can be attributed to occlusion within tree stems.

An example of how the presented measurements can be used to model forests in 3D space based on a continuous voxel grid approach is provided in Fig. 3.5 for a

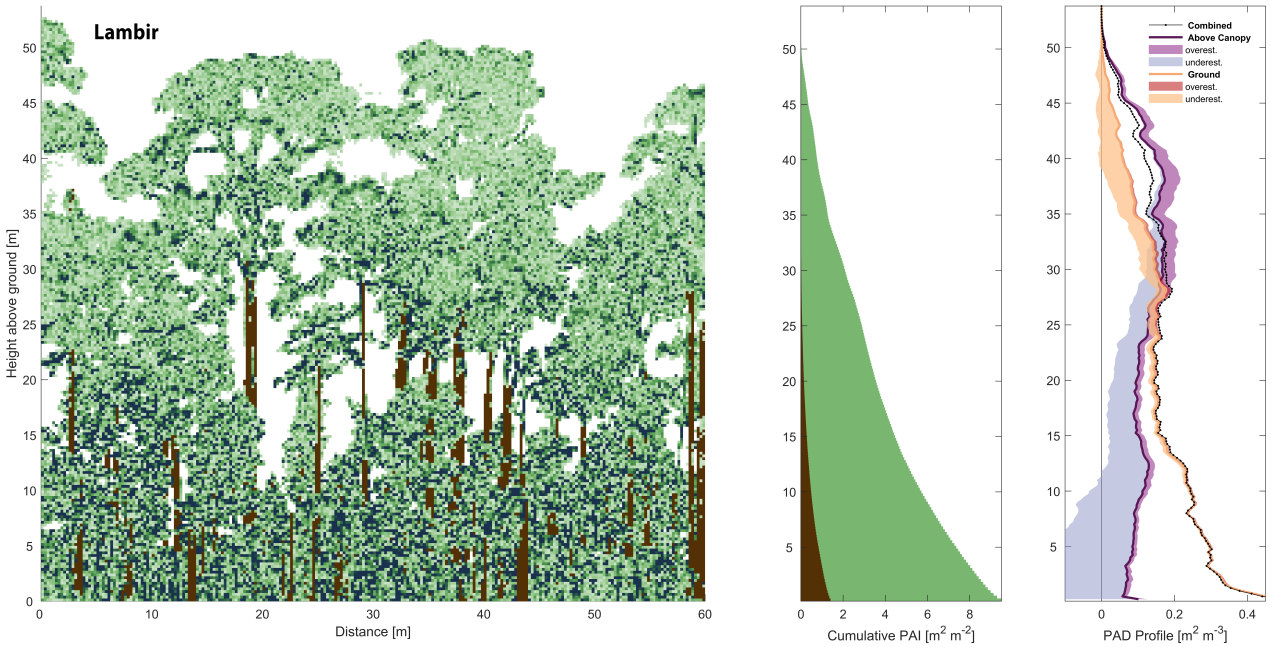

Fig. 3.5: 3D voxel grid of a tropical evergreen forest at Lambir Hills. The illustration shows voxel densities at 25 cm resolution from low (light green) to high (dark blue) of a 10 m deep transect and the corresponding cumulative plant area index (PAI). The right most panel shows how plant area density (PAD) profiles of the 60 x 60 m plot can be biased by using only above canopy or ground measurements, as compared to the combined measurements with almost no occlusion. The shading shows underestimation to the left and overestimation to the right of the mean.

tropical rainforest (Lambir) and in Fig. 3.6 for a temperate mixed forest (Laegern). The vertical cumulative plant area index shows that plant material is spread more evenly over a taller canopy in a multi-layered tropical rainforest, whereas it is more condensed in a closed-canopy single-layered temperate forest. The overall PAI values witin the displayed transects are almost identical, but with a much smaller contribution by the understory and no midstory in the temperate forest.

The forest canopy structure, including fine-scale gap distribution, is captured at high level of detail and coverage when combining ground and above canopy measurements. This can be considered as a reference for modeling canopies and associated processes such as light absorption and distribution from natural (solar radiation) as well as artificial sources (active remote sensing). Individually though, the measurements can show a considerable bias in plant area density compared to the combined dataset due to occlusion (e.g. when treating occluded voxels as zero PAD). This effect is different at the tropical (Fig. 3.5) than at the temperate site (Fig. 3.6). Mean vertical PAD in the tropical forest is underestimated on average by 38% in the upper canopy (>25 m above ground) when only using scans from the ground, whereas it is 11% over- and 50% underestimated in the upper and lower canopy respectively when only using measurements from above the canopy. In the temperate forest, mean vertical PAD derived from ground measurements is almost identical as derived from the combined dataset, whereas it is underestimated by 32% and 56%

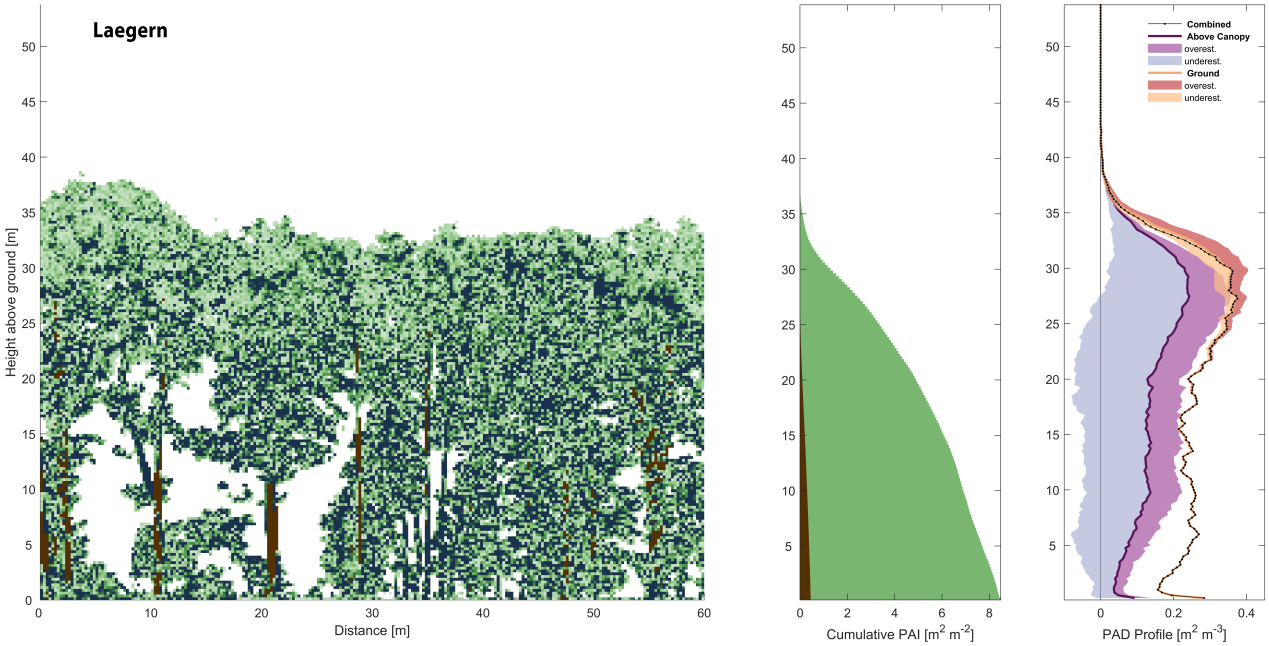

Fig. 3.6: 3D voxel grid of a temperate mixed forest at Laegern. The illustration shows voxel densities at 25 cm resolution from low (light green) to high (dark blue) of a 10 m deep transect and the corresponding cumulative plant area index (PAI). The right most panel shows how plant area density (PAD) profiles of the 60 x 60 m plot can be biased by using only above canopy or ground measurements, as compared to the combined measurements with almost no occlusion. The shading shows underestimation to the left and overestimation to the right of the mean.

in the upper (>20 m) and lower canopy (<20 m) respectively when using UAVLS scans only.

Filling occluded voxels can reduce some of the errors, especially in the lower canopy, as shown in Suppl. Fig. S5. Below 20 m canopy height, filling gaps of UAV measurements at Laegern leads to an overestimation of 73.3% and 6.2% when using the mean of each height layer or the overall mean of the plot respectively. At Lambir, the error is reduced to 7.8% and 1.7% respectively for above canopy measurements. In the upper canopy, however, the change is small and even results in a stronger overestimation at Laegern when using ground measurements.

The mean vertical PAD profile can be misleading when comparing plant area densities though, since under- and overestimation of individual voxels' PAD can cancel each other out at each height layer. Therefore, we show the shaded areas of under- and overestimation in Figs. 3.5 and 3.6 and the total root mean squared error (RMSE) for the mean PAD profiles and the PAD of individual vegetated voxels in Tab. 3.1, using PAD derived from the combined dataset as a reference. The results indicate that PAD overestimation of voxels close to occlusion and zero PAD of occluded voxels can balance each other out to a certain degree, especially in height layers close to the detection limit. This effect is more prominent at the temperate forest site, where canopy material, gaps and occlusion are spatially less structured and clumped along the vertical axis than in the tropical forest.

Tab. 3.1: Root mean squared errors (RMSE) of mean vertical plant area density (PAD, m^2m^{-3}) profiles and voxel PAD of vegetated voxels derived from either ground based measurements (TLS) or above canopy measurements (Tower TLS or UAVLS) only, as compared to the PAD values derived from the combined dataset for a tropical (Lambir Hills) and temperate forest (Laegern). Mean PAD is 0.16 and 0.64 m^2m^{-3} for profile and voxel values in the tropical forest, whereas it is 0.21 and 0.61 m^2m^{-3} in the temperate forest.

Forest Site	Ground		Above Canopy	
	profile	voxel	profile	voxel
Tropical	0.0265	0.2957	0.1047	0.6465
Temperate	0.0050	0.2448	0.1115	0.9852

3.4 Discussion and conclusions

Measuring the three-dimensional distribution and density of plant material in dense tropical and temperate forests is challenging due to occlusion, the effect of elements blocking the measurement and leading to unobserved volumes in 3D space. These measurements are highly relevant though, since terrestrial laser scanning is emerging as a reference for non-destructive biomass estimations (Stovall *et al.*, 2017; Momo Takoudjou *et al.*, 2018), tree and canopy reconstruction (Béland *et al.*, 2014a; Grau *et al.*, 2017), testing of new methodologies and algorithm development (Fassnacht *et al.*, 2018; Abegg *et al.*, 2017) as well as the use in radiative transfer models for simulating radiation-canopy interactions for studies of light availability and absorption, satellite mission development and sensor simulations (Schneider *et al.*, 2014; Vincent *et al.*, 2017; Gastellu-Etchegorry *et al.*, 2017; Morsdorf *et al.*, 2018). Occlusion is often mentioned as a main source of uncertainty when deriving related products but is usually not quantified, especially for very high-resolution close-range measurements. Therefore, it is generally unknown to what degree occlusion influences the measurements in dense forests.

When using above canopy or ground measurements alone, we found considerable remaining occlusion in the mid- and understory and at the top of canopy, respectively, at the two dense forest sites we analyzed. However, considering the very dense canopies of the sampled tropical and temperate forests, we also found an unprecedented level of detail and coverage. Terrestrial laser scanning on the ground showed extremely good results and almost no occlusion up to about 25-30 m above ground, when applying a relatively dense measurement scheme with distances of 10-20 m between laser scans. This has been identified as an ideal sampling scheme by Wilkes *et al.* (2017) based on their qualitative assessment of the point clouds at a range of forest sites, but without yet quantifying the actual coverage or occlusion. Our results confirm the suitability of TLS for voxel-based forest reconstruction as well as stem reconstruction and biomass estimations, as has been previously shown when comparing results to destructive sampling (Disney *et al.*, 2018). At the temperate

forest site, additional scans from outside the plot could have potentially helped to further reduce occlusion on top of canopy according to Wilkes *et al.* (2017). This is a potential limitation of the scan pattern applied in this study. However, occlusion transects shown in Figs. 3.3 and S6 show no border effects towards the edges of the plot. Moreover, Abegg *et al.* (2017) also found that the most important and efficient scan locations for forest inventory applications are towards the center of the plot, while applying a regular distribution of scan locations.

For simulating the interaction of incident radiation with the canopy, occlusion in the uppermost parts of the crowns is crucial and should not be neglected though. Increasing occlusion towards the canopy top is not only related to gap fraction and distribution. The probability of occlusion in a certain canopy volume also generally increases with distance from the scanner due to the higher probability of intersection with plant material and the decreasing sampling density (Abegg *et al.*, 2017). The underestimation of plant area density in the upper canopy of the tropical rainforest illustrates the relevance of the issue. In a less clumped and lower canopy, as can be found in broadleaved temperate forests, some of the occlusion effects such as an overestimation of voxel density close to occlusion and unobserved voxels were averaged out for overall plant area density (Fig. 3.6).

Measurements from above the canopy, such as from a canopy crane, tower or an unmanned aerial vehicle, can provide a good coverage of the top few meters of the canopy. However, occlusion in the mid- and understory is considerable and can even affect the dominant canopy layer. As a result, we found a strong underestimation of plant area density especially in lower canopy layers. The above canopy measurements we performed would therefore not have been suitable for a complete canopy reconstruction. For UAVLS in very dense forests, it might be necessary to improve the scan pattern for a better overlap and larger number of scan angles. We were only flying in east-west direction along the slope, limiting the scan angles to vary in north-south direction only. Moreover, occluded voxels could be filled based on surrounding voxels to mitigate the overall underestimation, but the implementation and performance of such methods depend on the application, the total amount and spatial distribution of occlusion.

Therefore, we generally recommend the use of UAVLS as an addition to ground measurements, in sparser forests, or under leaf-off conditions. The latter is promising for the more effective larger-scale mapping of tree stems than with TLS, but with an expected lower geometric accuracy due to the larger footprint size. Supplementary Figure S7 illustrates the differences in level of detail between TLS and UAVLS point clouds measured under leaf-on and leaf-off conditions. Even without occlusion, we would expect that mainly the stem and potentially some larger branches could be resolved. UAVLS observations as acquired in this study are thus generally better suited for voxel-based forest reconstructions than explicit 3D modeling. The measurements from the canopy crane well complemented the measurements from the ground,

but only for a limited extent around the crane. Depending on the surrounding topography and distribution of emerging trees, the reach of the scans varied between about hundred meter to several hundred meters but with an irregular distribution pattern (see Suppl. Fig. S8). Therefore, UAVLS systems could provide a much more regular coverage, whereas tower measurements are limited in possible scan directions. The added benefit is more localized to smaller patches or trees close to the tower or crane location. Yet, TLS measurements from a tower or crane can be a more cost-efficient solution if the scanner is already available, and can provide an alternative in places where UAV flights are restricted or permits difficult to obtain.

Besides the differences in above canopy measurement techniques, there seem to be differences in the distribution of laser returns and occlusion due to the different canopy architecture at the two particular forest sites studied here. Our results showed a more uniform distribution of plant material along a larger vertical profile at the tropical rainforest site in Borneo compared to the dense temperate mixed forest at Laegern. The more diverse and differentiated crowns at the tropical forest site might lead to more potential niche space for a larger number of individuals and species with different traits. Similarly to the better penetration of laser pulses through the tropical forest canopy, radiation might spread more evenly among a larger number of individuals than at the temperate forest site. This can potentially lead to a better usage of radiation and efficiency in photosynthesis of the forest (Williams *et al.*, 2017; Fotis & Curtis, 2017). In contrast, most of the UAVLS laser pulses and thus potentially most incident radiation was blocked by a dense upper canopy layer at the temperate forest site at Laegern. This layer is comprised by a few large European beech trees, restricting total diversity, biomass and potentially light use efficiency of the forest by the dominance of few individuals.

To quantify the actual differences between this particular tropical and temperate forest in terms of the amount of radiation interacting and being absorbed in different layers of the canopy and resulting light availability, the forests would need to be represented and simulated in a 3D radiative transfer model. For this purpose, a complete coverage of the canopy in 3D space is necessary, especially including the uppermost parts of the crowns. Our results showed that the above canopy measurements complement terrestrial laser scanning on the ground to mitigate occlusion in the uppermost canopy. We demonstrate a unique sampling of dense forests with an almost complete coverage in 3D space at unprecedented resolution with negligible remaining occlusion. This builds the basis for further studies. The presented examples of 3D voxel grids show the potential for the use in radiative transfer models, but also reveal some of the major challenges sampling these ecosystems. The major challenge in tropical forests is the tall canopy and the sampling within emerging tree crowns, whereas in dense temperate forests a closed canopy with few larger gaps can be difficult to penetrate from the ground as well as from above the canopy.

To conclude, we demonstrate the ability of close-range laser scanning systems as a combination of terrestrial laser scanning on the ground as well as from a canopy crane and UAV platform for very high-resolution forest modeling with a complete coverage of dense tropical and temperate forest canopies. The quantification of occlusion showed that measurements from above the canopy or the ground alone can have considerable occlusion leading to a bias in derived products. An improved flight pattern in different directions with a smaller spacing between flight lines could reduce occlusion in UAVLS measurements, but needs to be further tested. Similarly, further research is needed for possible in-filling of occluded voxels. Based on the analysis on two dense temperate and tropical forest plots, we recommend the use of UAV or canopy crane platforms as an addition to ground-based measurements, in sparser forests, or under leaf-off conditions. Terrestrial laser scanning on the ground alone can provide a sufficient sampling of the canopy when there is no need to derive information on the distribution of leaves or branches at the top of the canopy. For a complete coverage especially in tropical rainforests, the fusion of above canopy and ground measurements is advised, paving the way for future studies on radiation-canopy interactions or micrometeorology.

Acknowledgements

This study has been supported by the University of Zurich Research Priority Program on Global Change and Biodiversity (URPP GCB). The research carried out at the Jet Propulsion Laboratory, California Institute of Technology, was under a contract with the National Aeronautics and Space Administration. Government sponsorship is acknowledged. We thank Dr. Tomoaki Ichie, Dr. Eri Yamasaki and Prof. Dr. Kentaro Shimizu for their support in organizing and performing the field work at the Lambir Hills NP. We thank Carla Guillén Escribà and Victoria Scholl for their help during the field work at the Laegern forest. Permits and access to the Lambir Hills National Park research site (Miri Division, Sarawak) have been granted by the Forest Department Sarawak, as with research permit no. NCCD.907.4.4(JLD.13)-181 and park permit no. 128/2016. UAVLS flight operations and data processing were performed by Aeroscout, Switzerland. Reference herein to any specific commercial product, process, or service by trade name, trademark, manufacturer, or otherwise, does not constitute or imply its endorsement by the United States Government or the Jet Propulsion Laboratory, California Institute of Technology.

3.5 Supplementary Material

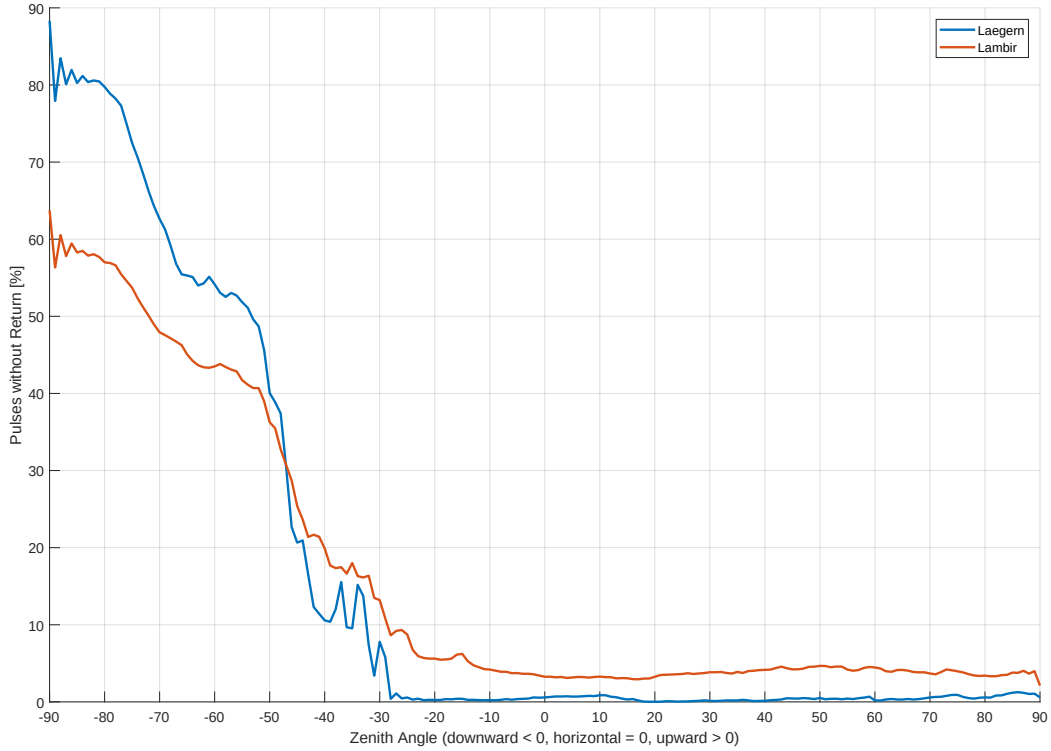

Fig. S1: Percentage of pulses without return per zenith angle in degrees for the terrestrial laser scans performed with the Riegl VZ-1000. The zenith angles range from straight downward (-90) to straight upward (90) scan angles, where zero is in horizontal direction. This figure combines horizontal and tilted scans covering the whole sphere (360 x 360 degrees) for the temperate Laegern site (blue line) and the tropical Lambir site (red line). Scans were conducted with active short range detection, which means that the minimum measurement distance is around 1.5 m. High percentages of pulses without return in downward directions are due to the tilt head and tripod obstructing the pulses or measurements close to the ground.

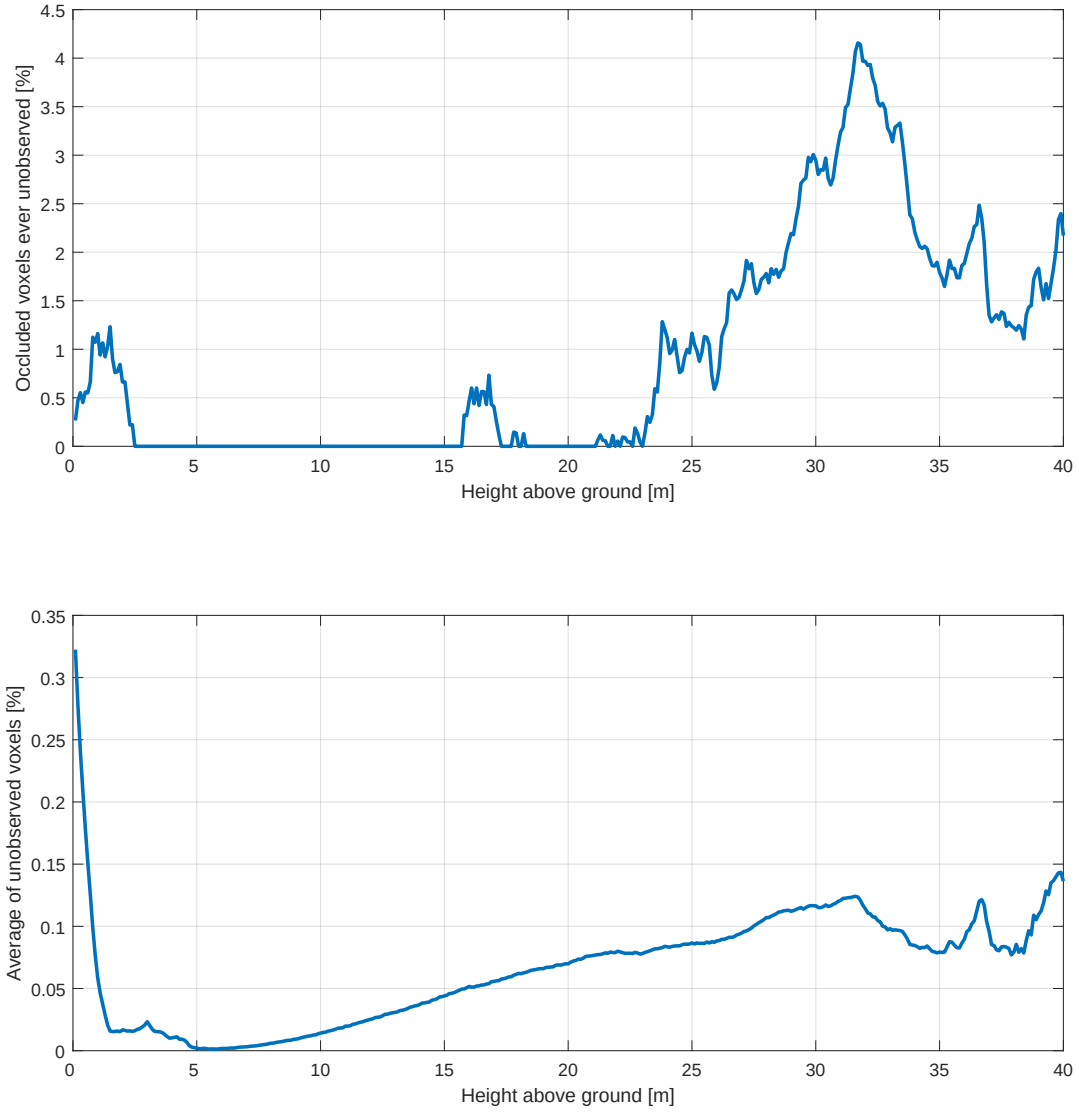

Fig. S2: Amount of occluded voxels that have ever been unobserved in any scan per height level (upper panel) and the average number of unobserved voxels over all scans (lower panel) at the temperate Laegern site. A maximum of 4.2% of occluded voxels that have not been observed at 32 m height above ground could indicate possible gaps, which have not been modeled due to the omission of pulses without returns.

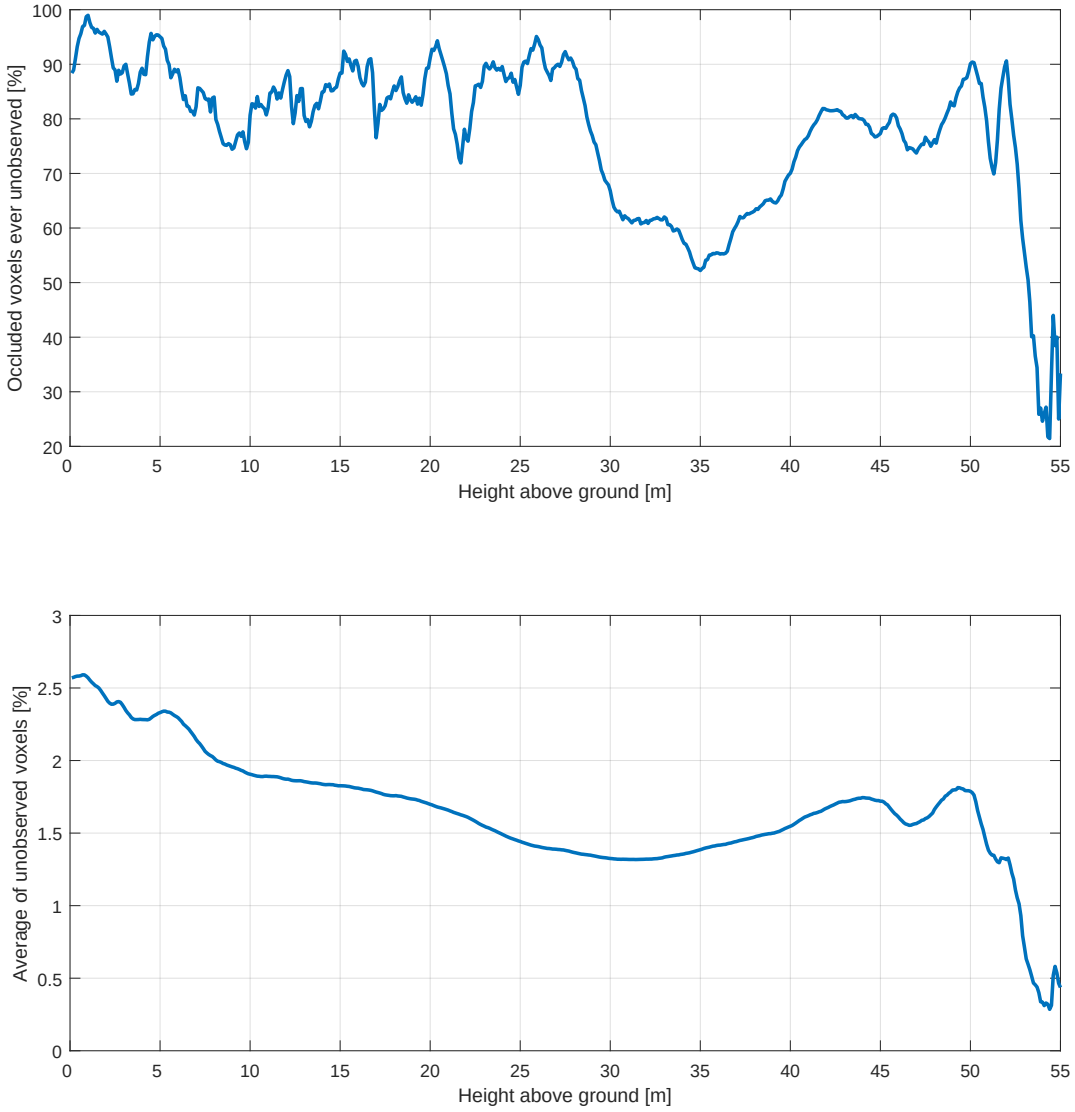

Fig. S3: Amount of occluded voxels that have ever been unobserved in any scan per height level (upper panel) and the average number of unobserved voxels over all scans (lower panel) at the tropical Lambir site. The very dense understory and tree cover on the ground led to a high number of obstructed pulses without a measured return, and thus a high percentage of occluded voxels that have not been observed in certain scans in height levels up to about 27 m.

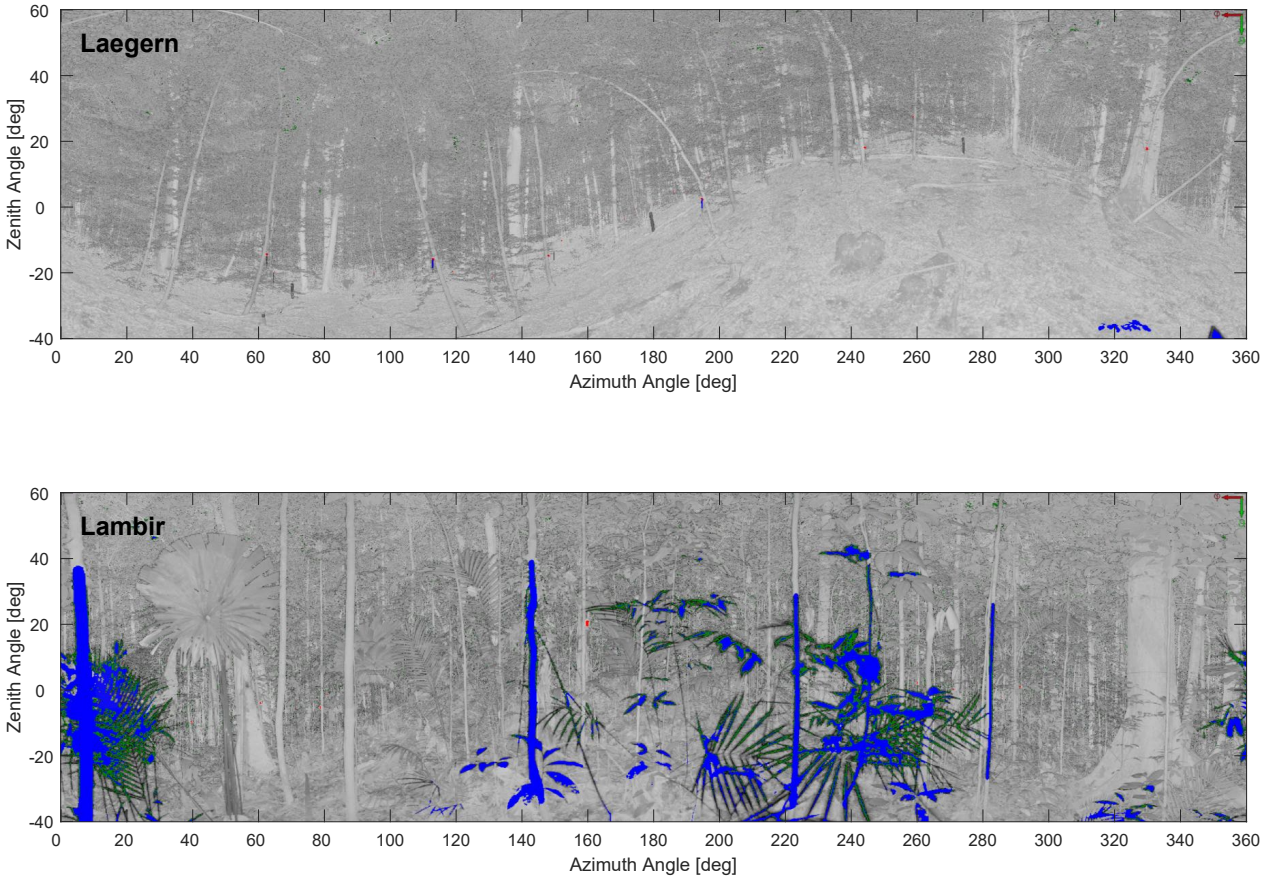

Fig. S4: Grayscale reflectance images of a horizontal terrestrial laser scan at Laegern (top panel) and Lambir (lower panel). Areas without measurements are marked blue. This is due to obstructing elements below the minimum measurement distance or energy leaving the scene through gaps without return. The latter is seldom at these sites due to the high density of the forests. However, the former appears often especially at the tropical site in Lambir due to the dense understory.

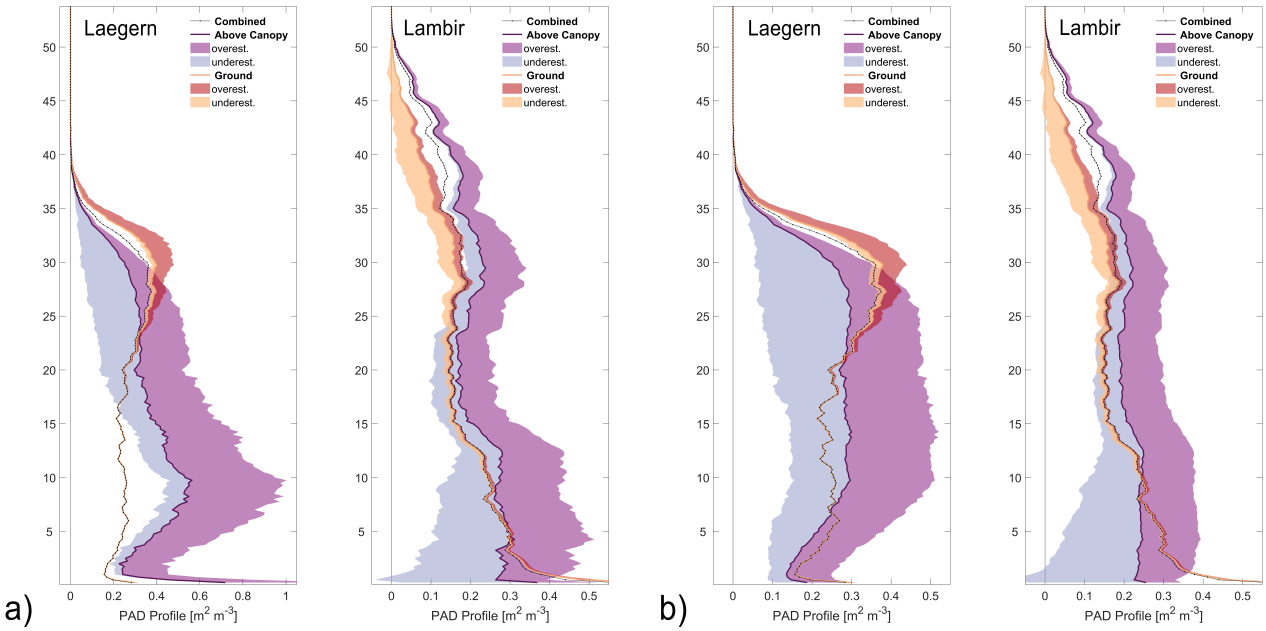

Fig. S5: PAD profiles and voxel based difference per height layer when a) occluded voxels were filled with the average non-occluded voxel PAD of the respective height layer and b) with the average of the whole voxel grid. In case of the UAVLS acquisition from above the canopy, filling occluded voxels with the height layer average led to a strong overestimation in lower layers where occlusion is large. Using the total forest average solves this issue, but still leads to a large voxel-based under- and overestimation.

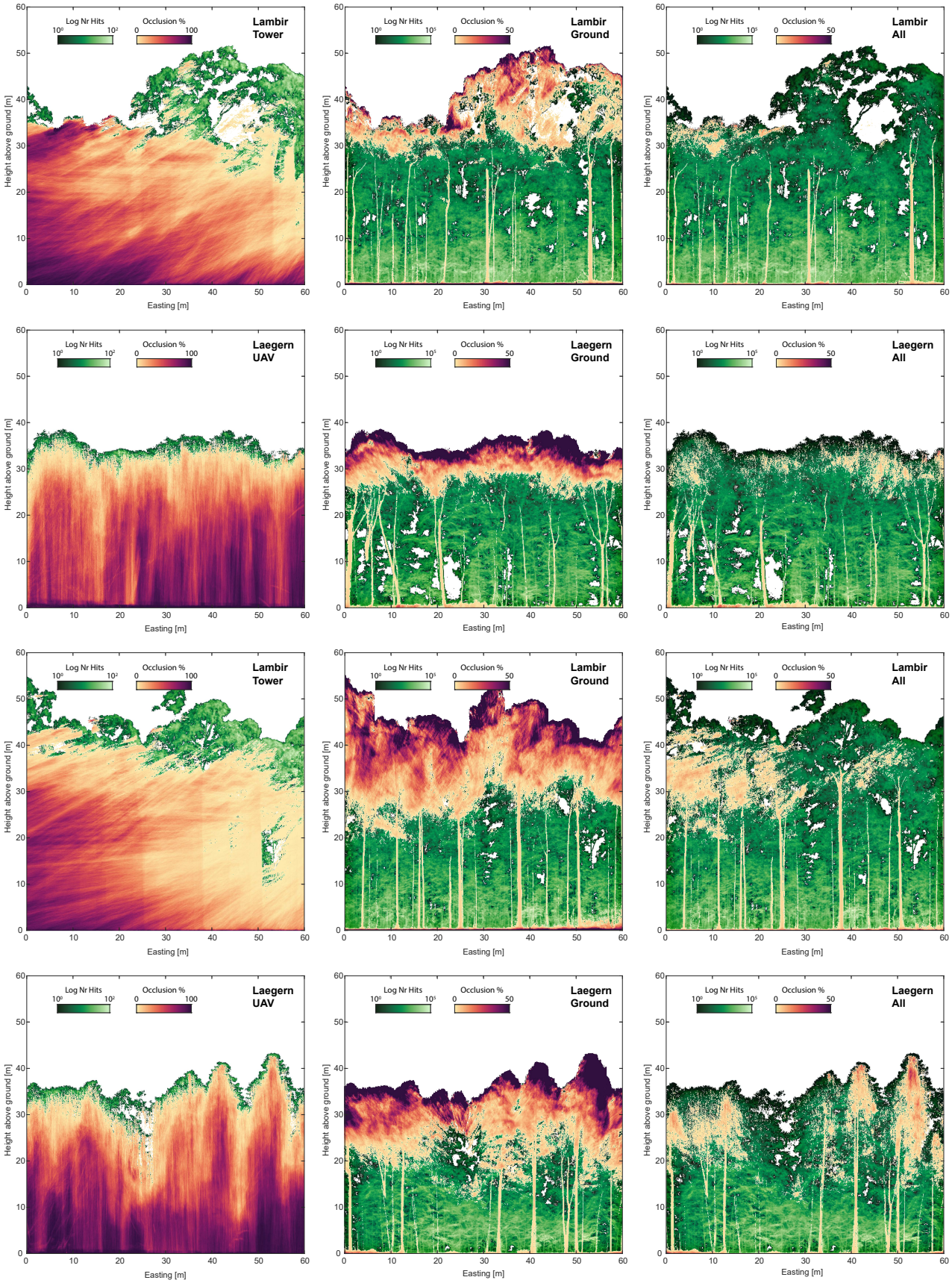

Fig. S6: Percentage occlusion of 20 m deep transects through tropical and temperate forests according to Fig. 3.3, but showing the upper and lower transects of the 60 x 60 m plots as shown in Fig. 3.1.

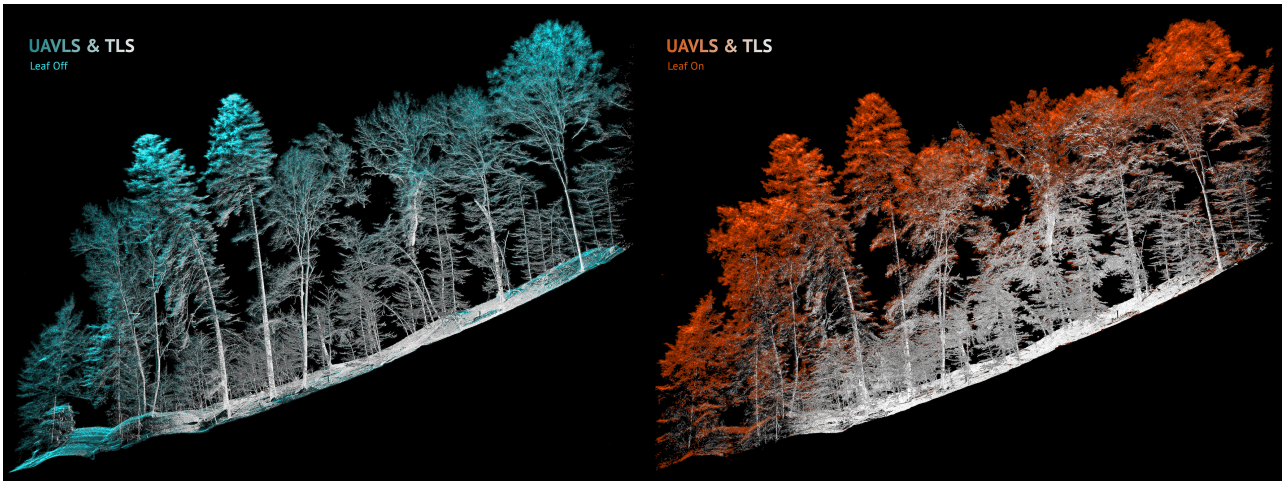

Fig. S7: Illustration of differences in level of detail between UAVLS (colored) and TLS (gray) point clouds of a transect through the temperate forest site at Laegern during leaf off (left, UAVLS in magenta) and leaf on (right, UAVLS in orange) conditions. On the left side of the transect, there are two evergreen conifers that remain the same during both acquisitions.

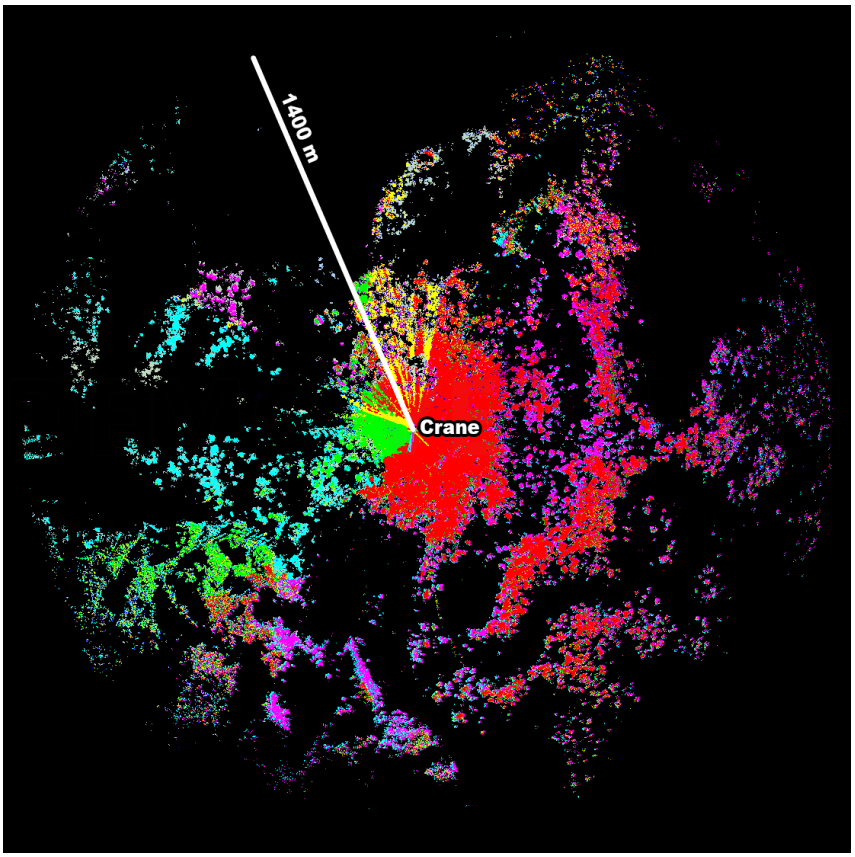

Fig. S8: Top down illustration of the point clouds acquired from the upper two platforms of the canopy crane. Unique colors are assigned to the point clouds of each scan location on the platforms. The total reach of the TLS scans is up to 1400 m, but with variable coverage depending on topography and occlusion of crane elements and large trees close to the canopy crane.

3.6 References

Abegg M, Kükenbrink D, Zell J, Schaepman M, Morsdorf F (2017) Terrestrial Laser Scanning for Forest InventoriesTree Diameter Distribution and Scanner Location Impact on Occlusion. *Forests*, **8**, 184.

Åkerblom M, Raumonen P, Casella E, *et al.* (2018) Non-intersecting leaf insertion algorithm for tree structure models. *Interface Focus*, **8**, 20170045.

Åkerblom M, Raumonen P, Mäkipää R, Kaasalainen M (2017) Automatic tree species recognition with quantitative structure models. *Remote Sensing of Environment*, **191**, 1–12.

Ashton PS (2005) Lambir's Forest: The World's Most Dive Known Tree Assemblage? In: *Ecological Studies*, vol. 174 (eds. Roubik DW, Sakai S, Hamid Karim AA), pp. 191–216. Springer New York.

Asner GP, Martin RE, Suhaili AB (2012) Sources of Canopy Chemical and Spectral Diversity in Lowland Bornean Forest. *Ecosystems*, **15**, 504–517.

Béland M, Baldocchi DD, Widlowski JL, Fournier Ra, Verstraete MM (2014a) On seeing the wood from the leaves and the role of voxel size in determining leaf area distribution of forests with terrestrial LiDAR. *Agricultural and Forest Meteorology*, **184**, 82–97.

Béland M, Widlowski JLL, Fournier Ra (2014b) A model for deriving voxel-level tree leaf area density estimates from ground-based LiDAR. *Environmental Modelling and Software*, **51**, 184–189.

Calders K, Newnham G, Burt A, *et al.* (2015) Nondestructive estimates of above-ground biomass using terrestrial laser scanning. *Methods in Ecology and Evolution*, **6**, 198–208.

Calders K, Origo N, Burt A, *et al.* (2018) Realistic Forest Stand Reconstruction from Terrestrial LiDAR for Radiative Transfer Modelling. *Remote Sensing*, **10**, 933.

Danson FM, Disney MI, Gaulton R, Schaaf C, Strahler A (2018) The terrestrial laser scanning revolution in forest ecology. *Interface Focus*, **8**, 20180001.

Disney MI, Boni Vicari M, Burt A, Calders K, Lewis SL, Raumonen P, Wilkes P (2018) Weighing trees with lasers: advances, challenges and opportunities. *Interface Focus*, **8**, 20170048.

Eysn L, Pfeifer N, Ressl C, Hollaus M, Grafl A, Morsdorf F (2013) A Practical Approach for Extracting Tree Models in Forest Environments Based on Equirectangular Projections of Terrestrial Laser Scans. *Remote Sensing*, **5**, 5424–5448.

Fassnacht FE, Latifi H, Hartig F (2018) Using synthetic data to evaluate the benefits of large field plots for forest biomass estimation with LiDAR. *Remote Sensing of Environment*, **213**, 115–128.

Fotis AT, Curtis PS (2017) Effects of structural complexity on within-canopy light environments and leaf traits in a northern mixed deciduous forest. *Tree Physiology*, **142**, 155–184.

Gastellu-Etchegorry JP, Lauret N, Yin T, *et al.* (2017) DART: Recent Advances in Remote Sensing Data Modeling With Atmosphere, Polarization, and Chlorophyll Fluorescence. *IEEE Journal of Selected Topics in Applied Earth Observations and Remote Sensing*, **10**, 2640–2649.

Gastellu-Etchegorry JP, Yin T, Lauret N, *et al.* (2016) Simulation of satellite, airborne and terrestrial LiDAR with DART (I): Waveform simulation with quasi-Monte Carlo ray tracing. *Remote Sensing of Environment*, **184**, 418–435.

Grau E, Durrieu S, Fournier R, Gastellu-Etchegorry JP, Yin T (2017) Estimation of 3D vegetation density with Terrestrial Laser Scanning data using voxels. A sensitivity analysis of influencing parameters. *Remote Sensing of Environment*, **191**, 373–388.

Guillén Escribà C, Schneider FD, Tedder A, *et al.* (in review) Remotely sensed within-species functional trait variation of a temperate forest. *Ecology and Evolution*.

Hackenberg J, Spiecker H, Calders K, Disney M, Raumonen P (2015) SimpleTree An Efficient Open Source Tool to Build Tree Models from TLS Clouds. *Forests*, **6**, 4245–4294.

Harrison RD (2011) Emptying the Forest: Hunting and the Extirpation of Wildlife from Tropical Nature Reserves. *BioScience*, **61**, 919–924.

Heinzel J, Huber M (2016) Detecting Tree Stems from Volumetric TLS Data in Forest Environments with Rich Understory. *Remote Sensing*, **9**, 9.

Hiromi T, Ichie T, Kenzo T, Ninomiya I (2012) Interspecific variation in leaf water use associated with drought tolerance in four emergent dipterocarp species of a tropical rain forest in Borneo. *Journal of Forest Research*, **17**, 369–377.

Kenzo T, Ichie T, Watanabe Y, Yoneda R, Ninomiya I, Koike T (2006) Changes in photosynthesis and leaf characteristics with tree height in five dipterocarp species in a tropical rain forest. *Tree Physiology*, **26**, 865–873.

Kükenbrink D, Schneider FD, Leiterer R, *et al.* (2017) Quantification of hidden canopy volume of airborne laser scanning data using a voxel traversal algorithm. *Remote Sensing of Environment*, **194**, 424–436.

Manfroi OJ, Kuraji K, Suzuki M, *et al.* (2006) Comparison of conventionally observed interception evaporation in a 100-m2 subplot with that estimated in a 4-ha area of the same Bornean lowland tropical forest. *Journal of Hydrology*, **329**, 329–349.

Momo Takoudjou S, Ploton P, Sonké B, *et al.* (2018) Using terrestrial laser scanning data to estimate large tropical trees biomass and calibrate allometric models: A comparison with traditional destructive approach. *Methods in Ecology and Evolution*, **9**, 905–916.

Morsdorf F, Eck C, Zgraggen C, Imbach B, Schneider F, Kükenbrink D (2017) UAV-based LiDAR acquisition for the derivation of high-resolution forest and ground information. *Leading Edge*, **36**.

Morsdorf F, Kükenbrink D, Schneider FD, Abegg M, Schaepman ME (2018) Close-range laser scanning in forests: towards physically based semantics across scales. *Interface Focus*, **8**, 20170046.

Raumonen P, Kaasalainen M, Åkerblom M, *et al.* (2013) Fast Automatic Precision Tree Models from Terrestrial Laser Scanner Data. *Remote Sensing*, **5**, 491–520.

Schneider FD, Leiterer R, Morsdorf F, Gastellu-Etchegorry JP, Lauret N, Pfeifer N, Schaepman ME (2014) Simulating imaging spectrometer data: 3D forest modeling based on LiDAR and in situ data. *Remote Sensing of Environment*, **152**, 235–250.

Schneider FD, Morsdorf F, Schmid B, Petchey OL, Hueni A, Schimel DS, Schaepman ME (2017) Mapping functional diversity from remotely sensed morphological and physiological forest traits. *Nature Communications*, **8**.

Stovall AE, Vorster AG, Anderson RS, Evangelista PH, Shugart HH (2017) Non-destructive aboveground biomass estimation of coniferous trees using terrestrial LiDAR. *Remote Sensing of Environment*, **200**, 31–42.

Vincent G, Antin C, Laurans M, Heurtebize J, Durrieu S, Lavalley C, Dauzat J (2017) Mapping plant area index of tropical evergreen forest by airborne laser scanning. A cross-validation study using LAI2200 optical sensor. *Remote Sensing of Environment*, **198**, 254–266.

Widlowski JL, Côté JF, Béland M (2014) Abstract tree crowns in 3D radiative transfer models: Impact on simulated open-canopy reflectances. *Remote Sensing of Environment*, **142**, 155–175.

Wilkes P, Lau A, Disney M, *et al.* (2017) Data acquisition considerations for Terrestrial Laser Scanning of forest plots. *Remote Sensing of Environment*, **196**, 140–153.

Williams LJ, Paquette A, Cavender-Bares J, Messier C, Reich PB (2017) Spatial complementarity in tree crowns explains overyielding in species mixtures. *Nature Ecology & Evolution*, **1**, 63.

Yin T, Lauret N, Gastellu-Etchegorry JP (2016) Simulation of satellite, airborne and terrestrial LiDAR with DART (II): ALS and TLS multi-pulse acquisitions, photon counting, and solar noise. *Remote Sensing of Environment*, **184**, 454–468.

Chapter

4

Spatio-temporal modelling of light extinction in two contrasting forests

Kükenbrink, D., Schneider, F.D., Schmid, B., Gastellu-Etchegorry, J.-P., Schaepman, M.E., Morsdorf, F.

This section is based on the article:
"Spatio-temporal modelling of light extinction in two contrasting forests",
in review by Remote Sensing of Environment.

D.K., F.D.S., B.S., J.P.G., M.E.S., F.M designed study
D.K. performed research and all authors contributed to the writing,
with main contribution by D.K.

Abstract

The three-dimensional distribution of light within forest ecosystems is a major driver for species competition, coexistence as well as forest ecosystem functioning, productivity, and diversity. However, accurate knowledge about the three-dimensional distribution of light within the canopy is difficult to obtain due to the complex structure and light-matter interactions of forest ecosystems. Recent advances in three-dimensional forest reconstruction as well as the use of radiative transfer modelling based on close-range laser scanning and spectroscopy provide new insights to spatio-temporal variations in light distribution within a forest canopy.

We used high resolution laser scanning data coupled with *in-situ* leaf optical properties measurements to parameterize the DART radiative transfer model for a temperate deciduous forest on the Laegern mountain, Switzerland and for a tropical rain forest located in the Lambir Hills national park, Borneo, Malaysia. The terrestrial and UAV laser scanning point cloud allowed for a forest canopy reconstruction and radiative transfer analysis within the canopy in very high detail; both in the vertical as well as in the horizontal domain.

We analyse the impact of the two contrasting forests, both in terms of structure as well as of optical properties, on the extinction of photosynthetic active radiation (PAR, 400 nm - 700 nm) for a whole diurnal cycle at the northern hemisphere solar solstice. We show that PAR extinction is mainly driven by the canopy structure, resulting in an exponential light extinction profile for the temperate study site and a more linear extinction profile in the tropical case. The larger heterogeneity in canopy structure for the tropical study site also resulted in larger variability in light extinction throughout the whole canopy. The differing optical properties of leaves are found to have only a minor influence on the light extinction profile. The comparison of the DART modeled light extinction profiles with a simpler Beer-Lambert approximation showed differences of up to $>$ 30% in the upper canopy, illustrating the need for such detailed 3D modelling of light distribution within forest ecosystems.

With the proposed approach we are now able to model and analyse the spatio-temporal heterogeneity in 3D light distribution within forest ecosystems. This can give us important insights into light related mechanisms driving species coexistence, competition and diversity in complex forest ecosystems.

4.1 Introduction

Light availability plays a major role in defining species competition and coexistence as well as forest ecosystem functioning, productivity, and diversity. Studies have shown that canopy structure strongly influences the distribution of light within the canopy and therefore also influences the within canopy variability of light-use efficiency and productivity (e.g. Stark *et al.*, 2012; Morton *et al.*, 2014, 2016; Widlowski *et al.*, 2011). It is reported (e.g. Niinemets, 2007, 2012) that light availability typically varies up to 50-fold within a closed vegetation stand, and even within the crown of an isolated individual tree, significant variation in light may occur (Baldocchi *et al.*, 2002; Kükenbrink *et al.*, 2019; Valladares, 2003). The extensive variability of light availability within the canopy induces extensive modifications of foliage structure and physiology such that it is hardly possible to find two leaves with the exact same combination of leaf-trait values (Niinemets, 2012). Seasonal and diurnal changes in light availability within the canopy promote leaf plasticity allowing for leaves to adapt to changing light conditions within the canopy (e.g. Keenan & Niinemets, 2017; Niinemets *et al.*, 2003; Valladares *et al.*, 2016). For a better understanding of ecosystem functioning and productivity of forest ecosystems, advanced knowledge of the distribution as well as the utilization of light within the canopy is vital. However, quantification of the amount of incoming light reaching the three-dimensional forest canopy is challenging. Measurement of spatially contiguous, three-dimensional light distribution is still relatively scarce for forest canopies, mostly due to the difficult access and to the high spatial and temporal variability of light distribution within the canopy. For this reason, multiple models of varying complexity have been developed to simulate and quantify the distribution and utilization of light within the canopy.

Global and regional land surface models often employ a relatively simple assumption of an exponential decrease of incoming light within the canopy based on Beer's law of light extinction (e.g. in MOSES (Cox *et al.*, 1999), LPJ (Sitch *et al.*, 2003), and SiB3 (Denning *et al.*, 2003)). This assumption, however, completely neglects the presence of diffuse irradiance, as well as horizontal and vertical heterogeneity in canopy structure. So-called two-stream models resolve upward and downward radiation streams as well as diffuse and direct radiation (Jogireddy *et al.*, 2006). Alton *et al.* (2007b) further improved the above mentioned two-stream model by treating the canopy as multiple discrete vertical layers and explicitly modelling leaf orientation rather than averaging irradiance into a mean light profile.

However, these radiative transfer schemes largely neglect the large impact of canopy structure and architecture on the distribution of direct and diffuse solar radiation within the canopy. Fisher *et al.* (2017) identified the radiative transfer component in dynamic global vegetation models (DGVMs) as one of the biggest sources of uncertainty when modelling ecosystem functioning, productivity and development. In such models , canopy architecture is represented in varying levels of detail, from

simple big-leaf models such as LPJ (e.g. Sitch *et al.*, 2003) to cohort or even individual based parameterization (e.g. the Ecosystem Demography models ED (Moorcroft *et al.*, 2001) or ED2 (Medvigy *et al.*, 2009)). However, these models sometimes fail to represent the actual structural complexity found in forest ecosystems, especially those of high species richness where species with fundamentally different architecture and leaf traits may coexist on small areas.

McElhinny *et al.* (2005) described the importance of the characterization of forest structure for ecosystem functioning and highlighted the link between structure and diversity. Canopy structure can affect photosynthesis within the canopy (Kira *et al.*, 1969; Chen *et al.*, 2012), light-use efficiency (Duursma & Mäkelä, 2007; Walcroft *et al.*, 2005) and net ecosystem CO_2 exchange (Baldocchi *et al.*, 2001; Law *et al.*, 2001) due to its influence on light interception and light distribution within the canopy. An accurate description of the vertical and horizontal arrangement of vegetation material is therefore vital and summarizing stand structural attributes such as variability in tree height, and diameter at breast height, species richness and composition falls short to provide this information.

New laser-scanning technologies, especially the cost-effectiveness and practicality of terrestrial laser scanning (TLS), introduced a new way in which we are able to quantify and understand dynamics in ecosystem structure and function (Danson *et al.*, 2007, 2018). Schneider *et al.* (2019) showed that by combining ground based TLS measurements with above-canopy TLS or unmanned aerial vehicle laser scanning (UAVLS), even very complex forest structures can be represented in high detail with a minimum amount of occlusion within the canopy. Calders *et al.* (2018) highlighted the potential in using TLS measurements for forest reconstruction and radiative transfer modelling. Morton *et al.* (2016) used Airborne Laserscanning (ALS) to parameterize the DART radiative transfer model to analyse light utilization in the Amazon rain forest. However, the reduced point density of the ALS system compared to the TLS acquisitions did not allow for a highly detailed representation of the tropical forest as shown in e.g. Calders *et al.* (2018).

In this study we modeled within canopy light distribution of two contrasting forests of a temperate mixed forest site and a tropical lowland mixed rain forest. We define 'light' here as the spectrally resolved incoming radiation in the photosynthetically active radiation (PAR) region (400-700 nm) and demonstrate the effect of light-matter interactions within the canopy. We use the Discrete Anisotropic Radiative Transfer model DART, parameterized with high-resolution TLS and UAVLS acquisitions and coupled with *in-situ* and *in-vivo* leaf level measurements of leaf and bark optical properties based on portable spectroradiometers (see also Schneider *et al.*, 2014) for both canopies. Our main research questions were: (1) how do the two forest ecosystems differ in terms of canopy structure and leaf optical properties, (2) how do these structural and optical differences affect light distribution and extinction within the canopy, both under clear-sky and complete diffuse illumination conditions, and

(3) how do the 3D simulated extinction profiles compare with the ones following a Beer-Lambert approximation?

4.2 Materials and Methods

4.2.1 Study sites

For the purpose of this study we analyze light extinction in two contrasting forest ecosystems (temperate and tropical) with dense and tall canopies around 30 to 50 m in height. The temperate site is a mixed old-growth forest on the southern slope of the Laegern mountain in Switzerland ($47°28'42.1''$N, $8°21'51.7''$E, 688 m above sea level). The forest is dominated by beech (*Fagus sylvatica* L.) with 12 further tree species, with about 70% deciduous broadleaf trees and about 30% evergreen coniferous trees (Schneider *et al.*, 2017). We selected a plot of 60 x 60 m within a non-managed 5.5 ha research area. A detailed description of the forest and environmental conditions can be found in Eugster *et al.* (2007). Canopy height ranges from 30 to 40 m for the single-layer canopy.

The tropical site is located in the Lambir Hills National Park on the island of Borneo, Malaysia. The lowland mixed rainforest at this site is the world's most diverse forest yet studied in terms of tree species richness with perhaps 2500 species in total (Ashton, 2005). The vegetation is classified as lowland mixed dipterocarp forest and as moist lowland tropical forest in the Holdridge system (Asner *et al.*, 2012). The most abundant species are belonging to the Euphorbiaceae and Dipterocarpaceae families. We again selected a 60 x 60 m plot northwest of a canopy crane centered in a 4-ha research area. Manfroi *et al.* (2006) give a detailed description of the plot. The canopy crane provides access to the top of canopy, e.g. for measurements of leaf optical properties. The canopy crane is 80 m tall with a 75 m long rotating jib, providing access to all layers of the canopy from ground to above canopy level (Kenzo *et al.*, 2006). Canopy height ranges from 30 to 50 m with some emergent trees reaching up to 70 m (Hiromi *et al.*, 2012).

4.2.2 LiDAR Data

Three-dimensional measurements of canopy structure were acquired using a Riegl VZ-1000 terrestrial laser scanning (TLS) device covering an area of 1 ha for the tropical forest site and 60 x 60 m for the temperate forest site, following a near-regular scanning pattern. To complement laser measurements from the ground, TLS scans from multiple platforms of the canopy crane were acquired in the tropical forest. For the temperate forest, we used UAV based laser scanning for above canopy measurements. The LiDAR UAV set-up combined the OxTS xNAV550 IMU/GPS dual-GPS-antenna navigation solution and the RIEGL VUX-1UAV laser scanner mounted on the industrial

Scout B1-100 UAV helicopter produced by Aeroscout GmbH, Switzerland (Morsdorf *et al.*, 2017). For a detailed description on the acquisition and processing of the high resolution laser point cloud see Schneider *et al.* (2019).

4.2.3 Optical properties data

Leaf optical properties (LOP) for the tropical forest site were acquired using an ASD FieldSpec Pro spectroradiometer (Analytical Spectral Devices, Boulder, Colorado) with an added plant probe and leaf-clip. The foreoptic allowed us to calculate leaf reflectance and transmittance by using a white and a black reference panel with known reflectance and by following the procedure described in Miller *et al.* (1992) (for a detailed description of the LOP retrieval procedure, see Kükenbrink *et al.* (2019)). The instrument was set to reflectance mode to acquire the LOPs. Samples of 30 individual trees of 19 different species within the reach of the canopy crane's gondola were acquired at different positions of the crown (sunlit, transitional, and shaded positions). For each of the 30 crowns, 10 leaf samples were acquired with three LOP measurements per leaf. LOP measurements of the understorey were acquired from leaves accessible from the ground.

LOP samples for the temperate study site were collected from two individual beech trees during a field campaign in 2009. Leaf samples were taken from the upper, middle, and lower part of the crown. Reflectance and transmittance were measured in the laboratory at three positions on the abaxial and adaxial side of the leaf. The measurements were performed using an integrating sphere coupled to a field spectroradiometer (ASD FieldSpec 3, Analytical Spectral Devices, Boulder, Colorado). Further details on the acquisition of LOPs for the temperate site can be found in Schneider *et al.* (2014).

For parameterization of the optical properties of the forest floor and bark, multiple samples of leaf litter and bark were measured in the field using a field spectrometer (ASD FieldSpec Pro) coupled with a leaf-clip (for litter samples) for both study sites.

4.2.4 Parameterization of radiative transfer model

The radiative transfer model used in this study for light extinction modelling is the Discrete Anisotropic Radiative Transfer Model DART (v5.6.0) (Gastellu-Etchegorry *et al.*, 2015). DART simulates three-dimensional heterogeneous landscapes represented by a voxel grid with a predefined size (i.e. 60 x 60 m grid extent with a voxel side length of 0.25 m). Each voxel follows a turbid medium assumption (i.e., random distribution of infinitely small planar elements) parameterized by it's leaf area density, leaf angular distribution, and optical properties. A DART voxel can include vegetation turbid media as well as discrete triangles with an arbitrary size, independent of the voxel size to simulate objects not following the turbid medium assumption (e.g. tree trunk and branches). In ray tracing, two types of radiation interactions are

simulated: volume interaction within turbid voxels (Gastellu-Etchegorry *et al.*, 2004), and surface interaction on triangles (Gastellu-Etchegorry, 2008). Further details on the DART model can be found in (Gastellu-Etchegorry *et al.*, 2012, 2015).

In this study, the flux tracking mode of DART was used with sun and atmosphere as the only radiation sources. The approach to parameterize the DART model is closely following the one described in Kükenbrink *et al.* (2019), where the irradiance field around a single isolated tree was modeled and analysed. Optical properties of tree crowns, understorey, bark, and litter were parameterized using the optical measurements described in Section 4.2.3. To represent the vertical variability in LOPs, the vertically distributed LOP measurements were assigned to their respective layers within the voxel grid. The forest structure and leaf area density distribution within the canopy was defined as described in Section 4.2.4a based on the TLS measurements described in Section 4.2.2. The leaf angle distribution for the temperate forest was defined as plagiophile, following the work by Schneider *et al.* (2014) on the same study site. Leaf angle distribution for the tropical site was defined as spherical following a simplifying assumption performed in many studies where actual leaf angle distributions are not known (e.g. Alton *et al.*, 2007a; Chen *et al.*, 2012; Mariscal *et al.*, 2004; Vincent *et al.*, 2017). As tree trunks and larger branches do not follow the turbid medium assumption, they were modeled as discrete, opaque objects as described in Section 4.2.4b with optical properties derived as described in Section 4.2.3. In order to enable a direct comparison of light extinction profiles between the two study sites, the whole canopy was normalized based on a DTM derived from the TLS point cloud. To simulate the atmosphere, DART can be used with standard gas and aerosol models as contained in the MODTRAN model (Berk *et al.*, 1987). We used the mid-latitude summer and the tropical gas model for the temperate and tropical forest site respectively. For the aerosol model the rural model with a visibility of 23 km was used for both sites.

For both study sites, solar angles for a complete diurnal cycle for the northern hemisphere summer solstice (21st of June) was simulated in two hours intervals plus additional simulations for solar noon conditions. The 3D distribution of solar irradiance of a single waveband in the photosynthetic active radiation (PAR) regime (400 - 700 nm) within the forest canopies was simulated. Here, the considered DART output is a three-dimensional radiative budget with the amount of energy (in W m^{-2} nm^{-1}) irradiant, absorbed and scattered at each voxel. The radiative budget can be further decomposed into direct, diffuse and coupled irradiance (irradiance after coupling with the atmosphere).

4.2.4a Plant area density estimation

Plant area density for each turbid medium voxel was estimated using the laser scanning data described in Section 4.2.2 (for details on processing of the data, i.e. co-registration of point clouds etc., see Schneider *et al.* (2019)). The plant area density

value per voxel (m^2 m^{-3}) was estimated using the AMAPVox Software package (version 1.0.1 r3410ffbe) developed by "botAnique Modélisation de l'Architecture des Plantes et des végétations" AMAP (Vincent *et al.*, 2017). The AMAPVox model is tracing all laser pulses through a predefined voxel grid and calculates for each voxel the local transmittance computed from the ratio between exiting and entering energy normalized by the mean optical path length (Vincent *et al.*, 2017). To exclude tree trunks and major branches from the plant area density estimation, as these violate the turbid medium assumption for the selected voxel size, laser returns from the tree trunks and major branches were excluded from the plant area density estimation (see also Section 4.2.4b). The estimated plant area density was multiplied by the voxel height (0.25 m) to convert to the plant area index (PAI [m^2 m^{-2}]) values per voxel, which is required for the parameterisation of DART.

4.2.4b Stem and branch model extraction

Laser returns from tree trunk and major branches were filtered from the co-registered point cloud based on a reflectance threshold value (-5 dB) using the RiscanPro Software suite. Woody material tend to reflect more energy in the wavelength used by the TLS (1550 nm), making a separation between woody material and leaf material possible, but not perfect. For the temperate forest case, an earlier acquired TLS acquisition during leaf-off state was used to extract stems and major branches, helping with the separation between woody and foliage material. To refine the filtered point cloud it was voxelized into a voxel grid with a voxel side length of 5 cm. Voxels with a low count of high reflectance returns were filtered out (e.g. for Laegern, only voxels with at least 5 TLS returns or 2 UAVLS returns were used. For Lambir, a height adaptive filtering was applied with the following thresholds: minimum 5 TLS returns per voxel $<$15 m above ground, minimum 3 TLS returns per voxel between 15 and 25 m, and minimum 2 TLS returns per voxel between 25 and 35 m). Smaller isolated voxel clusters (less than 5 connected voxels) were excluded from the wood structure binary voxel grid. The refined binary voxel grid was then converted into a 3D mesh object and written into a wavefront object file importable into DART.

4.2.5 Light extinction analysis

Light extinction was calculated based on modeled PAR irradiance per voxel and the baseline irradiance modeled above the top of canopy for each simulated solar angle:

$$Extinction = 1 - \frac{E}{max(E)} \tag{4.1}$$

where E denotes the simulated irradiance for each voxel and $max(E)$ denotes the baseline irradiance above the canopy (i.e. the maximum possible irradiance above the forest canopy). Differences in light extinction between the temperate and tropical forest were analysed in terms of canopy structure, diurnal cycle, as well

as leaf optical influences on the simulated light extinction. Additionally, the light extinction distribution under total diffuse illumination conditions was analysed and compared to the solar- and atmosphere-coupled simulations. Finally, light extinction in the proximity of larger wood structures was analysed for both study sites.

4.2.5a Comparison to Beer-Lambert approximated extinction

Canopy transmittance is commonly estimated with the so called Beer-Lambert law (Monsi & Saeki, 2005), which assumes an exponential reduction in irradiance with increasing penetration into the canopy. According to the Beer-Lambert law, transmittance through the forest canopy can be written as:

$$\tau_i = \exp(-kPAI_i) \tag{4.2}$$

where PAI_i is the cumulative PAI until the i^{th} canopy layer and k is the attenuation coefficient assuming a spherical leaf angle distribution and dependent on the solar zenith angle (θ):

$$k = \frac{1}{2\cos(\theta)} \tag{4.3}$$

The average extinction profile based on the above Beer-Lambert approximation is finally the inverse of τ_i. The Beer-Lambert approximated light extinction curve was estimated with a vertical resolution of 0.25m, corresponding to the vertical voxel size used in the DART simulations. The Beer-Lambert approximated average light extinction profiles were compared to the ones based on the complex 3D representation of the canopy using the DART model.

4.3 Results

The distribution of PAR radiation is strongly driven by the canopy structure of the forest. Figure 4.1 shows the canopy structure and distribution of vegetation material inside the canopies of the two study sites for a 60 m wide and 10 m deep transect of the study sites. The temperate forest shows a very dense and homogeneous upper canopy layer, followed by a less dense understorey. More than 50% of the total plant material can be found at levels higher than 20 m above ground (corresponds to the upper 40% of the canopy). For the tropical forest, however, more than 50% of the total plant material can be found at levels higher than 13 m above ground (corresponds to the upper 60% of the canopy). The canopy structure of the tropical forest is characterized by a very heterogeneous, but dense overstorey with varying tree heights, followed by a less dense mid-storey and a very dense understorey. Interestingly, even though the canopy structure differs drastically between the two analysed forests, the total vertically accumulated plant material (quantified as plant area index (PAI)) does not differ a lot between the two ecosystems, suggesting that

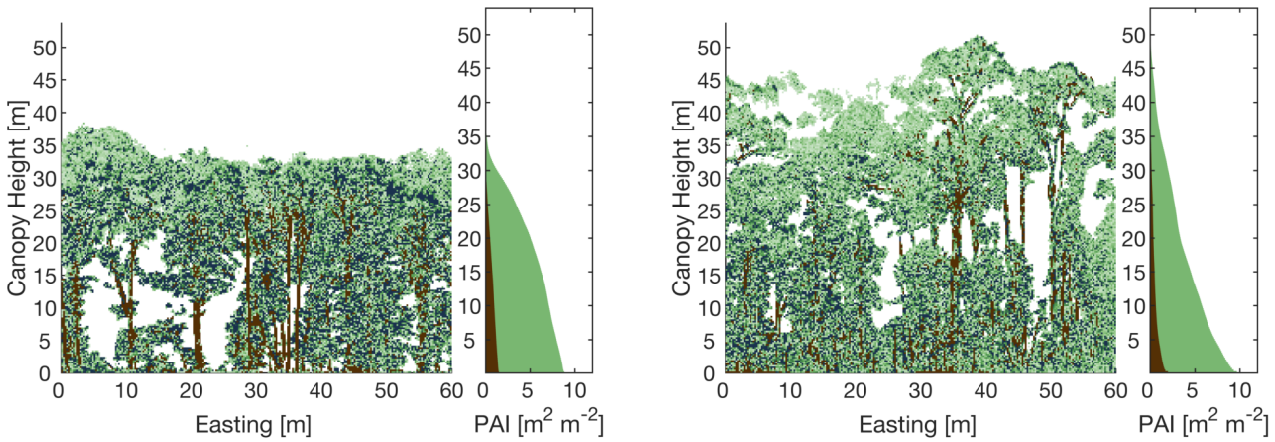

Fig. 4.1: Vegetation density grids of a 60 m wide and 10 m deep transect for the (a) Laegern (Northing: 10 - 20 m) and (b) the Lambir (Northing: 40 - 50 m) study site. The illustration shows vegetation area volume densities [m^2 m^{-3}] at 25 cm voxel resolution from low (light green) to high (dark green). The right panel shows the cumulative plant area index (PAI) (all 10 m deep transects are shown in the supplementary material).

the difference in canopy structure between the two forests is mainly due to the different distribution of plant material rather than the total amount of plant material.

4.3.1 Light extinction - temperate vs. tropical forest

The difference in canopy structure between the two study sites clearly has an influence on the light distribution inside the canopy. Figure 4.2 shows the average diurnal extinction of PAR for the same transect as shown in Figure 4.1 as well as four horizontal slices through the canopy at 0, 25, 50, and 75% canopy height. The average extinction over the whole diurnal cycle is visualized (for Figures 4.2a and 4.2b, average per 10 m deep transects and over time, for Figures 4.2c and 4.2d only average over time per pixel are shown). Due to the very dense and homogeneous upper layer in the temperate forest, most of the incoming PAR is already extinct after just few meters into the canopy. Only the few canopy gaps within the study site allow for more radiation passing into the lower canopy parts. These canopy gaps also allow more light to pass into lower strata during specific solar positions, which can be seen by brighter linear features protruding into the canopy at certain angles especially in Figure 4.2a. The dense upper canopy layer in the temperate forest results in a typical exponential light extinction curve as shown in Figure 4.3a. The tropical forest on the other hand shows a much more heterogeneous distribution of PAR extinction throughout the whole canopy, mainly due to the many vertical canopy gaps caused by the large canopy height variance allowing the light to pass into lower strata of the canopy. This results in an average light extinction profile for the whole study site with a more linear character as shown in Figure 4.3a. For the Laegern study site, already 86% of the incoming irradiance is extinct at 50% canopy height, whereas for the Lambir case only 58% of the incoming light is extinct at the same height level.

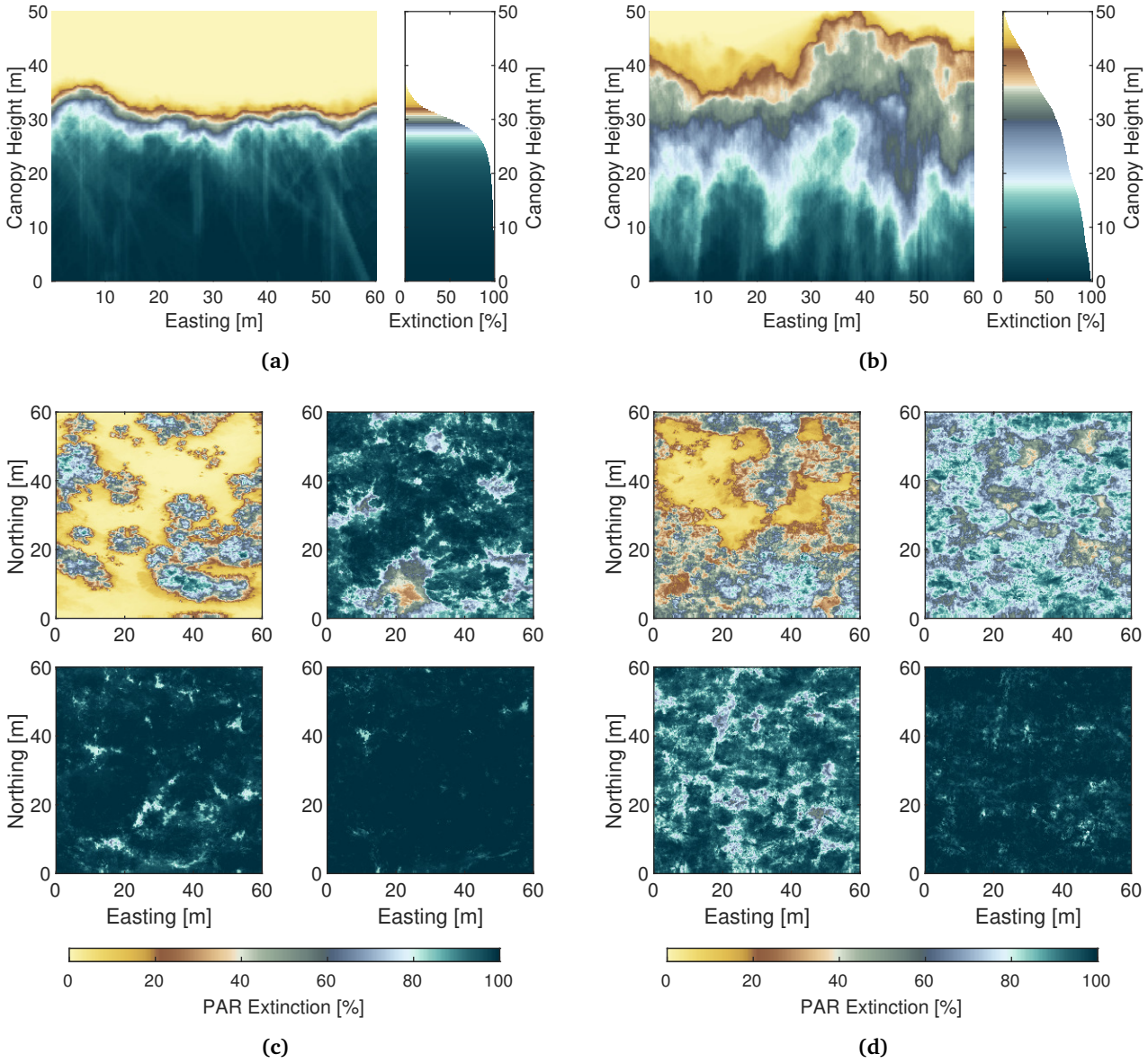

Fig. 4.2: Average diurnal light extinction for a 10 m deep transect for the Laegern (a) and Lambir (b) study site. The 10 m deep transect is oriented East-West and is located between Northings 10 - 20 m and 40 - 50 m for the Laegern and Lambir study site respectively. The right panel shows the average light extinction profile for the entire transect (all 10 m deep transects are shown in the supplementary material). The lower panel shows four horizontal slices through the entire 60 x 60 m study sites at the Laegern (c) and Lambir (d) forest. The slices were taken at 75% (top left), 50% (top right), 25% (bottom left) and 0% (bottom right) of the total canopy height of the respective forest, where 0% denotes the forest floor and 100% maximum canopy height.

Figure 4.3 also shows the comparison between the DART simulated average light extinction profile for Laegern and Lambir and a Beer-Lambert approximated extinction profile, neglecting the complex interaction between light and the 3D structure of the forest. The Beer-Lambert approximation generally overestimated extinction within the canopy, where the difference to the DART simulated extinction is higher in the upper crown layer (up to 30% difference in the upper 20% of the canopy height) and gets smaller towards the bottom of the canopy (0.5% and 3.8% at 10% canopy height for Laegern and Lambir respectively).

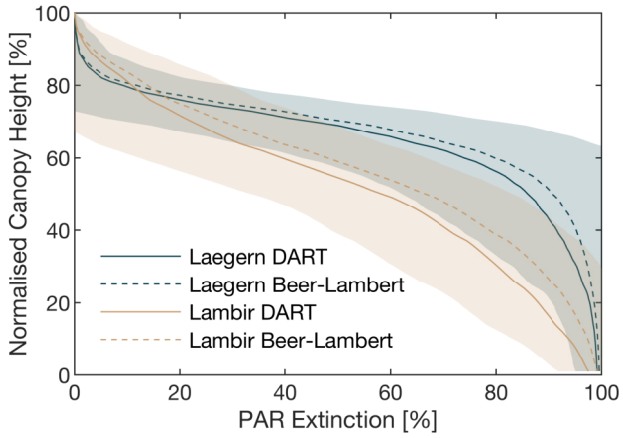

(a)

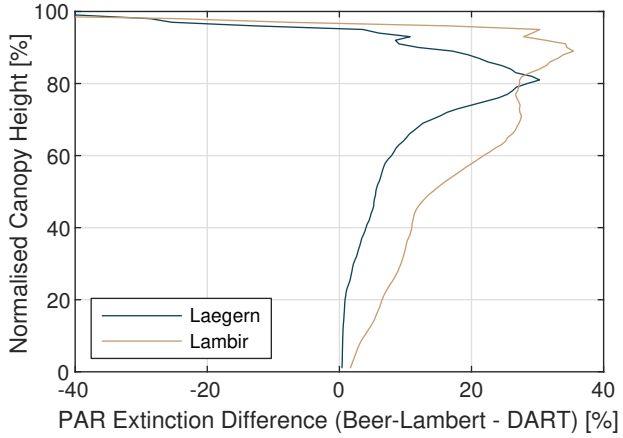

(b)

Fig. 4.3: DART modelled vs. Beer Lambert approximated average light extinction profiles. (4.3a) shows the average light extinction profiles as modelled by DART vs. Beer Lambert approximation for the entire 60 x 60 m study plots. The shaded areas in (4.3a) denotes the standard deviation in light extinction for the DART modelled extinction. (4.3b) shows the relative difference between DART modelled light extinction profiles and the ones based on the Beer-Lambert approximation. 100% canopy height denotes maximum canopy height of the entire plot to enable a comparison with the Beer-Lambert approximated light extinction profiles. Comparison is shown for solar noon conditions.

4.3.2 Light extinction - diurnal simulations

For the diurnal variation in PAR distribution, multiple simulations have been conducted in two-hour intervals between 15 minutes after sunrise and 15 minutes before sunset for the respective study sites, plus a simulation at solar maximum for the date of the northern hemisphere solstice (21st of June). Figure 4.4 shows the vertical change in light extinction over the course of a single day (northern hemisphere solstice) for the two study sites. The average light extinction profile per study site was calculated for each simulation. Light extinction profiles between simulated solar angles were linearly interpolated. Due to the multiple vertical gaps in the canopy of the tropical forest larger variations in light extinction can be observed with changing solar angles. For both study sites, minimum extinction for all canopy layers can be

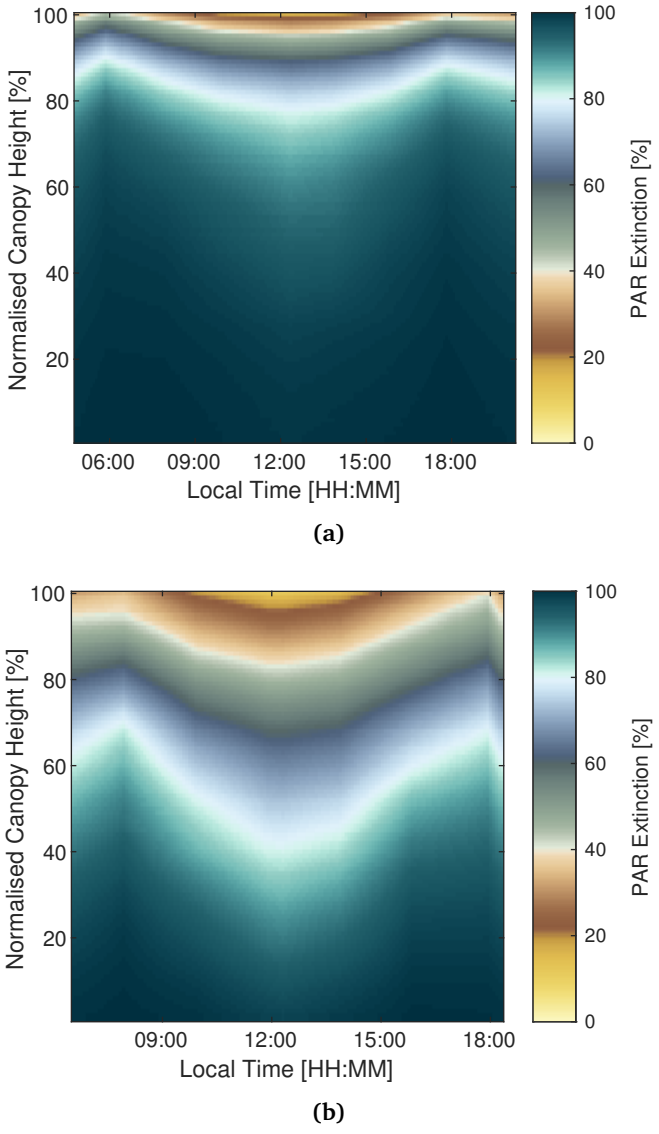

Fig. 4.4: Vertical diurnal changes in light extinction for Laegern (a) and Lambir (b). For each simulated solar angle, the average light extinction per height level for the whole 60 x 60 m was calculated. Light extinction profiles between simulated solar angles were linearly interpolated. 100% canopy height denotes the height of the convex surface fitted to the digital surface model (DSM).

observed during mid-day, whereas maximum extinction for all height layers are not observed closest to sunrise or sunset.

4.3.3 Light extinction - the role of LOP

In order to analyse how leaf optical properties affect light distribution within the canopy we ran a simulation each with the LOPs of the other forest. Figure 4.5 shows the four light extinction profiles for the 60 x 60 m study plots with their proper LOPs and with the exchanged ones from the other forest. The extinction decreases slightly (<5% below 80% canopy height) in the Laegern case when we assign LOPs from the Lambir test site. The biggest difference can be observed in the upper canopy layer with an increase in available light of up to 12% (upper 2% of the canopy). By

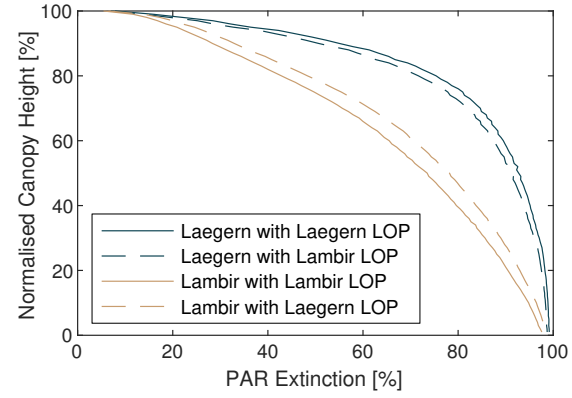

(a)

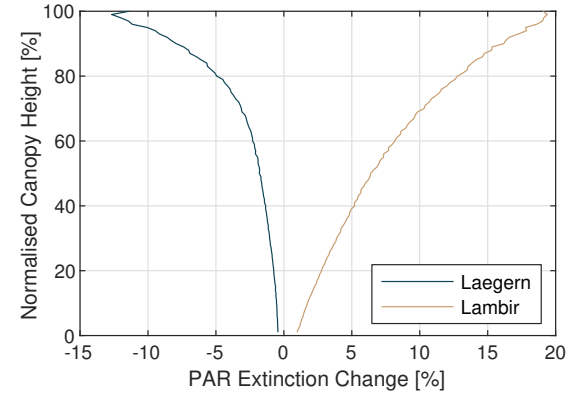

(b)

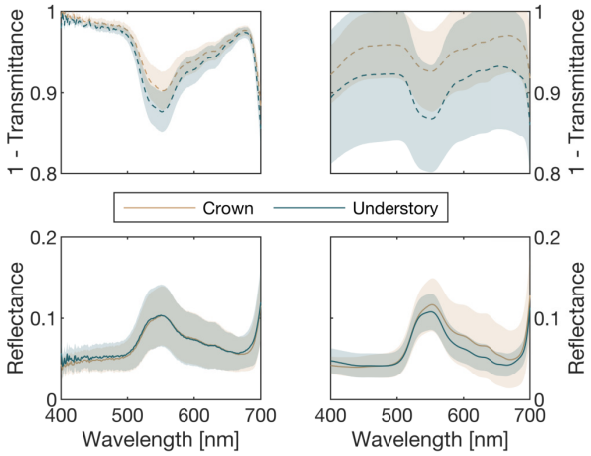

(c)

Fig. 4.5: Sensitivity of light extinction profiles due to change in LOP. (a) Absolute change in PAR extinction when we exchange the LOPs of the two study sites. Solid lines denote the light extinction profile if the proper LOPs are assigned, dashed lines denote the light extinction profile with LOPs of the other study site assigned. (b) shows the relative change compared to the initial simulation with the properly assigned LOPs. Results are based on solar noon simulations. The average light extinction for the entire 60 x 60 m plots is shown. 100% canopy height denotes the height of the convex surface fitted to the digital surface model (DSM). (c) shows the average reflectance and transmittance used for parameterization of the DART model for Laegern (left) and Lambir (right) respectively.

assigning the temperate forest LOPs to the tropical forest site we observe a much larger change in light distribution throughout the whole canopy. We observe an

increase in extinction of more than 5% above 40% canopy height and even more than 12% above 80% canopy height. Therefore, the beech-dominated optical properties of the temperate forest site absorbed much more incoming solar radiation, than the optical properties of the tropical forest, adding to the explanation for the differences in light extinction profiles of the two test sites.

Figure 4.5c shows the measured reflectance and transmittance for the two study sites in the simulated spectral region between 400 and 700 nm. The LOPs for Laegern and Lambir were acquired differently with an integrating sphere and a leaf-clip, respectively (see Section 4.2.3). As the LOPs for the Laegern study site are dominated by beech trees, the variance in LOP within this single species is relatively small compared with the observed variance at the Lambir site caused by the high species richness with highly diverse optical characteristics of the leaves. For both study sites, larger differences between leaves from the upper and lower parts of the crowns or understory can be observed for the transmittance, whereas the difference in reflectance between leaves of the two vertical canopy compartments are smaller.

4.3.4 Light extinction - diffuse illumination conditions

The radiative transfer through the forest canopies at complete diffuse illumination conditions (i.e. complete overcast skies) were simulated within DART by not simulating the radiative transfer through the atmosphere and defining the diffuse irradiance fraction to the total irradiance to be 1. In that way, no direct irradiance from the sun is simulated and the only illumination source is the diffuse sky illumination. Figure 4.6 shows the diffuse PAR extinction for the same transects as shown in Figure 4.2. Due to the missing direct irradiance part, the light distribution within the canopy is much more homogeneous with well defined layering. However, the average light extinction profiles for the shown transects (Figures 4.6a and 4.6b) as well as for the whole study plots (Figure 4.6c) do not differ much from the case where we have direct solar irradiance from the sun and diffuse sky light. Due to the more homogeneous distribution of the light within the canopy, also the variance in light extinction per height layer was decreased (shown as the standard deviation of the light extinction as shaded areas in Figure 4.6c).

4.3.5 Light extinction in wood proximity

Based on the wood structure model derived as described in section 4.2.4b we were able to analyse the light extinction as a function of distance from larger wood bodies (tree trunks and major branches). Figure 4.7 shows the relation of extinction to distance of larger wood bodies at different canopy height layers (between 2 m and 31 m or 47 m above canopy for Laegern and Lambir, respectively, in 5 m height intervals). Wood bodies generally had a larger influence on extinction in the upper canopy layers mainly due to the higher overall irradiance levels. Due to the already largely extinct light in the lower canopy layers, the distance to wood bodies does

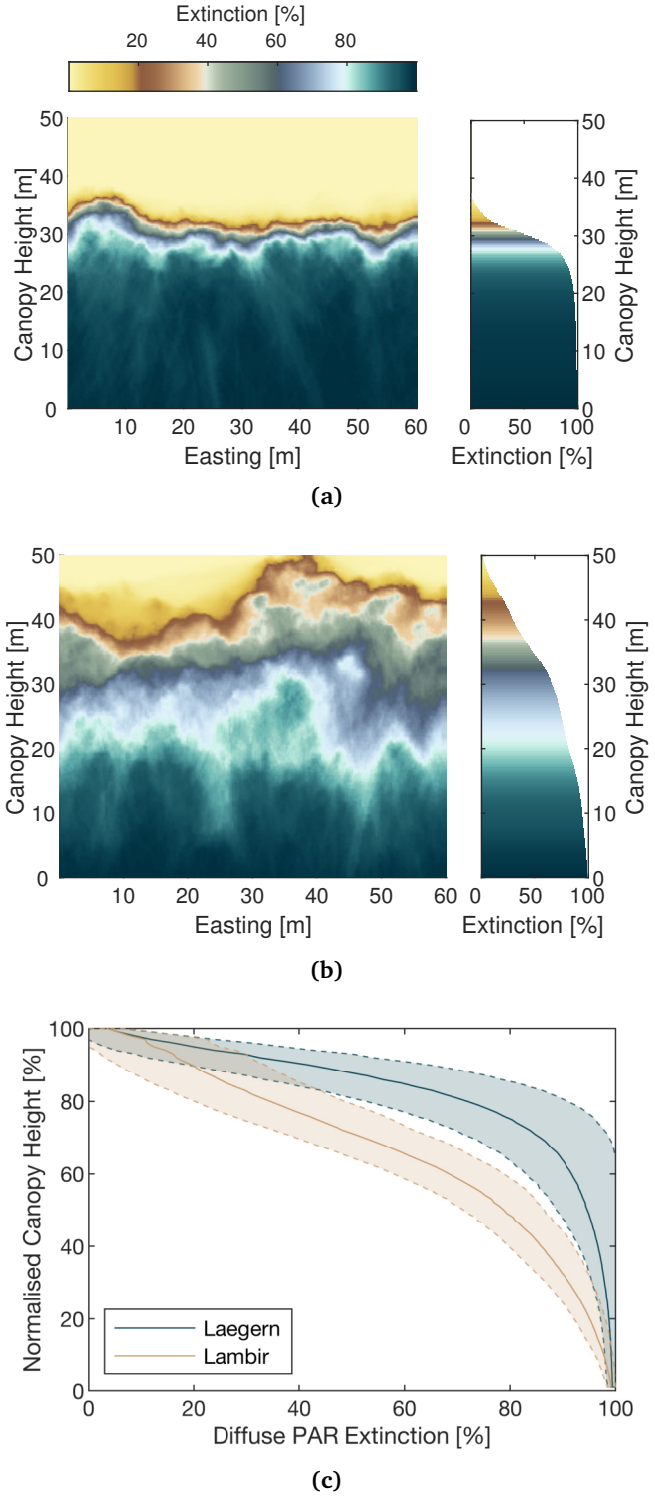

Fig. 4.6: Diffuse light extinction profiles for the corresponding transects shown in Figure 4.1 and 4.2 for the Laegern (a) and the Lambir (b) study site. The average diffuse light extinction of the 10 m deep transect is shown. The right panel shows the average diffuse light extinction profile for the entire transect (all 10 m deep transects are shown in the supplementary material). The average diffuse light extinction profile for both study sites is shown in (c). The shaded areas in (c) denotes the variance in diffuse light extinction for the respective height level. 100% canopy height denotes the height of the convex surface fitted to the digital surface model (DSM).

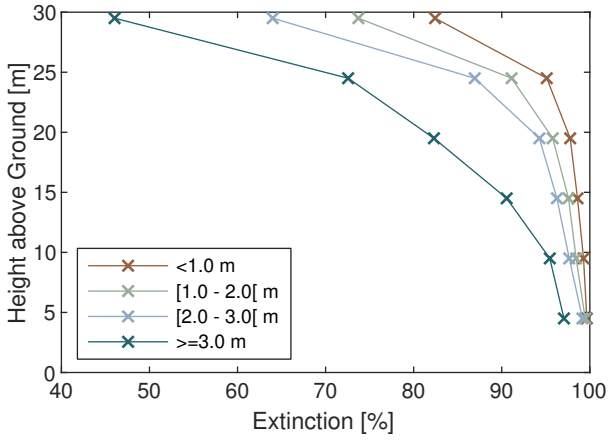

(a)

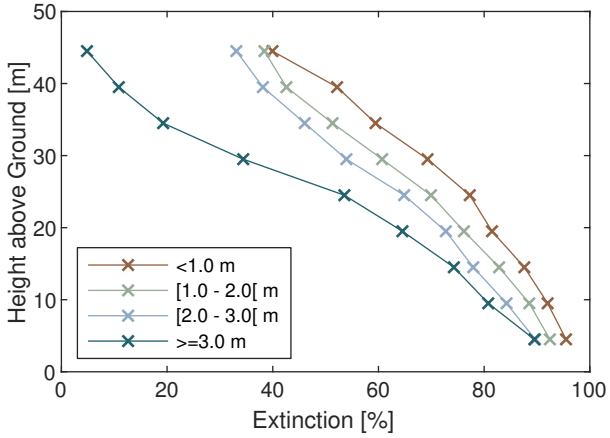

(b)

Fig. 4.7: Extinction profiles as a function of distance from wood material for the Laegern (a) and Lambir (b) study plots.

not strongly affect simulated irradiance. Nevertheless, between 2 and 7 m above ground, the average light extinction difference between < 1 and > 3 m distance was 2.6% and 6% for the Laegern and Lambir study plots, respectively. With increasing height above ground, the differences in extinction with increasing distance from wood material become larger. Between 17 m and 22 m above ground, the average light extinction difference between < 1 and > 3 m distance was 15.5% and 17% for the Laegern and Lambir study plots, respectively.

4.4 Discussion

4.4.1 Light extinction - temperate vs. tropical forest

The comparison of light extinction between a temperate forest patch dominated by a single species and a species-rich tropical forest patch has shown that the contrasting canopy structure is fundamental for explaining the distribution of light within the canopy. The heterogeneous distribution of canopy material in the tropical forest

allows more light to pass into lower strata, possibly explaining the abundance of shade tolerant species in the middle- and understorey of the canopy. Williams *et al.* (2017) showed that a mixture of species shows larger crown-complementarity (i.e. vertically non-overlapping crowns) compared with forests dominated by a single species as found in our temperate study site. According to Williams *et al.* (2017), crown complementarity is a mechanism related to light interception and use that links biodiversity with ecosystem productivity. Williams *et al.* (2017) showed that greater crown complementarity found in species-rich canopy mixtures lead to increased stem biomass overyielding. Therefore a mixture of fast growing shade-intolerant species with slow-growing shade-tolerant species can enhance productivity in forests (Kelty, 1989; Morin *et al.*, 2011; Schmid & Niklaus, 2017; Williams *et al.*, 2017; Huang *et al.*, 2018), but also leads to a more heterogeneous distribution in canopy material and intercepted light, shown in this paper's comparison.

The differences in species composition, canopy complementarity and structure and ultimately available light within the canopy will further influence the canopy turnover and development of the two showcased study sites. In the old-growth forest found at the Laegern, there is no particular gain for a single individual to grow in size to capture more light. According to King (1990), this forest patch already reached the so-called evolutionary stable state (ESS), where a gain in canopy height of a single individual is not favorable anymore. In the tropical site, however, where multiple species compete for light, evolutionary considerations are more complex, because different species may use different strategies to capture light and allocate biomass to plant organs. Therefore, it is harder to predict how a multi-species ESS vertical canopy profile should look like and conceivably it might be more heterogeneous than for monocultures. An indication for this has been observed in a grassland biodiversity experiment by Wacker *et al.* (2009).

The heterogeneous canopy structure found in the Lambir case is both the result of the high diversity of tree species present and allows for more niches of additional species with varying resource-use strategies to find their matching biotope space to thrive. The more complex canopy structure may therefore also be used as an indicator for high diversity (see also McElhinny *et al.*, 2005). The question to which degree a heterogeneous canopy structure is a consequence or cause (via feedback effects) of diversity is largely unexplored (see e.g. Sapijanskas *et al.*, 2014).

Zellweger *et al.* (2019) showed that the vegetation structure not only drives the interception of solar radiation, but also affects microclimatic conditions within the canopy on temporal and spatial scales. However, information on the 3D distribution of light, vital for analysing microclimatic conditions within the forest is still rare. We show that with the proposed approach a modelling of the light regime in any forest canopy is possible in unprecedented detail. The high level of detail has a large impact on computational costs, limiting the size of forest patches that can be analyzed. However, as Figure 4.3 shows, the DART-simulated light extinction profiles also differ

largely from the Beer-Lambert approximated light extinction profiles (difference up to >30% in the upper canopy). The difference between DART modeled and Beer-Lambert approximated light extinction might even be larger, if less detailed information on the distribution of canopy material is available. Additionally, the Beer-Lambert approximation does not account for diffuse irradiance nor for multiple scattering, why small scale variations in the irradiance field due to the heterogeneity of the canopy can not be addressed with such a simplifying approach. This underlines the need for such high detailed modelling of the light regime in forest ecosystems. Especially as the radiative transfer through the forest ecosystems is recognized as one of the largest sources of uncertainty in dynamic global vegetation models (DGVMs), where often simplifying assumptions on the distribution of plant material is assumed (e.g. Big Leaf assumption) (Alton *et al.*, 2007a; Fisher *et al.*, 2017). The proposed approach could also be used as a benchmark for DGVMs to assess the level of detail needed for an accurate simulation of the 3D radiative transfer through the canopy, possibly allowing for more accurate modelling of the radaitive transfer also on larger scales. With data from NASA's Global Ecosystem Dynamics Investigation (GEDI) instrument soon available, more wide spread (however without wall-to-wall global coverage) information regarding the distribution of vegetation material will be gained. From this we could improve our understanding of the differences in canopy structure of different forest canopies, further improving the parameterization of forest structure in DGVMs.

Even-though the proposed approach can deliver 3D light extinction maps at high level of detail, they are still based on simplifying assumptions (e.g. turbid medium assumption, neglecting the specular reflectance term of leaves (see Section 4.4.3), use of standard atmosphere models etc.), which may add sources of uncertainty in the modeled light extinction products. However, we argue that the proposed approach delivers information about the 3D light distribution in forest ecosystem in a complexity and at a level of detail we have not yet seen.

4.4.2 Light extinction - diurnal cycle

Vegetation structure further affects light interception and distribution over the whole diurnal cycle. Due to the heterogeneous canopy structure found in the tropical forest, an increased variability in available light for any canopy layer can be observed compared to the temperate forest. This assures that also species in lower canopy strata receive enough light over the diurnal cycle to be productive and competitive. In the case of the Laegern forest on the other hand, the variability in available light over the whole diurnal cycle within the lower stratum of the canopy is minimal, reducing the opportunities for competing species to grow. However, the seasonal leaf-fall pattern in the temperate forest allows some early-growing understorey herbs to coexist with the large canopy trees.

The diurnal simulations have shown that for both study sites, minimum extinction throughout the whole canopy can be observed during mid-day at solar maximum conditions. However, interestingly, maximum extinction is not observed right after sunrise or before sunset for both study sites as stated in Section 4.3.2. This could be explained by the fact that light extinction, as defined in this paper, is a relative term based on the maximum solar irradiance observed above the forest canopy. Due to the low solar angle at the beginning and end of the day, nearly 100% of the radiation is diffuse-sky illumination rather than direct solar irradiance, reducing the total incoming radiation on the top of canopy to a minimum. This also reduces the difference in light conditions between the top of and within the canopy, resulting also in lower light extinction throughout the canopy. The distribution of leaf angles also affects the diurnal distribution of light within the canopy, as certain leaf and solar angle combinations will promote or prevent the distribution of light within the canopy (e.g. Wang *et al.*, 2007). In this study, a single leaf angle distribution function per study site (i.e. plagiophile for temperate and spherical for tropical forest) was used to parameterize the forest canopy, which could lead to a bias when simulating light extinction. Measuring accurate 3D leaf angle distribution functions is still a challenge. However, recent studies have shown the potential of high resolution TLS measurements for the retrieval of accurate leaf angle distribution (e.g. Li *et al.*, 2018; Liu *et al.*, 2019; Vicari *et al.*, 2019).

Seasonal differences in light extinction were not analysed in this study. An analysis of the seasonal variation in light extinction would require multiple laser scanning and LOP acquisitions distributed across the year in order to adequately represent seasonal changes in canopy structure and LOP. However, especially in the case of the temperate, deciduous forest site, seasonal changes in canopy structure and leaf-optical properties can have large impacts on the distribution of light within the canopy, allowing seasonal growing periods for certain species (e.g. wild garlic, *Allium ursinum* L., in early spring). These seasonal changes in light conditions should be addressed in future studies. Morton *et al.* (2016) analysed diurnal and seasonal variability in light utilization in an Amazon forest, however they assumed a constant canopy structure and constant LOPs over the year.

4.4.3 Light extinction - the role of LOP

Compared to the vegetation structure, leaf optical properties only had a small influence on the distribution of light within the canopy. The change in simulated light extinction when we exchanged LOPs of the two study sites depended on the canopy height and was generally smaller for the Laegern than for the Lambir study site. However, this observed change was purely based on differences in the measured reflectance and transmittance values, which do not account for specular components of the LOPs. Due to the entirely different anatomical and morphological structures of temperate and tropical leaves (i.e. waxy leaf surface found in the tropics), it is

believed that larger differences in specular reflectance could exist, probably resulting in a bigger influence of the leaves' optical properties on the distribution of light within the canopy. The specular reflectance distribution functions of leaves were neither measured nor modelled in this study. We emphasize the need for further analysis of the influence of the specular term on the light distribution and suggest future studies on the matter, including geometrical-optical modelling of small leaves including a specular component.

A certain source of uncertainty associated with the modeled light extinction can be expected from the assignment of the LOP onto the virtual forest canopy. First of all, the leaf optical properties for Laegern and Lambir were acquired using two different approaches (Laboratory measurement with integrating sphere for the Laegern forest vs. non-destructive LOP sampling using a leaf-clip add-on to the ASD spectroradiometer for the Lambir forest), possibly leading to some systematic differences between measured LOPs with the different approaches. Hovi *et al.* (2017) found that reflectance measured using a leaf-clip is on average 14% higher compared with measurements using a single integrating sphere. Second of all, as it was not possible to assign LOP to the different tree species within the DART scene, we opted for a random assignment of the measured LOPs to the vegetation turbid medium voxels.

We argue that the above stated sources of uncertainty only have a minor influence on the modeled light extinction. First, the findings in this study showed that substantially different LOPs only resulted in relatively small changes in modeled light extinction of up to 10-15% at the top of canopy and less than 3% below 20% of the normalised canopy height. This assumption is also supported by the findings of Kükenbrink *et al.* (2019) and Stuckens *et al.* (2009), where differences in simulated irradiance or reflectance values were small when LOPs were varied within realistic boundaries.

In this study, we only analysed light extinction within the PAR spectral region between 400 and 700 nm, as the majority of light harvested for photosynthesis is located within these wavelengths. However, Chen & Blankenship (2011) found that under light-limiting conditions, certain plants adapted to deep shade also can use wavelengths greater than 700 nm for photosynthesis due to a modification in the plant's chlorophyll (Chen *et al.*, 2010; Chen & Blankenship, 2011; Miyashita *et al.*, 1996). However, when light interception is studied in relation to plant's health and growth, an analysis based on photon flux density (i.e. measured in μmol m^{-2} s^{-1}) might be better suited because the rate of photosynthesis depends on the number of photons received, rather than photon energy (i.e. measured in W m^{-2}) (Jones *et al.*, 2003).

4.4.4 Light extinction - diffuse illumination conditions

Especially in the tropics, diffuse-sky irradiance is the dominant illumination source rather than direct sunlight due to high cloud coverage. Therefore it is important to also analyse the distribution of light within the canopy under diffuse illumination conditions. Alton *et al.* (2007b) found that light-use efficiency (LUE) is increased by 28% to 33% for a temperate and tropical forest, respectively, under diffuse illumination conditions. It is believed that the LUE enhancement under diffuse illumination is due to a sharing of the canopy radiation-load. Alton *et al.* (2007b) argue that, under direct sunlight, a sizeable fraction of the foliage is either light-saturated or not receiving enough sunlight to photosynthesize efficiently. Our simulation with total diffuse irradiance conditions showed that the distribution of light within the canopy was much more homogeneous at both sites compared with conditions under direct sunlight. A more even distribution of light within the canopy could potentially be a further explanation for an increased LUE and productivity of a forest.

4.4.5 Light extinction in wood proximity

Due to the separation of wood and leaf material in the laser acquisitions, it is possible to analyse light extinction in the vicinity of major trunks and branches. This analysis further highlights the complexity of radiation measurements within the canopy, as wood material can have an effect on observed incoming radiation at several meters distance from the tree trunk or major branches. In this study, we modeled the 3-dimensional wood structure based on the amount of detected laser returns from wood material within each voxel. This can result in discontinuous trunk and branch structures within the model due to occlusion effects caused by dense understorey (especially in the tropical site) or trunks and branches (Kükenbrink *et al.*, 2017; Schneider *et al.*, 2019). A continuous representation of the wood structure could have been achieved by using a quantitative structure model (QSM) as introduced by Raumonen *et al.* (2013) and already employed by Calders *et al.* (2018) to reconstruct a temperate forest for radiative transfer modelling. However, a successful performance of the QSM model requires a highly detailed representation of the wood structure. Missing parts of branches or trunks can cause the QSM model to fail, which would have been especially a problem in the tropical site, where dense understorey often obstructed a clear view of the lower trunk area. We therefore opted for the stated simpler approach for representing the wood structure within the DART model.

4.5 Conclusion

We conclude that a detailed three-dimensional forest reconstruction is essential for accurate modelling of the light distribution within a forest canopy. In this

study we developed an approach to model and analyse the spatial heterogeneity of light distribution at an unprecedented level of detail in the vertical, horizontal and temporal domains. We showed that the radiative transfer of photons through the forest canopy was mainly driven by the canopy structure, whereas optical properties of leaves had a smaller impact on the distribution of light within the canopy. The comparison of the simulated light extinction profiles with the ones produced using a Beer-Lambert approximation revealed the necessity of such a complex representation of the 3D canopy structure in order to accurately represent the radiative transfer of photons through the forest canopy. The proposed approach may serve as a benchmark to assess the impact of level of detail necessary to represent a forest canopy structure as well as optical characteristics in a radiative transfer model. This will further improve radiative transfer approximations in dynamic global vegetation models (DGVMs), further advancing the understanding of the importance of light distribution within a forest canopy. This is particularly important when DGVMs shall represent a high level of detail allowing to assess primary productivity and other processes well. The presented study allows to develop trade-off's between accurate estimates of primary productivity versus detailed representation of canopy structure and physiology. High resolution 3D laser-scanning data with *in-situ* and *in-vivo* measured optical characteristics in combination with a 3D radiative transfer model reveal insights of small scale variability of light availability and distribution within a canopy and therefore advance our understanding of light-matter interactions driving species coexistence, competition and diversity in complex forest canopies.

Acknowledgement

This study has been supported by the University of Zurich Research Priority Program on Global Change and Biodiversity (URPP GCB).The research carried out at the Jet Propulsion Laboratory, California Institute of Technology, was under a contract with the National Aeronautics and Space Administration. Government sponsorship is acknowledged. We thank Dr. Tomoaki Ichie, Dr. Eri Yamasaki and Prof. Dr. Kentaro Shimizu for their support in organizing and performing the field work at the Lambir Hills NP. Permits and access to the Lambir Hills National Park research site (Miri Division, Sarawak) have been granted by the Forest Department Sarawak, as with research permit no. NCCD.907.4.4(JLD.13)-181 and park permit no. 128/2016. UAVLS flight operations and data processing were performed by Aeroscout, Switzerland.

4.6 Supplementary Material

4.6.1 Additional PAI transects

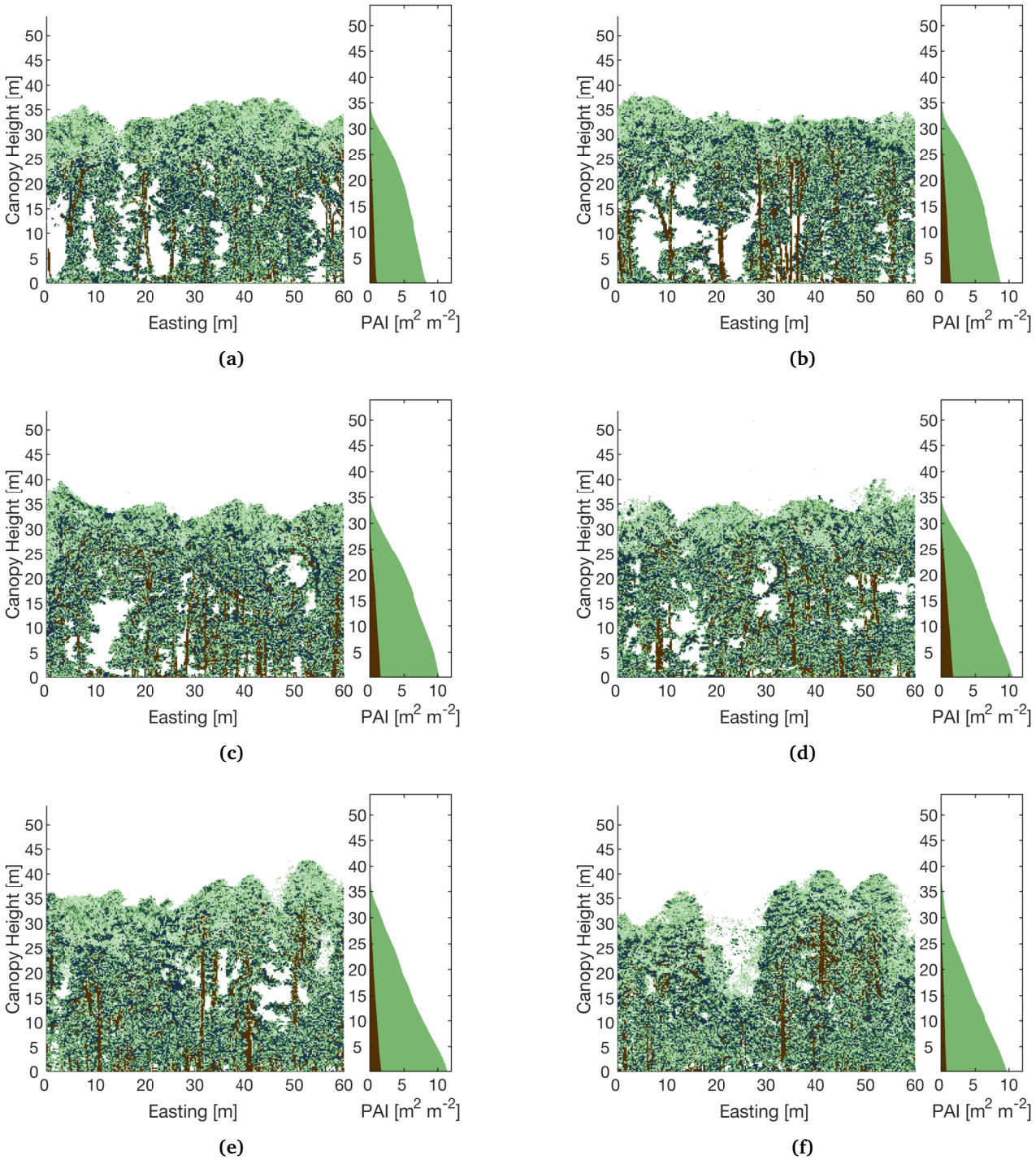

Fig. S4.1: All 10 m deep PAI transects for the Laegern study site. (a) Northing 0 - 10 m, (b) Northing 10 - 20 m (same as Figure 4.1a), (c) Northing 20 - 30 m, (d) Northing 30 - 40 m, (e) Northing 40 - 50 m, (f) Northing 50 - 60 m.

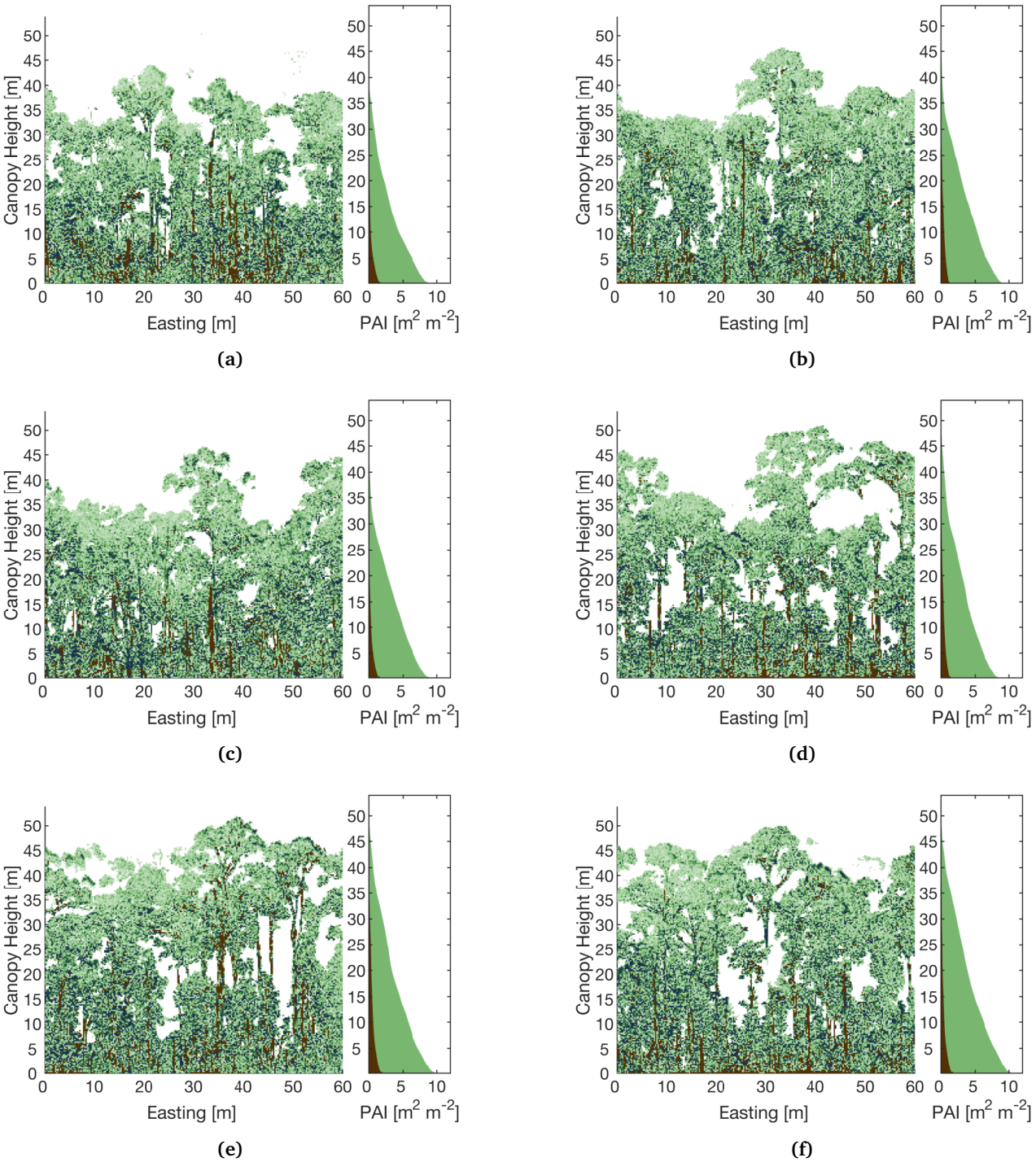

Fig. S4.2: All 10 m deep PAI transects for the Lambir study site. (a) Northing 0 - 10 m, (b) Northing 10 - 20 m, (c) Northing 20 - 30 m, (d) Northing 30 - 40 m, (e) Northing 40 - 50 m (same as Figure 4.1b), (f) Northing 50 - 60 m.

4.6.2 Additional light extinction transects

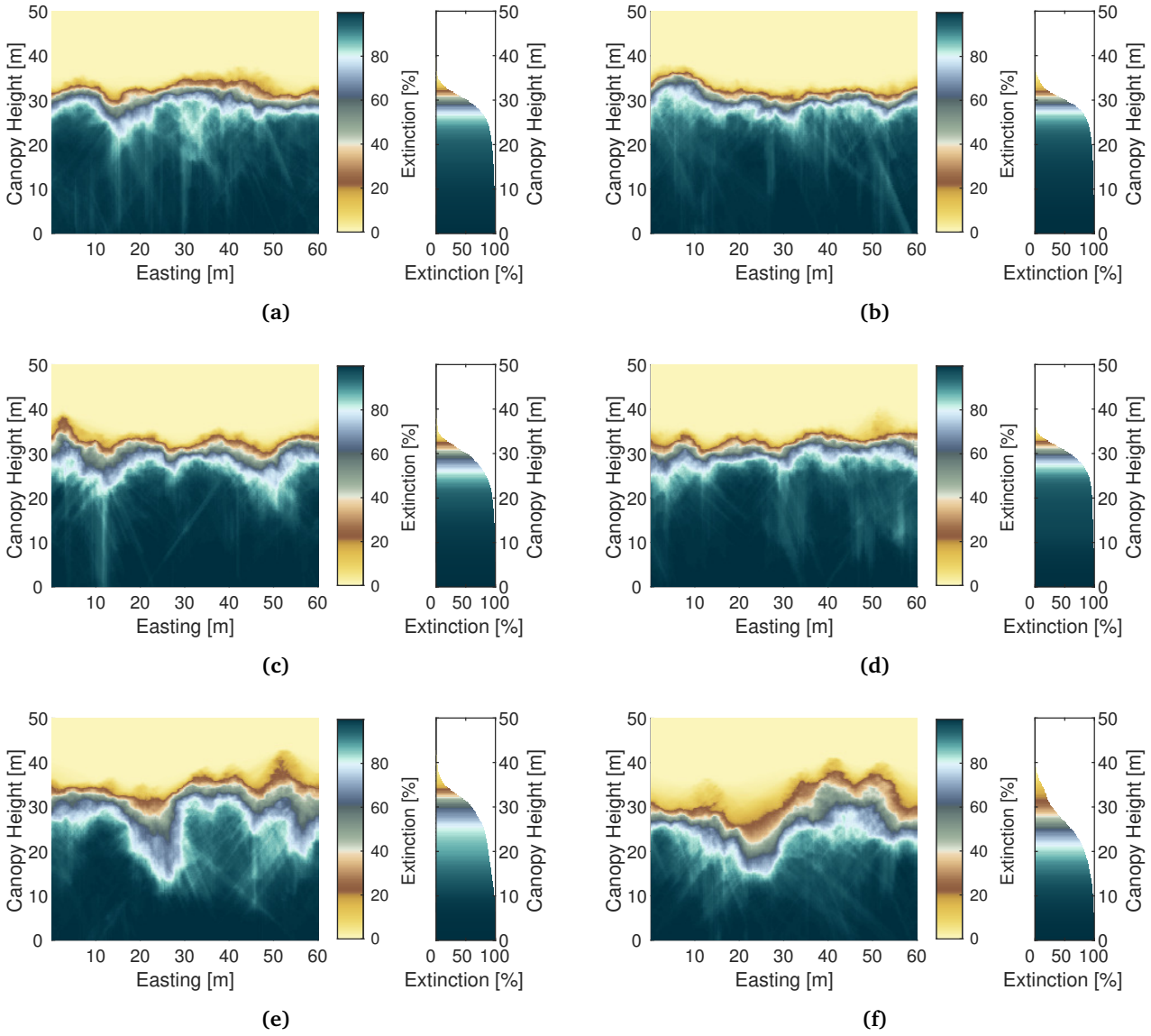

Fig. S4.3: All 10 m deep average diurnal light extinction transects for the Laegern study site. (a) Northing 0 - 10 m, (b) Northing 10 - 20 m (same as Figure 4.2a), (c) Northing 20 - 30 m, (d) Northing 30 - 40 m, (e) Northing 40 - 50 m, (f) Northing 50 - 60 m.

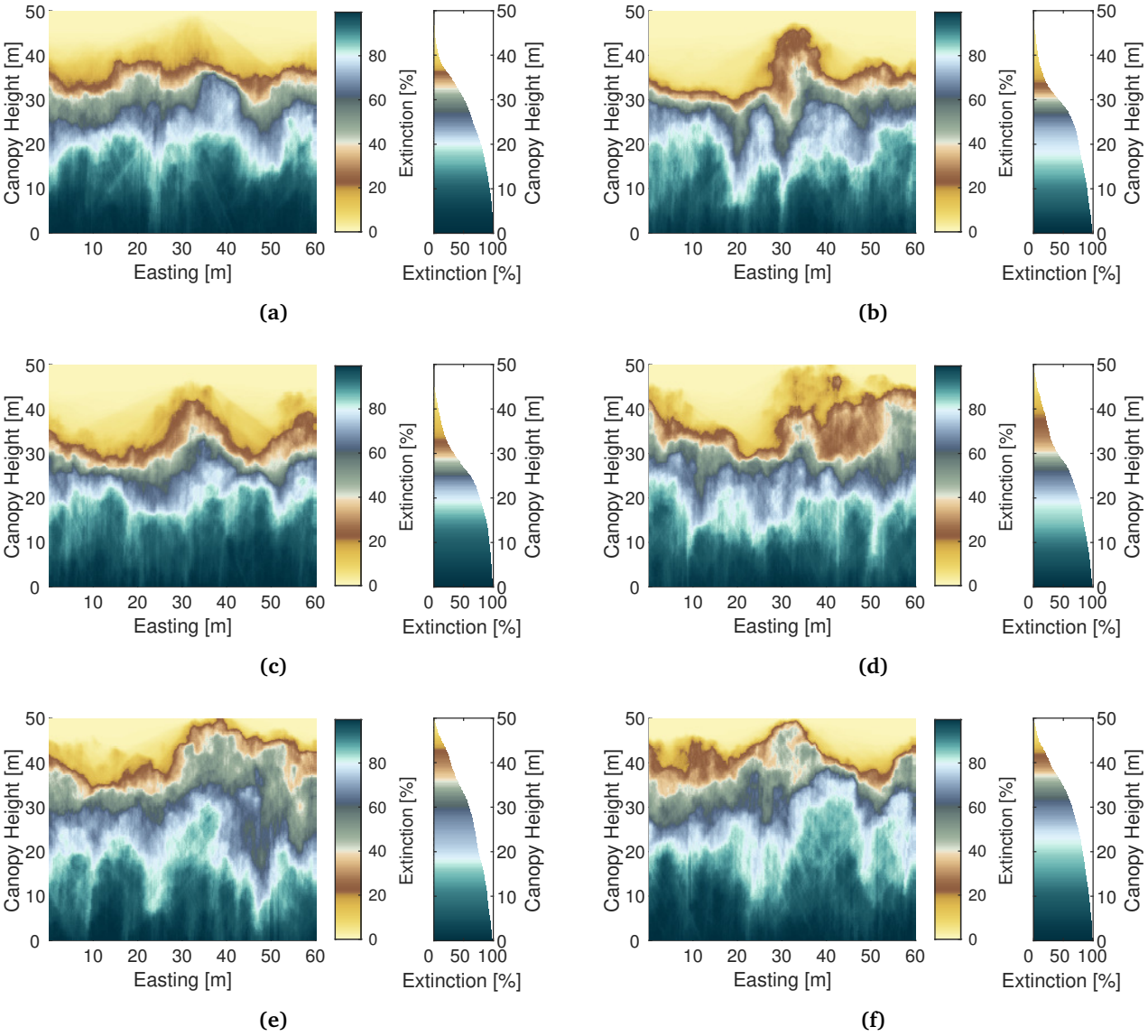

Fig. S4.4: All 10 m deep average diurnal light extinction transects for the Lambir study site. (a) Northing 0 - 10 m, (b) Northing 10 - 20 m, (c) Northing 20 - 30 m, (d) Northing 30 - 40 m, (e) Northing 40 - 50 m (same as Figure 4.2b), (f) Northing 50 - 60 m.

4.6.3 Additional light extinction transects under diffuse conditions

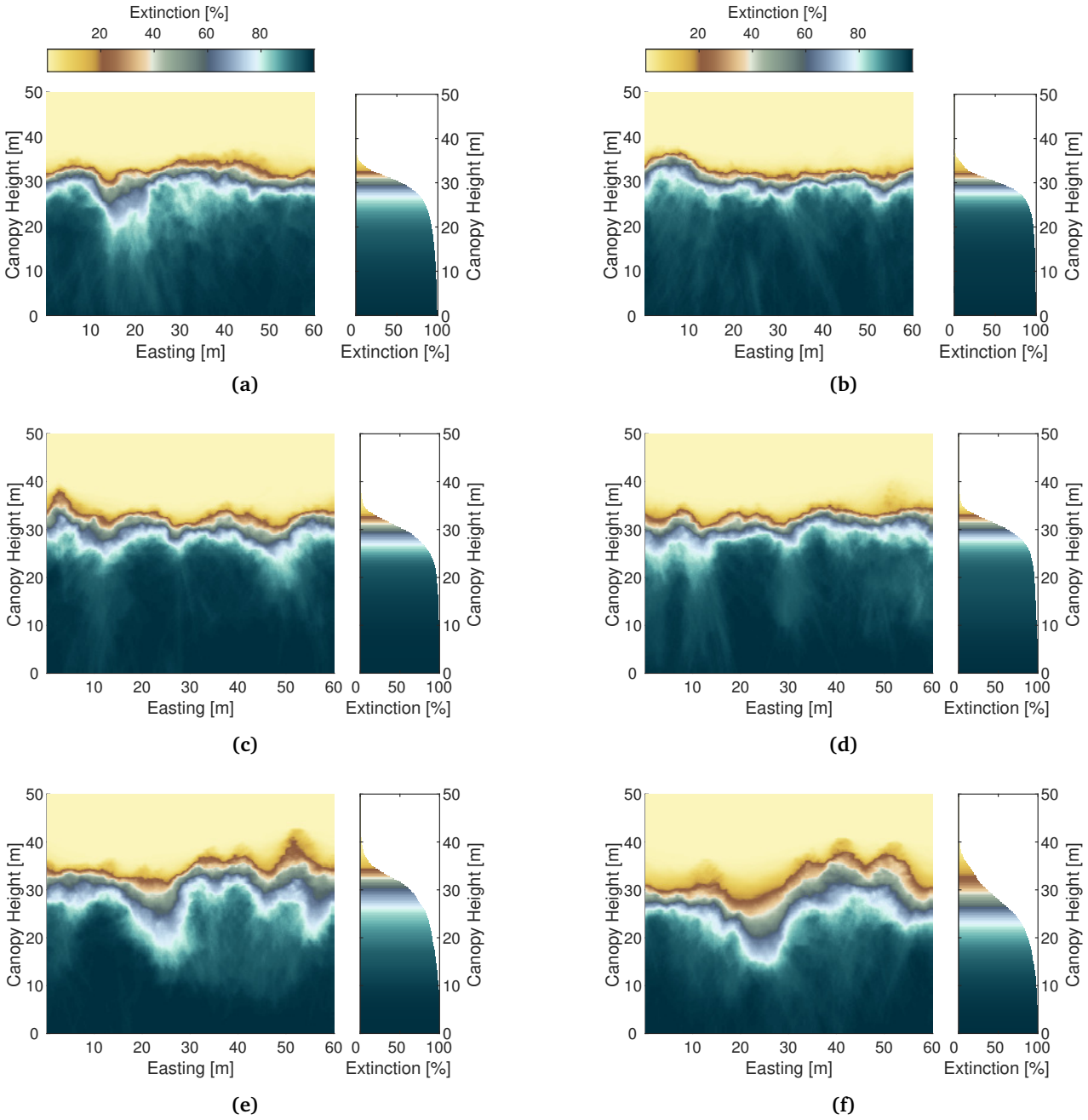

Fig. S4.5: All 10 m deep light extinction transects for the Laegern study site under complete diffuse irradiance conditions at solar noon. (a) Northing 0 - 10 m, (b) Northing 10 - 20 m (same as Figure 4.6a), (c) Northing 20 - 30 m, (d) Northing 30 - 40 m, (e) Northing 40 - 50 m, (f) Northing 50 - 60 m.

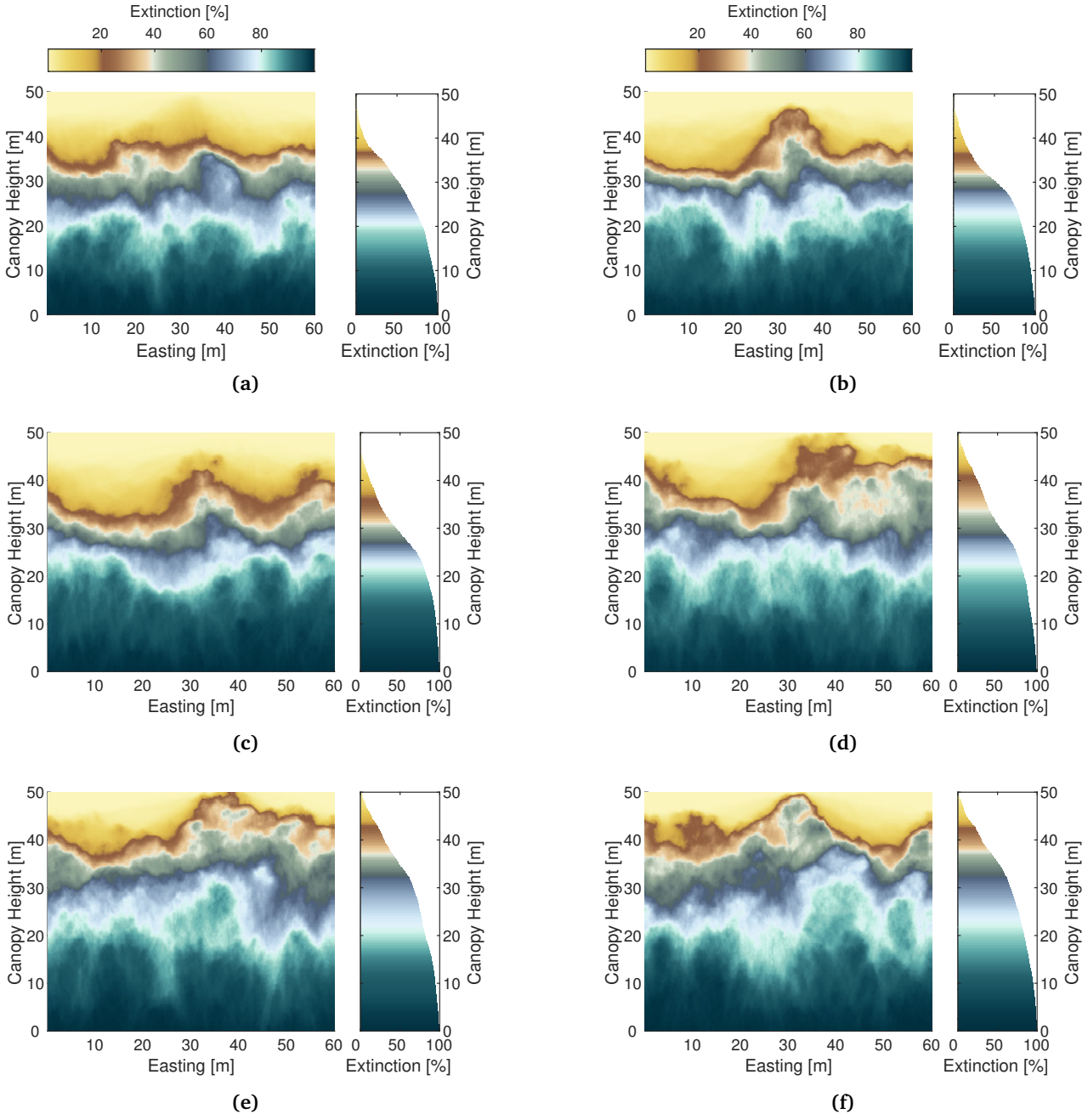

Fig. S4.6: All 10 m deep light extinction transects for the Lambir study site under complete diffuse irradiance conditions at solar noon. (a) Northing 0 - 10 m, (b) Northing 10 - 20 m, (c) Northing 20 - 30 m, (d) Northing 30 - 40 m, (e) Northing 40 - 50 m (same as Figure 4.6b), (f) Northing 50 - 60 m.

4.6.4 LiDAR extracted wood structure

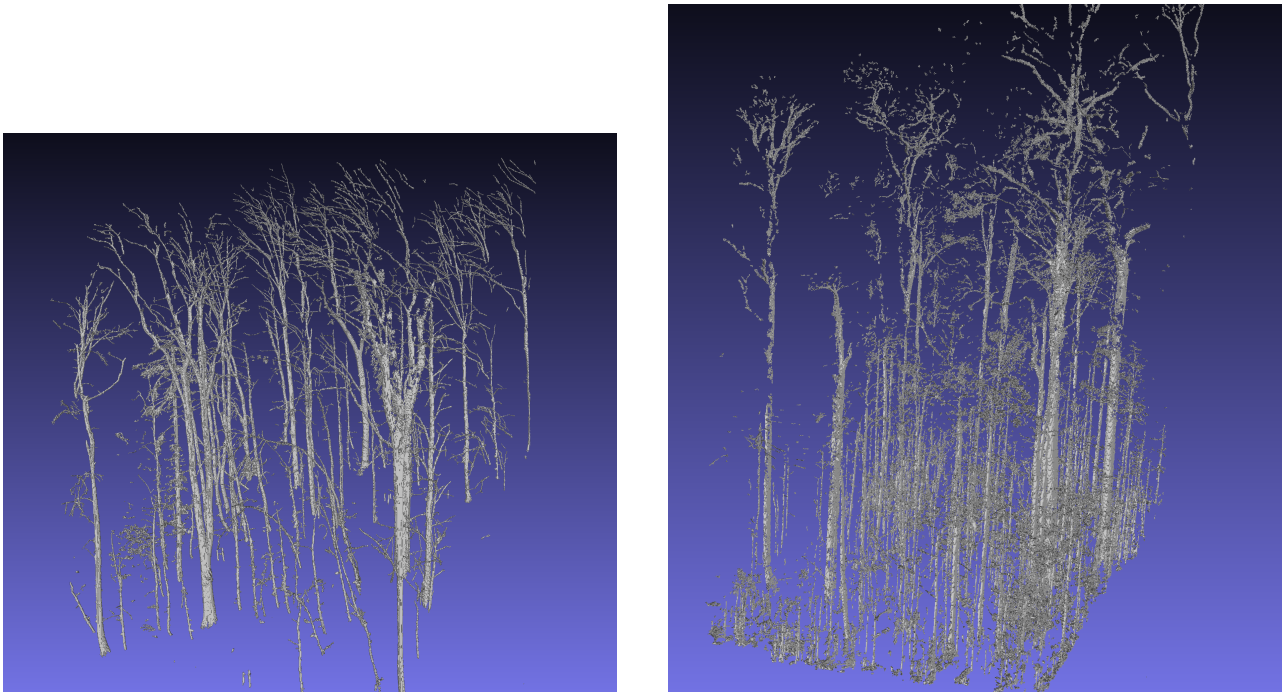

(a) (b)

Fig. S4.7: Subset (30 x 30 m^2) of the LiDAR extracted major trunks and branch structure for the parameterization of the opaque wood structure within DART. (a) Laegern, (b) Lambir.

4.7 References

Alton PB, Ellis R, Los SO, North PR (2007a) Improved global simulations of gross primary product based on a separate and explicit treatment of diffuse and direct sunlight. *Journal of Geophysical Research Atmospheres*, **112**, 1–12.

Alton PB, North PR, Los SO (2007b) The impact of diffuse sunlight on canopy light-use efficiency, gross photosynthetic product and net ecosystem exchange in three forest biomes. *Global Change Biology*, **13**, 776–787.

Ashton PS (2005) Lambir's Forest: The World's Most Dive Known Tree Assemblage? In: *Pollination Ecology and the Rain Forest*, pp. 191–216. Springer-Verlag, New York.

Asner GP, Martin RE, Suhaili AB (2012) Sources of Canopy Chemical and Spectral Diversity in Lowland Bornean Forest. *Ecosystems*, **15**, 504–517.

Baldocchi D, Falge E, Gu L, *et al.* (2001) FLUXNET: A New Tool to Study the Temporal and Spatial Variability of Ecosystem-Scale Carbon Dioxide, Water Vapor, and Energy Flux Densities. *Bulletin of the American Meteorological Society*, **82**, 2415–2434.

Baldocchi DD, Wilson KB, Gu L (2002) How the environment, canopy structure and canopy physiological functioning influence carbon, water and energy fluxes of a temperate broad-leaved deciduous forest - An assessment with the biophysical model CANOAK. *Tree Physiology*, **22**, 1065–1077.

Berk A, Bernstein L, Robertson D (1987) MODTRAN: A Moderate Resolution Model For LOWTRAN. Tech. rep., Spectral Sciences. Inc., Burlington.

Calders K, Origo N, Burt A, *et al.* (2018) Realistic Forest Stand Reconstruction from Terrestrial LiDAR for Radiative Transfer Modelling. *Remote Sensing 2018, Vol. 10, Page 933*, **10**, 933.

Chen JM, Mo G, Pisek J, Liu J, Deng F, Ishizawa M, Chan D (2012) Effects of foliage clumping on the estimation of global terrestrial gross primary productivity. *Global Biogeochemical Cycles*, **26**, 1–18.

Chen M, Blankenship RE (2011) Expanding the solar spectrum used by photosynthesis. *Trends in Plant Science*, **16**, 427–431.

Chen M, Schliep M, Willows RD, Cai ZL, Neilan BA, Scheer H (2010) A Red-Shifted Chlorophyll. *Science*, **329**, 1318–1319.

Cox PM, Betts RA, Bunton CB, Essery RLH, Rowntree PR, Smith J (1999) The impact of new land surface physics on the GCM simulation of climate and climate sensitivity. *Climate Dynamics*, **15**, 183–203.

Danson FM, Disney MI, Gaulton R, Schaaf C, Strahler A (2018) The terrestrial laser scanning revolution in forest ecology. *Interface Focus*, **8**, 20180001.

Danson FM, Hetherington D, Morsdorf F, Koetz B, Allgower B (2007) Forest Canopy Gap Fraction From Terrestrial Laser Scanning. *IEEE Geoscience and Remote Sensing Letters*, **4**, 157–160.

Denning SA, Nicholls M, Prihodko L, Baker I, Vidale PL, Davis K, Bakwin P (2003) Simulated variations in atmospheric CO2 over a Wisconsin forest using a coupled ecosystem-atmosphere model. *Global Change Biology*, **9**, 1241–1250.

Duursma RA, Mäkelä A (2007) Summary models for light interception and light-use efficiency of non-homogeneous canopies. *Tree Physiology*, **27**, 859–870.

Eugster W, Zeyer K, Zeeman M, Michna P, Zingg a, Buchmann N, Emmenegger L (2007) Methodical study of nitrous oxide eddy covariance measurements using quantum cascade laser spectrometery over a Swiss forest. *Biogeosciences*, **4**, 927–939.

Fisher RA, Koven CD, Anderegg WRL, *et al.* (2017) Vegetation Demographics in Earth System Models: a review of progress and priorities. *Global Change Biology*, pp. 1–20.

Gastellu-Etchegorry J, Grau E, Lauret N (2012) DART : A 3D Model for Remote Sensing Images and Radiative Budget of Earth Surfaces. In: *Modeling and Simulation in Engineering* (ed. Alexandru C), pp. 1–40. CESBIO - CNES, CNRS (UMR 5126), IRD, Universite de Toulouse, Toulouse, France.

Gastellu-Etchegorry JP (2008) 3D modeling of satellite spectral images, radiation budget and energy budget of urban landscapes. *Meteorology and Atmospheric Physics*, **102**, 187–207.

Gastellu-Etchegorry JP, Martin E, Gascon F (2004) DART: A 3D model for simulating satellite images and studying surface radiation budget. *International Journal of Remote Sensing*, **25**, 73–96.

Gastellu-Etchegorry JP, Yin T, Lauret N, *et al.* (2015) Discrete Anisotropic Radiative Transfer (DART 5) for Modeling Airborne and Satellite Spectroradiometer and LIDAR Acquisitions of Natural and Urban Landscapes. *Remote Sensing*, **7**, 1667–1701.

Hiromi T, Ichie T, Kenzo T, Ninomiya I (2012) Interspecific variation in leaf water use associated with drought tolerance in four emergent dipterocarp species of a tropical rain forest in Borneo. *Journal of Forest Research*, **17**, 369–377.

Hovi A, Forsström P, Mõttus M, Rautiainen M (2017) Evaluation of Accuracy and Practical Applicability of Methods for Measuring Leaf Reflectance and Transmittance Spectra. *Remote Sensing*, **10**, 25.

Huang Y, Chen Y, Castro-Izaguirre N, *et al.* (2018) Supplementary Material For: Impacts of species richness on productivity in a large-scale subtropical forest experiment. *Science*, **362**, 80–83.

Jogireddy V, Cox PM, Huntingford C, Harding RJ, Mercado LM (2006) An improved description of canopy light interception for use in a GCM land-surface scheme: calibration and testing against carbon fluxes at a coniferous forest. *Hadley Centre technical note*, **63**, 1–13.

Jones HG, Archer N, Rotenberg E, Casa R (2003) Radiation measurement for plant ecophysiology. *Journal of Experimental Botany*, **54**, 879–889.

Keenan TF, Niinemets Ü (2017) Global leaf trait estimates biased due to plasticity in the shade. *Nature Plants*, **3**, 16201.

Kelty MJ (1989) Productivity of New England Hemlock/Hardwood Stands as Affected by Species Composition and Canopy Structure. *Forest Ecology and Management*, **28**, 237–257.

Kenzo T, Ichie T, Watanabe Y, Yoneda R (2006) Changes in photosynthesis and leaf characteristics with tree height in five dipterocarp species in a tropical rain forest Changes in photosynthesis and leaf characteristics with tree height in. *Tree Physiology*, **26**, 865–873.

King DA (1990) The Adaptive Significance of Tree Height. *The American Naturalist*, **135**, 809–828.

Kira T, Shinozaki K, Hozumi K (1969) Structure of forest canopies as related to their primary productivity. *Plant and Cell Physiology*, **10**, 129–142.

Kükenbrink D, Hueni A, Schneider FD, Damm A, Gastellu-Etchegorry JP, Schaepman ME, Morsdorf F (2019) Mapping the Irradiance Field of a Single Tree: Quantifying Vegetation-Induced Adjacency Effects. *IEEE Transactions on Geoscience and Remote Sensing*, pp. 1–18.

Kükenbrink D, Schneider FD, Leiterer R, Schaepman ME, Morsdorf F (2017) Quantification of hidden canopy volume of airborne laser scanning data using a voxel traversal algorithm. *Remote Sensing of Environment*, **194**, 424–436.

Law BE, Cescatti A, Baldocchi DD (2001) Leaf area distribution and radiative transfer in open-canopy forests. *Tree Physiology*, **21**, 777–788.

Li Y, Su Y, Hu T, Xu G, Guo Q (2018) Retrieving 2-D Leaf Angle Distributions for Deciduous Trees from Terrestrial Laser Scanner Data. *IEEE Transactions on Geoscience and Remote Sensing*, **56**, 4945–4955.

Liu J, Skidmore AK, Wang T, *et al.* (2019) Variation of leaf angle distribution quantified by terrestrial LiDAR in natural European beech forest. *ISPRS Journal of Photogrammetry and Remote Sensing*, **148**, 208–220.

Manfroi OJ, Kuraji K, Suzuki M, *et al.* (2006) Comparison of conventionally observed interception evaporation in a 100-m2 subplot with that estimated in a 4-ha area of the same Bornean lowland tropical forest. *Journal of Hydrology*, **329**, 329–349.

Mariscal M, Martens S, Ustin S, Chen J, Weiss S, Roberts D (2004) Light-transmission Profiles in an Old-growth Forest Canopy:Simulations of Photosynthetically Active Radiation by Using Spatially Explicit Radiative Transfer Models. *Ecosystems*, **7**, 454–467.

McElhinny C, Gibbons P, Brack C, Bauhus J (2005) Forest and woodland stand structural complexity: Its definition and measurement. *Forest Ecology and Management*, **218**, 1–24.

Medvigy D, Wofsy SC, Munger JW, Hollinger DY, Moorcroft PR (2009) Mechanistic scaling of ecosystem function and dynamics in space and time: Ecosystem Demography model version 2. *Journal of Geophysical Research: Biogeosciences*, **114**, 1–21.

Miller JR, Steven MD, Demetriades-Shah TH (1992) Reflection of layered bean leaves over different soil backgrounds: measured and simulated spectra. *International Journal of Remote Sensing*, **13**, 3273–3286.

Miyashita H, Ikemoto H, Kurano N, Adachi K, Chihara M, Miyachi S (1996) Chlorophyll d as a major pigment. *Nature*, **383**, 402.

Monsi M, Saeki T (2005) On the factor light in plant communities and its importance for matter production. 1953. *Annals of botany*, **95**, 549–67.

Moorcroft APR, Hurtt GC, Pacala SW (2001) A Method for Scaling Vegetation Dynamics : The Ecosystem Demography Model (ED). *Ecological Monographs*, **71**, 557–585.

Morin X, Fahse L, Scherer-Lorenzen M, Bugmann H (2011) Tree species richness promotes productivity in temperate forests through strong complementarity between species. *Ecology Letters*, **14**, 1211–1219.

Morsdorf F, Eck C, Zgraggen C, Imbach B, Schneider FD, Kükenbrink D (2017) UAV-based LiDAR acquisition for the derivation of high-resolution forest and ground information. *The Leading Edge*, **36**, 566–570.

Morton DC, Nagol J, Carabajal CC, *et al.* (2014) Amazon forests maintain consistent canopy structure and greenness during the dry season. *Nature*, **506**, 221–4.

Morton DC, Rubio J, Cook BD, *et al.* (2016) Amazon forest structure generates diurnal and seasonal variability in light utilization. *Biogeosciences*, **13**, 2195–2206.

Niinemets Ü (2007) Photosynthesis and resource distribution through plant canopies. *Plant, Cell & Environment*, **30**, 1052–1071.

Niinemets U (2012) Optimization of foliage photosynthetic capacity in tree canopies: towards identifying missing constraints. *Tree Physiology*, **32**, 505–509.

Niinemets Ü, Valladares F, Ceulemans R (2003) Leaf-level phenotypic variability and plasticity of invasive Rhododendron pontificum and non- .... *Plant Cell Environ*, pp. 941–956.

Raumonen P, Kaasalainen M, Åkerblom M, *et al.* (2013) Fast Automatic Precision Tree Models from Terrestrial Laser Scanner Data. *Remote Sensing*, **5**, 491–520.

Sapijanskas J, Paquette A, Potvin C, Kunert N, Loreau M (2014) Tropical tree diversity enhances light capture through crown plasticity and spatial and temporal niche differences. *Ecology*, **95**, 2479–2492.

Schmid B, Niklaus PA (2017) Complementary canopies. *Nature Ecology and Evolution*, **1**.

Schneider FD, Kükenbrink D, Schaepman ME, Schimel DS, Morsdorf F (2019) Quantifying 3D structure and occlusion in dense tropical and temperate forests using close-range LiDAR. *Agricultural and Forest Meteorology*, **268**, 249–257.

Schneider FD, Leiterer R, Morsdorf F, Gastellu-Etchegorry JP, Lauret N, Pfeifer N, Schaepman ME (2014) Simulating imaging spectrometer data: 3D forest modeling based on LiDAR and in situ data. *Remote Sensing of Environment*, **152**, 235–250.

Schneider FD, Morsdorf F, Schmid B, Petchey OL, Hueni A, Schimel DS, Schaepman ME (2017) Mapping functional diversity from remotely sensed morphological and physiological forest traits. *Nature Communications*, **8**, 1441.

Sitch S, Smith B, Prentice IC, *et al.* (2003) Evaluation of ecosystem dynamics, plant geography and terrestrial carbon cycling in the LPJ dynamic global vegetation model. *Global Change Biology*, **9**, 161–185.

Stark SC, Leitold V, Wu JL, *et al.* (2012) Amazon forest carbon dynamics predicted by profiles of canopy leaf area and light environment. *Ecology Letters*, **15**, 1406–1414.

Stuckens J, Somers B, Delalieux S, Verstraeten WW, Coppin P (2009) The impact of common assumptions on canopy radiative transfer simulations: A case study in Citrus orchards. *Journal of Quantitative Spectroscopy and Radiative Transfer*, **110**, 1–21.

Valladares F (2003) Light Heterogeneity and Plants: from Ecophysiology to Species Coexistence and Biodiversity. In: *Progress in botany* (ed. K Esser, U Lüttge WB&FH), pp. 439–471. Springer Berlin Heidelberg.

Valladares F, Laanisto L, Niinemets Ü, Zavala MA (2016) Shedding light on shade: ecological perspectives of understorey plant life. *Plant Ecology & Diversity*, **9**, 1–15.

Vicari MB, Pisek J, Disney M (2019) New estimates of leaf angle distribution from terrestrial LiDAR: Comparison with measured and modelled estimates from nine broadleaf tree species. *Agricultural and Forest Meteorology*, **264**, 322–333.

Vincent G, Antin C, Laurans M, Heurtebize J, Durrieu S, Lavalley C, Dauzat J (2017) Mapping plant area index of tropical evergreen forest by airborne laser scanning. A cross-validation study using LAI2200 optical sensor. *Remote Sensing of Environment*, **198**, 254–266.

Wacker L, Baudois O, Eichenberger-Glinz S, Schmid B (2009) Effects of plant species richness on stand structure and productivity. *Journal of Plant Ecology*, **2**, 95–106.

Walcroft AS, Brown KJ, Schuster WS, Tissue DT, Turnbull MH, Griffin KL, Whitehead D (2005) Radiative transfer and carbon assimilation in relation to canopy architecture, foliage area distribution and clumping in a mature temperate rainforest canopy in New Zealand. *Agricultural and Forest Meteorology*, **135**, 326–339.

Wang WM, Li ZL, Su HB (2007) Comparison of leaf angle distribution functions: Effects on extinction coefficient and fraction of sunlit foliage. *Agricultural and Forest Meteorology*, **143**, 106–122.

Widlowski JL, Pinty B, Clerici M, *et al.* (2011) RAMI4PILPS: An intercomparison of formulations for the partitioning of solar radiation in land surface models. *Journal of Geophysical Research: Biogeosciences*, **116**.

Williams LJ, Paquette A, Cavender-Bares J, Messier C, Reich PB (2017) Spatial complementarity in tree crowns explains overyielding in species mixtures. *Nature Ecology and Evolution*, **1**.

Zellweger F, De Frenne P, Lenoir J, Rocchini D, Coomes D (2019) Advances in Microclimate Ecology Arising from Remote Sensing. *Trends in Ecology & Evolution*, **xx**, 1–15.

Chapter

5

Mapping the Irradiance Field of a Single Tree: Quantifying Vegetation-Induced Adjacency Effects

Kükenbrink, D., Hueni, A., Schneider, F.D., Damm, A., Gastellu-Etchegorry, J.-P., Schaepman, M.E., Morsdorf, F.

This section is based on the peer-reviewed article:
Mapping the Irradiance Field of a Single Tree:
Quantifying Vegetation-Induced Adjacency Effects.
IEEE Transactions on Geoscience and Remote Sensing, 2019 (), 1-18
DOI:10.1109/TGRS.2019.2895211
and is reprinted as the final submitted manuscript.
It has been modified to fit into the layout of this thesis.

D.K., A.H., F.D.S., A.D., M.E.S., and F.M. designed the study
D.K. and A.H. performed research and all authors wrote the article
with main contribution by D.K.

Abstract

Imaging spectroscopy is frequently used to assess traits and functioning of vegetated ecosystems. Applied reflectance and radiance based approaches critically rely on accurate estimates of surface irradiance. Accurate retrievals of surface irradiance are, however, non- trivial and often error prone, thus causing inaccurate estimates of vegetation information. We analyse the irradiance field surrounding an isolated tree using the three-dimensional radiative transfer model DART in high spatial (25 cm) and spectral (1 nm, 350 - 2500 nm) resolution. We validate modeled irradiance with in situ measurements and quantify the impact of erroneous surface irradiance estimates on the retrieval of vegetation indices. We observe irradiance gradients in cast shadows of $<$ 560% in the blue spectral range, while this gradient decreases with increasing wavelength and becomes negligible in the near infrared. Further, we quantify a vegetation induced decrease in irradiance of $<$ 6% in the visible spectral region and an increase of $<$ 7% in the near infrared outside the cast shadow. Commonly employed vegetation indices are also affected by such brightening or darkening effects. Outside the cast shadow, indices sensitive to the relative content of chlorophyll and carotenoids show an overestimation of $<$ 14%. The Photochemical Reflectance Index (PRI) shows an underestimation of $<$ 5%. Our study provides first quantitative insight in high spatial and spectral resolution, on the impact of vegetation on its surrounding irradiance field. Findings highlight important implications for vegetation assessments and provide the fundamental base to advance retrievals of vegetation traits and functioning from imaging spectroscopy data.

5.1 Introduction

Imaging spectroscopy is frequently used for vegetation canopy assessments. Major focus lies on the retrieval of physiological, biochemical and structural traits and on monitoring of spatio-temporal variations in vegetation functioning, health and status (Schaepman *et al.*, 2009, 2015; Ustin *et al.*, 2009). The ever increasing spatial, temporal and spectral resolution of sensors further allow the retrieval and monitoring of increasingly complex vegetation information such as functional diversity Schneider *et al.* (2017), or signals related to plant photosynthesis (e.g. sun-induced chlorophyll fluorescence) (Damm *et al.*, 2015a). Vegetation functioning can be analyzed by either measuring subtle changes of leaf reflected radiance or emitted fluorescence radiance by exploiting narrow atmospheric absorption features. For both approaches, accurate estimates of surface irradiance are crucial to retrieve either top-of-canopy (ToC) reflectance and related vegetation information or fluorescence. However, with increasing canopy complexity such as in forest ecosystems, accurate irradiance retrieval becomes a challenge. Particularly shadowing effects substantially influence the retrieval of ToC reflectance (Damm *et al.*, 2015b). Multiple scattering within vegetation canopy can further lead to subtle changes in the irradiance field causing a brightening or darkening of the pixels' apparent reflectance (Fawcett *et al.*, 2018). In order to properly describe the complex irradiance fields in these environments, one can no longer assume uniformly flat Earth surfaces or use coarse digital elevation models (DEM) which do not resolve small scale height variabilities (Fawcett *et al.*, 2018; Richter, 1990; Richter & Müller, 2005). There are already multiple approaches published trying to minimize the impact of varying illumination effects. Asner *et al.* (2015) or Malenovský *et al.* (2013), for example, propose to only consider sunlit pixels. Adler-Golden *et al.* (2002) suggested the use of matched filtering of reflectance data to detect and correct shadows. More sophisticated approaches employ auxiliary data to approximate irradiance variation caused by small scale canopy height variations: Friman *et al.* (2011) used a digital object model derived from LiDAR data to better represent the canopy surface. However, approaches employing an elevation model to represent the canopy surface often assume the surface to be opaque, which is a simplifying assumption that is often violated, especially in forest canopies. More recent approaches try to overcome these issues by using complex three-dimensional radiative transfer models (Adeline *et al.*, 2013; Fawcett *et al.*, 2018) such as the Discrete Anisotropic Radiative Transfer Model DART (Gastellu-Etchegorry *et al.*, 2012, 2015).

Even though the problem of irradiance variabilities in surface reflectance retrievals has been discussed frequently and multiple approaches already exist trying to compensate such illumination effects, few studies actually quantified the effect of vegetation canopy on the surrounding irradiance field in a spectrally and spatially resolved manner. In fact, results of Fawcett *et al.* (2018) demonstrate that even with

best efforts (i.e. using a combination of DART RT modeling and high resolution digital object models), artifacts in retrieved ToC reflectance data are present due to the complexity of irradiance fields and multiple scattering in complex vegetation canopies. However, light scattering mechanisms of single leaves and agricultural crops have already been analysed. Huete (1987) demonstrated how multiple scattered light influences the spectral response of surrounding soils, shadows and vegetation in a crop canopy at different solar angles. Roberts *et al.* (1990); Roberts (1991) analysed adjacency effects caused by a single synthetic leaf positioned above backgrounds of different reflectance characteristics using a simplified radiative transfer model at multiple wavelengths in the visible and near infrared. In a more recent publication, Stuckens *et al.* (2009) analysed the impact of commonly used assumptions in radiative transfer models (e.g. the averaging of optical properties of randomly distributed leaves in a canopy and the representation of leaves as Lambertian scatterers) on simulated light scattering mechanisms for a citrus orchard. The work in (Stuckens *et al.*, 2009) further led to multiple studies where the impact of background soil on the retrieved spectral signature of citrus orchards was analyzed and a model for reducing such background effects was implemented (Tits *et al.*, 2013; van Beek *et al.*, 2015). Focusing more on cast shadows, Lynch (2015) analyzed and quantified the subtle changes in irradiance inside a shadow cast by an artificial object on a white surface with a commercial RGB camera, giving a more detailed insight into the completely non-binary shadow phenomenon. However, the three wavebands used in this study (red, green and blue) only cover a very small part of the electromagnetic spectrum interesting for vegetation studies. Focusing on light scattering in forest ecosystems, Hilker *et al.* (2008a,b) analyzed the effects of mutual shading of tree crowns on the prediction of photosynthetic light use efficiency in a coastal Douglas-fir forest. They mitigated the problem of modeling the translucent forest canopy by introducing a weighting, or transparency factor on the hillshade-derived shadow mask. However, also here, the variance in canopy lighting was only analyzed in a panchromatic manner, not accounting for different shadowing and brightening effects at changing wavelengths induced by neighboring trees. Takala & Mõttus (2016) analyzed the spatial variation of the canopy photochemical reflectance index (PRI) with shadow fraction caused by leaf-level irradiation conditions. Even though they were able to analyze the irradiance conditions at different wavelengths, they were not able to directly measure the irradiance at the analyzed leaves but used the irradiance conditions of neighboring roads to derive leaf-level irradiance. This is most probably highly influenced by multiple scattering and neighborhood effects, making the transfer to leaf-level irradiance difficult. In fact, the importance of diffuse sky radiation for the retrieval of canopy PRI (Damm *et al.*, 2015a) and the subsequent calculation of light use efficiency (Mõttus *et al.*, 2015) was recently documented.

In this study we model the irradiance field around a single isolated tree using the DART radiative transfer model and quantify the irradiance variability caused by the 3D object. The modeled irradiance values are validated with measured irradiance

values around the tree using field spectroradiometers. Finally, we evaluate the impact of erroneous irradiance estimates on the retrieval of reflectance and vegetation information

5.2 Study site and materials

5.2.1 Study site

For this experiment, a single isolated tree was selected located on top of a drumlin 23 km southeast of Zurich, Switzerland (47°16′31.333″N 8°48′46.870″E). The Linden tree (Tilia cordata.) is 11.8 m high with a crown diameter of 12 m. The crown base height is at 1.5 m and the tree shows an average Leaf Area Index (LAI) of 8.4 m^2 m^{-2} estimated with the approach described in Section 5.3.1a. The tree is surrounded by agriculturally used grassland that had been trimmed prior to the measurements. All measurements were performed on the 6^{th} of July 2017, just a few days after the northern hemisphere solar maximum. The sky was near-cloudless with a few temporary contrails and high cirrus clouds present and a visibility of up to 23 km.

5.3 Methods

5.3.1 DART Parameterization

The radiative transfer model used in this study to simulate the irradiance field around the tree was the Discrete Anisotropic Radiative Transfer Model DART (v5.6.0)(Gastellu-Etchegorry *et al.*, 2015). DART simulates three-dimensional heterogeneous landscapes in three operating modes: flux-tracking, LiDAR, and Monte Carlo. Generally, a DART scene is defined by a voxel grid with a predefined size (0.25 m in this study). It can simulate any scene element, including vegetation such as grass or tree crowns, with triangles. Additionally, complex three-dimensional objects represented as a triangular mesh with predefined optical properties can be imported. Here, vegetation is simulated as turbid medium, where each voxel can be parameterized by volume density, leaf angular distribution, and optical properties. A DART voxel can include vegetation turbid media as well as triangles with an arbitrary size, independent of the voxel size. In ray tracing, two types of radiation interactions are simulated: volume interaction within turbid voxels (Gastellu-Etchegorry *et al.*, 2004), and surface interaction on triangles (Gastellu-Etchegorry, 2008). Further details on the DART model can be found in (Gastellu-Etchegorry *et al.*, 2012, 2015).

In this study, the flux tracking mode was used with sun and atmosphere as the only radiation sources. The approach to parameterize the DART model is closely following the one described in Schneider *et al.* (2014), where at-sensor radiances

for airborne imaging spectrometer data were simulated and compared to actual measurements of the Airborne Prism Experiment (APEX) Sensor (Schaepman *et al.*, 2015). Optical properties of the tree crown and the surrounding surfaces were defined based on measurements described in Section 5.3.1c. The geometry of the tree crown as well as the vegetation density for each voxel was defined as described in Section 5.3.1a. The leaf angle distribution was defined as spherical, based on leaf angle measurements conducted on a tilia cordata in Kew Gardens, London by Jan Pisek from the Tartu Observatory, Estonia (unpublished data). Additionally, the stem was parameterized following the approach described in Section 5.3.1b. The optical property of the stem was defined according to the default bark optical property found in the DART optical properties database. The topography of the surface was extracted from drone images as described in Section 5.3.1d. To simulate the atmosphere, DART can be used with standard gas and aerosol models as contained in the MODTRAN model (Berk *et al.*, 1987). We used the mid-latitude summer gas model and the rural aerosol model with a visibility of 23 km. For each measured irradiance transect (see Section 5.3.2) a new DART simulation with modified solar angles (solar azimuth and elevation angle) according to the observed solar angles at the beginning of each transect were simulated. A total of 1873 wavelengths with 1 nm spectral resolution were simulated for each transect covering the spectral range of 350 - 2500 nm. Wavelengths associated with very low signal to noise ratios due to absorption bands have been excluded. The output of the DART model is a three-dimensional radiative budget with the amount of energy (in W m^{-2} nm^{-1}) irradiant, absorbed and scattered at each voxel. The radiative budget can be further decomposed into direct, diffuse and coupled irradiance (irradiance after coupling with the atmosphere). In this study, we distinguish between bottom of atmosphere (BoA) and top of canopy (ToC) irradiance. BoA irradiance is defined as the irradiance of a homogeneously illuminated flat surface uninfluenced by geometric scattering effects caused by surrounding 3D objects (e.g. shadowing effects, reduction of sky view factor etc.). ToC irradiance is the actual surface irradiance at each location including the geometric scattering effects. When calculating reflectance factors we distinguish between apparent ToC reflectance based on the BoA irradiance and true ToC reflectance based on the actual ToC irradiance.

5.3.1a Vegetation density estimation

Vegetation density for each turbid medium voxel was estimated using terrestrial laser scanning (TLS) measurements acquired on the same day as the irradiance measurements. The TLS instrument was operated at a wavelength of 1550 nm and a pulse repetition frequency of 150 kHz and a maximum range of 950 m (Riegl VZ-1000, Riegl, Austria). A detailed description of the TLS data acquisition is given in Table 5.1. A scan pattern of 0.02° spacing between pulses and a field of view of 100° by 90° in vertical and horizontal directions was used. A total of four scans approximately 20 - 30 m away from the tree trunk were acquired. The chosen scan

Tab. 5.1: TLS data acquisition specifications.

TLS Parameter	TLS specifications
Acquisition dates	6th of July 2017
TLS Sensor	Riegl VZ-1000
Laser wavelength [nm]	1550 nm
Beam divergence [mrad]	0.3
Beam width when leaving instrument [mm]	7
Laser pulse repetition rate PRR [kHz]	150
Max. measurement range [m]	950 m
Angular resolution [deg]	0.02
Accuracy [mm]	8
Precision [mm]	5

pattern minimized occlusion effects and enabled a detailed representation of the tree (Abegg *et al.*, 2017; Kükenbrink *et al.*, 2017). Cylindrical reflective targets were placed on and around the tree as tie-points for the subsequent scan position co-registration. The co-registration as well as the filtering of the point cloud was performed in Riegl's RiscanPro Software package (RiscanPro v2.0.2 r7440, Riegl, Austria). The TLS point cloud was further visually co-registered to the drone point cloud (see Section 5.3.1d).

The vegetation density values per voxel were estimated using the AMAPvox Software package (version 1.0.1 r3410ffbe) developed by "botAnique Modélisation de l'Architecture des Plantes et des végétations" AMAP (Vincent *et al.*, 2017). The AMAPvox model is tracing all laser pulses through a predefined voxel grid and calculates for each voxel the local transmittance computed from the ratio between exiting and entering energy normalized by the mean optical path length (Vincent *et al.*, 2017). As the model cannot distinguish between leaf and woody material, the output of each voxel is therefore defined as the Plant Area Density (PAD) per voxel.

5.3.1b Stem Model Extraction

While the turbid medium assumption of DART is valid for the tree crown, it does not hold for the tree trunk. We therefore excluded voxels of the tree trunk from the estimated vegetation density grid and modeled the tree trunk based on the TLS point cloud. We therefore extracted all laser returns reflected from the tree trunk including the first major branches of the tree and fitted a mesh around it using a screened poisson reconstruction (Kazhdan & Hoppe, 2013) implemented in the open-source 3D mesh processing software MeshLab (Version 2016.12)(Cignoni *et al.*, 2008). The extracted stem object can be imported into DART as a wavefront object file and is then treated as an opaque lambertian object that is not penetrable by solar radiation.

5.3.1c Optical Properties Measurements

Leaf optical properties (LOPs) were acquired using one of the field spectroradiometers described in Section 5.3.2, but with an added leaf-clip. The fore-optic allows us to calculate leaf reflectance and transmittance by using a white and a black reference panel with known reflectance and following the procedure described in Miller *et al.*

(1992):

$$\rho_t = \frac{\rho^*_{t,low} \times \rho_{B,high} - \rho^*_{t,high} \times \rho_{B,low}}{\rho_{B,high} - \rho_{B,low}} \tag{5.1}$$

$$\tau^2 = \frac{[\rho_{t,high} - \rho_t] \times [1 - \rho_t \times \rho_{B,high}]}{\rho_{B,high}} \tag{5.2}$$

where ρ_t and τ are the extracted reflectance and transmittance of the leaf, whereas $\rho^*_{t,low}$ and $\rho^*_{t,high}$ are the measured reflectance of the leaf with the white and the black reference panel as background respectively and $\rho_{B,high}$, $\rho_{B,low}$ are the measured relectance of the white and black reference panel without the leaf. The instrument was set to reflectance mode to acquire the LOPs. A total of 20 randomly selected leaves were sampled, 10 from the lower crown part and 10 from higher up the crown. For the DART parameterization, the crown was divided into an upper and lower half (height threshold set to half of TLS measured crown length) and the average LOP retrieved from the respective halves were assigned.

Radiance measurements from the ground surrounding the tree were also acquired with one of the field spectroradiometers without the use of a fore-optic. Four ground measurements were acquired located to the North-West, South-West, South-East, and North-East by averaging the measured radiance of a 1 m^2 patch. Reflectance values for these ground measurements were calculated by taking white reference measurements from spectralon panels before and after the ground measurements of each location.

5.3.1d Terrain extraction

The aerial ortho-mosaic of the study site was generated using a commercial DJI Inspire 1 drone with the X5 gimbal. A total of 98 images were acquired with an average flying altitude of 45.2 m above ground and with an along track overlap of 90%, while across track overlap was 85%. The matching of the geotagged images was done with AGISOFT Photoscan professional, resulting in a ground pixel resolution of 1.58 cm and a point density of 250 points/m^2. The re-projection error (relative error) was estimated to be 1.51 pixel, while the absolute error of the whole ortho-mosaic was estimated to be 0.84 m.

5.3.2 Irradiance Measurements

Irradiance measurements were performed with two ASD FieldSpec Pro spectro-radiometers (Analytical Spectral Devices, FieldSpec Pro) measuring the reflected radiance from a white reference spectralon, with nearly 100% lambertian scattering characteristics (Jackson *et al.*, 1992). One spectroradiometer was positioned on a sunlit patch over 30 m away from the tree to assure no influence of the tree on the measured irradiance. The spectralon was mounted on a tripod roughly one meter above ground and was leveled to be horizontal. The bare fibre optics (no for-optics

(a)

(b)

Fig. 5.1: Field spectroradiometer setup for irradiance measurements. Fig. 5.1a shows both instruments, one mounted on a combined sled/gimbal system and the reference system on a tripod and Fig. 5.1b shows a close-up onto the gimbal mount for the spectralon panel.

were used) with a field of view of 25° was positioned nadir looking, roughly 12 cm above the spectralon. This results in a footprint of 2.8 cm in radius. The second spectroradiometer was mounted onto a sled with the spectralon mounted on a passive gimbal with the fibre optics again positioned nadir looking, roughly 12 cm above the spectralon. With this setup, the spectralon itself was located 70 cm above the ground. The instrument setup can be seen in Fig. 5.1. Before and after the experiment, the two instruments were cross-calibrated by placing the sled mounted instrument next to the reference instrument and measuring the incoming irradiance with the two instruments at the same time for one minute.

The reference instrument on the sunlit patch ran throughout the whole experiment and acquired irradiance readings every five seconds. Several transects were acquired within the tree shadow with the spectroradiometer mounted on the sled, including the transition zone into the sunlit area. The transects were spaced 1 m apart from each other. Along the transects, five irradiance readings were acquired in short succession every 1 m, once the gimbal was stable. In total, 13 transects in south-north direction were acquired to measure the irradiance inside and in the transition zone of the tree's cast shadow. Additionally to the shadow transects, seven radial transects along the major cardinal directions (NE, E, SE, S, SW, W, NW) were acquired with a spacing

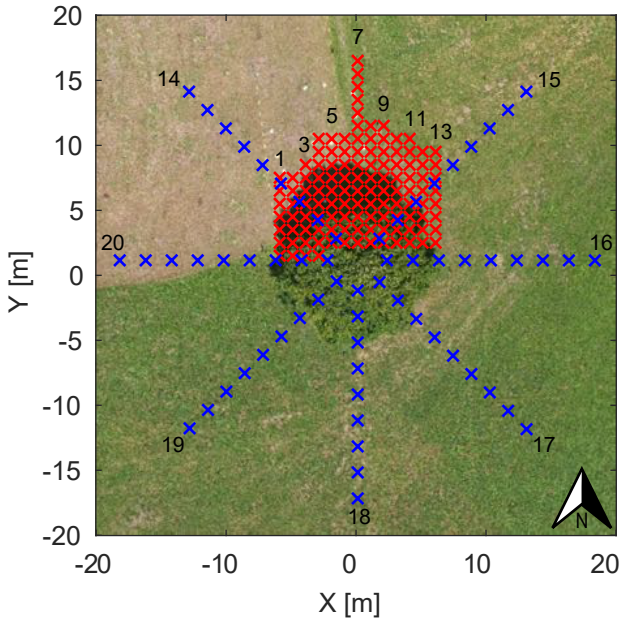

Fig. 5.2: Irradiance measurement pattern. Red: shadow transects (spacing: 1 m in x and y), blue: radial transects along major cardinal directions (spacing: 2 m). Reference irradiance measurement location outside shown image at local coordinate X=-24, Y=17. Odd numbered shadow and all radial transects are labeled for referencing purposes. Background image acquired from drone data

of the individual irradiance readings of 2 m. A detailed map of the measurement pattern with all measurement positions is shown in Fig. 5.2. The acquisition of all transects took 2 hours (11:16 until 13:06 UTC).

All field spectroradiometer data were stored in the spectral information system SPECCHIO to enable streamlined post-processing and ensure long-term data availability (Hueni *et al.*, 2009). ASD spectroradiometers exhibit radiometric discontinuities at the joints between the three separate detectors used in the full-range instruments (Hemmer *et al.*, 2000). Environmental temperatures drive the magnitude of these radiometric steps and affect the whole spectral range to a higher or lower degree (Hueni & Bialek, 2017). Such discontinuities were corrected at radiance level by applying a dedicated correction model to all spectra stored in SPECCHIO (Hueni & Bialek, 2017). Ground reflectance factors were calculated in SPECCHIO using linear irradiance estimations (Hueni *et al.*, 2017).

In order to make the sunlit reference measurements and the transect measurements comparable, the transect measurements were first calibrated to the reference instrument by using the cross-calibration measurements from the beginning and the end of the experiment. A cross-calibration factor for each transect measurement was acquired by linearly interpolating between the two cross-calibration measurements. The five irradiance readings per target location were averaged to receive the final irradiance value for each measurement location. In order to decouple the irradiance changes caused by the tree from possible irradiance variabilities caused by subtle changes in atmosphere conditions or solar angle, target irradiance measurements

were normalized using the reference irradiance measurements according to equation 5.3.

$$\bar{E}_{target} = \frac{E_{target}}{E_{ref}} \times 100 \tag{5.3}$$

where $\bar{E}_{target}$ is the normalized target irradiance, E_{target} is the cross-calibrated target irradiance and E_{ref} is the reference irradiance measured at the sunlit reference location at the time of the acquisition of E_{target}.

5.3.3 DART simulation validation

For each measured transect one DART simulation was performed to ensure the same solar angles within the simulation and the measurements. To compare DART simulation outputs with the measurements, a 2D irradiance map was generated from the 3D total irradiance grid. As we measured the irradiance on a spectralon panel at 70 cm above ground, we extracted the irradiance value at this height above ground from the voxel grid. The starting position of each shadow transect relative to the northernmost point of the tree trunk has been measured in the field and can therefore be matched to a location on the DART irradiance output. The starting point of the radial transects was chosen to be 2 m away from the closest point of the tree trunk. All subsequent measurements were 1 m apart for the shadow transects or 2 m apart for the radial transects. In that way, we were able to locate the measurement location on the extracted irradiance map. However, as some geolocational errors can be expected with these relative locational measurements, the average irradiance as well as the standard deviation of a 3x3 pixel window (75x75 cm) around the identified measurement location was extracted from the DART irradiance map.

5.3.4 Impact on Vegetation Indices

The impact of irradiance effects on the retrieval of commonly employed vegetation indices was evaluated by comparing vegetation indices retrieved assuming a flat, homogeneously illuminated surface (apparent ToC reflectance) with indices retrieved from true ToC reflectance values. DART outputs apparent ToC reflectances by default. True ToC reflectance values were derived by dividing the apparent ToC radiance simulated by DART with the ToC irradiance values derived from the DART 3D radiative budget. This represents a perfect atmospheric correction where all illumination effects are accounted for, whereas the apparent ToC reflectance image represents the typical reflectance image uncorrected for illumination effects caused by surrounding objects. In order to decouple changes in the modeled reflectance and vegetation indices products due to varying irradiance from changes due to different ground materials, we parameterized the surface to be completely covered by grass with a single reflectance spectrum measured on the South-Eastern side of the tree.

Vegetation indices are an empirical approach to relate light measurements to vegetation information. However, wrong estimates of surface irradiance pose an additional sensitivity to these indices and complicate their interpretation, even if properly calibrated for a specific site, vegetation type and phenological period (Damm *et al.*, 2015b). The choice in vegetation indices was based on those incorporating spectral information in the VIS/NIR wavelength regions since they are strongly affected by illumination effects and are of high importance in the functioning of vegetation. The chosen indices include the photochemical reflectance index (PRI) indicative for the de-epoxidation state of xanthophylls and often applied as a proxy for light use efficiency (LUE) (Gamon *et al.*, 1992, 1997, 2015) (Eq. 5.4). Additionally, we applied two indices sensitive to the relative content of chlorophyll and carotenoids as proposed by Gitelson *et al.* (2006) (Eqs (5.5) and (5.6)):

$$PRI = \frac{r_{531} - r_{570}}{r_{531} + r_{570}} \tag{5.4}$$

$$CHL \propto [r_{540-560}^{-1} - r_{790}^{-1}] \times r_{790} \tag{5.5}$$

$$CAR \propto [r_{510-520}^{-1} - r_{560-570}^{-1}] \times r_{790} \tag{5.6}$$

where r_x denotes the reflectance at the specified wavelength x in nanometers. The subscripts in Eqs. 5.5 and 5.6 indicate wavelength ranges used for the calculation of both indices. The wavelength subscripts $r_{x_1-x_2}$ denotes the average reflectance between x_1 and x_2 nm.

5.4 Results

5.4.1 Modeled Irradiance

A total of 3560 DART simulations (20 solar positions corresponding to the transect acquisition times at 178 wavelengths with band width of 1nm) were evaluated to analyze the influence of the isolated tree on the surrounding irradiance pattern. An additional 1873 simulations were analyzed for the main South-North shadow transect (transect #7) for a spectrally higher resolved irradiance spectrum to be compared to the spectroradiometer measured irradiance. All simulations were performed on the cloud computing infrastructure ScienceCloud (S3IT) provided by the University of Zurich.

Fig. 5.3 shows the ToC irradiance changes relative to the BoA irradiance for 540 nm and 800 nm. Blue colors denote a decrease and red colors denote an increase in irradiance due to the presence of the tree. From Fig. 5.3 we can clearly distinguish an influence of the tree onto the surrounding irradiance field, also outside of the apparent cast shadow. At 540 nm, the irradiance north of the tree a few meters (1-2 m) outside of the cast shadow is still 4-6% decreased relative to the BoA irradiance.

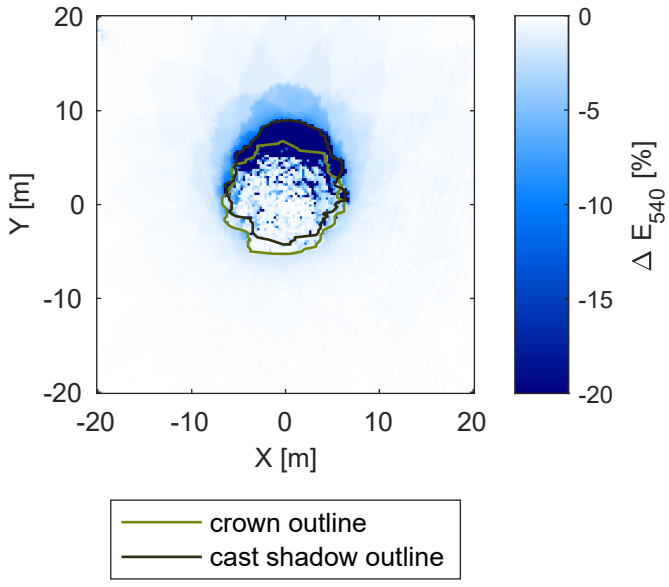

(a)

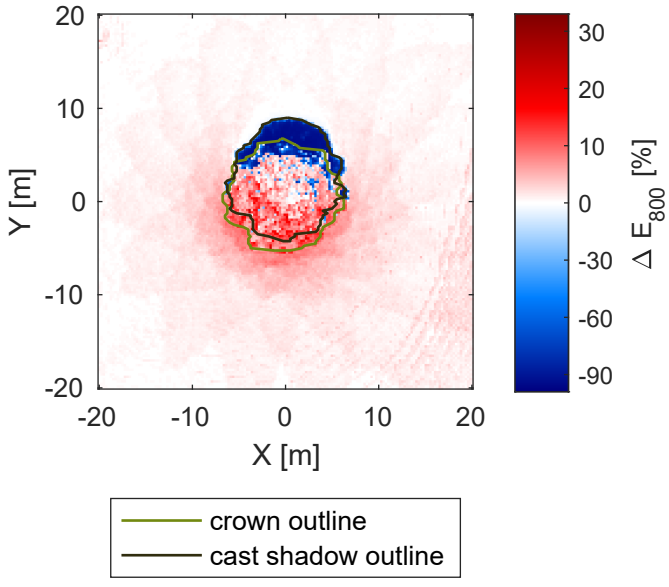

(b)

Fig. 5.3: ToC surface irradiance changes as modeled by DART at (5.3a) 540nm and (5.3b) 800nm. Relative changes compared to modeled BoA irradiance are shown. Red colors denote an increase in irradiance due to the tree's presence, blue colors denote a decrease in irradiance due to the tree's presence. The tree crown outline and the cast shadow outline are marked with green and black lines respectively.

To the south of the tree, barely any influence of the tree on the surface irradiance is distinguishable at 540 nm. On the other hand, at 800 nm the tree shows its biggest influence to the south of the tree, where the surface irradiance is increased by 6 to 7% even two meters away from the outer rim of the tree crown. The influence of the tree decreases with increasing distance, reaching less than 1% of irradiance increase at roughly 12 m away from the outer rim of the tree crown. The increase in irradiance is also visible on the southern side of the tree crown itself. The slight

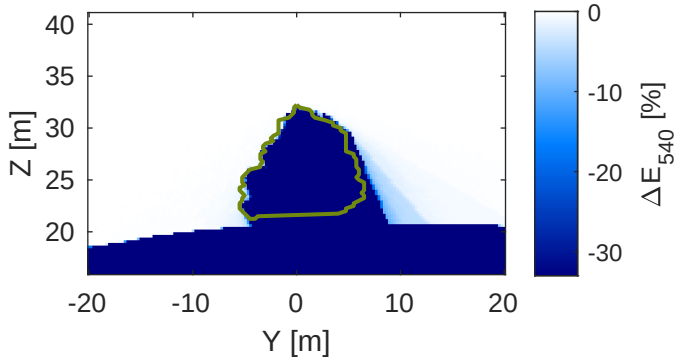

(a)

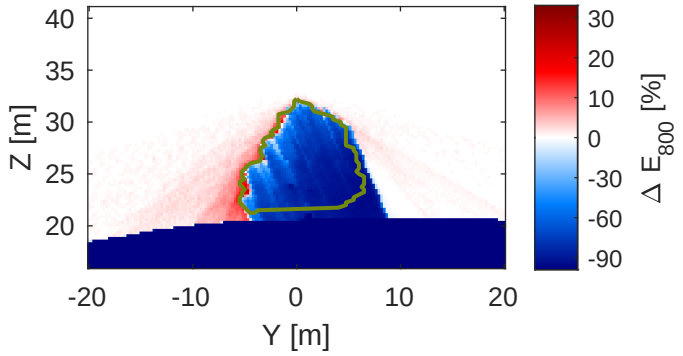

(b)

Fig. 5.4: Vertical DART profile of the modeled radiative budget in South - North direction. South is to the left of the figure. The crown outline is shown with a green line. Relative changes compared to the BoA irradiance are plotted as differences of ΔE. Red colors denote an increase in irradiance due to the tree's presence, blue colors denote a decrease in irradiance due to the tree's presence. (5.4a) shows the vertical profile at 540nm, (5.4b) at 800nm.

increase in irradiance at 800 nm in the South-Eastern corner of the image is not due to the tree but caused by the increasing slope of the terrain and the discrete voxel representation of the three-dimensional scene inside DART, where vertical voxel faces can illuminate or shadow lower neighboring voxels.

In Fig. 5.4, a vertical profile through the middle of the tree in the South-North direction is shown. This shows the brightening or darkening effect caused by the tree also in the third dimension and highlights the possibility to analyze vertical light availability and extinction profiles using DART.

5.4.2 Measured Irradiance

Fig. 5.5 shows the mean irradiance spectrum measured at the reference instrument over the whole measurement period as well as the irradiance time series for two wavelengths (540 nm and 800 nm). Except for a few local minima in irradiance most probably caused by high cirrus clouds blocking the direct solar path, the sunlit irradiance stayed relatively stable and shows a steady decrease after solar noon at 11:31 (UTC). Due to an instrument malfunction between 12:26 and 13:05 no

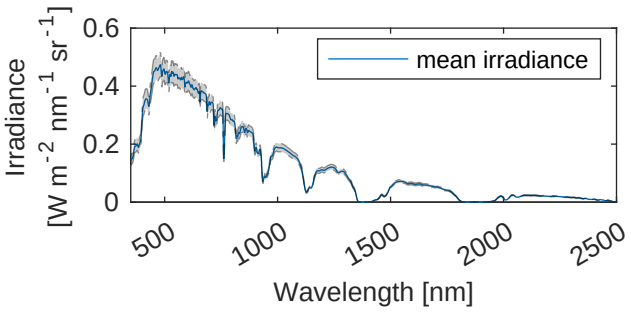

(a)

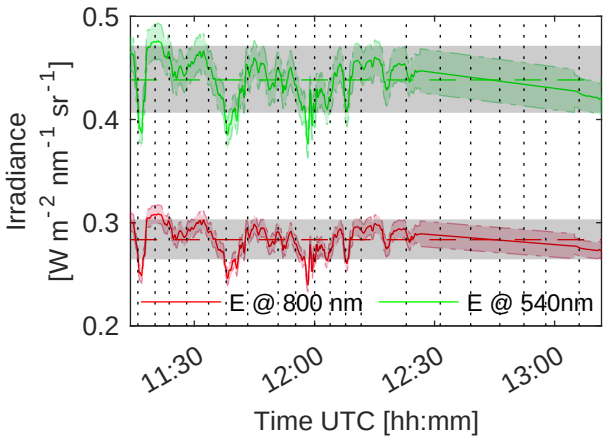

(b)

Fig. 5.5: Sunlit reference irradiance measurements. (5.5a) shows the mean irradiance spectrum measured with the reference instrument. The gray area denotes the standard deviation over the whole measurement period plus the uncertainty associated with the irradiance measurements. (5.5b) shows the reference irradiance time series over the whole measurement period at 540nm (green) and 800 nm(red). The green and red transparent area denotes the uncertainty associated with the irradiance measurement. The mean irradiance for the respective wavelength is shown with a dashed line. The gray boxes denote the measurement uncertainty and the +/- standard deviation over the whole measurement period for the respective wavelength. The gray dotted vertical lines denote the start time of a new transect. For transects 15 to 19, reference irradiance values have been interpolated due to an instrument malfunction. The uncertainty introduced due to the interpolation of the data gap was estimated based on the irradiance variability 15 minutes before and after the gap and added to the total uncertainty associated with the irradiance measurements for the interpolated irradiance values.

reference irradiance measurements have been acquired and the data gap was filled using linear interpolation. A total of five transects are affected by this measurement gap (radial transects 15 to 19). However, the error introduced due to the missing reference irradiance is assumed to be small (i.e. +/-3.26% in the VIS, +/-3.5% in the NIR, and +/-6% in the SWIR region, based on the standard deviation of the measured reference irradiance 15 minutes before and after the measurement gap). Furthermore, a large decrease or increase in solar irradiance would be visible in the transect measurements allowing for an identification of the discrepancy between interpolated reference irradiance and actual irradiance. The main analysis performed in this study is focused on the shadow transects (transect numbers 1 to 13) for which the reference irradiance time series is complete. The only exceptions are transects

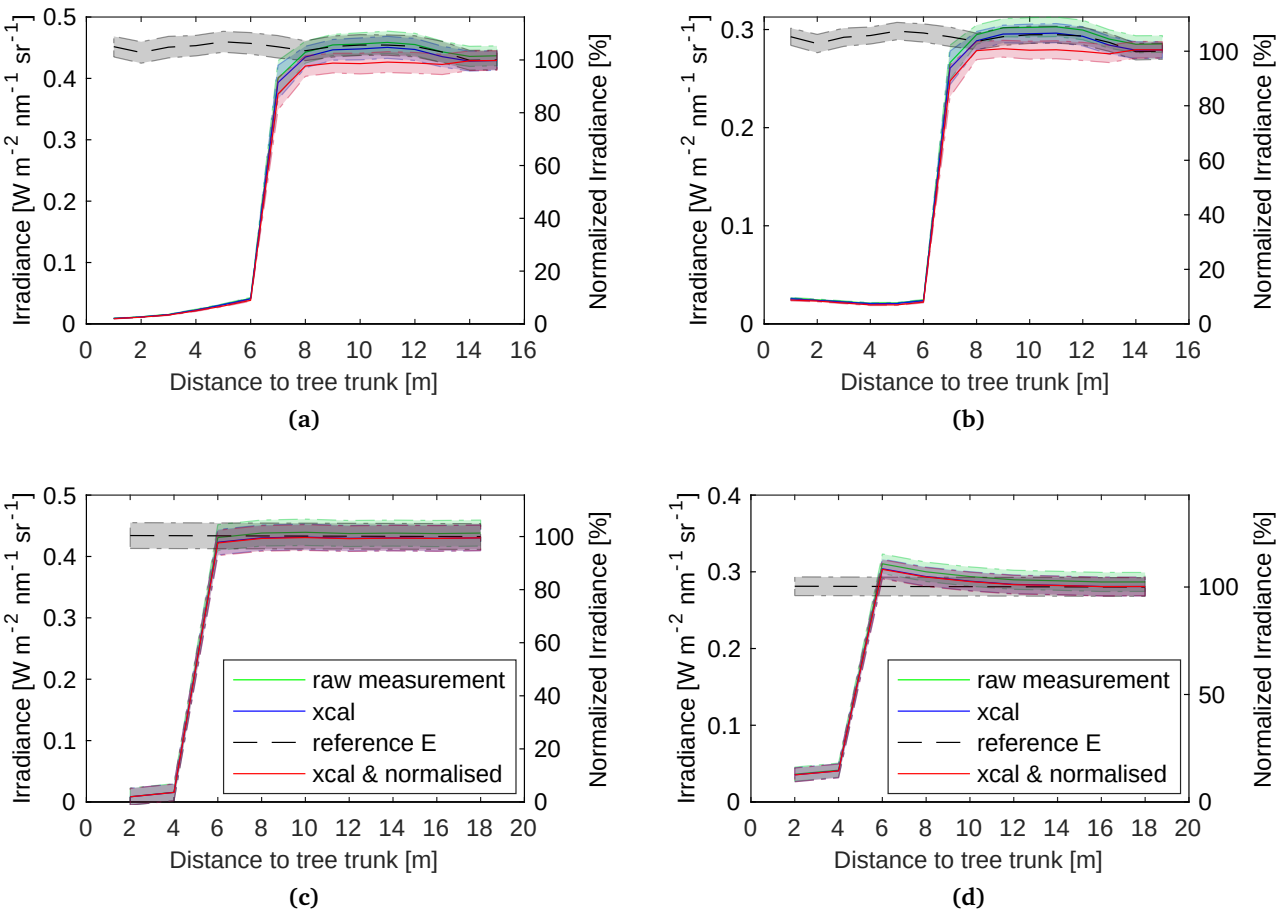

Fig. 5.6: Measured irradiance for transect #7 and #18 at 540nm (5.6a and 5.6c) and at 800nm (5.6b and 5.6d). Measured raw irradiance in green, measurements cross-calibrated with reference instrument in blue and cross-calibrated plus normalized measurements in red. Normalization has been performed according to the irradiance at the reference instrument during the target acquisition. The irradiance at the reference instrument is shown using a dashed black line (reference E). Shaded area in respective colors denote the uncertainty associated with the irradiance measurement plus the standard deviation of the five irradiance readings per target. Note that the reference irradiance values for transect 18 (Figures 5.6c and 5.6d) have been interpolated.

18 (North - South transect) and 19 (North-East - South-West transect) showing the irradiance fields on the southern side of the tree. A linear interpolation of the data gap is a simplifying solution for this problem. A better model to describe the irradiance change over the course of a day would include Lambert's cosine law and reflect the change in airmasses also leading to a non-linear decrease in transmittance of the atmosphere. However, given the date, time of day, length of the experiment as well as the latitude, the error introduced by using a simple linear interpolation is assumed to be minor.

Fig. 5.6 shows the irradiance of transect numbers 7 and 18 (South-North transect in the middle of the tree and North-South transect on the Southern side of the tree) at 540 nm and 800 nm. Fig. 5.6 clearly shows the wavelength dependent behavior of the irradiance with increasing distance from the tree. The first few measurements were located inside the cast shadow of the tree, followed by a small transition

zone and a longer sunlit area. The irradiance at 540 nm increases inside the cast shadow caused by the gain in sky view factor with increasing distance from the tree. The visible range of the spectrum and especially the blue spectral range is highly influenced by atmospheric scattering. A reduced sky view factor therefore further decreases the diffuse atmospheric irradiance component on the ground, which is still observable outside of the apparent cast shadow. As wavelengths in the near-infrared region are less affected by atmospheric scattering, this effect is not visible in the cast shadow at 800 nm. On the southern side of the tree a different effect is visible, where the irradiance at the border to the cast shadow spikes at 800 nm and then decreases again with increasing distance from the tree. This can be explained by an additional diffuse irradiance component caused by the high backwards scattering characteristics of vegetation in the near-infrared region. This irradiance increase in close vicinity of the tree can be observed in all transects facing towards the sun. This effect is not apparent in the visible domain as shown in Fig. 5.6c.

5.4.3 DART simulation validation

Figures 5.7 and 5.8 show the comparison between simulated and measured irradiance averaged over all sunlit and shadowed targets for transect #7 both in absolute and normalized numbers. Normalization in Fig. 5.8 is based on the measured reference irradiance at the time. DART generally overestimates the surface irradiance compared to the measured irradiance. In the visible spectral range (350 - 700 nm) the overestimation is at 12% on average and 9.3% in the near infrared (701 - 1000 nm) for sunlit targets. In the short-wave infrared (1001 - 2500 nm) the average overestimation is at 10.9% (wavelength inside absorption features highlighted in gray and green in Fig. 5.7 and Fig. 5.8 were excluded from these statistics). For the shadowed targets DART overestimates the surface irradiance by 37.4% in the visible range. For the NIR and SWIR region, DART underestimates the surface irradiance in average by 1.5 and 16.5%. However, due to the large variability in irradiance in the shadowed areas, the simulated and measured irradiance values lie within their respective uncertainty bounds (standard deviation of all shadowed and sunlit targets of transect #7 for modeled irradiance, uncertainty plus standard deviation of all shadowed and sunlit targets of transect #7 for measured irradiance).

The overall good fit between DART simulated and spectroradiometer measured irradiance patterns with an R^2 of 0.997 can also be seen in Fig. 5.9, where the absolute measured and modeled surface irradiance are plotted against each other. The 1:1 line shown in Fig. 5.9 also highlights the slight overestimation of DART modeled irradiance.

When analyzing single transects at selected wavelengths, we observe a strong agreement in ToC irradiance patterns between measured and modeled ToC irradiance. Fig. 5.10 shows that the stated darkening effect of the tree on the northern side in the blue spectral range as well as the brightening effect of the tree especially on the

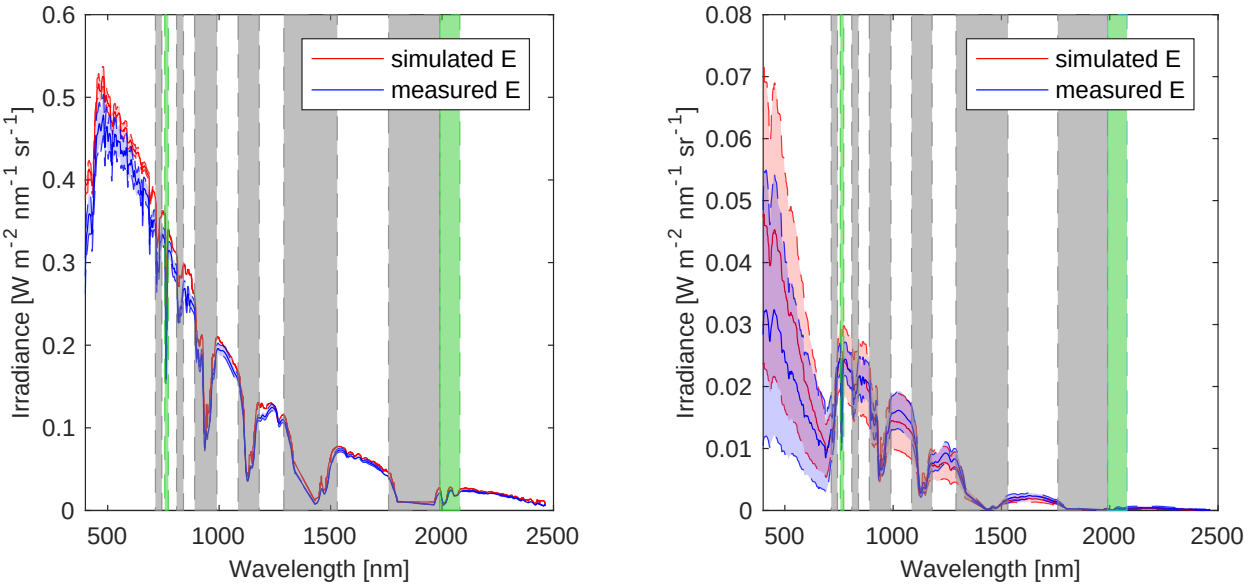

Fig. 5.7: Average irradiance spectra for sunlit (5.7a) and shadowed (5.7b) targets of transect #7. Simulated irradiance in red and measured irradiance in blue. Standard deviation over all sunlit and shadowed modeled irradiance in transparent red areas. Standard deviation over all sunlit and shadowed measured irradiance plus uncertainty associated with the spectrometer irradiance measurements in transparent blue areas. Absorption bands due to water vapor or atmospheric gases are highlighted in gray or green columns respectively.

southern side in the near infrared region are both observable in the measured as well as the modeled surface irradiance pattern.

5.4.4 Impact on Vegetation Indices

The results shown above illustrate the impact of vegetation on the surrounding irradiance field. Related uncertainties will translate to the calculation of higher level remote sensing products such as vegetation indices or vegetation biochemical properties and compromise their reliability. Selected vegetation indices (i.e. PRI, CHL, CAR) were derived using true and apparent ToC reflectance values to quantify the impact of illumination effects on retrieved vegetation information. In Fig. 5.11 the difference between PRI, CHL, and CAR derived from apparent and true ToC reflectance values is shown relative to the value range observed for the respective vegetation products derived from the measured leaf and ground optical properties (see Section 5.3.1c). Red colors therefore denote an increase of the respective vegetation index value when the presence of the tree is not considered in the calculation of ToC reflectance. On the other hand, blue colors denote a decrease of the respective vegetation index values when the processing neglects the presence of the tree. These changes can be observed outside (i.e. up to 10 m distance) the apparent cast shadow. CHL and CAR show an overestimation of up to 10-14% (relative to the observed value range of the respective vegetation product derived from the leaf and ground optical properties measurements) close to the edge of the tree and the cast shadow if only apparent

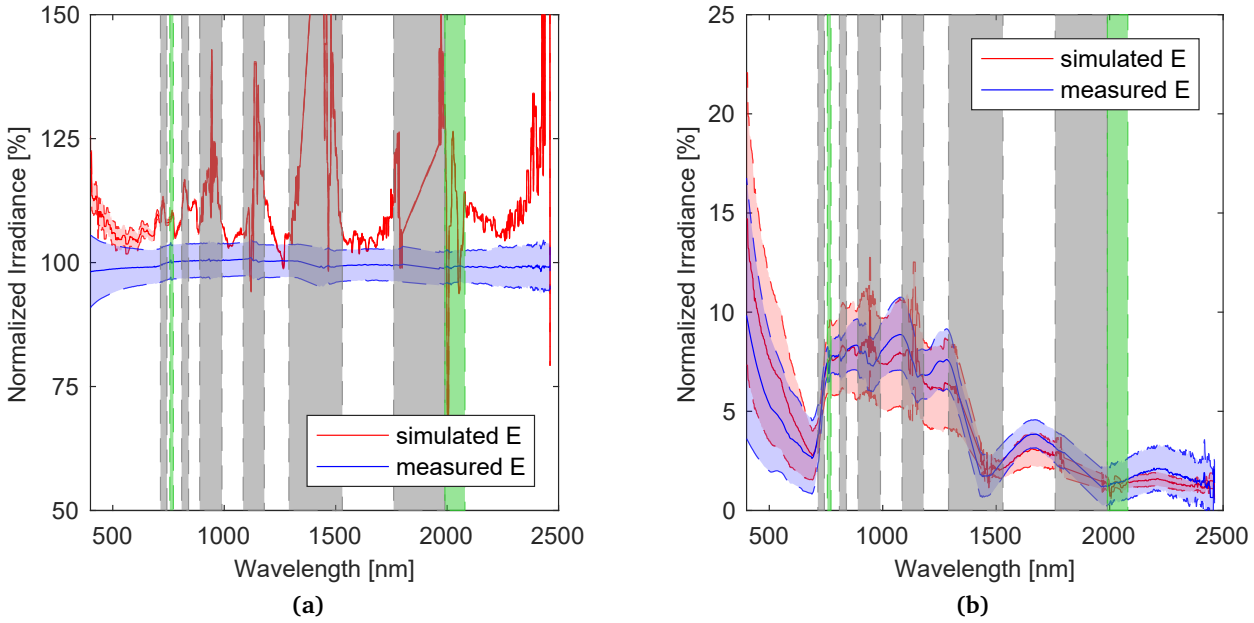

Fig. 5.8: Average normalized irradiance spectra for sunlit (5.8a) and shadowed (5.8b) targets in transect #7. Simulated irradiance in red and measured irradiance in blue. Standard deviation over all sunlit and shadowed modeled irradiance in transparent red areas. Standard deviation over all sunlit and shadowed measured irradiance plus uncertainty associated with the spectroradiometer irradiance measurements in transparent blue areas. Normalization based on the irradiance values measured at the reference instrument location. Absorption bands due to water vapor or atmospheric gases are highlighted in gray or green columns respectively.

ToC reflectance values are used to derive these vegetation products. At 4 m distance from outer rim of the tree crown and cast shadow, the overestimation is still up to 6%. As both CHL and CAR rely on reflectance values in the NIR spectral domain, they also show a slightly larger impact on the southern side of the tree due to the pronounced backscattering characteristic of the tree in the NIR region. By relying on reflectance values in the green spectral range, PRI shows a contrary behavior, where a larger influence on the northern side of the tree is discernible. Due to the employed wavelength for the calculation of the PRI, the general difference between the PRI derived from true and apparent ToC reflectance is contrary to the other vegetation indices. PRI inside the cast shadow is overestimated by up to 90% of the observed PRI range derived from the leaf and ground optical properties measurements when using apparent ToC reflectance to calculate PRI. PRI outside the cast shadow is slightly underestimated by up to 5% when using apparent ToC reflectance. The PRI outside the cast shadow is therefore much less affected by the presence of the tree than the other discussed vegetation indices. However, due to the very narrow wavelength region used to calculate the index (531 nm and 570 nm) and the thus inherent narrow value range of the PRI close to 0, the stated relative values have to be taken with caution.

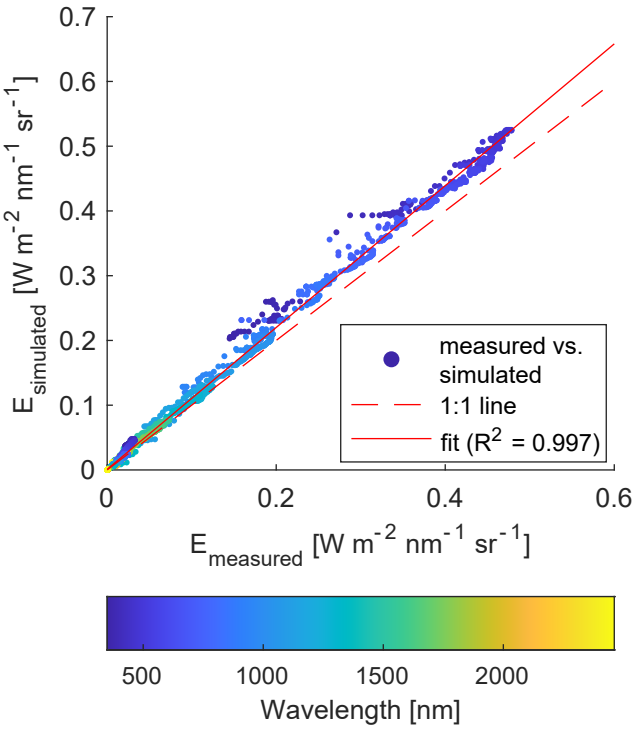

Fig. 5.9: Measured vs. simulated irradiance scatterplot for transect #7.

5.5 Discussion

5.5.1 Modeled Irradiance

Due to the numerous parameters used by DART to simulate the experimental site and the atmosphere, several sources of uncertainty for the modeled irradiance values can be identified, e.g. vegetation density per voxel (i.e. plant area density PAD), provided leaf optical properties (LOP), or the leaf angle distribution. The AMAPvox software used to estimate PAD per voxel from TLS acquisitions tends to overestimate Plant Area Index (PAI) values obtained from vertical integration of PAD profiles as compared to PAI estimates derived from average gap fractions using LAI2200 measurements in a tropical forest (Vincent *et al.*, 2017). Observed differences, however, reflect the fact that distribution of foliage is strongly spatially structured which is not properly accounted for in PAI estimates derived from mean gap fraction per elevation angle as performed with the LAI2200 instrument (Vincent *et al.*, 2017). However, TLS derived PAD and PAI estimates using similar approaches as the one in AMAPvox showed good results (e.g. estimated leaf area lay within 14% from the reference measurement acquired by leaf harvesting for a savanna environment as reported in Béland *et al.* (2011)) rendering this approach superior to previously established methods using optical measurements often not able to vertically resolve the PAD distribution in the canopy (e.g. Béland *et al.*, 2011, 2014a,b; Grau *et al.*, 2017).

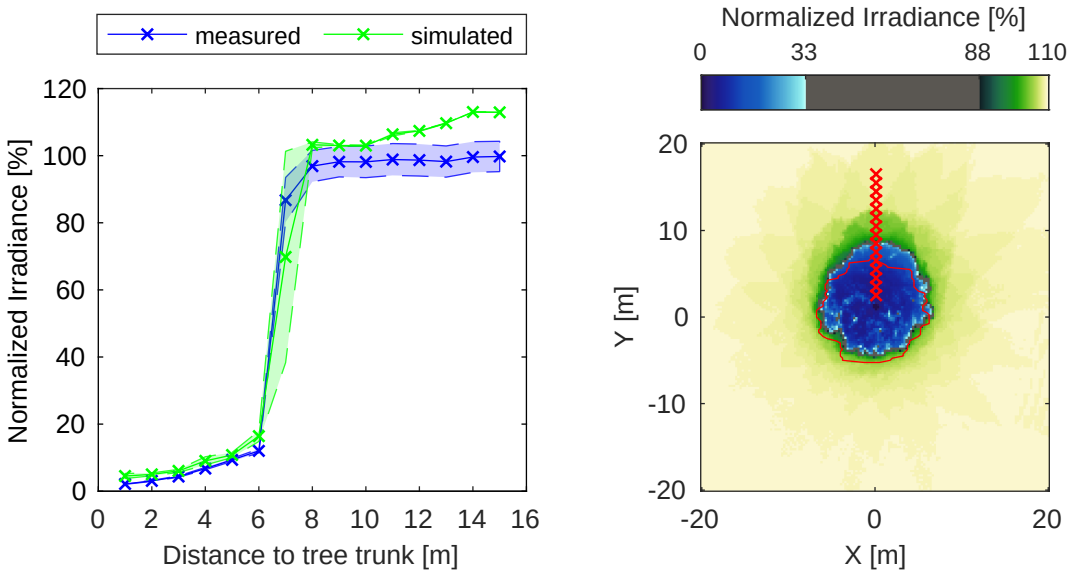

(a)

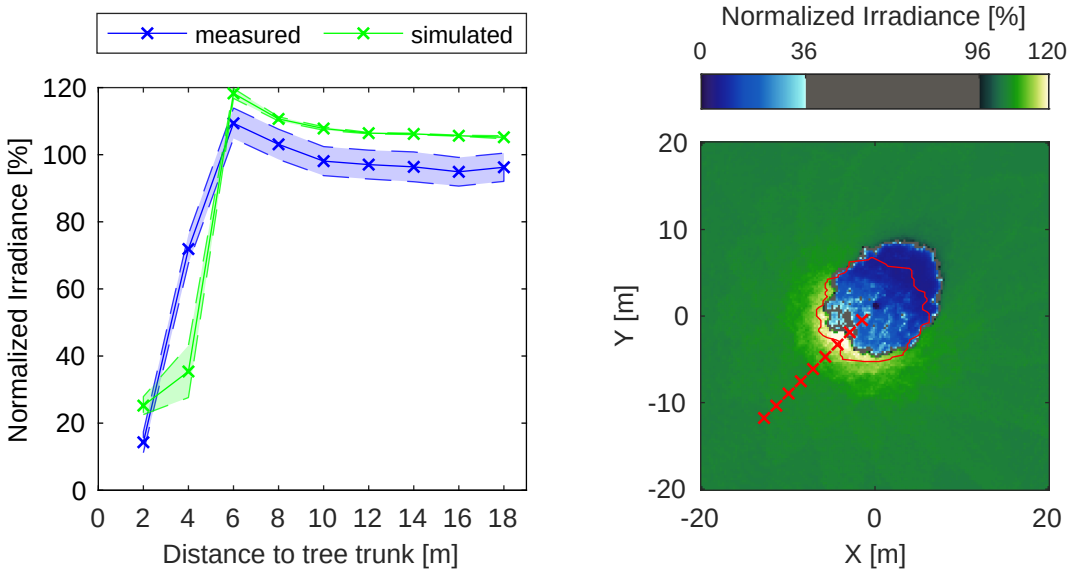

(b)

Fig. 5.10: Measured vs. simulated irradiance for transects #7 (5.10a) at 470nm and #19 (5.10b) at 781nm. Left panels show the normalized irradiance transects for measured (blue) and simulated (green) irradiance. Irradiance normalization has been performed based on measured irradiance at the reference location. Right panels show DART simulated normalized irradiance at 70 cm above ground with the crown outline and target locations highlighted in red.

Leaf optical properties are recognised as one of the major components driving the radiation regime of forest canopies. Thus LOP are also key input parameters for leaf and canopy radiative transfer models (Feret *et al.*, 2008; Lukeš *et al.*, 2017). It is therefore of great importance to know the uncertainties associated with the LOP measurements. Especially LOP retrieved from leaf clip measurements are known to have differing reflectance and transmittance when compared to the well established procedure using a single integrating sphere (Hovi *et al.*, 2017). However,

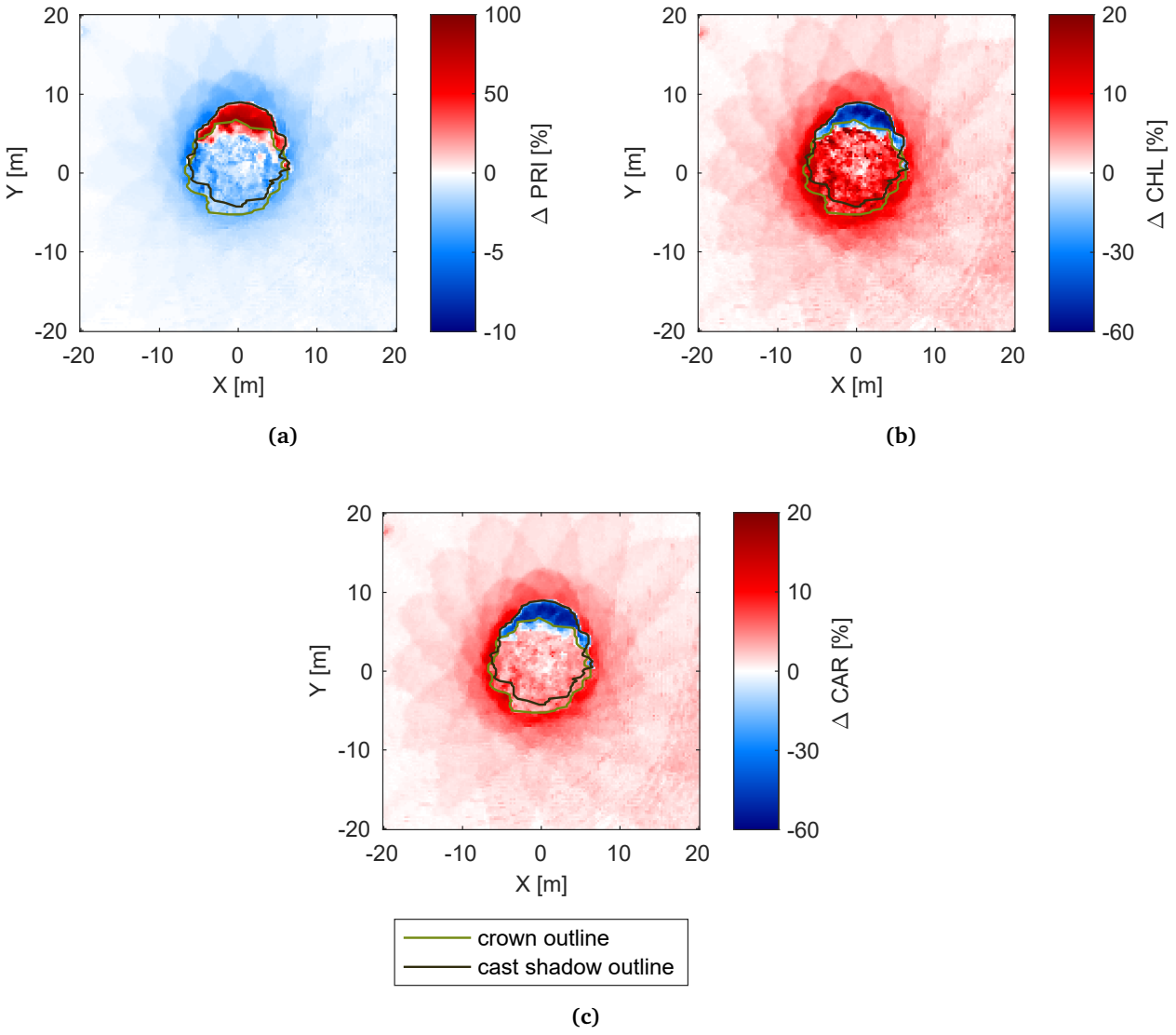

Fig. 5.11: Impact of the tree onto the retrieval of commonly employed vegetation indices. Red (blue) colors denote an overestimation (underestimation) of the derived product when not accounting for the tree's presence (i.e. when using apparent ToC reflectance values). $\Delta CAR = aCAR - tCAR$ where $aCAR$ is the vegetation index derived using apparent ToC reflectance values and $tCAR$ is the vegetation index derived using true ToC reflectance values. The changes are shown relative to the observed value range of the respective vegetation indices derived from the leaf and ground optical properties (c.f. Section 5.3.1c).

the assessment of the uncertainty associated with the LOP measurements is a non-trivial task. Nevertheless, we assume that even larger errors associated with the LOP measurements will not significantly impact the modeled surface irradiance values and patterns and therefore the findings of this study. This assumption is also based on the findings by Stuckens *et al.* (2009), where they analysed commonly used assumptions in radiative transfer models such as the averaging of LOP for entire crowns. They found that no measurable error could be found in the simulated reflectance images if an averaged LOP was used instead of a more accurate assignment with varying LOP throughout the crown. A more detailed analysis on the uncertainty associated

with the measured LOP and the impact on simulated surface irradiance is given in Appendix 5.7.1e.

Also leaf angle distribution (LAD) plays an important role in the radiative transfer through tree canopies (Asner, 1998), but also in the estimation of PAD per voxel (Béland *et al.*, 2011). As an automatic estimation of LAD from TLS data is still a challenge, we assumed a spherical leaf angle distribution for the whole crown. This assumption is commonly performed in literature (e.g. Alonzo *et al.*, 2015; Verhoef *et al.*, 2014; Vincent *et al.*, 2017) and was reported to be acceptable for mapping effective LAI in a heterogeneous mixed forest from aerial discrete return lidar in Richardson *et al.* (2009). We further had leaf angle measurements from a different tree of the same species available (Pisek, Tartu Observatory, unpublished data), proving the assumed spherical leaf angle distribution to be adequate.

No measurements of the atmospheric composition during the experiment are available, hindering an accurate, time-dependent parameterization of the atmosphere. We used the DART standard aerosol model for rural areas as a stable reference. The visibility was set to 23 km, which is the value usually observed for clear summer days in Switzerland. The gas model which describes the vertical distribution of gases in the atmosphere and its scattering characteristics was defined as the DART standard mid-latitude summer model. In order to reduce this source of uncertainty, additional measurements using a sun-photometer should be used in future experiments. The temporal variability in solar irradiance further require temporally high resolved measurements of the atmospheric composition in order to fully reflect the influence of the atmosphere, adding even more to the complexity. We therefore opted for the use of a simple DART standard atmosphere parameterization, which is applicable for most nearly clear sky situations and is a common approach found in literature (e.g. Borel *et al.*, 2009; Damm *et al.*, 2015b; Disney *et al.*, 2006; Laurent, 2013). We consider this source of uncertainty not to impact the main findings of our study and drawn conclusions.

Several radial lobes around the tree can be distinguished in the DART derived irradiance maps. This is caused by the user defined discrete scattering directions in which DART is able to scatter light (Yin *et al.*, 2013). In all performed simulations a total amount of 100 directions in the whole 4π space was defined plus an additional 100 directions in the sun's hot-spot up- and downward direction. In order to remove these lobes, the amount of directions has to be increased at the cost of computational expense. Again, this undersampling does not impact our results and conclusions.

5.5.2 Measured Irradiance

Even though we used the field spectroradiometer measurements as a source for validating DART modeled irradiance, multiple sources of uncertainties associated with the irradiance measurements from the spectroradiometers have to be accounted for (cf. Hueni *et al.* (2017) for a comprehensive review of sources of uncertainties).

An in-depth analysis on the uncertainty budget for the irradiance measurements is given in Appendix 5.7.1. The biggest source of uncertainty associated with the irradiance measurements is believed to be found in the spectralon panel, especially due to degradation effects of the spectralon panel over time (see Appendix 5.7.1b), but also due to dirt build up during the experiment. The spectralon panels suffer from a gradual degradation over time which is most pronounced in the blue and visible spectral range. Möller *et al.* (2003) showed that over the course of only one year, a degradation of up to 1% in reflectance can be observed depending on the wavelength. They even showed that over the course of a single day a degradation of the reference panel can be observed. Hueni *et al.* (2017) also showed and quantified the panel degradation by comparing the measured reflectance to a new, pristine panel. They showed that the degradation affected the whole spectral range with the visible range being the most susceptible, showing degradation of up to 20% below 400 nm. Above 600 nm the degradation was reported to be less than 5%. We argue that this is one of the main reasons for the overestimation of the DART modeled irradiance values. However, the influence of the aging effect can be reduced with proper storage and could be quantified by frequently calibrating the spectralon panels with a pristine and calibrated reference spectralon panel that is ideally only used in laboratory environment. Unfortunately, such a calibration was not performed for this study due to a missing pristine and calibrated spectralon panel.

5.5.3 DART simulation validation

Even though a fixed measuring grid with the tree trunk and the major cardinal directions as a reference was laid out, the exact localization of each irradiance measurement location in the DART simulated irradiance products is likely a source of uncertainty in this experiment. To overcome this issue, the average simulated irradiance in a 75x75cm area around the localized measurement point was taken and the standard deviation inside this window was calculated. Nevertheless, an inaccurate localization of the measurement location inside the DART irradiance product could still be an explanation for some larger discrepancies between modeled and measured irradiance found especially at the shadow borders.

The results have shown that even though the irradiance pattern between measured and modeled irradiance fit well, the DART simulated values usually overestimated the measured irradiance. A reason for this overestimation, as already mentioned in Section 5.5.1, could be the parameterization of the atmosphere inside DART. As seen in Fig. 5.5b, also minor changes in atmospheric conditions in a seemingly bright and sunny day can cause a significant variation of irradiation during a short time window (i.e. up to 10% depending on wavelength) on the measured baseline irradiance. Also differences in observed and modeled extra-terrestrial solar irradiance could have an influence on the modeling performance of the surface irradiance. However,

the impact of such differences in extra-terrestrial solar irradiance is small and not accountable to the overestimation in modeled irradiance.

Because DART has many input parameters, each one with its own uncertainty, a whole uncertainty budget for the DART modeled irradiance is believed to be out of the scope of this study. Nevertheless, a quantified uncertainty budget for the DART modeled irradiance including several sensitivity studies for the input parameters is still needed and should be considered for future studies.

However, measured irradiance could have an influence on the observed overestimation too. As mentioned in Section 5.5.2, spectralon panels degrade over time, especially at lower wavelengths. This could be a further explanation for the larger overestimation in modeled irradiance, especially below 500 nm.

5.5.4 Impact on Vegetation Indices

The presence of a tree causes a wavelength dependent impact on surface irradiance of up to 7% that directly translates to retrieved ToC reflectance and subsequently calculated vegetation indices. It was found that this effect can be even more pronounced for vegetation indices using the near-infrared and the visible domain, such as the chlorophyll index or the carotenoid index (Hueni *et al.*, 2017). Fig. 5.11 shows that an overestimation of up to 14% in CAR or CHL can be expected when we use apparent ToC reflectances to calculate the indices instead of actual target reflectance values. Even though this may not sound as much, it is of high relevance. Fox *et al.* (2003) stated in their paper on the Traceable radiometry underpinning terrestrial- and helio-studies (TRUTHS) instrument that for long-term climate studies we need less than 1% uncertainty. Therefore, a tree induced irradiance change of 7% for a single wavelength or a change of 14% for a vegetation index is relevant. Already Roberts *et al.* (1990); Roberts (1991) reported a similar halo effect especially pronounced in the near-infrared, where the downward radiant flux measured at a certain distance from the leaf was increased by up to 20%.

Figures 5.3 and 5.11 show a brightness gradient for ToC irradiance and vegetation indices across the tree crown. These effects are especially pronounced for the irradiance field in the NIR spectrum as well as in the vegetation indices containing wavelengths in the NIR spectrum (CAR and CHL). This has serious implications for the retrieval of biochemical and biophysical parameters as well as of vegetation functioning from imaging spectroscopy data. For fully illuminated parts of the crown, oriented to the sun (i.e. an illumination angle close to 0 degrees) vegetation indices show errors of up to 2.5%, 10.6%, and 4.8% for PRI, CHL, and CAR respectively. For shaded crown pixels oriented away from the sun and mainly receiving diffuse irradiance, errors are up to 30%, 10.6%, and 8.9% for PRI, CHL, and CAR respectively. These findings suggest that the robustness of commonly employed approaches that only take sunlit pixels to derive these parameters (e.g. Asner, 2007; Schneider *et al.*, 2017) is compromised. Our findings suggest that only the flat area on the very

top of the tree (i.e. the area that represents the assumed illumination conditions in terms of illumination angle and fraction of diffuse to direct irradiance) can be assumed to be unaffected by these adjacency effects. How these effects scale with increasing pixel size and related varying contributions of isotropic, volumetric and geometric-optical scattering has to be determined. Unfortunately, measuring the actual irradiance on the crown surface is a complicated task, making the validation of the modeled irradiance values on the crown surface and the retrieval of vegetation indices of such pixels a challenge. Nevertheless, such adjacency effects are likely often neglected and a more in-depth analysis of these effects also at the crown level and at different scales is needed in order to fully understand their influence on the retrieval of vegetation status and functioning. In addition, induced adjacency effects have a direct implication for the assessment of sub-pixel material abundances: Multiple scattering caused by illumination effects determine the mixing of spectral signatures non-linear and thus introduce uncertainties in estimated unmixing results (cf. Borel & Gerstl (1994); Ray & Murray (1996); Roberts *et al.* (1993); Somers *et al.* (2009, 2014)). Radiative transfer models such as DART are valuable tools to analyze and quantify these very complex adjacency effects due to anisotropy, absorption and multiple scattering in the vegetation canopy. The implemented modeling approach reveals that DART is able to accurately model such irradiance patterns and could therefore be used to analyze these complex light interactions in even more detail.

In this study, only the irradiance change induced by a single isolated tree was analyzed and discussed. However, Fawcett *et al.* (2018) observed substantial border effects around tree crowns and concluded that the irradiance field is even more complex in presence of several trees due to multiple scattering effects. Also Stuckens *et al.* (2009) confirmed a significant change in simulated scene reflectance for varying placements of citrus trees in an orchard. For future studies it is of interest to analyze the impact on the irradiance field caused by multiple trees and the light interactions between the trees, possibly giving insights on species co-existence strategies. The DART radiative transfer model could be a useful tool to analyze the radiative transfer through the forest canopy, describing the light interaction inside the canopy. This has further implications for large scale ecosystem demography models for which Fisher *et al.* (2017) identified the radiative transfer through the canopy as one of the biggest sources of uncertainty.

5.6 Conclusion and Outlook

We conclude on the significance of spatial and spectral irradiance variability caused by 3D objects and the need to accurately model irradiance fields for reliable retrievals of geophysical information from imaging spectroscopy data. Measured and simulated irradiance demonstrate that shadow is a non-linear phenomenon showing a large variability in irradiance of up to 560% for blue wavelengths (450nm) and up to

17% for red wavelengths (680nm). However, beyond the visible spectral range, the variability of irradiance inside the cast shadow is negligible. Isolated trees substantially influence the irradiance field of its surrounding that goes far beyond the apparent cast shadow. In certain wavelength regions, even the surrounding at the sun-facing side is substantially impacted.

Our findings showed that the presented modeling approach is able to simulate and predict the extremely complex interactions of radiation with the canopy in unprecedented spectral and spatial resolution. Fisher *et al.* (2017) identified the modeling of the radiative transfer through the canopy as one of the biggest sources of uncertainty in current ecosystem and vegetation dynamics models. We suggest using 3D modeling approaches to exploit these complex interactions and evaluate the influence of simplifications in the radiative transfer on e.g. modeled absorbed photosynthetically active radiation (APAR), gross primary productivity (GPP), or light availability. The combination of experimental data and 3D modeling can reveal substantial insights to advance understanding of light-related mechanisms driving species coexistence, competition and diversity in complex forest canopies.

5.7 Supplementary Material

5.7.1 Uncertainty considerations

5.7.1a ASD radiometric uncertainty

The ASD radiometric uncertainty was based on an uncertainty budget provided by ASD. It is traceable to the NIST irradiance scale and includes further components (lamp current, distance from lamp to panel, panel reflectance, wavelength calibration and instrument long-term stability). The uncertainty is in the range to be expected from such calibration setups as used by ASD, e.g. the radiance transfer standard RASTA shows similar uncertainties (Taubert *et al.*, 2013).

5.7.1b Spectralon panel uncertainty

Spectralon panels suffer from a number of uncertainties. These comprise the reflective properties as well as short-term and long-term degradations. The reflectance of the panel is different from unity, and the reflectance factors of the panel and the associated uncertainties are defined in the calibration report given by the manufacturer (Helder *et al.*, 2012). These reflectance factors and uncertainties are however only true for the illumination and observation angles during calibration. Information about the specific bidirectional reflectance distribution function (BRDF) of Spectralon panels can be obtained by calibration in specialized laboratories (Deadman *et al.*, 2011). Short term degradations involve the accumulation of particles during the field use and have been reported to range around 0.5% (Deadman *et al.*, 2011),

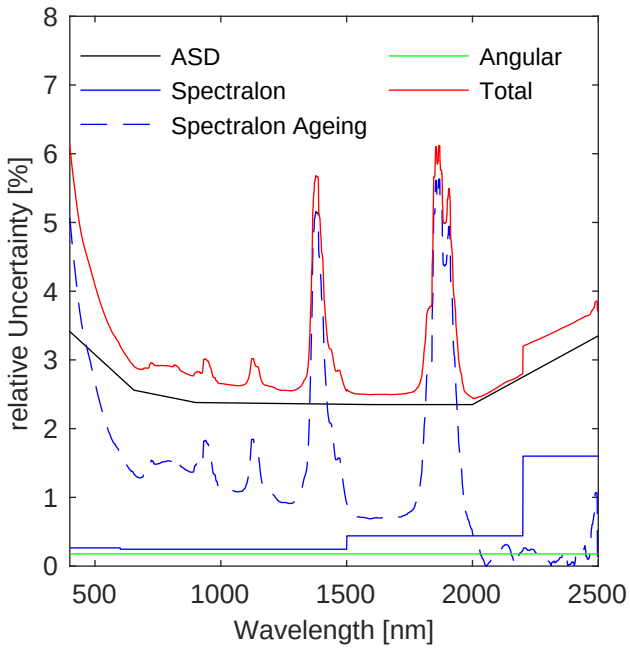

Fig. S5.1: Relative uncertainty contributions to the total uncertainty associated with the irradiance measurements using an ASD hand-held spectrometer and a spectralon panel mounted on a gimbal

but are obviously largely dependent on the environmental conditions and should be assessed specifically during each field experiment. Long term changes in reflectivity are not only associated with exposure to high levels of UV radiation, but also due to the storage (Möller *et al.*, 2003). The panels used during this experiment are not strictly traceable to a standard due to their storage and field usage since their last calibration. To account for the resulting uncertainties, we include the following uncertainty budget components: uncertainty of reflectance as provided by supplier and uncertainty due to storage and use. The latter was estimated from a comparative experiment, measuring the reflected solar irradiance over eight different panels during stable midday conditions in summer 2015. The storage and use uncertainty utilized in this study was calculated as the mean reflectance factor difference relative to the most recently calibrated panel.

5.7.1c Angular uncertainty of the gimbal

The uncertainty contribution to the total uncertainty associated with the irradiance measurements due to the leveling performance of the gimbal was assessed by measuring the angular displacement from a perfect horizontal alignment after a movement of the whole measurement device. This angular displacement was measured 20 times to receive an average angular displacement (0.23 degrees) from the perfect horizontal alignment. The contribution of the angular displacement to the total uncertainty of the measured irradiance was performed by calculating the expected irradiance on a completely flat surface based on the measured irradiance of the tilted surface defined by the tilt angles and the solar angle as described in Gulin *et al.*

(2013). According to Gulin *et al.* (2013), calculation of the direct irradiance incident on a tilted surface B_φ is purely geometrical:

$$B_\varphi = \frac{B_h}{\cos\theta_z}\cos\theta = B_h r_b, \tag{5.1}$$

where B_h is the direct horizontal solar irradiance, r_b is the direct irradiance conversion factor

$$r_b = \max(0, \frac{\cos\theta}{\cos\theta_z}) \tag{5.2}$$

and Θ is the angle of incidence, e.e., the angle between the sun direction and the normal direction of a tilted surface:

$$\cos\theta = \cos\theta_z\cos\beta + \sin\theta_z\sin\beta\cos(\gamma_s - \gamma) \tag{5.3}$$

where θ_z and γ_s are the solar zenith and azimuth angles respectively. γ and β are the measured angular displacement of the spectralon panel from a perfect horizontal alignment. As we measured the irradiance on the tilted surface (B_φ) we have to solve equation 5.1 for B_h. The difference between B_h and B_φ then gives the uncertainty associated with the irradiance measurement due to the alignment performance of the gimbal.

5.7.1d Total uncertainty associated with irradiance measurements

Fig. S5.1 shows the different contributions to the total relative uncertainty associated with the irradiance measurements. Note that the uncertainty associated with the spectralon panel does not account for aging effects as it is based on a calibration certificate of a new pristine spectralon panel. For older, used spectralon panels, the uncertainty contribution of the spectralon panel is assumed to be much larger especially in the visible spectral range.

5.7.1e Influence of LOP on simulated irradiance

Extracted leaf optical properties to paramiterize the DART model may be influenced by significant uncertainties. However, an estimation of the uncertainty associated with the retrieved LOP is a non-trivial task. In order to assess the impact of changing LOP on the modeled irradiance, we performed additional DART simulations, where we changed the LOP based on literature values found for the same tree species (tilia), but with a different genus (platyphyllos instead of cordata) in the LOPEX database (Hosgood *et al.*, 1995). Even though the LOP found in the LOPEX database show large variance in reflectance and transmittance (see Fig. S5.2), it can give us an idea about the range in LOP for tilia trees. We performed four additional DART simulations with the two LOP found in the LOPEX database for transect #7

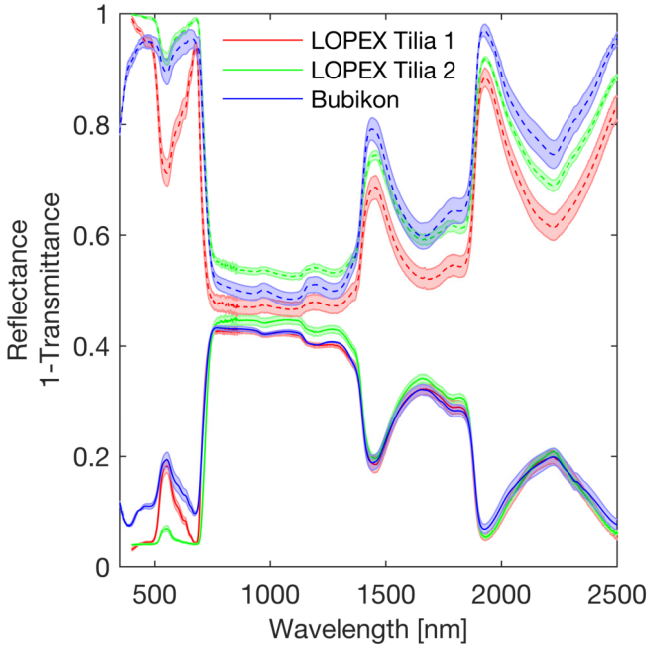

Fig. S5.2: Comparison between the two LOP entries for Tilia trees in the LOPEX database (Hosgood *et al.*, 1995) and the measured LOP for this experiment (Bubikon).

and #19 at 540nm and at 781nm (also compare with Fig. 5.10). We opted for a wavelength at 540nm instead of 470nm, as the reflectance and transmittance values show larger differences at this wavelength, possibly showing also larger impacts on modeled irradiance values. Fig. S5.3 shows the range and the difference in modeled irradiance when we use the LOPs derived from the LOPEX database as compared to the original simulation based on the measured LOP. Even though the difference in reflectance and transmittance of the measured leaves and retrieved form the LOPEX database is relatively large (up to 80% in transmittance at 540nm when measured transmittance is compared with transmittance for LOPEX Tilia 1), the impact on simulated irradiance is marginal. Outside shadowed areas, the difference in modeled irradiance is less than 0.2% at 540nm with distance to tree trunk of more than 8m and less than 1.7% at 781nm after 6m distance to tree trunk. Only within shadowed areas the relative difference between original simulation and the ones based on changed LOPs are larger (up to 22% at 540nm and up to 12% at 781nm), however as the absolute amount of irradiance in these shadowed areas is very low, the absolute difference is nearly negligible with 0.004 W m^{-2} nm^{-1} sr^{-1} and 0.009 W m^{-2} nm^{-1} sr^{-1} at 540nm and 781nm respectively. We can therefore conclude that a change in LOP due to measurement errors would only have a minor effect on the modeled surface irradiance values.

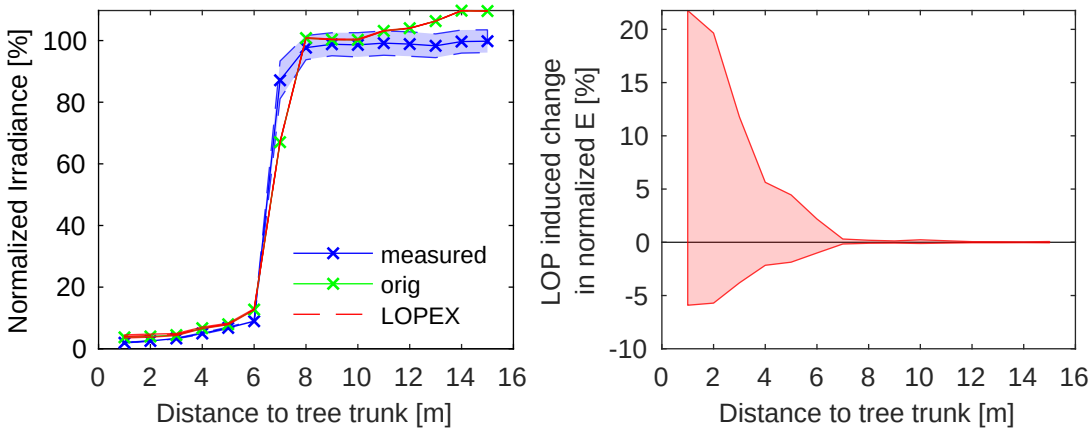

(a)

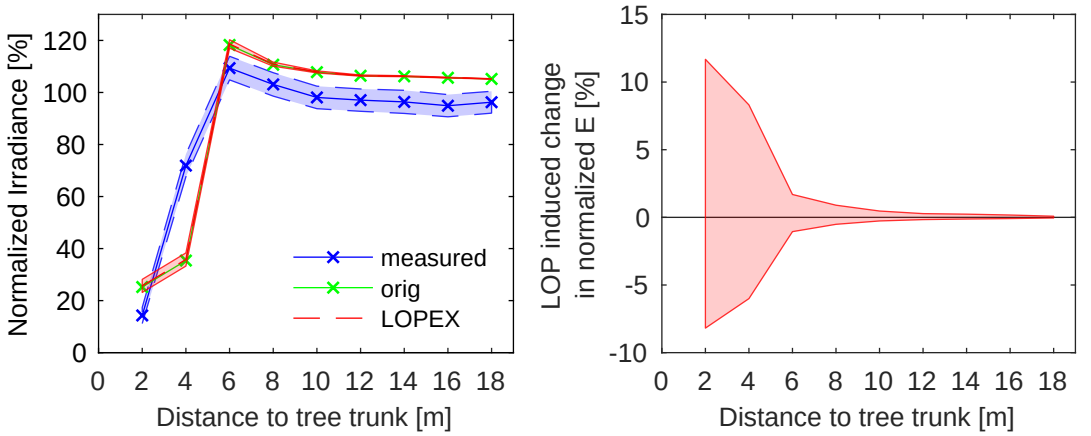

(b)

Fig. S5.3: Measured vs. simulated irradiance for transects #7 (5.10a) at 540nm and #19 (5.10b) at 781nm. Left panels show the normalized irradiance transects for measured (blue) and simulated irradiance with original LOP parameterization (green) and with LOP parameterization based on tilia entries found in the LOPEX database (Hosgood *et al.*, 1995) in red. Irradiance normalization has been performed based on measured irradiance at the reference location. The red shaded area denotes the range in simulated irradiance based on the variance in LOP of the LOPEX databse. Right panels show relative change in normalized irradiance when comparing the original simulation with measured LOP with the simulations based on LOPEX LOP.

Acknowledgment

The research leading to these results has received funding from the European Union's 7th Framework Programme (FP7/2014 - 2018) under EUFAR2 contract n°312609. The contributions of Andreas Hueni, Fabian D. Schneider, Felix Morsdorf, and Michael E. Schaepman are supported by the University of Zurich Research Priority Program on 'Global Change and Biodiversity'. Contributions of Andreas Hueni are also supported by MetEOC-3 project, which has received funding from the EMPIR programme co-financed by the participating states and from the European Unions Horizon 2020 research and innovation programme. The research carried out at the Jet Propulsion Laboratory, California Institute of Technology, was under a contract with the National Aeronautics and Space Administration. Government sponsorship is acknowledged.

The authors would like to thank Jan Pisek from the Tartu Observatory, Estonia for providing leaf angle measurements of a tilia cordata measured in Kew Gardens, London. They would also like to thank the Science IT group S3IT (University of Zurich, UZH) and especially Sergio Maffioletti, for their support on running the Radiative transfer simulations on their cloud computing environment. We further acknowledge the help of Dr. Laura Mihai from the National Institute for Laser, Plasma and Radiation Physics, Romania, during her short term scientific mission at UZH. This work was supported by a STSM Grant from COST Action OPTIMISE ES1309. We would also like to thank the anonymous reviewers for their valuable comments.

5.8 References

Abegg M, Kükenbrink D, Zell J, Schaepman ME, Morsdorf F (2017) Terrestrial laser scanning for forest inventories-tree diameter distribution and scanner location impact on occlusion. *Forests*, **8**, 1–29.

Adeline K, Chen M, Briottet X, Pang S, Paparoditis N (2013) Material reflectance retrieval in urban tree shadows with physics-based empirical atmospheric correction. In: *Urban Remote Sensing Event (JURSE), 2013 Joint*, 2, pp. 279–283. Sao Paulo.

Adler-Golden SM, Matthew MW, Anderson GP, Felde GW, Gardner JA (2002) An Algorithm for De-Shadowing Spectral Imagery. In: *SPIE*, vol. 4816, pp. 203–210.

Alonzo M, Bookhagen B, McFadden JP, Sun A, Roberts DA (2015) Mapping urban forest leaf area index with airborne lidar using penetration metrics and allometry. *Remote Sensing of Environment*, **162**, 141–153.

Asner GP (1998) Biophysical and Biochemical Sources of Variability in Canopy Reflectance. *Remote Sensing of Environment*, **64**, 234–253.

Asner GP (2007) Carnegie Airborne Observatory: in-flight fusion of hyperspectral imaging and waveform light detection and ranging for three-dimensional studies of ecosystems. *Journal of Applied Remote Sensing*, **1**, 013536.

Asner GP, Martin RE, Anderson CB, Knapp DE (2015) Quantifying forest canopy traits: Imaging spectroscopy versus field survey. *Remote Sensing of Environment*, **158**, 15–27.

Béland M, Baldocchi DD, Widlowski JL, Fournier RA, Verstraete MM (2014a) On seeing the wood from the leaves and the role of voxel size in determining leaf area distribution of forests with terrestrial LiDAR. *Agricultural and Forest Meteorology*, **184**, 82–97.

Béland M, Widlowski JL, Fournier RA (2014b) A model for deriving voxel-level tree leaf area density estimates from ground-based LiDAR. *Environmental Modelling & Software*, **51**, 184–189.

Béland M, Widlowski JL, Fournier RA, Côté JF, Verstraete MM (2011) Estimating leaf area distribution in savanna trees from terrestrial LiDAR measurements. *Agricultural and Forest Meteorology*, **151**, 1252–1266.

Berk A, Bernstein L, Robertson D (1987) MODTRAN: A Moderate Resolution Model For LOWTRAN. Tech. rep., Spectral Sciences. Inc., Burlington.

Borel C, Ewald K, Manzardo M, Wamsley C, Jacobson J (2009) Adjoint Radiosity based Algorithms for retrieving target Reflectances in urban area shadows. In: *Proceedings of 6th EARSeL SIG IS workshop*. Tel Aviv.

Borel CC, Gerstl SA (1994) Nonlinear spectral mixing models for vegetative and soil surfaces. *Remote sensing of environment*, **47**, 403–416.

Cignoni P, Cignoni P, Callieri M, *et al.* (2008) MeshLab: an Open-Source Mesh Processing Tool. *Sixth Eurographics Italian Chapter Conference*, pp. 129–136.

Damm A, Guanter L, Paul-Limoges E, *et al.* (2015a) Far-red sun-induced chlorophyll fluorescence shows ecosystem-specific relationships to gross primary production: An assessment based on observational and modeling approaches. *Remote Sensing of Environment*, **166**, 91–105.

Damm A, Guanter L, Verhoef W, Schläpfer D, Garbari S, Schaepman M (2015b) Impact of varying irradiance on vegetation indices and chlorophyll fluorescence derived from spectroscopy data. *Remote Sensing of Environment*, **156**, 202–215.

Deadman A, Behnert I, Fox N, Griffith D (2011) Laboratory panel and radiometer calibration. In: *2011 IEEE International Geoscience and Remote Sensing Symposium*, pp. 3883–3886. IEEE.

Disney M, Lewis P, Saich P (2006) 3D modelling of forest canopy structure for remote sensing simulations in the optical and microwave domains. *Remote Sensing of Environment*, **100**, 114–132.

Fawcett D, Verhoef W, Schläpfer D, Schneider F, Schaepman M, Damm A (2018) Advancing retrievals of surface reflectance and vegetation indices over forest ecosystems by combining imaging spectroscopy, digital object models, and 3D canopy modelling. *Remote Sensing of Environment*, **204**, 583–595.

Feret JB, François C, Asner GP, *et al.* (2008) PROSPECT-4 and 5: Advances in the leaf optical properties model separating photosynthetic pigments. *Remote Sensing of Environment*, **112**, 3030–3043.

Fisher RA, Koven CD, Anderegg WRL, *et al.* (2017) Vegetation Demographics in Earth System Models: a review of progress and priorities. *Global Change Biology*, pp. 1–20.

Fox N, Aiken J, Barnett J, *et al.* (2003) Traceable radiometry underpinning terrestrial- and helio-studies (TRUTHS). *Advances in Space Research*, **32**, 2253–2261.

Friman O, Tolt G, Ahlberg J (2011) Illumination and shadow compensation of hyperspectral images using a digital surface model and non-linear least squares estimation. *Proceedings of SPIE Remote Sensing 2011*, p. 8180.

Gamon J, Peñuelas J, Field C (1992) A narrow-waveband spectral index that tracks diurnal changes in photosynthetic efficiency.

Gamon JA, Kovalchuck O, Wong CY, Harris A, Garrity SR (2015) Monitoring seasonal and diurnal changes in photosynthetic pigments with automated PRI and NDVI sensors. *Biogeosciences*, **12**, 4149–4159.

Gamon JA, Serrano L, Surfus JS (1997) The photochemical reflectance index: An optical indicator of photosynthetic radiation use efficiency across species, functional types, and nutrient levels. *Oecologia*, **112**, 492–501.

Gastellu-Etchegorry J, Grau E, Lauret N (2012) DART : A 3D Model for Remote Sensing Images and Radiative Budget of Earth Surfaces. In: *Modeling and Simulation in Engineering* (ed. Alexandru C), pp. 1–40. CESBIO - CNES, CNRS (UMR 5126), IRD, Universite de Toulouse, Toulouse, France.

Gastellu-Etchegorry JP (2008) 3D modeling of satellite spectral images, radiation budget and energy budget of urban landscapes. *Meteorology and Atmospheric Physics*, **102**, 187–207.

Gastellu-Etchegorry JP, Martin E, Gascon F (2004) DART: A 3D model for simulating satellite images and studying surface radiation budget. *International Journal of Remote Sensing*, **25**, 73–96.

Gastellu-Etchegorry JP, Yin T, Lauret N, *et al.* (2015) Discrete Anisotropic Radiative Transfer (DART 5) for Modeling Airborne and Satellite Spectroradiometer and LIDAR Acquisitions of Natural and Urban Landscapes. *Remote Sensing*, **7**, 1667–1701.

Gitelson AA, Keydan GP, Merzlyak MN (2006) Three-band model for noninvasive estimation of chlorophyll, carotenoids, and anthocyanin contents in higher plant leaves. *Geophysical Research Letters*, **33**, 2–6.

Grau E, Durrieu S, Fournier R, Gastellu-etchegorry Jp, Yin T (2017) Estimation of 3D vegetation density with Terrestrial Laser Scanning data using voxels . A sensitivity analysis of influencing parameters . *Remote Sensing of Environment*, **191**, 373–388.

Gulin M, Vasak M, Baotic M (2013) Estimation of the global solar irradiance on tilted surfaces. *17th International Conference on Electrical Drives and Power Electronics (EDPE 2013)*, p. 6.

Helder D, Thome K, Aaron D, *et al.* (2012) Recent surface reflectance measurement campaigns with emphasis on best practices, SI traceability and uncertainty estimation. *Metrologia*, **49**.

Hemmer TH, Westphal TL, Jackson L, Hwy M (2000) Lessons learned in the post-processing of field spectroradiometric data covering the 0 . 4 to 2 . 5 im wavelength region. *Proceedings of SPIE*, **4049**, 249–260.

Hilker T, Coops NC, Hall FG, Black TA, Wulder MA, Nesic Z, Krishnan P (2008a) Separating physiologically and directionally induced changes in PRI using BRDF models. *Remote Sensing of Environment*, **112**, 2777–2788.

Hilker T, Coops NC, Schwalm CR, Jassal RS, Black TA, Krishnan P (2008b) Effects of mutual shading of tree crowns on prediction of photosynthetic light-use efficiency in a coastal Douglas-fir forest. *Tree physiology*, **28**, 825–834.

Hosgood B, Jacquemoud S, Andreoli G, Verdebout J, Pedrini G, Schmuck G (1995) Leaf optical properties experiment 93 (LOPEX93). *Ispra Italy'European Commission, Joint Research Centre Institute of Remote Sensing Applications*.

Hovi A, Forsström P, Mõttus M, Rautiainen M (2017) Evaluation of Accuracy and Practical Applicability of Methods for Measuring Leaf Reflectance and Transmittance Spectra. *Remote Sensing*, **10**, 25.

Hueni A, Bialek A (2017) Cause, Effect, and Correction of Field Spectroradiometer Interchannel Radiometric Steps. *IEEE Journal of Selected Topics in Applied Earth Observations and Remote Sensing*, **10**, 1542–1551.

Hueni A, Damm A, Kneubuehler M, Schlapfer D, Schaepman ME (2017) Field and Airborne Spectroscopy Cross Validation -Some Considerations. *IEEE Journal of Selected Topics in Applied Earth Observations and Remote Sensing*, **10**, 1117–1135.

Hueni A, Nieke J, Schopfer J, Kneubühler M, Itten KI (2009) The spectral database SPECCHIO for improved long-term usability and data sharing. *Computers and Geosciences*, **35**, 557–565.

Huete AR (1987) Soil and sun angle interactions on partial canopy spectra. *International Journal of Remote Sensing*, **8**, 1307–1317.

Jackson RD, Clarke TR, Susan Moran M (1992) Bidirectional calibration results for 11 spectralon and 16 BaSO4reference reflectance panels. *Remote Sensing of Environment*, **40**, 231–239.

Kazhdan M, Hoppe H (2013) Screened poisson surface reconstruction. *ACM Transactions on Graphics*, **32**, 1–13.

Kükenbrink D, Schneider FD, Leiterer R, Schaepman ME, Morsdorf F (2017) Quantification of hidden canopy volume of airborne laser scanning data using a voxel traversal algorithm. *Remote Sensing of Environment*, **194**, 424–436.

Laurent VCE (2013) *Coupled canopy-atmosphere modelling for radiance-based estimation of vegetation properties*. Ph.D. thesis, Wageningen University.

Lukeš P, Homolová L, Navrátil M, Hanuš J (2017) Assessing the consistency of optical properties measured in four integrating spheres. *International Journal of Remote Sensing*, **38**, 3817–3830.

Lynch DK (2015) Shadows. *Applied Optics*, **54**, B154.

Malenovský Z, Homolová L, Zurita-Milla R, *et al.* (2013) Retrieval of spruce leaf chlorophyll content from airborne image data using continuum removal and radiative transfer. *Remote Sensing of Environment*, **131**, 85–102.

Miller JR, Steven MD, Demetriades-Shah TH (1992) Reflection of layered bean leaves over different soil backgrounds: measured and simulated spectra. *International Journal of Remote Sensing*, **13**, 3273–3286.

Möller W, Nikolaus KP, Höpe A (2003) Degradation of the diffuse reflectance of spectralon under low-level irradiation. *Metrologia*, **40**.

Mõttus M, Takala TLH, Stenberg P, Knyazikhin Y, Yang B, Nilson T (2015) Diffuse sky radiation influences the relationship between canopy PRI and shadow fraction. *ISPRS Journal of Photogrammetry and Remote Sensing*, **105**, 54–60.

Ray TW, Murray BC (1996) Nonlinear spectral mixing in desert vegetation. *Remote Sensing of Environment*, **55**, 59–64.

Richardson JJ, Moskal LM, Kim SH (2009) Modeling approaches to estimate effective leaf area index from aerial discrete-return LIDAR. *Agricultural and Forest Meteorology*, **149**, 1152–1160.

Richter R (1990) A fast atmospheric correction algorithm applied to Landsat TM images. *International Journal of Remote Sensing*, **11**, 159–166.

Richter R, Müller A (2005) Deshadowing of satellite/airborne imagery. *International Journal of Remote Sensing*, **26**, 3137–3148.

Roberts DA (1991) *Separating Spectral Mixtures of Vegetation and Soils*. Ph.D. thesis, University of Washington.

Roberts DA, Adams JB, Smith MO (1990) Predicted distribution of visible and near-infrared radiant flux above and below a transmittant leaf. *Remote Sensing of Environment*, **34**, 1–17.

Roberts DA, Smith MO, Adams JB (1993) Green,Vegetation, Nonphotosynthetic Vegetation, and Soil in AVIRIS Data. *Remote Sensing of Environment*, **V. 44**, p. 255–269.

Schaepman ME, Jehle M, Hueni A, *et al.* (2015) Advanced radiometry measurements and Earth science applications with the Airborne Prism Experiment (APEX). *Remote Sensing of Environment*, **158**, 207–219.

Schaepman ME, Ustin SL, Plaza AJ, Painter TH, Verrelst J, Liang S (2009) Earth system science related imaging spectroscopy-An assessment. *Remote Sensing of Environment*, **113**, S123–S137.

Schneider FD, Leiterer R, Morsdorf F, Gastellu-Etchegorry JP, Lauret N, Pfeifer N, Schaepman ME (2014) Simulating imaging spectrometer data: 3D forest modeling based on LiDAR and in situ data. *Remote Sensing of Environment*, **152**, 235–250.

Schneider FD, Morsdorf F, Schmid B, Petchey OL, Hueni A, Schimel DS, Schaepman ME (2017) Mapping functional diversity from remotely sensed morphological and physiological forest traits. *Nature Communications*, **8**, 1441.

Somers B, Cools K, Delalieux S, Stuckens J, Van der Zande D, Verstraeten WW, Coppin P (2009) Nonlinear Hyperspectral Mixture Analysis for tree cover estimates in orchards. *Remote Sensing of Environment*, **113**, 1183–1193.

Somers B, Tits L, Coppin P (2014) Quantifying nonlinear spectral mixing in vegetated areas: Computer simulation model validation and first results. *IEEE Journal of Selected Topics in Applied Earth Observations and Remote Sensing*, **7**, 1956–1965.

Stuckens J, Somers B, Delalieux S, Verstraeten WW, Coppin P (2009) The impact of common assumptions on canopy radiative transfer simulations: A case study in Citrus orchards. *Journal of Quantitative Spectroscopy and Radiative Transfer*, **110**, 1–21.

Takala TL, Mõttus M (2016) Spatial variation of canopy PRI with shadow fraction caused by leaf-level irradiation conditions. *Remote Sensing of Environment*, **182**, 99–112.

Taubert DR, Hollandt J, Sperfeld P, *et al.* (2013) Providing radiometric traceability for the calibration home base of DLR by PTB. *AIP Conference Proceedings*, **1531**, 376–379.

Tits L, Somers B, Stuckens J, Farifteh J, Coppin P (2013) Integration of in situ measured soil status and remotely sensed hyperspectral data to improve plant production system monitoring: Concept, perspectives and limitations. *Remote Sensing of Environment*, **128**, 197–211.

Ustin SL, Gitelson Aa, Jacquemoud S, Schaepman M, Asner GP, Gamon Ja, Zarco-Tejada P (2009) Retrieval of foliar information about plant pigment systems from high resolution spectroscopy. *Remote Sensing of Environment*, **113**, S67–S77.

van Beek J, Tits L, Somers B, Deckers T, Janssens P, Coppin P (2015) Reducing background effects in orchards through spectral vegetation index correction. *International Journal of Applied Earth Observation and Geoinformation*, **34**, 167–177.

Verhoef W, Tol CVD, Middleton EM (2014) Vegetation Canopy Fluorescence and Reflectance Retrieval By Model Inversion Using Optimization. In: *5th International Workshop on Remote Sensing of Vegetation Fluorescence*, 1, pp. 759–770.

Vincent G, Antin C, Laurans M, Heurtebize J, Durrieu S, Lavalley C, Dauzat J (2017) Mapping plant area index of tropical evergreen forest by airborne laser scanning. A cross-validation study using LAI2200 optical sensor. *Remote Sensing of Environment*, **198**, 254–266.

Yin T, Gastellu-Etchegorry JP, Lauret N, Grau E, Rubio J (2013) A new approach of direction discretization and oversampling for 3D anisotropic radiative transfer modeling. *Remote Sensing of Environment*, **135**, 213–223.

Chapter

6

Synthesis

The complex distribution of light within vegetated canopies is the major driver for ecosystem functioning, productivity and diversity. However, understanding of the complex light-matter interactions within forest ecosystems is still limited. Recent advances in the field of remote sensing allow for an accurate 3D assessment of the forest structure. In combination with 3D radiative transfer models (e.g. DART (Gastellu-Etchegorry *et al.*, 2015)) and dynamic global vegetation models (e.g. the Ecosystem Demography Models ED (Moorcroft *et al.*, 2001) and ED2 (Medvigy *et al.*, 2009)), these data can reveal important insights into light related mechanisms within the canopy as well as into forest ecosystem functioning and productivity.

In this Chapter, we provide a comprehensive overview and discussion of our findings, general contributions to the research field and suggestions for future research, broadening our understanding of the radiative transfer in forest ecosystems.

6.1 Main findings

The thesis is structured by four main research questions (RQ) formulated in Chapter 1 and addressed in Chapters 2 to 5:

> I. How can we quantify the actual observed canopy volume by laser scanning instruments and how much is the occluded volume affected by laser acquisition parameters or vegetation phenology?
>
> II. How well can we represent the three-dimensional canopy structure with close-range laser scanning instruments (TLS and UAVLS) for the parameterization of a radiative transfer model and is there a bias introduced by occluded canopy volume when quantifying vegetation densities?
>
> III. How are contrasting canopy structures and optical characteristics as found in a temperate and a tropical forest affecting the distribution of solar light within the canopy?
>
> IV. How does vegetation influence the irradiance field around it? What are the consequences of vegetation induced adjacency effects for processing and analysis of imaging spectroscopy data?

In the following four subsections, the main findings of the four research questions are presented and discussed.

6.1.1 How can we quantify the actual observed canopy volume by laser scanning instruments and how much is the occluded volume affected by laser acquisition parameters or vegetation phenology?

Canopy structure plays a crucial role in forest ecosystem functioning and processes as it, among other things, influences energy fluxes between the atmosphere and forest (Shugart *et al.*, 2010; Xue *et al.*, 2011; Yang & Friedl, 2003). Laser scanning technologies are increasingly used for forest canopy structure assessments. The ability to map the 3D forest structure in a spatially continuous manner is a clear advantage in respect to traditional field survey techniques (see Section 1.1 and e.g. (Asner *et al.*, 2012; Næsset, 2004; Roberts *et al.*, 2007)). However, accuracy and level of detail of derived forest structure parameters from laser scanning measurements are affected by occlusion effects (e.g. Béland *et al.*, 2011, 2014a,b; Hilker *et al.*, 2010; Korpela *et al.*, 2012; Kükenbrink *et al.*, 2017; Schneider *et al.*, 2019). In Chapter 2 we introduced an approach to map occlusion in ALS acquisitions and quantified the amount of vegetation material not detected by the laser scanning system due to occlusion effects. Undetected vegetation material was quantified by cross-comparing ALS acquisition with those from a TLS campaign. Due to the complementary characteristics of the two acquisition geometries (above canopy vs. within canopy acquisitions) accurate assessments of undetected vegetation material can be performed, provided understorey occlusion in the TLS acquisitions is minimal (see also Chapter 3 and Section 6.1.2).

For a dense temperate forest on the Laegern mountain, Switzerland, we showed that even at relatively high pulse densities (11 pulses/m^2), at least 25% of the forest canopy volume remains occluded in ALS acquisitions under leaf-on conditions. Comparison with TLS acquisitions further showed that roughly 28% of the vegetation elements detected by the TLS acquisitions were not detected by the ALS system due to occlusion effects. By combining leaf-on and leaf-off ALS acquisitions, we were able to recover roughly 7% of the occluded vegetation elements that were undetected in the leaf-on acquisition. Due to missing foliage material during leaf-off conditions, occlusion is greatly reduced compared to leaf-on acquisitions (1.4% of total canopy volume versus 25% under leaf-on conditions).

Higher pulse densities increased the amount of observable canopy volume, however, a saturation of observed canopy volume with increasing pulse density was observed. A finding which is supported by previous studies (Ko *et al.*, 2012; Leiterer *et al.*, 2015a,b; Lim *et al.*, 2008; Treitz *et al.*, 2012).

We also showed, that an increased flight-strip overlap has strong advantages and improves the amount of detected vegetation material drastically. The observed fraction of total forest volume increased from 57% with a single flight strip coverage (single observation angle) to 81% with three flight strips covering the same area (three different observation angles). A finding that was essential also for answering

research question 2 (RQ2) in Chapter 3, where dense TLS scan-patterns were used in order to capture the 3D canopy structure of two contrasting and complex forests (see Section 6.1.2).

As stated in Chapter 2, flight strip overlap, or observational overlap in general, and pulse density is never fully decoupled and is therefore difficult to assess and quantify separately. We therefore concluded that further investigations of the effects of multiple observation geometries on the amount of occlusion should be performed. Abegg *et al.* (2017) used the proposed approach as stated in Section 2 and analysed optimal TLS scan pattern arrangements for forest plot inventories, demonstrating that an even distribution of scan locations within the plot with similar distances between locations and the edge of the plot, provides the best overall visibility of the stand. Schneider *et al.* (2019) (see Chapter 3) further analysed advantages of combining within canopy and above canopy LiDAR acquisitions for forest structure analysis using the approach described in Chapter 2.

6.1.2 How well can we represent the three-dimensional canopy structure with close-range laser scanning instruments (TLS and UAVLS) for the parameterization of a radiative transfer model and is there a bias introduced by occluded canopy volume when quantifying vegetation densities?

Airborne laser scanning measurements are already an established data source for regional and even national forest inventories (see e.g. Leiterer *et al.*, 2015b; Wulder *et al.*, 2012). However, restrictions in acquired point densities, beam diameter, as well as flight strip arrangements often limit the level of detail retrieved from such measurements. Retrieval of structural information on an individual tree level are therefore often limited to simple geometric parameters such as tree position, height, crown dimensions etc. (Kaartinen *et al.*, 2012; Larsen *et al.*, 2011; van Leeuwen & Nieuwenhuis, 2010), for which assessments on the canopy level with so-called area-based approaches are often preferred (e.g. Næsset, 2004; Shugart *et al.*, 2010; Vastaranta *et al.*, 2012). For accurate 3D reconstruction of the forest canopy for modelling complex light-matter interactions within the canopy (see Chapter 4), much higher levels of detail are needed, where also the major branching structure and small scale variabilities in vegetation density within the canopy is resolved. Close-range laser scanning technologies with their smaller beam diameter and their significant larger point densities showed promising results in reconstructing complex 3D forest structures (e.g. Calders *et al.*, 2018; Morsdorf *et al.*, 2018; Schneider *et al.*, 2019, see also Section 1.1 and Chapter 3). However, measuring the 3D distribution and density of plant material in dense forest canopies is challenging due to occlusion effects. These measurements are highly relevant though, since terrestrial laser scanning is emerging as a reference for non-destructive biomass estimation (Momo Takoudjou *et al.*, 2018; Stovall *et al.*, 2017), tree and canopy reconstruction (Béland *et al.*,

2014a; Grau *et al.*, 2017), testing of new methodologies and algorithm development (Fassnacht *et al.*, 2018; Abegg *et al.*, 2017), as well as the use in radiative transfer models for simulating radiation-matter interactions for studies of light availability and absorption (see also Chapter 4), satellite mission development and sensor simulation (Schneider *et al.*, 2014; Vincent *et al.*, 2017; Gastellu-Etchegorry *et al.*, 2017; Morsdorf *et al.*, 2018). Occlusion is often assumed to be a main source of uncertainty in forest structure assessments, but is usually not quantified. Therefore it is generally unknown to what degree occlusion influences the measurements in dense forests (Schneider *et al.*, 2019).

In Chapter 3 we followed up on the approach described in Chapter 2 and applied the same approach in order to quantify the amount of occluded canopy volume in close-range laser scanning acquisitions for two contrasting and dense forest canopies (temperate deciduous forest patch at the Laegern, Switzerland and tropical rain forest in the Lambir Hills National Park, Borneo Malaysia). We analysed the advantages of acquiring measurements from within the forest canopy as well as from above the canopy by taking TLS acquisitions from a canopy crane for the tropical and UAVLS acquisitions for the temperate forest plot. We further analysed the bias introduced into plant area density estimates (PAD) if only measurements from the ground or from above the canopy are acquired.

We found that TLS measurements from the ground for the two portrayed study sites delivered very good results, provided a dense sampling scheme is utilized (distances of 10-20 m between laser scans). Almost no occlusion up to about 25-30 m above ground was found. The results therefore confirmed the suitability of TLS for voxel-based forest reconstruction, wood structure reconstruction using so-called quantitative structure modeling (QSM) (Raumonen *et al.*, 2013, 2015), and biomass estimations, as has been previously shown when comparing results to destructive sampling (Disney, 2018). To simulate the interaction of incident solar radiation with the canopy and in order to tackle the challenge posed by the third research question (see Chapter 4), occlusion in the uppermost parts of the crowns is crucial and should not be neglected. Measurements from above the canopy, such as from a canopy crane or by UAVLS, can fill the missing parts of the occluded upper canopy layers. However, analysed separately, close-range laser acquisitions from above the canopy showed large occluded areas in the mid- and understory. As a result, strong underestimation of plant area density (PAD) especially in lower canopy layers were found. We are therefore suggesting to complement ground-based TLS measurements with above canopy measurements in order to acquire the highest possible level of detail to reconstruct the complex 3D canopy structure. In fact, we found that by combining measurement from the ground with the ones from above the canopy, that less than 2% of the total canopy volume was occluded in the two portrayed study sites, allowing us to reconstruct the two study sites at an unprecedented level of detail. This builds the baseline for the study of complex light-matter interactions

within forest canopies and with vegetated landscapes in general which was discussed in detail in Chapter 4 and 5 with the main findings summarized in Sections 6.1.3 and 6.1.4.

6.1.3 How are contrasting canopy structures and optical characteristics as found in a temperate and a tropical forest affecting the distribution of solar light within the canopy?

In Chapter 3 as well as in Section 6.1.2 we established that close-range laser scanning measurements deliver information on the 3D canopy structure in unprecedented levels of detail. This is essential for detailed 3D forest canopy reconstructions (Calders *et al.*, 2018) as a prerequisite for the modelling of complex, small-scale light-matter interactions within forest ecosystems (see Section 6.1.2). Information on the 3D distribution of solar light is essential for the study of forest ecosystem functioning, productivity as well as diversity. Canopy structure strongly influences the distribution of light within the canopy and therefore influences the within canopy variability of light-use efficiency and productivity (e.g. Stark *et al.*, 2012; Morton *et al.*, 2014, 2016; Widlowski *et al.*, 2011). Strong variabilities in light availability within vegetation canopies have been reported (e.g. Baldocchi *et al.*, 2002; Kükenbrink *et al.*, 2019; Niinemets, 2007; Niinemets & Keenan, 2012; Valladares, 2003), largely affecting morphological as well as physiological traits within the canopy. Niinemets (2012) stated that it is hardly possible to find two leaves with the exact same combination of leaf-trait values inside the canopy. Seasonal and diurnal changes in light availability within the canopy promote leaf plasticity allowing for leaves to adapt to changing light conditions within the canopy (e.g. Keenan & Niinemets, 2017; Niinemets *et al.*, 2003; Valladares *et al.*, 2016). This highlights the necessity of a detailed modelling of the radiative transfer through forest canopies not only in the horizontal and vertical, but also in the temporal domain.

In Chapter 4 we established an approach to model complex light-matter interactions in the photosynthetically active radiation (PAR 400 - 700 nm) regime for two complex and dense temperate and tropical forest plots, that were already introduced in Chapter 3. We were able to reconstruct and simulate the radiative transfer through the forest canopy at a voxel side length of 0.25 m which allows us to analyse the 3D light distribution within the canopy at unprecedented level of detail using the DART radiative transfer model (Gastellu-Etchegorry *et al.*, 2015). We showed that PAR extinction is mainly driven by the canopy structure, resulting in an exponential light extinction profile for the temperate study site and a more linear extinction profile in the tropical case. The homogeneous dense upper canopy layer found at the temperate study plot, which is dominated by beech trees (*Fagus Sylvatica* L.), absorbed most of the incoming solar radiation already within the first few meters of the canopy. The larger heterogeneity in canopy structure for the tropical study site also resulted in larger variability in light extinction throughout the whole canopy. Interestingly, even

though canopy structure for the two study sites are fundamentally different, the total amount of plant material represented as the vertically accumulated plant area index (PAI) is similar between the two study sites. The differences in canopy structure are therefore mainly due to differences in the distribution of plant material, rather than the total amount of plant material. The heterogeneous canopy structure found in the tropical forest site is both the result of high functional diversity and allows for more niches of additional species with varying resource-use strategies to find their matching biotope space to thrive. More complex canopy structures may therefore also act as an indicator for high diversity (see also McElhinny *et al.*, 2005). However, the question to which degree a heterogeneous canopy structure is a consequence or cause (via feedback effects) of diversity is largely unexplored (see e.g. Sapijanskas *et al.*, 2014).

Measured leaf optical properties showed large differences between the temperate and tropical forest sites. However, the differing LOPs are found to have only a minor influence on the light extinction profile (when compared to the influence of canopy structure) as was shown by exchanging the LOPs from the two study sites. The beech-dominated optical properties of the temperate study plot absorbed much more incoming solar radiation than the optical properties of the tropical forest, adding to the explanation of the differences in light extinction profiles of the two study plots.

The comparison of DART modelled 3D light extinction with a plot-level approximation using the Beer-Lambert law (Monsi & Saeki, 2005), clearly showed the necessity of such high detailed 3D radiative transfer models for the analysis of light distribution within forest canopies. The direct comparison showed that the Beer-Lambert approximated light extinction curve showed more than 30% larger extinction in the upper canopy than the DART simulated light extinction profiles. This finding is also of high relevance to many dynamic global vegetation models (DGVMs), as these models often rely on simplifying representations for the canopy structure using so-called big-leaf models (e.g. LPJ (Sitch *et al.*, 2003)) or cohort and individual based parameterization of the canopy structure (e.g. the Ecosystem Demography Models ED (Moorcroft *et al.*, 2001) or ED2 (Medvigy *et al.*, 2009)). However, these models often fail to represent the actual structural complexity found in forest ecosystems. Therefore, Alton *et al.* (2007) and Fisher *et al.* (2017) identified the radiative transfer component in DGVMs as one of the biggest sources of uncertainty when modelling ecosystem functioning, productivity and development. The proposed approach shown in Chapter 4 could be used as a benchmark for DGVMs to assess the level of detail needed for an accurate simulation of the 3D radiative transfer through the canopy, possibly allowing for more accurate modelling of the radiative transfer also on larger scales.

Regarding the question on how accurately DART is able to simulate the radiative transfer in forest ecosystems, Schneider *et al.* (2014) reported good performance of DART in simulating imaging spectroscopy data by cross-comparison of the simulated at-sensor radiances to actual measured radiances by the Airborne Prism Experiment

APEX instrument (Schaepman *et al.*, 2015) over the Laegern mountain, Switzerland. Further validation of the DART model has been conducted in (Kükenbrink *et al.*, 2019) and is discussed in Chapter 5 and Section 6.1.4. Furthermore, DART compared well to other radiative transfer models of different levels of complexity in all four stages of the radiative model intercomparison (RAMI) exercise (Pinty *et al.*, 2001, 2004; Widlowski *et al.*, 2007, 2015).

6.1.4 How does vegetation influence the irradiance field around it? What are the consequences of vegetation induced adjacency effects for processing and analysis of imaging spectroscopy data?

Imaging spectroscopy is frequently used for vegetation canopy assessments, with major focus on the retrieval of physiological, biochemical, and structural traits and monitoring of spatio-temporal variations in vegetation functioning, health, and status (Schaepman *et al.*, 2009, 2015; Ustin *et al.*, 2009). The ever-increasing spatial, temporal, and spectral resolution of sensors further allow the retrieval and monitoring of increasingly complex vegetation information such as functional diversity (Schneider *et al.*, 2017) or signals related to plant photosynthesis (e.g., sun-induced chlorophyll fluorescence) (Damm *et al.*, 2015). In order to retrieve such information on vegetation functioning and health, accurate estimates on surface irradiance are crucial. Accurate retrievals of surface irradiance are, however, nontrivial and often error-prone, thus causing inaccurate estimates of vegetation information.

In Chapter 5 we analyzed the irradiance field surrounding an isolated Linden tree (*Tilia cordata*, tree height 11.8 m) using the DART radiative transfer model (Gastellu-Etchegorry *et al.*, 2015) in a high spatial (25 cm) and spectral (1 nm, 350 - 2500 nm) resolution. The single tree was located on a small hill south-east of Zurich, Switzerland. The DART model was parameterized using TLS and *in-situ* spectroscopy measurements for the structural and optical information of the tree and its surroundings respectively. The parameterization process described in Chapter 4 and 5 are very similar, in fact the study portrayed in Chapter 5 built the framework for the forest reconstruction shown in Chapter 4. DART simulated irradiance values were validated with *in-situ* irradiance measurements around the isolated tree. Furthermore, the impact of erroneous surface irradiance estimates on commonly used vegetation indices retrieved from imaging spectroscopy data was analysed. The chosen indices include the Photochemical Reflectance Index (PRI), indicative for the deepoxidation state of xantophylls and often applied as a proxy for light use efficiency (LUE) (Gamon *et al.*, 1992, 1997, 2015), and two indices sensitive to the relative content of chlorophyll (CHL) and carotenoids (CAR) as proposed in (Gitelson *et al.*, 2006).

The comparison of DART modelled with measured irradiance values showed high agreement throughout the whole analysed spectrum. Generally, DART slightly

overestimates surface irradiance compared to the measured irradiance. For sunlit areas, in the visible spectral range (350-700 nm), the overestimation is at 12% on average, 9.3% in the near infrared (NIR, 701 - 1000 nm) range and 10.9% in the short-wave infrared (SWIR 1001 - 2500 nm). Only within strong absorption bands, larger biases between measured and modelled irradiance values were observed and were therefore also excluded from the validation results. For shadowed areas, DART overestimates the surface irradiance by 37.3% in the visible range. For the NIR and SWIR regions, DART underestimates the surface irradiance in average by 1.5% and 16.5% respectively. However, due to the large variability in irradiance in shadowed areas, simulated and measured irradiance values lie within their respective uncertainty bounds. The generally high agreement between DART simulated and *in-situ* measured irradiance values underlines the feasibility of DART to study also small scale variabilities in the distribution of light in vegetated canopies. This is a major finding, legitimating the use of the DART model in the study portrayed in Chapter 4.

The findings of Chapter 5 showed that the single isolated tree has large wavelength dependent impact on the surrounding irradiance field. We found, that the cast-shadow is a completely non-binary phenomenon, where a gradient with changes of up to 560% in irradiance in the blue spectral range was found. This large gradient within the cast shadow decreased with increasing wavelength and was finally not observed anymore in the NIR wavelength range. But also outside the cast shadow, significant impact of the tree on the irradiance field was found. Due to the decreased sky-view factor, reducing the amount of diffuse sky illumination, irradiance in the visible range on the northern side of the tree was decreased by up to 6%. Due to the large backward scattering behaviour of vegetation in the NIR region, an increase in irradiance of up to 7% to the south of the tree was observed. The influence of the tree on the irradiance field was observed up to 15 m distance to the tree trunk. Such brightening and darkening effects further show large impact on derived vegetation parameters. Outside the cast shadow, indices sensitive to the relative content of chlorophyll (CHL) and carotenoids (CAR) show an overestimation of up to 14% and the PRI shows an underestimation of up to 5% if such vegetation induced adjacency effects are not considered for.

We therefore concluded that accurate estimates of the irradiance field, especially around 3D vegetation objects, is of very high importance for reliable retrievals of geophysical information from imaging spectroscopy data. We showed that the presented modelling approach is able to simulate and predict the extremely complex interactions of radiation with the canopy in unprecedented spectral and spatial resolution. This finding is essential for the justification of the approach used in the study portrayed in Chapter 4.

6.2 General contributions

The interaction of solar radiation with vegetation canopies is recognized as one of the most critical processes represented in land surface models (LSMs) and vegetation models (Alton *et al.*, 2007; Fisher *et al.*, 2017). Fisher *et al.* (2017) stated that the development of accurate modelling of the partitioning of solar radiation within the canopy should receive highest priority in further development of dynamic global vegetation models (DGVMs). Major focus should be laid firstly on how radiation interacts with the scattering elements and the treatment of diffuse radiation, secondly on how the canopy structure should be represented. This thesis addresses these issues and develops a framework in order to study the complex light-matter interactions within vegetated canopies.

Due to the difficulty to get horizontally, vertically and temporally high resolved measurements of the light environment within vegetation canopies, modelling of the solar radiation regime using radiative transfer models is a viable alternative. Three-dimensional radiative transfer models (such as the DART model (Gastellu-Etchegorry *et al.*, 2015)) further give the opportunity to analyse also small scale variabilities in light availability within complex canopy structures. However, in order to parameterize the 3D radiative transfer model, an accurate representation and reconstruction of the forest canopy is essential (e.g. Morton *et al.*, 2016; Shugart *et al.*, 2010; Stark *et al.*, 2015)

Morsdorf *et al.* (2018, see Chapter 1.1) portrayed the potential of close-range laser scanning measurements for forest structure assessment and reconstruction. However, significant biases in important canopy structure parameters (e.g. vegetation densities quantified as plant area density (PAD)) could arise due to occlusion effects (e.g. Abegg *et al.*, 2017; Béland *et al.*, 2014b; Kükenbrink *et al.*, 2017; Schneider *et al.*, 2019). In Chapter 2 we introduced an approach to map occluded canopy volume in laser scanning measurements and analysed the occluded canopy volume from airborne laser scanning measurements. Due to lower pulse densities (compared to close-range laser scanning acquisitions) as well as a reduced amount of observation angle per canopy volume, a significant part of the forest canopy is occluded especially under leaf-on conditions. This finding suggests that the level of detail is not sufficient for reconstructing the forest canopy from ALS measurements and modelling small scale light-matter interactions down to the forest floor. This has further implications for global carbon storage assessments based on ALS or even from space borne LiDAR instruments. If up to 28% of canopy material for a temperate mixed forest stand under leaf-on conditions is not detected by ALS systems (Kükenbrink *et al.*, 2017), larger biases in quantified biomass from ALS and also space-borne LiDAR systems can be expected. For larger-scale analysis of the radiative transfer through forest ecosystems, or for spectroscopy sensor simulations (as shown in Schneider *et al.*, 2014), forest reconstruction from ALS measurements is a viable alternative to time-

consuming and more small scale focused close-range laser scanning techniques. ALS acquisitions further bring a certain advantage in terms of perspective, especially in conjunction with large scale imaging spectroscopy sensor simulations. Larger occluded space in the understory will have negligible impact on simulations of such sensors that mainly measure the top of canopy.

In Chapter 3 we showed that a dense TLS scan pattern and the combination of acquisitions from within and above the canopy results in a 3D representation of the forest structure in unprecedented levels of detail with minimal occlusion as quantified by using the approach described in Chapter 2. This builds the baseline for a high detail 3D radiative transfer model parameterization for the modelling of complex light-matter interactions within the canopy.

In Chapter 4 we finally used the 3D point cloud acquired and analyzed in Chapter 3 to reconstruct the forest and parameterize the DART model based on the structural information retrieved from close-range laser scanning as well as spectroscopy measurements. This allowed us to simulate the distribution of solar radiation within the forest canopies in very high resolution in the horizontal, vertical as well as temporal domain. 3D radiative transfer modeling of the light regime in forest ecosystems is not a completely new research topic (e.g. Côté *et al.*, 2009; Morton *et al.*, 2016; Musselman *et al.*, 2015; Widlowski *et al.*, 2014), but, to our knowledge, no study was able to reconstruct and model the complex 3D light regime at this level of detail. Calders *et al.* (2018) was able to reconstruct the 3D forest structure at a similar level of detail using TLS acquisitions, however they did not use this forest reconstruction to simulate the 3D distribution of solar radiation within the canopy. The detailed information on how solar radiation is scattered within the canopy can give us important insights into forest ecosystem functioning, productivity as well as into species competition and coexistence. This will further improve radiative transfer approximations in dynamic global vegetation models (DGVMs) (see Fisher *et al.*, 2017), further advancing the understanding of light distribution within a forest canopy also at larger scales. Enabling more accurate radiative transfer modelling on larger scales may further help improve higher level vegetation products derived from e.g. MODIS data, which often rely on coupled radiative transfer approximations for satellite data processing (e.g. Knyazikhin *et al.*, 1998a,b; Myneni *et al.*, 1997; Pisek & Chen, 2007).

A more detailed analysis on the influence of vegetation canopies on the surrounding irradiance field was given in Chapter 5, where we simulated the spectrally resolved (300 - 2500 nm) 3D irradiance field around an isolated tree. The findings of this contribution are two-fold. Firstly, complex 3D vegetation canopies can have a significant impact on the irradiance field around it, possibly introducing biases in vegetation parameters retrieved from imaging spectroscopy data. Such products often rely on accurate surface irradiance estimates. However, most approaches do not account for such small-scale, vegetation induced adjacency effects resulting in

significant biases in the retrieved products. Secondly, due to extensive *in-situ* irradiance reference measurements conducted in this study using field spectroradiometers, we were able to validate DART modelled irradiances. This showed us first of all a good performance of DART in modelling irradiance values over the whole simulated spectral domain (300 - 2500 nm). Secondly the applicability of the DART model was proven for the simulation of complex light regimes within forest canopies (Chapter 4). In Chapter 4 we further added to the complexity by not just analysing the 3D light regime around a single isolated tree, but how multiple trees shape the irradiance field within a forest. Further research is needed in order to analyse how different individuals affect light availability within a forest canopy.

6.3 Final considerations and future directions

The findings portrayed in this thesis bring forward some open questions not yet thoroughly discussed in the individual chapters. These open issues highlight various research opportunities for the future. In the following sections, some open issues and potential future directions are discussed.

6.3.1 Open issues

The findings portrayed in Chapter 4 and 5 both suggest that leaf optical properties only have a minor influence on the modelled light regime in vegetation canopies. In both studies, leaf optical properties are solely described by their reflectance and transmittance characteristics as measured by a leaf-probe (bi-directional reflectance (hot-spot) measurements according to nomenclature by (Schaepman-Strub *et al.*, 2006)) or an integrating sphere (commercial integrating spheres usually employ a directional-hemispherical illumination-view geometry (Hovi *et al.*, 2017)). Geometrical scattering characteristics or so-called specular reflectance characteristics cannot be resolved with such measurements and bi-directional reflectance distribution function (BRDFs) can therefore not be retrieved (Hovi *et al.*, 2017). Therefore, all scattering elements (i.e. leaves, bark) are parameterized as lambertian scatterers, completely neglecting the geometrical scattering aspects of the different scatterers. Especially in the tropics, however, it is assumed that the often waxy surface of the leaves of many species could have a significant specular reflectance term, possibly affecting the distribution of light within the canopy (Bone *et al.*, 1985). DART is able to include a specular term for the leaf optical properties, therefore the influence of specular reflectance on the distribution of light within the canopy could be modelled. However, measurements of BRDFs of small leaves are still scarce (e.g. Biliouris *et al.*, 2007; Bousquet *et al.*, 2005) and should therefore be a focus area for future studies. Storage of such measurements in spectral libraries such as the SPECCHIO database (Hueni *et al.*, 2009) would ensure a broad and long-term data availability. Additionally,

effects of leave curvature on light scattering and photosynthesis have been reported (e.g. Smith *et al.*, 1997), however its impact on the distribution of solar light within the canopy is a further subject for future studies.

Another generalizing assumption taken for the parameterization of the DART model is the definition of the leaf angle distribution (LAD). LAD was defined to be constant for the whole study sites based on literature values or plot-level hemispherical photographs. However, studies suggest that LAD can vary largely within the canopy (e.g. Vicari *et al.*, 2019). Three-dimensionally resolved information on the leaf inclination angles would therefore be beneficial for a more accurate parameterization of the forest canopy within DART. The high point-densities found in TLS measurements were found to enable a retrieval of leaf-inclination angles from TLS measurements with high accuracy (Li *et al.*, 2018; Liu *et al.*, 2019; Vicari *et al.*, 2019). An accurate parameterization of leaf inclination for each turbid medium voxel should therefore be considered for future studies. However, limitations of the achievable level of detail in 3D canopy reconstructions exist. Due to wind, the acquired point cloud resembles more a turbid medium than a collection of discrete objects (i.e. leaves), making the retrieval of accurate leaf inclination angles difficult.

In many studies on the radiative transfer within forest canopies (e.g. Morton *et al.*, 2016; Schneider *et al.*, 2014), wood structure is often inaccurately represented or neglected all together, even though wood structure is known to have significant effects on the radiative transfer in forest canopies (Malenovsky *et al.*, 2008). In this thesis we introduced a simple approach to extract woody structure from the LiDAR point-cloud based on differences in reflected intensities between woody and leaf material. A more sophisticated approach would be the use of a quantitative structure model (QSM) to reconstruct the woody structure from laser point clouds (see e.g. Åkerblom *et al.*, 2017; Calders *et al.*, 2018; Hackenberg *et al.*, 2015; Raumonen *et al.*, 2013, 2015). While such an approach would be applicable for the temperate forest site, with nearly no understorey growth, QSM models often fail in dense tropical forests due to the dense understorey often occluding parts of the lower tree trunks. Future studies should focus on improving QSM performance in dense tropical forests, which would also improve the parameterization of the woody structure in radiative transfer models, which has an arguably strong influence on the distribution of light within the canopy. However, limitations of the level of detail in wood structure reconstruction can be expected, as smaller branches or twigs are not sufficiently resolved in the acquired 3D point cloud (Abegg *et al.*, submitted).

6.3.2 From local to regional and global scale

A larger drawback of the portrayed framework for modelling complex light-matter interactions within forest canopies is the relatively small scale applicability of this approach. In Chapter 3 and 4 we only analysed a forest patch of 60 x 60 m in size. However, canopy structure, species composition and therefore also the distribution

of light within the canopy vary strongly in space and time. A general conclusion for the inter-play between forest structure and light availability based on the two contrasting forest plots portrayed in Chapters 3 and 4 can therefore not be drawn. This thesis lays out a framework for further analysis of the light regime in different forest plots or for benchmarking the needed complexity for achieving the level of accuracy needed for different applications at varying scales (see also Section 6.3.4).

For light regime analysis at larger scales, the time consuming nature of acquiring high density TLS acquisitions may be a limitation of the portrayed approach. Laser scanning acquisitions on UAV platforms could increase the scale of such analysis with only minor compromises concerning level of detail in acquired forest structure information (Morsdorf *et al.*, 2018; Schneider *et al.*, 2019). Regional, up to national scale acquisitions of forest structural information could be acquired from ALS acquisitions, however with larger compromises especially in lower canopy layers as discussed in Chapter 2 (Kükenbrink *et al.*, 2017). These larger scale applications would also call for some reduction in detail for the radiative transfer modelling, as the complex 3D RT models such as DART require substantial computational power. Also for this, an extensive benchmark testing of the sensitivity of certain input parameters to the RT models (e.g. vegetation density, leaf optical properties, leaf angle distribution, voxel resolution etc.) would be necessary (see also Section 6.3.4).

The quest for near-global information on forest structure is also a major incentive for the spaceborne LiDAR mission Global Ecosystem Dynamics Investigation (GEDI, Stavros *et al.*, 2017) which was deployed in November 2018 to the International Space Station (ISS). The acquired near-global coverage (up to 50° North and South) could deliver the highly needed structural information for the parameterisation of large-scale radiative transfer and dynamic global vegetation models, though at a much reduced level of detail. With a footprint of 25 m, GEDI will likely sample an integrated signal of multiple trees. The accuracy at which the 3D structure of forests with varying canopy densities can be derived from these measurements has yet to be analysed. Recent studies simulating the GEDI waveform showed good results in retrieving forest structural information when comparing the simulated waveform metrics against those derived from large-footprint, full-waveform lidar data from NASA's airborne Land, Vegetation, and Ice Sensor (LVIS) (Hancock *et al.*, 2019). It has yet to be analysed, if such large-footprint data on forest structure would be feasible to study the radiative transfer through forest ecosystem at very large scales.

Radiative transfer model based sensor fusion of LiDAR and imaging spectroscopy instruments could potentially help in acquiring accurate, large scale structural and physiological forest canopy parameters from large footprint laser instruments and space or airborne imaging spectrometer data using a Look Up Table (LUT) approach (Koetz *et al.*, 2007). Furthermore, machine learning based radiative transfer model emulation showed promising results, decreasing the computational demands of radiative transfer models by approximating their output by means of statistical

machine learning (e.g Gómez-Dans *et al.*, 2016; Rivera *et al.*, 2015; Verrelst *et al.*, 2016; Vicent *et al.*, 2018). This is a promising approach, possibly allowing for large- and even global-scale analysis of the radiative transfer through forests without the computational restrictions inherent in physical radiative transfer models.

6.3.3 From light availability to modelling of vegetation functioning

In this thesis, we mainly studied the solar energy (measured in W m^{-2}) irradiant in 3D space. This allows us to study 3D light availability and distribution in forest ecosystems. However, direct conclusions on light usage or vegetation functioning cannot be drawn from these modelled energy flux densities as photosynthesis depends on the number of photons received (also called photosynthetic photon flux density (PPFD), measured in μmol m^{-2} s^{-1}), rather than the photon energy (Jones *et al.*, 2003). As the conversion from energy flux, or irradiance, to photon flux density is dependent on wavelength and therefore varies within the PAR wavelength region (400 - 700 nm), a straight forward conversion from simulated PAR irradiance to PPFD is only possible based on approximations or by simulating more individual wavelengths instead of a single waveband with a width covering the PAR wavelength region as performed in Chapter 4.

In order to advance the analysis of vegetation functioning, modelled absorbed photoysnthetically active radiation (APAR) should be converted to light usage. Shadowing and light saturation effects can affect light utilization of photosynthetically active materials (e.g. Doughty & Goulden, 2009; Morton *et al.*, 2016). In order to establish a three-dimensionally resolved map of light utilization, a model converting the absorbed photosynthetically active radiation as modelled by DART to light utilization considering limiting factors would have to be established. For this, additional measurements of the photosynthetic light response curve at leaf-level for the different plant species for different light conditions (shaded, sunlit, saturated etc.) are necessary, following the approach described in e.g. Kitajima *et al.* (1997), or have to be taken from literature (Morton *et al.*, 2016). This would allow us to analyse 3D variations in light utilization within the canopy and could give us important insights into vegetation functioning, species competition and coexistence in regards to different light usage strategies.

When analysing different light usage strategies it might be also of interest to analyse solar radiation outside the strict PAR wavelength region. Chen & Blankenship (2011) reported an adaptation in certain plants under light-limiting conditions to be able to utilize light at wavelengths greater than 700 nm for photosynthesis due to modifications in the plant's chlorophyll (Chen *et al.*, 2010; Chen & Blankenship, 2011; Miyashita *et al.*, 1996).

6.3.4 Benchmarking for Dynamic Vegetation and Earth System models

Fisher *et al.* (2017) highlighted the importance of solar radiation partitioning and the physics of shading within and between individuals and cohorts for further development of dynamic global vegetation models (DGVMs). In this thesis we showed an approach to reconstruct forest structure and analyse complex light-matter interactions for any forest canopy at unprecedented level of detail. How the knowledge gained in this thesis can be implemented into DGVMs, such as the Ecosystem Demography model ED (Moorcroft *et al.*, 2001) or ED2 (Medvigy *et al.*, 2009), is still an unresolved challenge. For larger scale models, the level of detail shown in this thesis might be too high to be handled efficiently. The modelling framework established in this thesis could also be used to evaluate sensitivities of structural and physiological parameters on the distribution of light in forest ecosystems in more detail. This would allow us to find compromises between complexity of forest reconstruction and the level of accuracy needed for an improved modelling of light-matter interactions in DGVMs. In Chapter 4 we showed that the light extinction profiles estimated by using the Beer-Lambert law of light extinction can deliver a reasonable approximation of the more complex simulated light extinction profiles using the DART model. However, such an approximation does not account for diffuse illumination or multiple scattering and therefore shows relatively large biases (up to 30% in upper canopy layers) compared to the more complex DART simulations. Nevertheless, this finding showed that a reasonable approximation of the light extinction profile could be retrieved, as long as we have detailed information on the canopy structure. Unfortunately, detailed contiguous information on the canopy structure at larger scales are still rare (e.g. Leiterer *et al.*, 2015b; Wulder *et al.*, 2012). With data from the GEDI space-borne laser slowly becoming available, the pathway is set for near-global scale analysis on variations in canopy structure (see also 6.3.2).

When we are able to accurately acquire 3D forest structure information and model the light interactions within varying forest canopies at larger scales, we would be able to massively improve large scale DGVMs and Earth system models, giving us important information on the functioning, development and productivity of forest ecosystems. With forests being a major carbon sink, this would further have large implications on the understanding of the global carbon cycle and the development of Earth's climate.

6.4 References

Abegg M, Kükenbrink D, Zell J, Schaepman ME, Morsdorf F (2017) Terrestrial laser scanning for forest inventories-tree diameter distribution and scanner location impact on occlusion. *Forests*, **8**, 1–29.

Abegg M, Ruedi B, Schaepman ME, Morsdorf F (????) Terrestrial Laser Scanning for Forest Inventories - Impact of Beam Diameter and Scanning Approach on Point Cloud Quality. *IEEE Transactions on Geoscience and Remote Sensing*, **submitted**, 1–15.

Åkerblom M, Raumonen P, Mäkipää R, Kaasalainen M (2017) Automatic tree species recognition with quantitative structure models. *Remote Sensing of Environment*, **191**, 1–12.

Alton PB, Ellis R, Los SO, North PR (2007) Improved global simulations of gross primary product based on a separate and explicit treatment of diffuse and direct sunlight. *Journal of Geophysical Research Atmospheres*, **112**, 1–12.

Asner GP, Mascaro J, Muller-Landau HC, *et al.* (2012) A universal airborne LiDAR approach for tropical forest carbon mapping. *Oecologia*, **168**, 1147–1160.

Baldocchi DD, Wilson KB, Gu L (2002) How the environment, canopy structure and canopy physiological functioning influence carbon, water and energy fluxes of a temperate broad-leaved deciduous forest - An assessment with the biophysical model CANOAK. *Tree Physiology*, **22**, 1065–1077.

Béland M, Baldocchi DD, Widlowski JL, Fournier RA, Verstraete MM (2014a) On seeing the wood from the leaves and the role of voxel size in determining leaf area distribution of forests with terrestrial LiDAR. *Agricultural and Forest Meteorology*, **184**, 82–97.

Béland M, Widlowski JL, Fournier RA (2014b) A model for deriving voxel-level tree leaf area density estimates from ground-based LiDAR. *Environmental Modelling & Software*, **51**, 184–189.

Béland M, Widlowski JL, Fournier RA, Côté JF, Verstraete MM (2011) Estimating leaf area distribution in savanna trees from terrestrial LiDAR measurements. *Agricultural and Forest Meteorology*, **151**, 1252–1266.

Biliouris D, Verstraeten WW, Dutré P, Van Aardt JA, Muys B, Coppin P (2007) A Compact Laboratory Spectro-Goniometer (CLabSpeG) to assess the BRDF of materials. Presentation, calibration and implementation on Fagus sylvatica L. leaves. *Sensors*, **7**, 1846–1870.

Bone RA, Lee DW, Norman JM (1985) Epidermal cells functioning as lenses in leaves of tropical rain-forest shade plants. *Applied optics*, **24**, 1408–1412.

Bousquet L, Lachérade S, Jacquemoud S, Moya I (2005) Leaf BRDF measurements and model for specular and diffuse components differentiation. *Remote Sensing of Environment*, **98**, 201–211.

Calders K, Origo N, Burt A, *et al.* (2018) Realistic Forest Stand Reconstruction from Terrestrial LiDAR for Radiative Transfer Modelling. *Remote Sensing 2018, Vol. 10, Page 933*, **10**, 933.

Chen M, Blankenship RE (2011) Expanding the solar spectrum used by photosynthesis. *Trends in Plant Science*, **16**, 427–431.

Chen M, Schliep M, Willows RD, Cai ZL, Neilan BA, Scheer H (2010) A Red-Shifted Chlorophyll. *Science*, **329**, 1318–1319.

Côté JF, Widlowski JL, Fournier RA, Verstraete MM (2009) The structural and radiative consistency of three-dimensional tree reconstructions from terrestrial lidar. *Remote Sensing of Environment*, **113**, 1067–1081.

Damm A, Guanter L, Paul-Limoges E, *et al.* (2015) Far-red sun-induced chlorophyll fluorescence shows ecosystem-specific relationships to gross primary production: An assessment based on observational and modeling approaches. *Remote Sensing of Environment*, **166**, 91–105.

Disney M (2018) Terrestrial LiDAR: a 3D revolution in how we look at trees. *New Phytologist*, pp. 0–2.

Doughty CE, Goulden ML (2009) Are tropical forests near a high temperature threshold? *Journal of Geophysical Research: Biogeosciences*, **114**, 1–12.

Fassnacht FE, Latifi H, Hartig F (2018) Using synthetic data to evaluate the benefits of large field plots for forest biomass estimation with LiDAR. *Remote Sensing of Environment*, **213**, 115–128.

Fisher RA, Koven CD, Anderegg WRL, *et al.* (2017) Vegetation Demographics in Earth System Models: a review of progress and priorities. *Global Change Biology*, pp. 1–20.

Gamon J, Peñuelas J, Field C (1992) A narrow-waveband spectral index that tracks diurnal changes in photosynthetic efficiency.

Gamon JA, Kovalchuck O, Wong CY, Harris A, Garrity SR (2015) Monitoring seasonal and diurnal changes in photosynthetic pigments with automated PRI and NDVI sensors. *Biogeosciences*, **12**, 4149–4159.

Gamon JA, Serrano L, Surfus JS (1997) The photochemical reflectance index: An optical indicator of photosynthetic radiation use efficiency across species, functional types, and nutrient levels. *Oecologia*, **112**, 492–501.

Gastellu-Etchegorry JP, Lauret N, Yin T, *et al.* (2017) DART: Recent advances in remote sensing data modeling with atmosphere, polarization, and chlorophyll fluorescence. *IEEE Journal of Selected Topics in Applied Earth Observations and Remote Sensing*, **10**, 2640–2649.

Gastellu-Etchegorry JP, Yin T, Lauret N, *et al.* (2015) Discrete Anisotropic Radiative Transfer (DART 5) for Modeling Airborne and Satellite Spectroradiometer and LIDAR Acquisitions of Natural and Urban Landscapes. *Remote Sensing*, **7**, 1667–1701.

Gitelson AA, Keydan GP, Merzlyak MN (2006) Three-band model for noninvasive estimation of chlorophyll, carotenoids, and anthocyanin contents in higher plant leaves. *Geophysical Research Letters*, **33**, 2–6.

Gómez-Dans JL, Lewis PE, Disney M (2016) Efficient emulation of radiative transfer codes using gaussian processes and application to land surface parameter inferences. *Remote Sensing*, **8**, 1–32.

Grau E, Durrieu S, Fournier R, Gastellu-etchegorry Jp, Yin T (2017) Estimation of 3D vegetation density with Terrestrial Laser Scanning data using voxels . A sensitivity analysis of influencing parameters . *Remote Sensing of Environment*, **191**, 373–388.

Hackenberg J, Spiecker H, Calders K, Disney M, Raumonen P (2015) SimpleTree - An efficient open source tool to build tree models from TLS clouds. *Forests*, **6**, 4245–4294.

Hancock S, Armston J, Hofton M, *et al.* (2019) The GEDI Simulator: A Large-Footprint Waveform Lidar Simulator for Calibration and Validation of Spaceborne Missions. *Earth and Space Science*, **6**, 294–310.

Hilker T, van Leeuwen M, Coops NC, Wulder Ma, Newnham GJ, Jupp DLB, Culvenor DS (2010) Comparing canopy metrics derived from terrestrial and airborne laser scanning in a Douglas-fir dominated forest stand. *Trees*, **24**, 819–832.

Hovi A, Forsström P, Mõttus M, Rautiainen M (2017) Evaluation of Accuracy and Practical Applicability of Methods for Measuring Leaf Reflectance and Transmittance Spectra. *Remote Sensing*, **10**, 25.

Hueni A, Nieke J, Schopfer J, Kneubühler M, Itten KI (2009) The spectral database SPECCHIO for improved long-term usability and data sharing. *Computers and Geosciences*, **35**, 557–565.

Jones HG, Archer N, Rotenberg E, Casa R (2003) Radiation measurement for plant ecophysiology. *Journal of Experimental Botany*, **54**, 879–889.

Kaartinen H, Hyyppä J, Yu X, *et al.* (2012) An international comparison of individual tree detection and extraction using airborne laser scanning. *Remote Sensing*, **4**, 950–974.

Keenan TF, Niinemets Ü (2017) Global leaf trait estimates biased due to plasticity in the shade. *Nature Plants*, **3**, 16201.

Kitajima K, Mulkey SS, Wright SJ (1997) Seasonal leaf phenotypes in the canopy of a tropical dry forest: Photosynthetic characteristics and associated traits. *Oecologia*, **109**, 490–498.

Knyazikhin Y, Martonchik J, Diner D, Myneni R, Verstraete M, Pinty B, Gobron N (1998a) Estimation of vegetation canopy leaf area index and fraction from atmosphere-corrected MISR data. *Journal of Geophysical Research*, **103**, 239–256.

Knyazikhin Y, Martonchik JV, Diner DJ, Myneni RB (1998b) Estimation of vegetation canopy leaf area index and fraction of absorbed photosynthetically active .... *Journal of Geophysical Research*, **103**.

Ko C, Sohn G, Remmel TK (2012) The impact of LiDAR point density on classifying tree genus: using geometric features and vertical profile features. In: *SilviLaser 2012*, pp. 67–74. Vancouver, Canada (September 16-19).

Koetz B, Sun G, Morsdorf F, Ranson K, Kneubühler M, Itten K, Allgöwer B (2007) Fusion of imaging spectrometer and LIDAR data over combined radiative transfer models for forest canopy characterization. *Remote Sensing of Environment*, **106**, 449–459.

Korpela I, Hovi A, Morsdorf F (2012) Understory trees in airborne LiDAR data - Selective mapping due to transmission losses and echo-triggering mechanisms. *Remote Sensing of Environment*, **119**, 92–104.

Kükenbrink D, Hueni A, Schneider FD, Damm A, Gastellu-Etchegorry JP, Schaepman ME, Morsdorf F (2019) Mapping the Irradiance Field of a Single Tree: Quantifying Vegetation-Induced Adjacency Effects. *IEEE Transactions on Geoscience and Remote Sensing*, pp. 1–18.

Kükenbrink D, Schneider FD, Leiterer R, Schaepman ME, Morsdorf F (2017) Quantification of hidden canopy volume of airborne laser scanning data using a voxel traversal algorithm. *Remote Sensing of Environment*, **194**, 424–436.

Larsen M, Eriksson M, Descombes X, Perrin G, Brandtberg T, Gougeon FA (2011) Comparison of six individual tree crown detection algorithms evaluated under varying forest conditions. *International Journal of Remote Sensing*, **32**, 5827–5852.

Leiterer R, Furrer R, Schaepman ME, Morsdorf F (2015a) Forest canopy-structure characterization: A data-driven approach. *Forest Ecology and Management*, **358**, 48–61.

Leiterer R, Torabzadeh H, Furrer R, Schaepman M, Morsdorf F (2015b) Towards Automated Characterization of Canopy Layering in Mixed Temperate Forests Using Airborne Laser Scanning. *Forests*, **6**, 4146–4167.

Li Y, Su Y, Hu T, Xu G, Guo Q (2018) Retrieving 2-D Leaf Angle Distributions for Deciduous Trees from Terrestrial Laser Scanner Data. *IEEE Transactions on Geoscience and Remote Sensing*, **56**, 4945–4955.

Lim K, Hopkinson C, Treitz P (2008) Examining the effects of sampling point densities on laser canopy height and density metrics. *The Forestry Chronicle*, **84**, 876–885.

Liu J, Skidmore AK, Wang T, *et al.* (2019) Variation of leaf angle distribution quantified by terrestrial LiDAR in natural European beech forest. *ISPRS Journal of Photogrammetry and Remote Sensing*, **148**, 208–220.

Malenovsky Z, Martin E, Homolova L, *et al.* (2008) Influence of woody elements of a Norway spruce canopy on nadir reflectance simulated by the DART model at very high spatial resolution. *Remote Sensing of Environment*, **112**, 1–18.

McElhinny C, Gibbons P, Brack C, Bauhus J (2005) Forest and woodland stand structural complexity: Its definition and measurement. *Forest Ecology and Management*, **218**, 1–24.

Medvigy D, Wofsy SC, Munger JW, Hollinger DY, Moorcroft PR (2009) Mechanistic scaling of ecosystem function and dynamics in space and time: Ecosystem Demography model version 2. *Journal of Geophysical Research: Biogeosciences*, **114**, 1–21.

Miyashita H, Ikemoto H, Kurano N, Adachi K, Chihara M, Miyachi S (1996) Chlorophyll d as a major pigment. *Nature*, **383**, 402.

Momo Takoudjou S, Ploton P, Sonké B, *et al.* (2018) Using terrestrial laser scanning data to estimate large tropical trees biomass and calibrate allometric models: A comparison with traditional destructive approach. *Methods in Ecology and Evolution*, **9**, 905–916.

Monsi M, Saeki T (2005) On the factor light in plant communities and its importance for matter production. 1953. *Annals of botany*, **95**, 549–67.

Moorcroft APR, Hurtt GC, Pacala SW (2001) A Method for Scaling Vegetation Dynamics : The Ecosystem Demography Model (ED). *Ecological Monographs*, **71**, 557–585.

Morsdorf F, Kükenbrink D, Schneider FD, Abegg M, Schaepman ME (2018) Close-range laser scanning in forests: towards physically based semantics across scales. *Interface Focus*, **8**, 20170046.

Morton DC, Nagol J, Carabajal CC, *et al.* (2014) Amazon forests maintain consistent canopy structure and greenness during the dry season. *Nature*, **506**, 221–4.

Morton DC, Rubio J, Cook BD, *et al.* (2016) Amazon forest structure generates diurnal and seasonal variability in light utilization. *Biogeosciences*, **13**, 2195–2206.

Musselman KN, Pomeroy JW, Link TE (2015) Variability in shortwave irradiance caused by forest gaps: Measurements, modelling, and implications for snow energetics. *Agricultural and Forest Meteorology*, **207**, 69–82.

Myneni RB, Nemani RR, Running SW (1997) Myneni, Nemani, Running_1997_Estimation of Global Leaf Area Index and Absorbed Par Using Radiative Transfer Models.pdf.

Næsset E (2004) Practical large-scale forest stand inventory using a small-footprint airborne scanning laser. *Scandinavian Journal of Forest Research*, **19**, 164–179.

Niinemets Ü (2007) Photosynthesis and resource distribution through plant canopies. *Plant, Cell & Environment*, **30**, 1052–1071.

Niinemets U (2012) Optimization of foliage photosynthetic capacity in tree canopies: towards identifying missing constraints. *Tree Physiology*, **32**, 505–509.

Niinemets Ü, Keenan TF (2012) Measures of Light in Studies on Light-Driven Plant Plasticity in Artificial Environments. *Frontiers in Plant Science*, **3**, 1–21.

Niinemets Ü, Valladares F, Ceulemans R (2003) Leaf-level phenotypic variability and plasticity of invasive Rhododendron pontificum and non- . . . . *Plant Cell Environ*, pp. 941–956.

Pinty B, Gobron N, Widlowski Jl, *et al.* (2001) Radiation transfer model intercomparison (RAMI) exercise. *Journal of Geophysical Research: Atmospheres*, **106**, 11937–11956.

Pinty B, Widlowski JL, Taberner M, *et al.* (2004) Radiation Transfer Model Intercomparison (RAMI) exercise: Results from the second phase. *Journal of Geophysical Research: Atmospheres*, **109**, n/a–n/a.

Pisek J, Chen JM (2007) Comparison and validation of MODIS and VEGETATION global LAI products over four BigFoot sites in North America. *Remote Sensing of Environment*, **109**, 81–94.

Raumonen P, Casella E, Calders K, *et al.* (2015) Massive-Scale Tree Modelling From Tls Data. *ISPRS Annals of Photogrammetry, Remote Sensing and Spatial Information Sciences*, **II-3/W4**, 189–196.

Raumonen P, Kaasalainen M, Åkerblom M, *et al.* (2013) Fast Automatic Precision Tree Models from Terrestrial Laser Scanner Data. *Remote Sensing*, **5**, 491–520.

Rivera JP, Verrelst J, Gómez-Dans J, Muñoz-Marí J, Moreno J, Camps-Valls G (2015) An emulator toolbox to approximate radiative transfer models with statistical learning. *Remote Sensing*, **7**, 9347–9370.

Roberts J, Tesfamichael S, Gebreslasie M, van Aardt J, Ahmed F (2007) Forest structural assessment using remote sensing technologies: an overview of the current state of the art. *Southern Hemisphere Forestry Journal*, **69**, 183–203.

Sapijanskas J, Paquette A, Potvin C, Kunert N, Loreau M (2014) Tropical tree diversity enhances light capture through crown plasticity and spatial and temporal niche differences. *Ecology*, **95**, 2479–2492.

Schaepman ME, Jehle M, Hueni A, *et al.* (2015) Advanced radiometry measurements and Earth science applications with the Airborne Prism Experiment (APEX). *Remote Sensing of Environment*, **158**, 207–219.

Schaepman ME, Ustin SL, Plaza AJ, Painter TH, Verrelst J, Liang S (2009) Earth system science related imaging spectroscopyAn assessment. *Remote Sensing of Environment*, **113**, S123–S137.

Schaepman-Strub G, Schaepman M, Painter T, Dangel S, Martonchik J (2006) Reflectance quantities in optical remote sensingdefinitions and case studies. *Remote Sensing of Environment*, **103**, 27–42.

Schneider FD, Kükenbrink D, Schaepman ME, Schimel DS, Morsdorf F (2019) Quantifying 3D structure and occlusion in dense tropical and temperate forests using close-range LiDAR. *Agricultural and Forest Meteorology*, **268**, 249–257.

Schneider FD, Leiterer R, Morsdorf F, Gastellu-Etchegorry JP, Lauret N, Pfeifer N, Schaepman ME (2014) Simulating imaging spectrometer data: 3D forest modeling based on LiDAR and in situ data. *Remote Sensing of Environment*, **152**, 235–250.

Schneider FD, Morsdorf F, Schmid B, Petchey OL, Hueni A, Schimel DS, Schaepman ME (2017) Mapping functional diversity from remotely sensed morphological and physiological forest traits. *Nature Communications*, **8**, 1441.

Shugart HH, Saatchi S, Hall FG (2010) Importance of structure and its measurement in quantifying function of forest ecosystems. *Journal of Geophysical Research: Biogeosciences*, **115**, 1–16.

Sitch S, Smith B, Prentice IC, *et al.* (2003) Evaluation of ecosystem dynamics, plant geography and terrestrial carbon cycling in the LPJ dynamic global vegetation model. *Global Change Biology*, **9**, 161–185.

Smith WK, Vogelmann TC, DeLucia EH, Bell DT, Shepherd KA (1997) Leaf Form and Photosynthesis. *BioScience*, **47**, 785–793.

Stark SC, Enquist BJ, Saleska SR, *et al.* (2015) Linking canopy leaf area and light environments with tree size distributions to explain Amazon forest demography. *Ecology Letters*, **18**, 636–645.

Stark SC, Leitold V, Wu JL, *et al.* (2012) Amazon forest carbon dynamics predicted by profiles of canopy leaf area and light environment. *Ecology Letters*, **15**, 1406–1414.

Stavros EN, Schimel D, Pavlick R, *et al.* (2017) ISS observations offer insights into plant function. *Nature Ecology and Evolution*, **1**.

Stovall AE, Vorster AG, Anderson RS, Evangelista PH, Shugart HH (2017) Non-destructive aboveground biomass estimation of coniferous trees using terrestrial LiDAR. *Remote Sensing of Environment*, **200**, 31–42.

Treitz P, Lim K, Woods M, Pitt D, Nesbitt D, Etheridge D (2012) LiDAR Sampling Density for Forest Resource Inventories in Ontario, Canada. *Remote Sensing*, **4**, 830–848.

Ustin SL, Gitelson Aa, Jacquemoud S, Schaepman M, Asner GP, Gamon Ja, Zarco-Tejada P (2009) Retrieval of foliar information about plant pigment systems from high resolution spectroscopy. *Remote Sensing of Environment*, **113**, S67–S77.

Valladares F (2003) Light Heterogeneity and Plants: from Ecophysiology to Species Coexistence and Biodiversity. In: *Progress in botany* (ed. K Esser, U Lüttge WB&FH), pp. 439–471. Springer Berlin Heidelberg.

Valladares F, Laanisto L, Niinemets Ü, Zavala MA (2016) Shedding light on shade: ecological perspectives of understorey plant life. *Plant Ecology & Diversity*, **9**, 1–15.

van Leeuwen M, Nieuwenhuis M (2010) Retrieval of forest structural parameters using LiDAR remote sensing. *European Journal of Forest Research*, **129**, 749–770.

Vastaranta M, Kankare V, Holopainen M, Yu X, Hyyppä J, Hyyppä H (2012) Combination of individual tree detection and area-based approach in imputation of forest variables using airborne laser data. *ISPRS Journal of Photogrammetry and Remote Sensing*, **67**, 73–79.

Verrelst J, Sabater N, Rivera JP, Muñoz-Marí J, Vicent J, Camps-Valls G, Moreno J (2016) Emulation of leaf, canopy and atmosphere radiative transfer models for fast global sensitivity analysis. *Remote Sensing*, **8**, 1–27.

Vicari MB, Pisek J, Disney M (2019) New estimates of leaf angle distribution from terrestrial LiDAR: Comparison with measured and modelled estimates from nine broadleaf tree species. *Agricultural and Forest Meteorology*, **264**, 322–333.

Vicent J, Verrelst J, Rivera-Caicedo JP, Sabater N, Munoz-Mari J, Camps-Valls G, Moreno J (2018) Emulation as an Accurate Alternative to Interpolation in Sampling Radiative Transfer Codes. *IEEE Journal of Selected Topics in Applied Earth Observations and Remote Sensing*, **11**, 4918–4931.

Vincent G, Antin C, Laurans M, Heurtebize J, Durrieu S, Lavalley C, Dauzat J (2017) Mapping plant area index of tropical evergreen forest by airborne laser scanning. A cross-validation study using LAI2200 optical sensor. *Remote Sensing of Environment*, **198**, 254–266.

Widlowski JL, Côté JF, Béland M (2014) Abstract tree crowns in 3D radiative transfer models: Impact on simulated open-canopy reflectances. *Remote Sensing of Environment*, **142**, 155–175.

Widlowski JL, Mio C, Disney M, *et al.* (2015) The fourth phase of the radiative transfer model intercomparison (RAMI) exercise: Actual canopy scenarios and conformity testing. *Remote Sensing of Environment*, **169**, 418–437.

Widlowski JL, Pinty B, Clerici M, *et al.* (2011) RAMI4PILPS: An intercomparison of formulations for the partitioning of solar radiation in land surface models. *Journal of Geophysical Research: Biogeosciences*, **116**.

Widlowski JL, Taberner M, Pinty B, *et al.* (2007) Third Radiation Transfer Model Intercomparison (RAMI) exercise: Documenting progress in canopy reflectance models. *Journal of Geophysical Research*, **112**, 1–28.

Wulder Ma, White JC, Nelson RF, *et al.* (2012) Lidar sampling for large-area forest characterization: A review. *Remote Sensing of Environment*, **121**, 196–209.

Xue BL, Kumagai T, Iida S, *et al.* (2011) Influences of canopy structure and physiological traits on flux partitioning between understory and overstory in an eastern Siberian boreal larch forest. *Ecological Modelling*, **222**, 1479–1490.

Yang R, Friedl MA (2003) Modeling the effects of three-dimensional vegetation structure on surface radiation and energy balance in boreal forests. *Journal of Geophysical Research*, **108**, 8615.

Curriculum vitae

Daniel Kükenbrink

Education

2014–2019 **University of Zurich, PhD candidate at the Remote Sensing Laboratories**
- Joint Research Activity - HYLIGHT for the integration of airborne hyperspectral imagery and laser scanning data (European Facility for Airborne Research EUFAR)
- REFETREE - Nichtwaldreferenzen für Biomasse
  Research activity by the Federal Office for the Environment (FOEN)
- University Research Priority Program on Global Change and Biodiversity
  URPP GCB: T-UpScaleFuncTraits
- PhD thesis: *Light regime modelling in structurally complex forests*

2012–2014 **University of Zurich, Master of Science**
- Major: Geography
- Minor: Atmospheric and Climate Science at ETH Zurich
- Specialization: Remote Sensing
- Master Thesis: *Biomass estimation from polarimetric L-band SAR data over Swiss temperate forests*

2008–2012 **University of Zurich, Bachelor of Science**
- Major: Geography
- Minor: Physics
- Bachelor Thesis: *Soil moisture estimation using SAR data*

2002–2007 **Kantonsschule Im Lee, Winterthur, Matura**
- Profile: Mathematics and Natural Sciences
- Specialization: Biology and Chemistry
- Matura Thesis: *We're on the eve of destruction - The political content of rock music during the Vietnam War.*

Teaching and supervision

2014–2019	Teaching assistant for various courses within the Department of Geography, University of Zurich. Namely: GEO113 Fernerkundung und Geographische Informationswissenschaft I - Earth Perspectives, GEO123 Fernerkundung und Geographische Informationswissenschaft II - Introduction to Cartography and Geovisualisation, GEO229 Small Group Teaching in Geography, GEO233 Fernerkundung und Geographische Informationswissenschaft III - Grundlagen Fernerkundung
2014–2019	Teaching and organization of outreach activities within the RSL, University of Zurich. Namely: Lecture in GEO233 and RSL Colloquium, Scientifica 2015, 2017 & 2019
2017–2019	MSc co-supervision, Manuel Luck. Title: *Morphological Traits in a Temperate Forest: Comparing UAV-LS and TLS Point Clouds*

Graduate courses and training

- PhD Seminars I & II
- Graduate School Retreat Seminar (I & II)
- Principles and Theory in Geography
- Scientific Writing
- Project Management
- Voice Training and Presentation Skills
- Job hunting with a PhD
- Wirtschafts-Know-How
- Scientific programming with Python
- Time- and Self-Management for PhD candidates
- DART workshop in Toulouse
- Various Conference Visits (see Publications and conference contributions)

Publications and conference contributions

Publications

Kükenbrink, D., Hueni, A., Schneider, F.D., Damm, A., Gastellu-Etchegorry, J.-P., Schaepman, M.E., & Morsdorf, F. (2019). Mapping the Irradiance Field of a Single Tree: Quantifying Vegetation-Induced Adjacency Effects. *IEEE Transactions on Geoscience and Remote Sensing 1-18*

Schneider, F.D., **Kükenbrink, D.**, Schaepman, M.E., Schimel, D.S., & Morsdorf, F. (2019). Quantifying 3D structure and occlusion in dense tropical and temperate forests using close-range LiDAR. *Agricultural and Forest Meteorology 268, 249-257*.

Morsdorf, F., **Kükenbrink, D.**, Schneider, F.D., Abegg, M., & Schaepman, M.E. (2018). Close-range laser scanning in forests - towards physical-based semantics across scales. *Interface Focus 8 (2), 1-10*.

Abegg, M., **Kükenbrink, D.**, Zell, J., Schaepman, M.E., & Morsdorf, F. (2017). Terrestrial laser scanning for forest inventories-tree diameter distribution and scanner location impact on occlusion. *Forests 8, 1-29*.

Morsdorf, F., Eck, C., Zgraggen, C., Imbach, B., Schneider, F.D., & **Kükenbrink, D.** (2017). UAV-based LiDAR acquisition for the derivation of high-resolution forest and ground information. *Leading Edge 36, 566-570*.

Kükenbrink, D., Schneider, F.D., Leiterer, R., Schaepman, M.E., & Morsdorf, F. (2017). Quantification of hidden canopy volume of airborne laser scanning data using a voxel traversal algorithm. *Remote Sensing of Environment 194, 424-436*.

Kükenbrink, D., Leiterer, R., Schneider, F.D., Schaepman, M.E., & Morsdorf, F. (2015). Voxel based occlusion mapping and plant area index estimation from airborne laser scanning data. *Proceedings of SilviLaser 2015-September 28-30, 232-234*.

Articles to be published

Kükenbrink, D., Schneider F.D., Schmid, B., Gastellu-Etchegorry, J.P.,Schaepman M.E., & Morsdorf F. (under Review). Spatio-temporal modelling of light extinction in two contrasting forests. *Remote Sensing of Environment*.

Bruggisser M., Hollaus M., **Kükenbrink D.**, & Pfeifer N. (accepted). Comparison of forest structure metrics derived from UAV LiDAR and ALS data. *Geo-Spatial Week 2019*.

Damm A., Morsdorf F., **Kükenbrink D.**, Backofen C., Haghighi E., Fritsche L., & Paul-Limoges E. (in preparation). Remote sensing of forest gas exchange: Considerations derived from a topographic perspective. *To be submitted to: Global Change Biodiveristy as Technical Advance.*

Conference Talks

Kükenbrink D., Schneider F.D., Hueni A., Schaepman M.E., & Morsdorf F. (2018). Spatio-temporal modelling of the light regime: tropical vs. temperate forest. *ForestSat 2018. 1-5 October. University of Maryland.*

Kükenbrink D., Schneider F.D., Hueni A., Damm A., Gastellu-Etchegorry J.-P., Schaepman M.E., & Morsdorf F. (2018). Spatio-temporal modelling of the light regime in forest canopies. *Finnish-Estonian Remote Sensing Seminar. 4-5 June. Tartu, Estonia. (invited)*

Kükenbrink D., Schneider F.D., Hueni A., Morsdorf F., & Schaepman M.E. (2017). Shadow compensation for imaging spectroscopy data using the Discrete Anisotropic Radiative Transfer model DART. *10th EARSeL SIG Imaging Spectroscopy Workshop. 18-21 April. Zurich, Switzerland.*

Kükenbrink D., Schneider F.D., Hueni A., Morsdorf F., & Schaepman M.E. (2016). Shadow compensation for imaging spectroscopy data using a radiative transfer approach. *ForestSat 2016. 14-18 November. Santiago de Chile, Chile.*

Kükenbrink D., Leiterer R., Schneider F.D., Schaepman M.E., & Morsdorf F. (2015). Voxel based occlusion mapping and plant area index estimation from airborne laser scanning data. *SilviLaser 2015. 28-30 September. La Grande Motte, France.*

Conference Poster

Kükenbrink D., Schneider F.D., Schmid B., Gastellu-Etchegorry J.-P., Schaepman M.E., & Morsdorf F. (2019). Spatio-temporal modelling of light extinction in a temperate and tropical forest. *Global Change and Biodiversity: Integrating the impact of earth and world drivers across scales. 30 June - 4 July. Monte Verita, Switzerland.*

Schneider, F.D., **Kükenbrink, D.**, Schaepman, M.E., & Morsdorf, F. (2016). Mapping the 3D structure of a tropical rainforest using terrestrial laser scanning - a quality assessment. ForestSAT. 14-18 November. Santiago de Chile, Chile.

Acknowledgements

First of all, I would like to thank my supervisors and advisors Felix Morsdorf, Andreas Hueni and Michael Schaepman for their valuable support, the interesting discussions, as well as their guidance throughout the entire PhD. It has been a great pleasure to work together and profit from your experience and knowledge. I would also like to thank Romain Teyssier for his valuable inputs during the commitee meetings throughout the PhD, giving me an interesting perspective onto my work from outside the RSL and the Department of Geography. I would further like to thank Alexander Damm and Bernhard Schmid for their valuable support and feedback on my work in the later stages of my PhD.

A great thank you goes out to all my fellow colleagues at the Remote Sensing Laboratories. I would like to specifically thank my office mates Beni, Carla, Dominic, Fabian, Jonas, Liv, Manuel, Marius, Marta, and Meinrad with whom I had the pleasure to share the J24 office over the course of my PhD. I am thankful for all the great moments and the very comfy and relaxed work environment we could share together. I was so lucky to not only have shared the office with you, but that we could also experience several personal highlights together. Travelling to Borneo, Chile, Patagonia or the US for field work and conferences are just a few of those. I would like to specifically thank Christoph, Fabian, Isabelle, Moritz and Philip with whom I enjoyed many interesting discussions about work and personal life. The occasional breaks on the kicker table with Christoph, Felix, Hendrik, Reik, Rogier, my office mates and many others as well as several cycling trips with Christoph were great occasions to relax the mind and restore some energy. Also unforgettable are the several concert visits with Devis, Dominic, Michele and Rogier. The occasional after work beers and BBQs were great occasions to get to know each other and to enjoy after work life. A special thanks goes out to Philip who gave me the opportunity to also work for the NPOC alongside my PhD. This work opportunity gave me a great counter-part to my PhD work and helped me to increase my network in the Swiss remote sensing community, for which I am grateful.

I am very grateful that I was able to pursue my PhD at the Remote Sensing Laboratories and for all the opportunities offered to me here. I am especially thankful that I have been provided the opportunity to perform field work at the Laegern and Hölstein forest as well as in several cities in Switzerland within the REFETREE project. One of the biggest highlights throughout my PhD was the opportunity to help Fabian with his field work in the Lambir Hills National Park in Borneo, which I will never forget. All these field work opportunities have been successful and a great experience thanks to the help of Fabian, Felix, Eri, Ewa, Manuel, Basil, Joan, Reik, and Zhaoju. I am also thankful to Fabian Schneider, Reik Leiterer, Meinrad Abegg, Jean-Philippe

Gastellu-Etchegorry, Alexander Damm and Bernhard Schmid for their contributions to the manuscript at various stages.

Finally my sincerest gratitude goes to my family and friends. First and foremost I am deeply thankful for my beloved Lona, who always supported me with so much love and care, who always pushed me up again when I reached a valley of the roller-coaster ride that is the PhD. With you I am confident that I can master every challenge that lies ahead of me! My deepest gratitude goes to my parents Lydia and Günter and my sister Anja with her husband Philipp and their son Lio, whom I can never thank enough for their ongoing support. A special thank you goes to other family members, my dear friends, and their partners who always supported me, pushed me up again, distracted me or put a smile on my face: Ruth, Roland, Judith, Silas, Fabian, Barbara, Daniele, Jan, Marc, Mario, Nic, Olivier, Sabrina, Wingman, Lorenz, Dave, Jill, Olivia, Jeremy, Joel, Je, Jasmin, Julian, and many more I might have forgotten to mention here.

Thank you all!